TOPICS IN THE PHENOMENOLOGY OF TWO NON-MINIMAL MODELS OF SUPERSYMMETRY BREAKING

by

Todd S. Garon

A dissertation submitted in partial fulfillment of
the requirements for the degree of

Doctor of Philosophy

(Physics)

at the

UNIVERSITY OF WISCONSIN–MADISON

2016

Date of final oral examination: May 18th, 2016

The dissertation is approved by the following members of the Final Oral Committee:

Lisa L. Everett , Professor, Physics
Vernon Barger, Professor, Physics
Yang Bai, Assistant Professor, Physics
Pupa Gilbert, Professor, Physics
Paul Terry, Professor, Physics

ACKNOWLEDGMENTS

I would like the thank my advisor, Lisa Everett for her unending support and advice, she has has my deepest admiration. I would also like to thank my collaborators: Vernon Barger, Bryan Kaufman, Brent Nelson, and Alex Stuart; I couldn't have done this without you all. Thank you to my committee; Professors Barger, Gilbert, Bai, and Terry. I would like to thank, Daniel Crow, Josh Isaacs, William Cottrell, James Osborne, Ben Stefanek, Jon Brown, James, Hanson, Ken Flanagan, Jason Milhone, and Frank Morton Park for useful physics discussions, and Aimee and Reneé Lefkow for their support. To my parents and friends, thank you very much.

CONTENTS

LIST OF TABLES

LIST OF FIGURES

ABSTRACT

In this thesis we look at two non-minimal models of supersymmetry breaking. In the first model, we study the phenomenology of deflected mirage mediation, a scenario where gravity, anomaly, and gauge mediation contribute to the soft masses, in light of the 7 and 8 TeV runs of the Large Hadron Collider (LHC) and the dark matter direct detection results from XENON and LUX. We find that the parameter space admits models with both simplified and compressed spectra, which should be visible in the next run of the LHC. We also look at the parameter space from the bottom up, using the electroweak fine-tuning measure and find that there are large regions of parameter space which are not fine-tuned. In the second, we look at models of flavored gauge mediation and explore models with a non-abelian flavor symmetry. In these models the MSSM messenger Yukawa couplings are connected by the non-abelian symmetry, forcing us to model them simultaneously. We comment on the spectra and model building challengers in this paradigm.

1.1 The Standard Model

The Standard Model of high-energy particle physics (SM), formulated by Glashow, Weinberg, and Salam [1–3], is an extremely successful description of nature, surviving tests all the way to the tera-electronvolt (TeV) scale at the Large Hadron Collider (LHC). It is a quantum field theory in (3+1) dimensions with Poincaré invariance describing the strong, weak, and electromagnetic interactions. These forces are mediated by gauge bosons, which appear in the theory by imposing that the Lagrangian has certain local gauge symmetries. The SM has spin one gauge bosons, spin one half fermions, and a single spin zero scalar, the Higgs doublet. The field content is given in Table 1.1.

There is a gauge boson associated with each gauge symmetry. The massless gluons g of $SU(3)_c$ mediate the strong interaction. $SU(2)_L$ only acts on the left-chiral fermions. $U(1)_Y$ acts on both left- and right-chiral fermions, proportional to their hypercharges. The $SU(2)_L \times U(1)_Y$ electroweak interaction spontaneously breaks to $U(1)_{EM}$, the electromagnetic interaction, after the Higgs field acquires a nonvanishing vacuum expectation value (vev). The photon, the gauge boson associated with $U(1)_{EM}$, is a mixture of the the neutral components of the W and B, the gauge bosons associated with $SU(2)_L$ and $U(1)_Y$, respectively. The linear combination of the W and B orthogonal to the photon, Z, and the charged components of W, $W^{\pm}$, gain masses and propagate the weak nuclear force.

The matter content of the SM is as follows. $L_i = (\nu_{Li}, e_{Li})^T$ are the left handed lepton doublets, containing a charged lepton and a neutrino, in the $(\mathbf{1}, \mathbf{2})_{-\frac{1}{2}}$ representation, under $(SU(3)_c, SU(2)_L)_{U(1)_Y}$. e_i are the right handed doublet with charges $(\mathbf{1}, \mathbf{1})_{-1}$. Each charged lepton comes in three flavors, electron, muon, and tau; each with an associated neutrino. The left-handed quark doublets $Q_i = (u_{Li}, d_{Li})^T$, contain a left-handed up and down-type quark in the $(\mathbf{3}, \mathbf{2})_{\frac{1}{6}}$ representation. The u_i and d_i are the related right-handed fields in the $(\mathbf{3}, \mathbf{1})_{\frac{2}{3}}$ and $(\mathbf{3}, \mathbf{1})_{-\frac{1}{3}}$ representation, respectively. The up (down) type fields come in three flavors as well: up (down),

charm (strange), top (bottom).

Scalars	Fermions	Vector Bosons	Representation
H			$\mathbf{(1,2)}_{\frac{1}{2}}$
	Q_i		$\mathbf{(3,2)}_{\frac{1}{6}}$
	u_i		$\mathbf{(3,\,1)}_{\frac{2}{3}}$
	d_i		$\mathbf{(3,\,1)}_{-\frac{1}{3}}$
	L_i		$\mathbf{(1,\,2)}_{-\frac{1}{2}}$
	e_i		$\mathbf{(1,\,1)}_{-1}$
		g	$\mathbf{(8,1)}_0$
		W	$\mathbf{(1,3)}_0$
		B	$\mathbf{(1,1)}_0$

Table 1.1: Fields in the SM organized by spin and representation under the gauge symmetries $(SU(3)_c, SU(2)_L)_{U(1)_Y}$. The index i labels the generation.

Finally, the Standard Model has a scalar field H, an $SU(2)_L$ doublet with hypercharge one half. In the SM, this field is assumed to have the following potential describing its self-interactions at the renormalizable level:

$$V = \mu^2|H|^2 + \lambda|H|^4, \tag{1.1}$$

in which the parameter μ^2 has dimension of mass-squared and λ is a dimensionless parameter (that must be greater than zero to avoid a runaway large field direction). The minimization condition for this potential is

$$\frac{\partial V}{\partial H^*} = 0 = \mu^2 H + 2\lambda|H|^2 H, \tag{1.2}$$

For $\mu^2 > 0$ and $\lambda > 0$, is minimum of the potential is at $H = 0$. However if $\mu^2 < 0$ and $\lambda > 0$, the minimum of the potential will no longer be at zero, and the Higgs field acquires a nonzero vev $\langle H \rangle = \sqrt{-\mu^2/2\lambda}$. This new minimum breaks $SU(2)_L \times U(1)_Y$ to $U(1)_{EM}$. In the process the W and Z bosons eat three degrees of freedom of H and gain masses proportional to the Higgs vev. From measurements of the W and Z masses and their properties, the Higgs vev is $\langle H \rangle \approx 174$ GeV and

$\mu^2 = \mathcal{O}(-(100\,\text{GeV})^2)$. The remaining degree of freedom, a single real scalar, is the physical SM Higgs boson. The mechanism for giving gauge bosons of Yang-Mills theories mass is known as the Higgs mechanism [4–7].

SM gauge invariance also allows the following Yukawa interactions between the SM fermions and the Higgs:

$$\mathcal{L}_Y = Y_{dij} Q_i^\dagger d_j H + Y_{eij} L_i^\dagger e_j H + Y_{uij} Q_i^\dagger u_j \tilde{H} + \text{h.c.}, \tag{1.3}$$

in which i, j indicate family indices and $\tilde{H} = \epsilon H^\dagger$, where ϵ is the completely antisymmetric $SU(2)$ tensor. The $Y_{d,e,u}$ are matrices of Yukawa couplings which determine the fermion mixing and masses after H develops a vev. The matter fields are in flavor eigenstates and can be rotated into mass eigenstates, through the rotations $u_L \to \mathcal{U}_L u_L$ and $d_L \to \mathcal{U}_d d_L$ with similar rotations for the right handed fields and leptons. In this mass basis, the Lagrangian is

$$\mathcal{L}_Y = Y^D_{dij} Q^\dagger_{mi} d_{mj} H + Y^D_{eij} L^\dagger_{mi} e_{mj} H + Y^D_{uij} Q^\dagger_{mi} u_{mj} \tilde{H} + \text{h.c.}, \tag{1.4}$$

where the subscript m denotes that the matter fields are in mass eigenstates, and the superscript D denotes that the matrix is diagonal.

The rotation from flavor to mass eigenstates also affect the interactions with the $W^\pm$. These interactions are proportional to $u_L^\dagger \gamma^\mu d_L$, where γ^μ are the gamma matrices, and u_L and d_L are vectors of left chiral up and down quarks. In the basis where the Yukawa couplings are diagonal, this term will is not be and there will be generation mixing. This mixing is parameterized by the Cabibbo Kobayashi Maskawa (CKM), quark-mixing matrix $V_{\text{CKM}} = \mathcal{U}_u \mathcal{U}_d^\dagger$. The CKM depends on three angles and a phase and can be written as the product of three rotations, as follows:

$$V_{\text{CKM}} = \begin{pmatrix} 1 & 0 & 0 \\ 0 & \cos\theta_{23} & \sin\theta_{23} \\ 0 & -\sin\theta_{23} & \cos\theta_{23} \end{pmatrix} \begin{pmatrix} \cos\theta_{13} & 0 & \sin\theta_{13} e^{i\delta} \\ 0 & 1 & 0 \\ -\sin\theta_{13} e^{-i\delta} & 0 & \cos\theta_{13} \end{pmatrix} \begin{pmatrix} \cos\theta_{12} & \sin\theta_{12} & 0 \\ -\sin\theta_{12} & \cos\theta_{12} & 0 \\ 0 & 0 & 1 \end{pmatrix}. \tag{1.5}$$

It can also be written in terms of an expansion in $\lambda \approx 0.225$, which is the Wolfenstein parameterization [8]. The (12) and (21) entries in the CKM are relatively large and generating these entries represents an important challenge in any model of quark flavor physics as we will see later.

The SM has 19 free parameters: 9 fermion masses, three quark mixing angles and a phase in the CKM matrix, the Higgs mass and its quartic coupling, the three gauge couplings, and the QCD vacuum angle. These 19 parameters characterize a theory that has been tested at low energy table top experiments, at colliders, and in astrophysical observations. It predicts the value of the ratio of the W and Z boson masses. The LHC has also discovered a scalar boson with a mass of about 125 GeV, and with the the couplings strengths of the SM Higgs scalar in the $\sqrt{s} = 7$ and 8 TeV data as of 2016 [9–12]. Fig. 1.1 shows the current couplings and their agreement with the predictions of the SM.

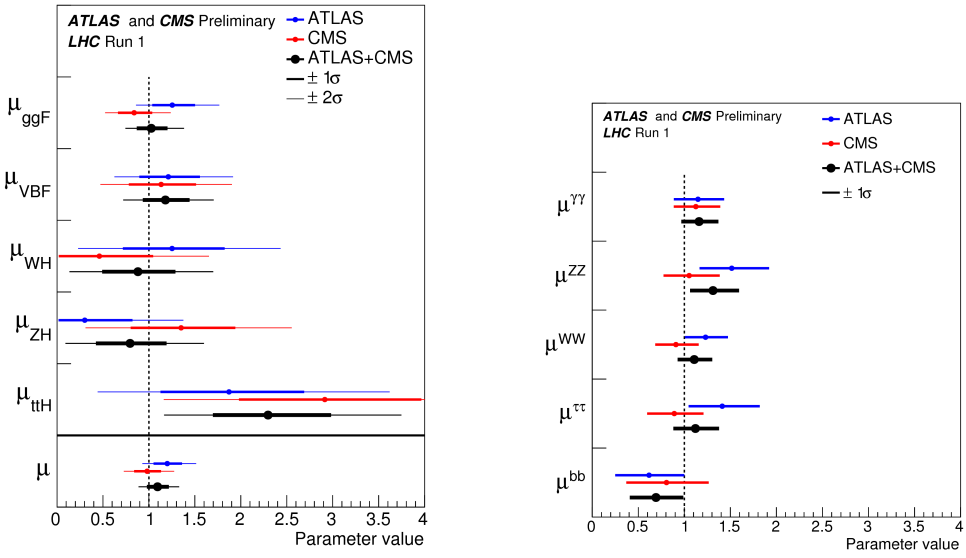

Figure 1.1: Combined signal strengths, ratio of measured to SM cross section or branch fraction, for Higgs production modes (left) and decay modes (right) at $\sqrt{s} = 7$ and 8 TeV using both ATLAS and CMS as of 2015 Ref. [11]. In the left panel the global signal strength is also shown. The dotted line corresponds to the SM signal strength of one.

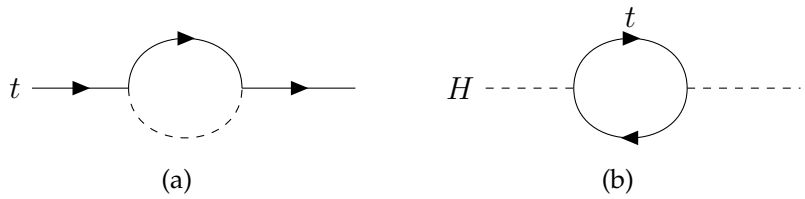

Figure 1.2: One loop diagrams leading to corrections to mass terms for a fermion t (a) and scalar H (b) from Yukawa couplings.

The SM, for all its success, has some deficiencies:

- The Hierarchy Problem:

  For a fermion interactions like emitting a photon, preserve the chirality of the fermion; a left-handed (right-handed) fermion remains a left-handed (right-handed) fermion. The only term in the Lagrangian that violates this symmetry, connecting the left- and right-handed fields, is the mass term $m\psi_L^\dagger\psi_R$. Any radiative corrections to the fermion mass must vanish as this mass goes to zero and chiral symmetry is restored. If there is a momentum cutoff Λ_{UV}, the correction from diagrams like those in Fig. 1.2a is proportional to

  $$\Delta m \propto m \ln \frac{\Lambda_{\text{UV}}}{m}. \tag{1.6}$$

  This chiral symmetry protects the fermion mass from large radiative corrections.

  The masses of fundamental scalar particles, like the μ^2 term for the Higgs, are unprotected by chiral symmetry and suffer from large radiative corrections. One example that appears in the SM are couplings to and corrections from the top quark. The top Yukawa coupling in Eq. (1.3) leads to a one loop correction,

Fig. 1.2b, to μ^2 that is quadratically divergent

$$\Delta\mu^2 = -\frac{3|y_t|^2}{8\pi^2}\Lambda_{\rm UV}^2 + \dots \tag{1.7}$$

$\Lambda_{\rm UV}$ is used to regulate the divergent loop integral, and can be interpreted as the scale at which new physics enters the theory, altering the high energy behavior. This quantum correction enters into the μ^2 term in Eq. (1.1) and the corrected term is

$$\mu^2 = \mu_0^2 + \Delta\mu^2, \tag{1.8}$$

where μ_0^2 is the parameter in the bare Lagrangian. Since $\mu^2 = \mathcal{O}(-(100\,\text{GeV})^2)$, for large $\Lambda_{\rm UV}^2$, the tree-level μ_0^2 must be of order $\Lambda_{\rm UV}^2$ in order to cancel and generate a small mass. If the SM is valid to the GUT or Planck scale, then this is a "fine-tuning" problem as $\mu_0^2 + \Delta\mu^2$ must precisely cancel for 26 to 32 orders of magnitude. Furthermore, this is an example of the "hierarchy problem" in any model with fundamental scalars, not just the SM , where the low energy theory has become extremely sensitive to high energy physics [13–17].

- EWSB:

  In the SM, the parameters that enter into the Higgs potential Eq. (1.1) are put in by hand. There is no mechanism driving μ^2 negative.

- Flavor Puzzle:

  Of the 19 parameters of the SM, 13 have to do with the flavor structure of the theory, spanning many orders of magnitude from the electron at half an MeV to the top quark at 173 GeV. The SM does not explain this hierarchy of scales, or why there are three generations of fermions.

- Cosmological Problems:

The SM also has a number of cosmological problems. The observed baryon asymmetry [18], i.e. why are there more baryons than anti-baryons in the universe, is larger than can be generated by the SM alone. Observations of galactic rotation curves [19, 20], the cosmic microwave background [21], and galaxy collisions like the Bullet Cluster [22] have indicated that there is non-baryonic cold dark matter in the universe, with no observed explanation. Similarly, measurements of supernovae [23, 24] and the CMB [21] have shown that the universe is expanding, this dark energy in the universe is unexplained.

1.2 Supersymmetry: What and Why

Well motivated candidates for physics beyond the SM are models that include supersymmetry (SUSY). Supersymmetry is proposed fundamental symmetry relating bosonic and fermionic degrees of freedom. In supersymmetry, every particle has a superpartner with opposite statistics — a boson (fermion) has a superpartner that is a fermion (boson), related by a supersymmetry transformation. The chiral symmetry that protects the mass of the fermion will also now protect the mass of the boson, alleviating the quadratic divergence of Eq. (1.7).

The operator Q_i, which generates a supersymmetry transformation, takes

$$Q_i|\text{Boson}\rangle = |\text{Fermion}\rangle, \qquad Q_i|\text{Fermion}\rangle = |\text{Boson}\rangle, \tag{1.9}$$

where i labels the generator $i = 1, 2, \ldots N$. Q_i is an anti-commuting spinor, and $\bar{Q}_i$ is also a symmetry generator. Q_i and $\bar{Q}_i$ have spin, so supersymmetry must be a symmetry of spacetime. The Q_i and $\bar{Q}_i$ form an algebra

$$\begin{aligned} \{Q_i^\alpha, \bar{Q}^{\dot{\alpha} j}\} &= 2\sigma^\mu_{\alpha\dot{\alpha}} P_\mu \delta_i^j, \\ \{Q_i, Q_i\} &= 0, \\ [Q_i, P^\mu] &= 0, \end{aligned} \tag{1.10}$$

where P^μ is momentum, σ^μ are the Pauli matrices, α and $\dot{\alpha}$ are spinor indices. Here

and in what follows we will assume only one pair of generators ($N = 1$). This is the case most relevant for phenomenology since it allows for chiral representations.

The single-particle irreducible representations of the the SUSY algebra containing both fermionic and bosonic states are called supermultiplets. In these states, the superpartners, can be transformed into each other through applications of SUSY and Lorentz transformations. The supermultiplets can also be repackaged into superfields, functions in superspace (see Refs. [25–27] for reviews of $N = 1$ supersymmetry). In extending the SM to include supersymmetry, Higgs and matter fields will be embedded into chiral supermultiplets, and gauge bosons will be embedded into vector supermultiplets. Each chiral supermultiplet has a complex scalar ϕ, a Weyl fermion ψ, and an auxiliary field F. For example, the electron will have a spin zero partner, the "selectron." A vector supermultiplet has a spin one vector gauge boson V_μ^a, a Majorana spinor λ^a, and an auxiliary field D^a, hence gauge fields have spin one half partners, the gauginos. These auxiliary fields can be eliminated using the equations of motion, but keep track of off-shell degrees of freedom. At the renormalizable level, the kinetic terms are taken to be canonical.

The renormalizable interactions are encoded in the superpotential W, a holomorphic function of supermultiplets. The superpotential is

$$W = L^i \Phi_i + \frac{1}{2} M^{ij} \Phi_i \Phi_j + \frac{1}{6} y^{ijk} \Phi_i \Phi_j \Phi_k.$$

The first term is a source term, absent unless there are gauge singlets. The second generates mass for vector-like fermions and triscalar couplings. The third generates Yukawa couplings and quartic couplings for the scalars. Integrating out the auxiliary fields generates the scalar potential of the theory

$$V = \sum_i \left| \frac{\partial W}{\partial \phi_i} \right|^2 + \frac{1}{2} \sum_{i,a} g_a^2 \left| \phi^{\dagger i} T^a \phi_i \right|^2, \tag{1.11}$$

where the T^a are the generators for the ath gauge group. Similarly Yukawa interac-

tions in the Lagrangian are generated by

$$\mathcal{L} = \frac{1}{2}\frac{\partial^2 W}{\partial\phi_i \partial\phi_j}\psi_i\psi_j + \text{h.c.} \tag{1.12}$$

If SUSY is an unbroken symmetry of nature, $-P^2$ will commute with Q, and the superpartners will have the same mass. In the IR, bosonic degrees of freedom associated with the electron or light quarks have not been observed, hence supersymmetry must be a broken symmetry i.e., the $N = 1$ SUSY theory is broken to $N = 0$. However, if this breaking comes from spontaneous symmetry breaking, the theory can still maintain many useful features including the taming of quadratic divergences. Depending on how the symmetry is broken, quadratic divergences may be reintroduced, however a subset of these terms, the "soft" terms, do not resurrect this divergence [28]. These soft terms in the Lagrangian can be parameterized as

$$\mathcal{L}_{\text{soft}} = -\left(\frac{1}{2}M_a\lambda^a\lambda^a + \frac{1}{6}a^{ijk}\phi_i\phi_j\phi_k + \frac{1}{2}b^{ij}\phi_i\phi_j\right) + \text{c.c.} - (\tilde{m}^2)^i_j\phi^{*j}\phi_i \tag{1.13}$$

where M_a are gaugino mass terms, a^{ijk} are trilinear couplings or a terms, the b^{ij} are bilinear mass terms, and finally the $\tilde{m}^2$ terms are additional scalar mass squares. Terms involving scalars boost scalar partner masses and induce new trilinear scalar interactions. The mass term for gauginos clearly splits the gaugino masses from the gauge boson masses.

Examples of the interactions in this theory are shown in Figs. 1.3, 1.4, and 1.5. Figure 1.3 shows the usual Yukawa couplings between the Higgs scalar and two quarks, but also its "supersymmetrications," quark-squark-Higgsino interactions also with strength y_t. There are also triscalar interactions between squarks and a Higgs scalars with strengths of $\mu^* y_t$ and a_t. For these five diagrams, the neutral Higgs can be replaced with the charged Higgs, and a top quark or squark with a bottom, as well. There are also quartic interactions Fig. 1.4 with strength y_t^2. There are also "supersymmetrications" of the usual gauge interactions Fig. 1.5 and scalar quartic couplings proportional to the gauge couplings squared.

Supersymmetric models have many desirable properties including:

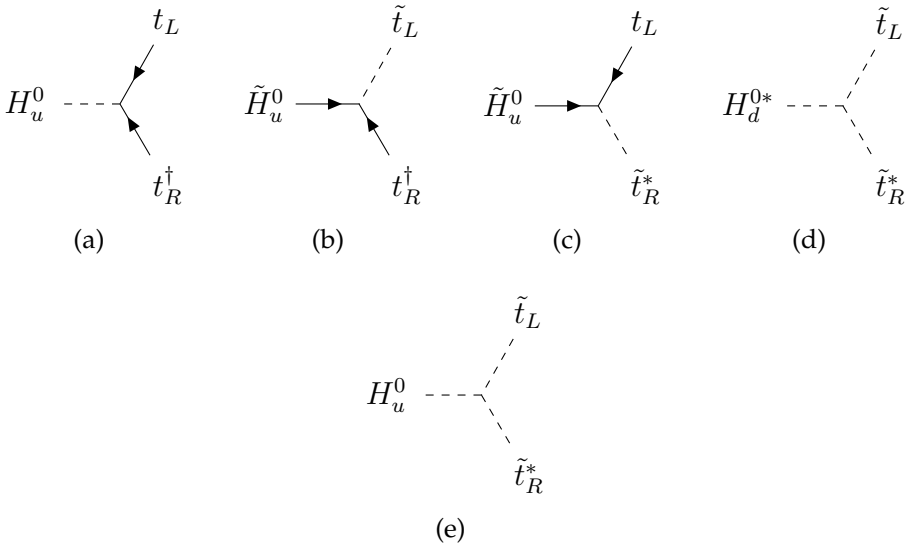

Figure 1.3: The top quark Yukawa coupling (a) and its "supersymmetrizations" (b) and (c) all with strength y_t. (d) and (e) are triscalar couplings with strength $\mu^* y_t$ and a_t, respectively.

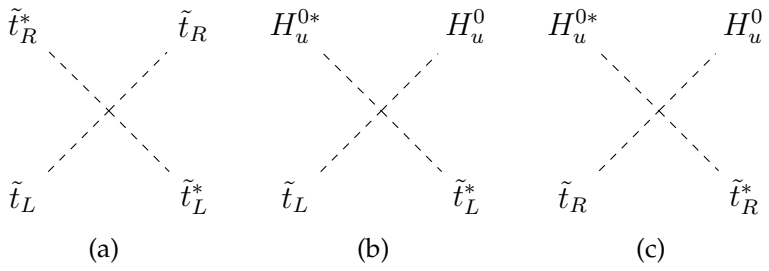

Figure 1.4: Examples of quartic scalar interactions with strength y_t^2.

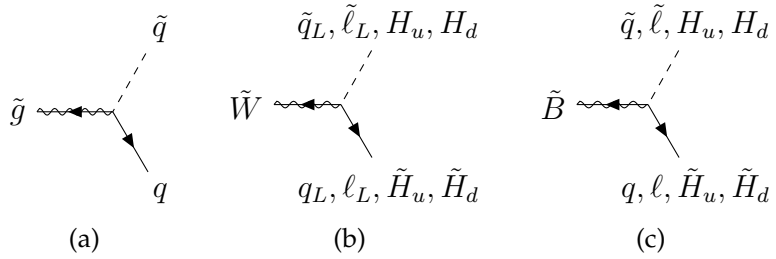

Figure 1.5: Couplings to the gluino, wino, and bino to superpartners.

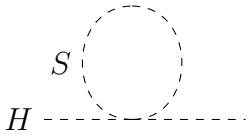

Figure 1.6: Feynman diagram for a scalar S coupled to the Higgs boson through a quartic coupling.

- A Solution to the Hierarchy Problem:

  Since every particle will have an associated superpartner, there will be scalar loops as in Fig. 1.6, which generate the correction

  $$\Delta\mu^2 = \frac{\lambda_S}{16\pi^2}\Lambda_{\text{UV}}^2, \tag{1.14}$$

  which differs from the fermion correction, Eq. (1.7) by a sign. Supersymmetry ensures that there are two complex scalars with $\lambda_S = |y_u|^2$, and furthermore that this cancellation is exact to all orders when SUSY is unbroken. Softly breaking supersymmetry leads to safe logarithmic divergences for scalar masses and can explain the "lightness" of the Higgs scalar compared to the Planck scale.

- Radiative EWSB:

  In SUSY models the Higgs potential is induced from the scalar potential of Eq. (1.11), and so the quartic couplings in the Higgs potential are propor-

tional to the gauge couplings in minimal models. Also there can be scenarios in which radiative correction to the Higgs mass-squared terms, due to SM and superpartner loops, drive an effective analogue to the μ^2 term negative, facilitating electroweak symmetry breaking. The origin of the electroweak scale is then tied to the scale of the splitting between the SM and superpartner masses. Clearly this splitting should not be much larger than the electroweak scale in the absence of tuning.

- Gauge coupling unification:

  In the SM, the value of the scale-dependent gauge couplings almost meet when running up from the the electroweak scale assuming no new physics at intermediate scales. The additional matter in a supersymmetric theory improves this unification, and the gauge couplings meet at roughly the GUT scale for TeV scale superpartners (Fig. 1.7) [29].

- Cosmological Gains:

  We will see that in many situations an important ingredient of supersymmetric extensions of the SM is the imposition of a discrete symmetry that distinguishes particles from superpartners. A symmetry of this type, often called R-parity, is needed to eliminate dimension four operators that mediate proton decay. If such a symmetry exists then the lightest supersymmetric particle (LSP) is stable on cosmological time scales. If it is the case that the LSP is electrically neutral and has electroweak scale cross sections, it is a natural candidate for a weakly interacting massive particle (WIMP), and can populate the measured relic density [30].

1.3 The MSSM

We now turn to the minimal extension of the SM to include TeV-scale SUSY, which is known as the minimal supersymmetric standard model (MSSM), defined to be the minimal extension of the SM with two Higgs doublets and conserved R-parity. The

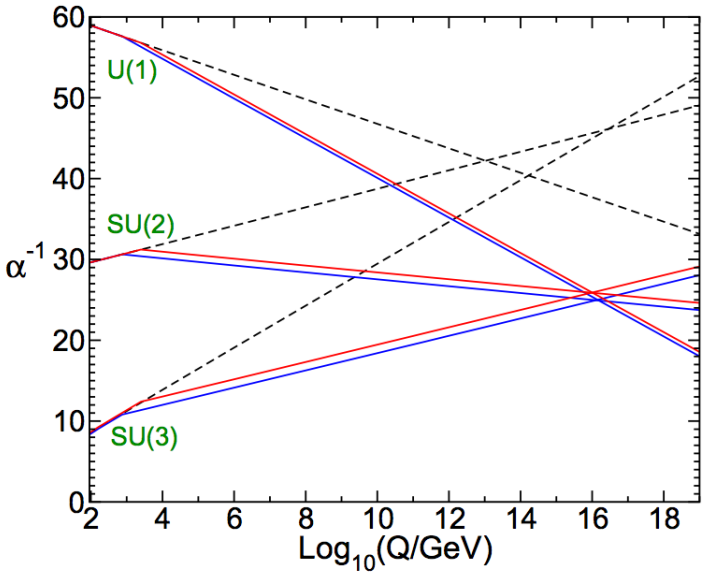

Figure 1.7: Two loop renormalization group running for the inverse of the gauge couplings α_a^{-1} in the Standard Model (dashed lines) and the MSSM (solid lines). In the MSSM case, the superpartner masses are treated as a common threshold varied between 750 GeV and 2.5 TeV, and $\alpha_3(M_Z)$ is varied between 0.117 and 0.120. Figure taken from Ref. [26].

field content of the MSSM is displayed in Table 1.2. The spin zero superpartners are the sfermions, like the stop $\tilde{t}$ or stau $\tilde{\tau}$, the spin one half partners of the gauge bosons are the gauginos, like the wino $\tilde{W}$, and the spin one half partners of the Higgs bosons are the Higgsinos $\tilde{H}$. The neutral (charged) spin half components of the $\tilde{W}$, $\tilde{B}$, and Higgsinos ($\tilde{W}$ and Higgsinos) mix into the neutralinos $\tilde{\chi}^0$ (charginos $\tilde{\chi}^{\pm}$). Like in the SM, when electroweak symmetry breaks, three degrees of freedom from the Higgs sector are eaten by the longitudinal components of the W and Z bosons. The remaining five degrees of freedom become two CP even eigenstates, the SM Higgs-like h and the heavy H, two charged states $H^{\pm}$, and a CP odd state A^0.

With the assumption of R-parity, the superpotential for the MSSM (neglecting

Scalars	Fermions	Vector Bosons	Representation
H_u	$\tilde{H}_u$		$(\mathbf{1},\mathbf{2})_{\frac{1}{2}}$
H_d	$\tilde{H}_d$		$(\mathbf{1},\mathbf{2})_{-\frac{1}{2}}$
$\tilde{Q}_i$	Q_i		$(\mathbf{3},\mathbf{2})_{\frac{1}{6}}$
$\tilde{\overline{u}}_i$	$\overline{u}_i$		$(\bar{\mathbf{3}},\mathbf{1})_{-\frac{2}{3}}$
$\tilde{\overline{d}}_i$	$\overline{d}_i$		$(\bar{\mathbf{3}},\mathbf{1})_{\frac{1}{3}}$
$\tilde{L}_i$	L_i		$(\mathbf{1},\mathbf{2})_{-\frac{1}{2}}$
$\tilde{\overline{e}}_i$	$\overline{e}_i$		$(\mathbf{1},\mathbf{1})_{1}$
	$\tilde{g}$	g	$(\mathbf{8},\mathbf{1})_{0}$
	$\tilde{W}$	W	$(\mathbf{1},\mathbf{3})_{0}$
	$\tilde{B}$	B	$(\mathbf{1},\mathbf{1})_{0}$

Table 1.2: Fields in the MSSM organized by spin and representation under the gauge symmetries $(SU(3)_c, SU(2)_L)_{U(1)_Y}$. The index i labels the generation.

neutrino masses) is

$$W_{\text{MSSM}} = \mu H_u H_d + y_u Q \overline{u} H_u + y_d Q \overline{d} H_d + y_e L \overline{e} H_d, \tag{1.15}$$

where gauge and flavor indices are suppressed, and superfields are denoted by their SM-like component. SUSY breaking in the context of the MSSM can be parameterized in the soft terms

$$\begin{aligned} -\mathcal{L} = &\left(\frac{M_3}{2}\tilde{g}\tilde{g} + \frac{M_2}{2}\tilde{W}\tilde{W} + \frac{M_1}{2}\tilde{B}\tilde{B} + \text{c.c.}\right) + m_{H_d}^2 |H_d|^2 + m_{H_u}^2 |H_u|^2 \\ &+ \tilde{Q}^\dagger m_{\tilde{Q}}^2 \tilde{Q} + \tilde{L}^\dagger m_{\tilde{L}}^2 \tilde{L} + \tilde{\overline{u}} m_{\tilde{\overline{u}}}^2 \tilde{\overline{u}}^\dagger + \tilde{\overline{d}} m_{\tilde{\overline{d}}}^2 \tilde{\overline{d}}^\dagger + \tilde{\overline{e}} m_{\tilde{\overline{e}}}^2 \tilde{\overline{e}}^\dagger - (b H_u H_d + \text{c.c.}) \\ &+ \left(\tilde{\overline{u}} a_u \tilde{Q} H_u + \tilde{\overline{d}} a_d \tilde{Q} H_d + \tilde{\overline{e}} a_a \tilde{L} H_d + \text{c.c.}\right). \end{aligned} \tag{1.16}$$

The mass terms split the masses of the partner and superpartners, and the scalar mass-squared matrices are generally not diagonal in the same basis as the fermions. The a terms are arbitrary complex couplings with dimensions of mass. In many theories, they are often are proportional to the Yukawa couplings such that $a_{ijk} = A_{ijk} y_{ijk}$. For phenomenological purposes since the Yukawa couplings are hierarchical for the charged fermions, it is useful to consider only the third generation:

$a_t = A_t y_t$, $a_b = A_b y_b$, $a_\tau = A_\tau y_\tau$. The mass squared parameter b leads to mixing between the up and down Higgs and is commonly written as $b = B_\mu \mu$.

The soft terms introduce many new parameters. The a terms and Yukawa couplings are both arbitrary 3×3 complex matrices with 9 magnitudes and 9 phases each, for 54 magnitudes and 54 phases. The soft mass squares are hermitian and each have 6 magnitudes and three phases, for a total of 30 magnitudes and 15 phases. There are also the complex masses μ, b, and the gaugino masses, the two real Higgs soft mass squares and the gauge couplings and QCD vacuum angle, for a total of 95 real magnitudes and 74 phases.

However, not all these parameters are physical. In the limit where the superpotential and soft supersymmetry breaking couplings are zero, there is a global $U(3)^5$ symmetry, parameterizing arbitrary rotations between particles of a given type. Each $U(3)$ has three angles and six phases so the $U(3)^5$ has 15 angles and 30 phases. With the interactions restored, there is a residual $U(1)_B \times U(1)_L$ symmetry parameterized by two phases, and so 15 angles and 28 phases can be removed. There are also two more global $U(1)$ symmetries, $U(1)_R$ and $U(1)_{\text{PQ}}$ in the Higgs sector, removing two more phases. This leaves 80 magnitudes and 44 phases, for a total of 124 parameters, or 105 new parameters after subtracting the 19 parameters of the SM [31–33].

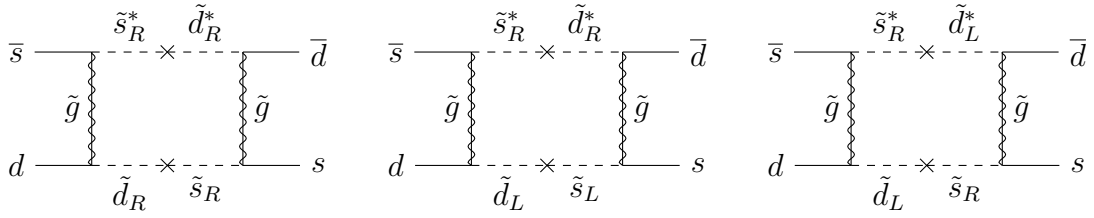

Figure 1.8: Box diagrams that contribute to $K - \bar{K}$ mixing containing squarks and gluinos.

These new parameters mix the left- and right-handed sfermion eigenstates. The diagonal terms in the mass matrix come from the soft mass squares and from electroweak symmetry breaking through the Higgs mechanism. There are off-

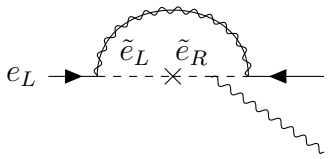

Figure 1.9: A supersymmetric contribution to the electric dipole moment of the electron from a trilinear term a_e.

diagonal masses that come from couplings of stops to Higgs scalars through the μ term in the scalar potential and through a terms. The mass squared matrix for the stop, assuming no mass squared terms coupling the stop to the other squark fields, is

$$\mathcal{L} = -(\tilde{t}_L^* \quad \tilde{t}_R^*) \begin{pmatrix} m_t^2 + \tilde{m}_{Q_3}^2 & v \sin\beta(a_t^* - \mu y_t \cot\beta) \\ v \sin\beta(a_t - \mu^* y_t \cot\beta) & m_t^2 + \tilde{m}_{\bar{u}_3}^2 \end{pmatrix} \begin{pmatrix} \tilde{t}_L \\ \tilde{t}_R \end{pmatrix}. \qquad (1.17)$$

The off-diagonal entries can lead to a light stop eigenstates. The sbottom and stau squarks mix as well.

The new mixing angles and phases in the soft SUSY breaking sector are constrained by searches for flavor changing neutral currents (FCNCs) or for EDMs [32, 33]. For example, if there are off-diagonal soft mass squares or a terms, coupling the first two generations, then there are strong constraints coming from K-$\bar{K}$ mixing as shown schematically in Fig. 1.8 [34]. In the absence of a theory of supersymmetry breaking, the flavor structure is arbitrary and generally leads to phenomenological problems. To alleviate these issues, there are three general strategies for model building: (i) degenerate masses for the first two generations in the IR [35], [36–38]; (ii) quark and squark masses that can be simultaneously diagonalized ("alignment") [39]; (iii) heavy multi-TeV, decoupled squarks [40]. Electric dipole moments, like that for the electron in Fig. 1.9, can be generated from nonzero phases in the gaugino masses or trilinear terms. Searches for these dipole moments have placed bounds on the imaginary parts of these terms and found that they are suppressed relative to the real parts [38].

In the MSSM, there are two complex Higgs doublets H_u and H_d. The neutral components have a potential

$$\begin{aligned} V = &\left(|\mu|^2 + m_{H_u}^2\right)|H_u^0|^2 + \left(|\mu|^2 + m_{H_d}^2\right)|H_d^0|^2 \\ &- (bH_u^0 H_d^0 + \text{c.c.}) + \frac{1}{8}\left(g^2 + g'^2\right)\left(|H_u^0|^2 - |H_d^0|^2\right)^2 . \end{aligned} \tag{1.18}$$

At the UV boundary condition, the masses of these doublets are typically positive and the minimum of the scalar potential is at the origin. $m_{H_u}^2$ will tend to run negative, because of a large positive contribution in the RG flow proportional to the top Yukawa. If $|\mu|^2 + \tilde{m}_{H_u}^2$ becomes negative then electroweak symmetry will break and generate vevs for H_u and H_d. The potential must be bounded from below, so $|\mu|^2$ and b must be about the same size. The μ term in Eq. (1.15) also affects the mass of the Z boson. The minimization of the scalar potential allows the b term of Eq. (1.13) and the μ term to be traded for $\tan\beta$, the ratio of the vacuum expectation values of H_u and H_d, the sign of μ, and the Z boson mass. In the limit of $\tan\beta \gtrsim 5$, the Z boson mass is

$$\frac{M_Z^2}{2} \approx -\tilde{m}_{H_u}^2 - |\mu|^2. \tag{1.19}$$

This formula highlights that μ needs to be of order the soft masses to engineer a cancellation and generate the Z boson mass. However, since μ is in the superpotential, there is no a priori connection between it and the soft SUSY breaking sector. This is a statement of the "μ problem" [41], an issue we will return to later.

The fine-tuned cancellation in the Z boson mass motivates the electroweak fine-tuning measure Δ_{EW} [42–54]. A model has low fine-tuning by this measure, if the contributions to the mass are of order $m_Z^2/2$, or high fine-tuning if they are not. The Z boson mass is

$$\frac{m_Z^2}{2} = \frac{m_{H_d}^2 + \Sigma_d^d - \left(m_{H_u}^2 + \Sigma_u^u\right)\tan^2\beta}{\tan^2\beta - 1} - \mu^2, \tag{1.20}$$

where $\Sigma_{u/d}^{u/d}$ are the loop corrections from the up or down quarks (explicit expressions

can be found in [44]). The expression for Δ_{EW} then takes the form

$$\Delta_{\text{EW}} = \text{max}_i |C_i|/(m_Z^2/2), \tag{1.21}$$

in which the C_i are the terms in Eq (1.20), for example $-m_{H_u}^2 \tan^2\beta/(\tan^2\beta - 1)$. As each of the C_i are defined at the electroweak scale, each is determined purely by the supersymmetric spectrum, independent of the high-scale dynamics and renormalization group running effects that yield that spectrum. For this reason, this fine-tuning assessment is often referred to as a determination of the degree of "electroweak naturalness" of a given model, and can be used to discriminate between different models. We return to this measure in Chapter 3.

At tree level, the mass of the SM-like eigenstate h is bounded from above by $m_h < m_Z|\cos 2\beta|$, which is clearly less than the measured value of 125 GeV [55, 56]. There are however large radiative corrections involving the third generation, most notably from the top quark and stop squarks. The correction takes the form

$$\Delta m_h^2 = \frac{3}{4\pi^2}\frac{m_t^4}{v^2}\left(\ln\frac{\tilde{m}_{t1}\tilde{m}_{t2}}{m_t^2} + \frac{X_t^2}{\tilde{m}_{t1}\tilde{m}_{t2}}\left(1 - \frac{X_t^2}{12\tilde{m}_{t1}\tilde{m}_{t2}}\right)\right), \tag{1.22}$$

where $X_t = A_t - \mu\cot\beta$ is the stop mixing parameter and $\tilde{m}_{ti}$ is the ith stop mass eigenstate. These corrections can bolster the Higgs mass, either through heavy stops, the first term in parentheses, or through "maximal-mixing" $X_t \sim -2.5$ of the stops, the second term.

LHC searches have so far seen no direct evidence for supersymmetric particles. Figure 1.10 summarizes the status of ATLAS searches through the end of the $\sqrt{s} = 7$ and 8 TeV runs with some preliminary 13 TeV results. Constraints on the lightest stop eigenstate are dependent on the dominant decay mode, but bounds are already about 700 GeV from searches for $\tilde{t}_1 \to t\tilde{\chi}_1^0$, Fig. 1.11 shows the current experimental reach at $\sqrt{s} = 7$ and 8 TeV. When the spectrum is compressed, and the mass difference between the stop and neutralino is small, these limits weaken because the dominant decays are to Wb and a neutralino, or a charm quark and a neutralino, more difficult channels with softer jets. Searches for gluino cascade

decays at $\sqrt{s} = 13$ TeV have placed a lower bound of almost 1.8 TeV on the gluino mass with almost an TeV scale neutralino LSP [57]. Exclusions with 3.2 fb^{-1} of $\sqrt{s} = 13$ TeV data are shown in Fig. 1.12. These bounds are typically generated in the context of a simplified model, with only a few new particles and interactions, and are thus model-dependent, but they give a rough ballpark for a general SUSY theory.

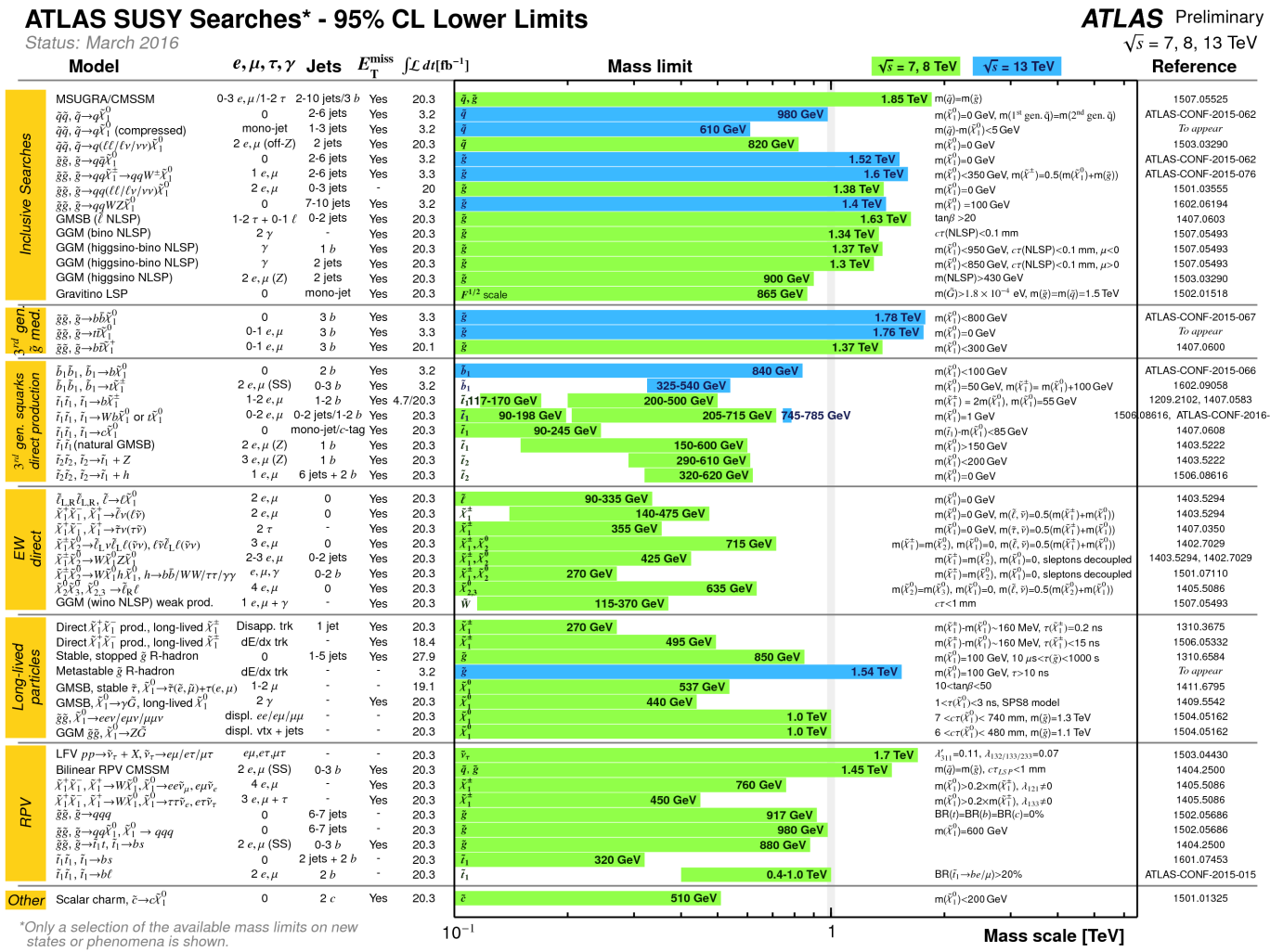

Figure 1.10: Mass reach for ATLAS SUSY searches using the $\sqrt{s} = 7$ TeV, 8 TeV, and 3.2 fb^{-1} 13 TeV data as of March 2016. Taken from [58].

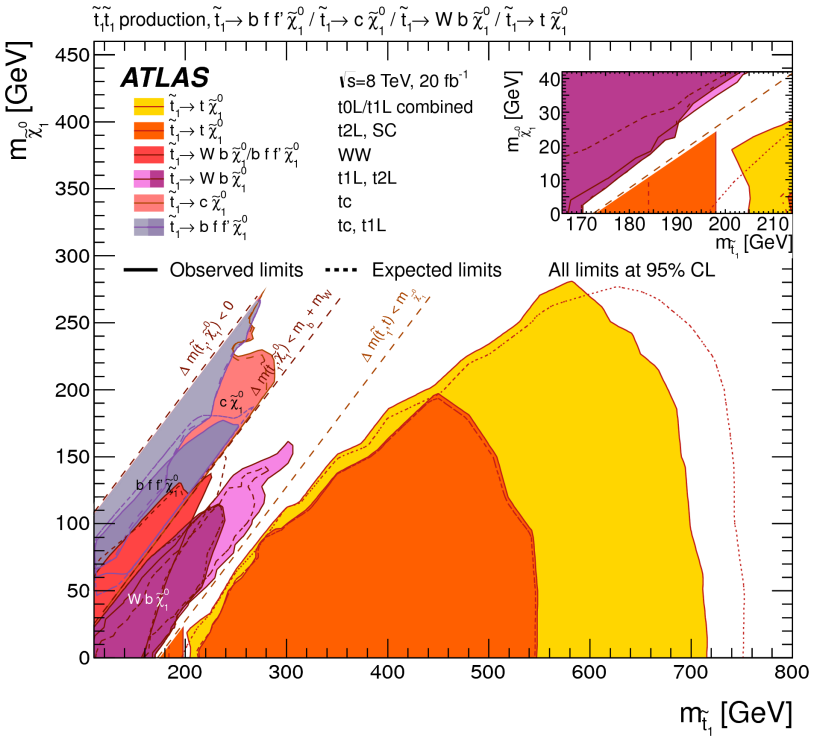

Figure 1.11: Exclusion limits, in the $\tilde{t}_q\ \tilde{\chi}_1^0$ plane, from the dedicated ATLAS searches for stop pair production with 20 fb^{-1} of data at $\sqrt{s} = 8$ TeV. The dashed and solid lines show the expected and observed limits, respectively, including uncertainties except that in the theoretical signal. Taken from [58].

1.4 Theories of SUSY Breaking

The parameters introduced in Eq. 1.13, in the absence of a theory of supersymmetry breaking, were purely schematic. Specific theories will generate, from a tractable number of parameters ($\ll 105$) , many, if not all, of the soft parameters and may lead to a phenomenologically viable spectrum in the IR.

Supersymmetry is broken when the minimum of the scalar potential Eq (1.11) is no longer at zero. The minimum will be lifted, and raised to a nonzero value, if any of the F^i or D^i auxiliary fields develops a nonzero vacuum expectation value.

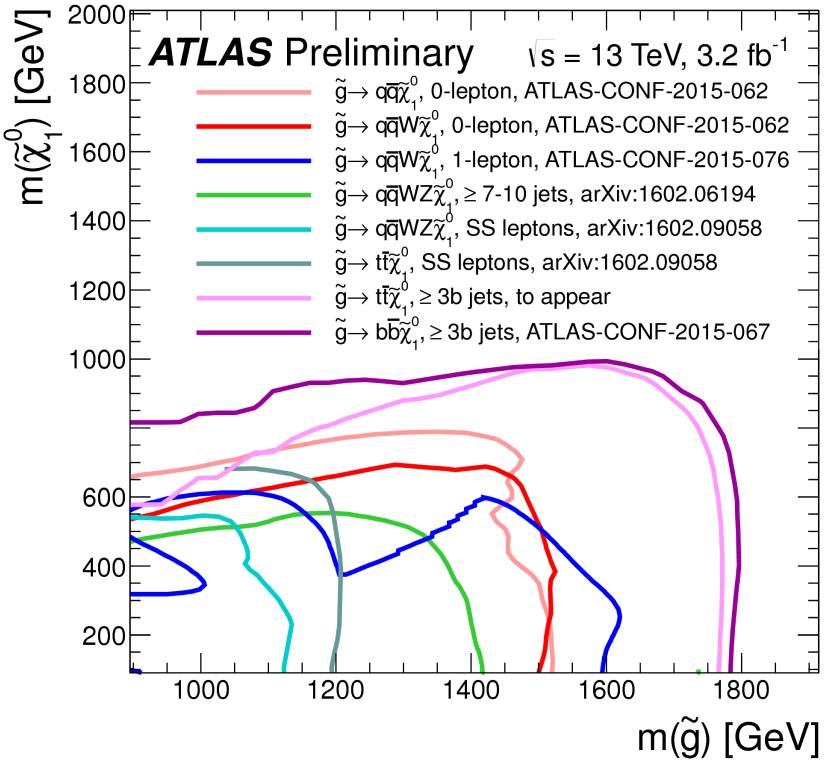

Figure 1.12: Exclusion limits, in the $\tilde{g}$ $\tilde{\chi}_1^0$ plane, from the dedicated ATLAS searches for gluino decay with 3.2 fb^{-1} of data at $\sqrt{s} = 13$ TeV. From the Atlas Supersymmetry Working Group [59]

An immediate result that follows from considering SUSY breaking in the observable sector at the renormalizable level is the well-known sum rule (the supertrace sum rule) [60]

$$\mathrm{STr}(m^2) = \sum_s (-1)^{2s}(2s+1)\mathrm{Tr}(m_s^2), \tag{1.23}$$

$$= \mathrm{Tr}(m_S^2) - 2\mathrm{Tr}(m_F^\dagger m_F) + 3\mathrm{Tr}(m_V^2) = 0, \tag{1.24}$$

where in the final equality is true if none of the gauge symmetries are anomalous. This conclusion is not phenomenologically viable as the non-observance of SUSY

at the LHC has set significant lower bounds on superpartner masses, as discussed previously and shown in Fig. 1.10.

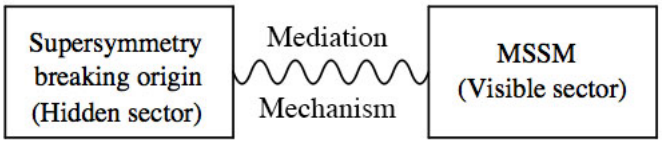

Figure 1.13: The schematic structure of hidden sector SUSY breaking.

A way around this difficulty is to move SUSY breaking to another, "hidden" sector decoupled from the "visible" MSSM fields at the renormalizable level, schematically illustrated in Fig. 1.13 [61–64]. In the general "hidden sector" paradigm, there are fields that break SUSY in the hidden sector e.g. by acquiring a nonzero F term, and the SUSY breaking effects are transmitted to the observable sector through suppressed interactions (i.e. nonrenormalizable, loop-suppressed, or both). It turns out that the dominate features of the MSSM soft terms are largely independent of the SUSY breaking sector, and instead mainly depend on the interactions that mediate SUSY breaking effects to the hidden sector.

There are three dominant mediation mechanisms: gravity, gauge, and bulk or anomaly mediation. In gravity mediation, effects that break supersymmetry are mediated by gravitational interactions leading to soft masses proportional the $M_{\rm P}^{-1}$ and tend to, in simple models, lead to universal soft terms. Gauge mediation involves integrating out SUSY breaking fields with gauge quantum numbers, leading to loop induced soft masses for the scalars and sfermions. In anomaly mediation, gravity mediates the breaking of supersymmetry through loops.

Gravity, Moduli and Anomaly Mediation

One possible mediation mechanism is due to gravitational interactions, which are suppressed by the Planck mass. In this framework, supersymmetry is gauged, realizing supergravity (see Refs [25, 65] for reviews). Supergravity interactions allow for the mediation of SUSY breaking effects in the hidden sector to be connected

to the MSSM sector. These interactions are prescribed by the superpotential, Kähler potential K (giving the field metric), and the gauge kinetic function f (a field dependent prefactor in the gauge interactions). In supergravity mediated scenarios, one imagines that there is a hidden sector that communicates with the visible sector through Planck suppressed operators. In many scenarios of interest (e.g. certain classes of string models) the effective-theory, at leading order in the Planck mass, is given by

$$W = W_{\text{visible}}(Q) - \frac{1}{M_P}\left(y^{Xijk} X Q_i Q_j Q_k + \frac{1}{2}\mu^{Xij} X Q_i Q_j\right), \tag{1.25}$$

$$K = \left(\delta^i_j + \frac{1}{M_P}\left(n^i_j X + \bar{n}^i_j\right) - c^i_j \frac{X^\dagger X}{M_{\rm P}^2}\right) Q^{\dagger j} Q_i, \tag{1.26}$$

$$f_a = \frac{1}{g_a^2}\left(1 - \frac{2k}{M_{\rm P}} X\right), \tag{1.27}$$

where Q_i is a visible sector field, X is a field with a SUSY breaking F term vev, and the c^j_i, k, μ^{Xij}, y^{Xijk}, and n^j_i are arbitrary couplings. If X is replaced with its F term vev F, then there will be gaugino masses, soft mass squares, a terms, and b terms of

$$M_a = k\frac{F}{M_{\rm P}}, \tag{1.28}$$

$$(m^2_Q)^i_j = (c^i_j + n^i_k \bar{n}^k_j)\frac{|F|^2}{M_{\rm P}^2}, \tag{1.29}$$

$$a^{ijk} = \frac{F}{M_P}\left(y^{Xijk} + n^i_p y^{pjk} + n^j_p y^{pik} + n^i_k y^{pij}\right), \tag{1.30}$$

$$b^{ij} = \frac{F}{M_P}\left(\mu^{Xij} + n^i_p \mu^{pj} + n^j n^{pi}\right). \tag{1.31}$$

For arbitrary c^i_j and n^i_j, the theory clearly results severe flavor problem. However, in scenarios with flavor diagonal c^i_j and n^i_j, the soft terms do not in general yield flavor-violating couplings at dangerous levels.

The so-called no-scale scenario has c^i_j and n^i_j equal to zero. In this scenario, scalar masses and a terms are induced through the renormalization group flow [66–70]. If all the $c^i_j = n^i_j = \delta^i_j$, then this model is minimal supergravity (mSUGRA),

also called the constrained MSSM (cMSSM), a five parameter model with universal gaugino $m_{1/2}$, scalar masses m_0, and a terms A_0. mSUGRA is already strongly constrained by current LHC searches, Figure 1.14 shows bounds from ATLAS using the $\sqrt{s} = 7$ and 8 TeV data. In this slice of the $(m_0, m_{1/2})$ plane, the Higgs mass can be accommodated with gluons above 1.5 TeV and squarks at about 3 TeV.

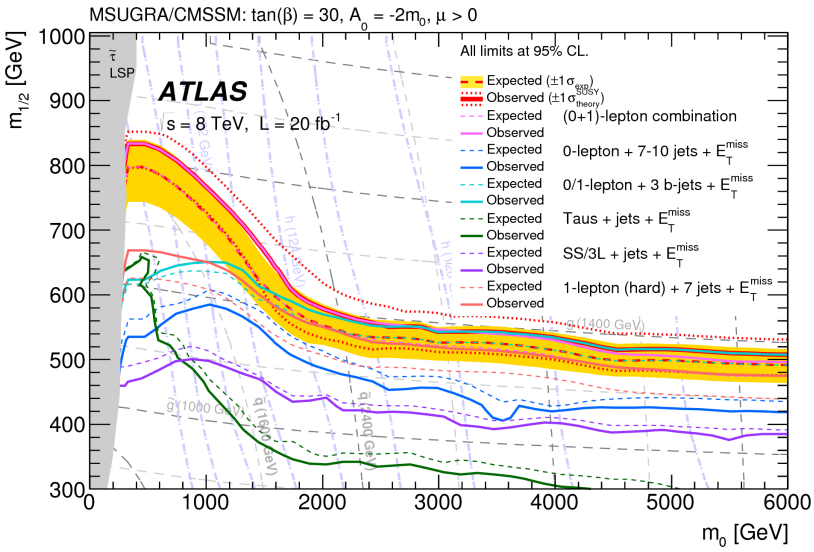

Figure 1.14: Exclusion limits at 95% CL for 8 TeV analyses in the $(m_0, m_{1/2})$ plane for the MSUGRA/CMSSM model with the remaining parameters set to $\tan\beta = 30$, $A_0 = -2m_0$, $\mu > 0$. Part of the model plane accommodates a lightest neutral scalar Higgs boson mass of 125 GeV. This plot is taken from [71].

In the context of string models, another large class of supergravity models is known as moduli mediation. In these models there are a number of moduli T_i which serve as the hidden sector fields [72–75]. These are massless fields with vevs that can parameterize a given string background. In these scenarios, we have (in

Planck units)

$$K = \hat{K} + \frac{Q^{\dagger j} Q_j}{(T_i + T_i)^{n_j^i}}, \tag{1.32}$$

$$\hat{K} = -\log\left(T_i + T_i^\dagger\right), \tag{1.33}$$

$$f_a = T_i, \tag{1.34}$$

where n_j denotes modular weights and $\hat{K}$ contains the kinetic terms for the moduli fields. In such scenarios, the SUSY breaking terms take the form

$$m_j^2 = \sum_m (\frac{1}{3} - n_j^m) \frac{|F_{T_m}|^2}{(T_m + T_m^\dagger)^2}, \tag{1.35}$$

$$M_a = \frac{1}{2} \sum_m \frac{F_m}{T_m + T_m^\dagger}, \tag{1.36}$$

$$a^{ijk} = -\sum_m (1 - n_m^i - n_m^j - n_m^k) \frac{F_{T_m}}{T_m + T_m^\dagger}. \tag{1.37}$$

The modular weights introduce a degree of non-universality into the soft masses.

Gravitational interactions can also mediate SUSY breaking to the observable sector via loops, a scenario known as anomaly mediation. If this mechanism is dominate over the tree level terms, one obtains gaugino masses, soft masses, and a terms of the form

$$M_a = \frac{\beta_a \alpha_a}{4\pi} \frac{F}{M_P}, \tag{1.38}$$

$$m_Q^2 = -\frac{1}{4} \left(\sum_{i=\text{Couplings}} \frac{\partial \gamma_Q}{\partial i} \beta_i \right) \left| \frac{F}{M_P} \right|^2, \tag{1.39}$$

$$a^{ijk} = -\beta_{y^{ijk}} \frac{F}{M_P}, \tag{1.40}$$

where F is the F term vev of the SUSY breaking field in the hidden sector, the β_ia are beta functions, and γ_Q are anomalous dimensions. The dominant contribution to the slepton masses, coming from the β functions for the $SU(2)_L$ and $U(1)_Y$ gauge groups, is negative leading to tachyons. There are a number of solutions to the

tachyonic slepton masses. There could be a new Higgs fields with large Yukawa couplings [76], gauge mediation (deflected anomaly mediation) [77], or a universal mass for the scalars [78]. In this thesis we will consider scenarios in which anomaly is put together with other mediation mechanisms at comparable levels, providing another remedy to the tachyonic slepton problem. These include adding moduli-mediated supergravity effects (mirage mediation) [79, 80], or as we will investigate later in this thesis, adding both gauge and moduli mediation (deflected mirage mediation) [81, 82].

Gauge Mediation

In gauge mediation the setup is quite different from supergravity in that the interactions between the sectors is mediated by renormalizable terms, but setup so that they originate at loop level and hence evade the supertrace theorem [83–91]. See [92] for a review. To achieve this, an additional sector of fields known as messenger fields are introduced, These fields are charged under the SM (typically N vector-like pairs of GUT multiplets e.g. of SU(5), to preserve gauge coupling unification). The N pairs of messenger fields Φ_i, $\overline{\Phi}_i$ couple directly to some hidden sector field X with the superpotential coupling

$$W_X = X\Phi_i\overline{\Phi}_i, \tag{1.41}$$

The hidden sector field X will develop a scalar and F term vev, generating a mass and F term for the messenger fields. This structure is illustrated in Fig. 1.15. This mass scale $M = \langle X \rangle$ may be anywhere from the GUT to TeV scales.

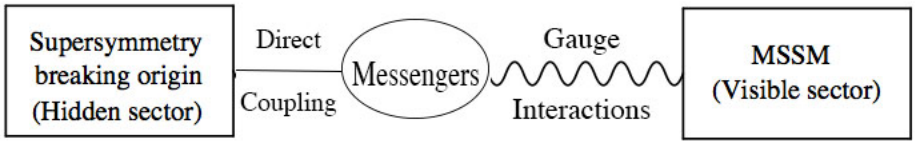

Figure 1.15: The schematic structure of gauge mediated susy breaking.

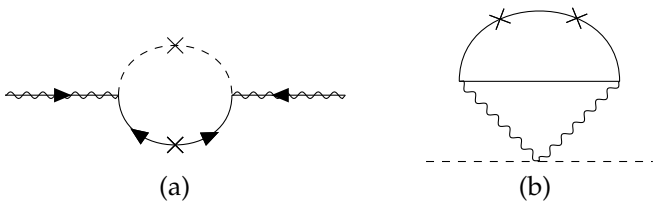

Figure 1.16: Feynman diagrams generating gaugino masses at one loop and scalar masses at two loops, with the scalar and fermion messengers in the loop.

When the messenger fields integrate out at M, there will be one loop diagrams, Fig. 1.16a, that generate gaugino masses. If there are no couplings between the MSSM and messenger fields then there will be two loop diagrams that generate soft masses, one of eight diagrams is shown in Fig. 1.16b. In the context of minimal gauge mediation, these messengers are N pairs of **5** and $\bar{\mathbf{5}}$ pairs of $SU(5)$ [93]. In the limit where $F \ll M^2$, the soft terms can be calculated either through Feynman diagrams Ref [94] or by wave-function renormalization Ref. [95, 96] and are

$$\begin{aligned} M_a &= \frac{\alpha_a}{4\pi} N \frac{F}{M}, \\ m_{\phi_i}^2 &= 2N \sum_a C_a(i) \left(\frac{\alpha_a}{4\pi}\right)^2 \left|\frac{F}{M}\right|^2, \\ a^{ijk} &= 0, \end{aligned}$$

where the $C_a(i)$ is the quadratic Casimir for the ath gauge group and the ith particle, and $\alpha_a = \frac{g_a^2}{4\pi}$. The a terms are generated at two loops and are suppressed. These masses are flavor diagonal because the SM gauge interactions preserve flavor as opposed to gravity which couples everything to everything else and hence there is an a priori suppression of flavor changing processes.

An additional difficulty in gauge mediation is getting the Higgs mass sufficiently heavy. In Eq. (1.22), either heavy stops or large mixing can buttress the Higgs mass. The a terms are zero at tree level and will not be driven large through running, leading to a relatively small mixing contribution. Hence the stops must be heavy,

with masses upward of $\mathcal{O}(5\text{ TeV})$ in minimal models of gauge mediation [97, 98].

1.5 Two Non-minimal Ways Forward

Minimal models are under siege. The LHC, with the discovery of the Higgs scalar and the non-observation of superpartners, has begun to narrow the parameter space through more accurate measurements of the Higgs mass and couplings, and ever increasing lower bounds on superpartners. Dark matter limits have also constrained the parameter space. One possibility that we explore in this thesis, is to look at non-minimal models of supersymmetry breaking.

One possibility explored in deflected mirage mediation (DMM), is to have a string-motivated mix of moduli, gauge, and anomaly mediation soft terms [81, 82]. In deflected mirage mediation, the gravity and anomaly mediation soft terms are comparable to the gauge mediation contribution at some messenger scale. DMM is a nine parameter model, with two steps of mediation and so has a rich space of possible phenomenology like compressed or simplified spectra [99–103].

We will explore DMM from two directions. In the first, Chapter 2 we will look from the top down at the phenomenology of DMM in light of the Higgs mass measurement and superpartner searches LHC7 and LHC8, by doing a scan over the parameter space, and looking at collider and dark matter constraints. We will see that the DMM framework admits simplified and compressed spectra, with novel signatures in future experiments. In the second, Chapter 3, we look at DMM from the bottom up using the electroweak fine-tuning measure, Δ_{EW}. In light of the non-observation supersymmetry, we might expect that a phenomenologically motivated measure may prove useful and we will use this criteria to reexamine the DMM parameter space.

On a completely different line of reasoning, in Chapter 4 we will examine a second non-minimal way froward, which is to consider a certain non-minimal class of GMSB models known as flavored gauge mediation. In these models Yukawa couplings are allowed between the messenger and matter fields [104–108]. These messenger-matter couplings sacrifice the flavor independent structure of gauge

mediation, as they introduce new flavor dependent contributions to the soft mass squares at two loops, as well as A terms at one loop. Specifically, if these messenger-matter contributions are negative and predominately affect the stop then we can have light, mixed stops and still achieve the measured value of the Higgs mass in gauge mediation.

Our specific approach is to model the interactions by positing a new horizontal non-abelian discrete symmetry between our Higgs and messenger SU(2) doublet(s), splitting the doublet and triplet members of the fiveplet. These doublets are placed into multiplets $\mathcal{H}_u$ and $\mathcal{H}_d$, which directly couples to a hidden sector field Δ

$$W = \lambda(\Delta \mathcal{H}_u \mathcal{H}_d), \tag{1.42}$$

where the parentheses denote contractions under the non-abelian symmetry [107]. When Δ acquires a vev, the MSSM Higgs doublets will acquire potentially large μ and b terms. In this framework, the interplay of a fine-tuned vacuum direction of Δ and the group structure leads to mixing between the members of the Higgs multiplets, and can lead to a small μ and B_μ for an MSSM-like Higgs eigenstate, and large masses and F terms for the messenger-like eigenstate(s). These new multiplets will have Yukawa couplings so the rotation to mass eigenstates yields

$$\begin{aligned} W_Y = {} & Y_u Q \overline{u} H_u + Y_d Q \overline{d} H_d + Y_e L \overline{e} H_d \\ & + Y'_{iu} Q \overline{u} M_{iu} + Y'_{di} Q \overline{d} M_{di} + Y'_{ei} L \overline{e} M_{di}, \end{aligned} \tag{1.43}$$

where the M_i are the heavy messenger states. These new messenger Yukawa couplings are non-trivially related to the MSSM Yukawa couplings though the non-abelian symmetry, and so there will be correlations in the messenger-matter mixing corrections. We will explore the model-building challenges, the phenomenology of two example toy scenarios, and discuss the model-building directions in this framework.

References

[1] S. L. Glashow, Nucl. Phys. **22**, 579 (1961).

[2] S. Weinberg, Phys. Rev. Lett. **19**, 1264 (1967).

[3] A. Salam, Conf. Proc. **C680519**, 367 (1968).

[4] F. Englert and R. Brout, Phys. Rev. Lett. **13**, 321 (1964).

[5] G. S. Guralnik, C. R. Hagen, and T. W. B. Kibble, Phys. Rev. Lett. **13**, 585 (1964).

[6] P. W. Higgs, Phys. Lett. **12**, 132 (1964).

[7] P. W. Higgs, Phys. Rev. Lett. **13**, 508 (1964).

[8] L. Wolfenstein, Phys. Rev. Lett. **51**, 1945 (1983).

[9] The ATLAS collaboration, Report No. ATLAS-CONF-2013-014 (2013).

[10] S. Chatrchyan et al., JHEP **06**, 081 (2013), arXiv:1303.4571 [hep-ex].

[11] The ATLAS and CMS collaborations, Report No. ATLAS-CONF-2015-044.

[12] G. Aad et al., Phys. Rev. Lett. **114**, 191803 (2015), arXiv:1503.07589 [hep-ex].

[13] S. Weinberg, Phys. Rev. **D13**, 974 (1976).

[14] S. Weinberg, Phys. Rev. **D19**, 1277 (1979).

[15] E. Gildener, Phys. Rev. **D14**, 1667 (1976).

[16] L. Susskind, Phys. Rev. **D20**, 2619 (1979).

[17] G. 't Hooft, NATO Sci. Ser. B **59**, 135 (1980).

[18] G. Steigman, Ann. Rev. Astron. Astrophys. **14**, 339 (1976).

[19] V. C. Rubin and W. K. Ford Jr., Astrophys. J. **159**, 379 (1970).

[20] V. C. Rubin, N. Thonnard, and W. K. Ford Jr., Astrophys. J. **238**, 471 (1980).

[21] P. A. R. Ade et al., Astron. Astrophys. **571**, A16 (2014), arXiv:1303.5076 [astro-ph.CO].

[22] D. Clowe, M. Bradac, A. H. Gonzalez, M. Markevitch, S. W. Randall, C. Jones, and D. Zaritsky, Astrophys. J. **648**, L109 (2006), arXiv:astro-ph/0608407 [astro-ph].

[23] A. G. Riess et al., Astron. J. **116**, 1009 (1998), arXiv:astro-ph/9805201 [astro-ph].

[24] S. Perlmutter et al., Astrophys. J. **517**, 565 (1999), arXiv:astro-ph/9812133 [astro-ph].

[25] J. Bagger and J. Wess, *Supersymmetry and supergravity* (Princeton university press, 1992).

[26] S. P. Martin, (1997), arXiv:hep-ph/9709356 [hep-ph].

[27] D. Bertolini, J. Thaler, and Z. Thomas, in Proceedings, Theoretical Advanced Study Institute in Elementary Particle Physics: Searching for New Physics at Small and Large Scales (TASI 2012) (2013), pp. 421–496, arXiv:1302.6229 [hep-ph].

[28] L. Girardello and M. T. Grisaru, Nucl. Phys. **B194**, 65 (1982).

[29] P. Langacker and N. Polonsky, Phys. Rev. **D47**, 4028 (1993), arXiv:hep-ph/9210235 [hep-ph].

[30] R. J. Gaitskell, Ann. Rev. Nucl. Part. Sci. **54**, 315 (2004).

[31] H. E. Haber, eprint: hep-ph/9709450.

[32] S. Dimopoulos and D. Sutter, eprint: hep-ph/9504415.

[33] D. J. H. Chung, L. L. Everett, G. L. Kane, S. F. King, J. D. Lykken, and L.-T. Wang, Phys. Rept. **407**, 1 (2005), arXiv:hep-ph/0312378 [hep-ph].

[34] G. Isidori, Y. Nir, and G. Perez, Ann. Rev. Nucl. Part. Sci. **60**, 355 (2010), arXiv:1002.0900 [hep-ph].

[35] J. F. Donoghue, H. P. Nilles, and D. Wyler, Phys. Lett. **B128**, 55 (1983).

[36] F. Gabbiani and A. Masiero, Nucl. Phys. **B322**, 235 (1989).

[37] M. Dine, R. G. Leigh, and A. Kagan, Phys. Rev. **D48**, 4269 (1993), arXiv:hep-ph/9304299 [hep-ph].

[38] F. Gabbiani, E. Gabrielli, A. Masiero, and L. Silvestrini, Nucl. Phys. **B477**, 321 (1996), arXiv:hep-ph/9604387 [hep-ph].

[39] Y. Nir and N. Seiberg, Phys. Lett. **B309**, 337 (1993), arXiv:hep-ph/9304307 [hep-ph].

[40] A. G. Cohen, D. B. Kaplan, and A. E. Nelson, Phys. Lett. **B388**, 588 (1996), arXiv:hep-ph/9607394 [hep-ph].

[41] J. E. Kim and H. P. Nilles, Phys. Lett. **B138**, 150 (1984).

[42] H. Baer, V. Barger, P. Huang, and X. Tata, JHEP **05**, 109 (2012), arXiv:1203.5539 [hep-ph].

[43] H. Baer, V. Barger, P. Huang, D. Mickelson, A. Mustafayev, and X. Tata, Phys. Rev. **D87**, 035017 (2013), arXiv:1210.3019 [hep-ph].

[44] H. Baer, V. Barger, P. Huang, D. Mickelson, A. Mustafayev, and X. Tata, Phys. Rev. **D87**, 115028 (2013), arXiv:1212.2655 [hep-ph].

[45] H. Baer, V. Barger, and D. Mickelson, Phys. Rev. **D88**, 095013 (2013), arXiv:1309.2984 [hep-ph].

[46] H. Baer, V. Barger, and M. Padeffke-Kirkland, Phys. Rev. **D88**, 055026 (2013), arXiv:1304.6732 [hep-ph].

[47] H. Baer, V. Barger, P. Huang, D. Mickelson, A. Mustafayev, W. Sreethawong, and X. Tata, JHEP **12**, [Erratum: JHEP06,053(2015)], 013 (2013), arXiv:1310.4858 [hep-ph].

[48] H. Baer, V. Barger, and D. Mickelson, Phys. Lett. **B726**, 330 (2013), arXiv:1303.3816 [hep-ph].

[49] H. Baer, V. Barger, P. Huang, D. Mickelson, A. Mustafayev, W. Sreethawong, and X. Tata, Phys. Rev. Lett. **110**, 151801 (2013), arXiv:1302.5816 [hep-ph].

[50] K. J. Bae, H. Baer, N. Nagata, and H. Serce, Phys. Rev. **D92**, 035006 (2015), arXiv:1505.03541 [hep-ph].

[51] H. Baer, V. Barger, D. Mickelson, and M. Padeffke-Kirkland, Phys. Rev. **D89**, 115019 (2014), arXiv:1404.2277 [hep-ph].

[52] H. Baer, V. Barger, P. Huang, D. Mickelson, M. Padeffke-Kirkland, and X. Tata, Phys. Rev. **D91**, 075005 (2015), arXiv:1501.06357 [hep-ph].

[53] H. Baer, V. Barger, and M. Savoy, (2015), arXiv:1509.02929 [hep-ph].

[54] K. J. Bae, H. Baer, V. Barger, M. R. Savoy, and H. Serce, Symmetry **7**, 788 (2015), arXiv:1503.04137 [hep-ph].

[55] R. A. Flores and M. Sher, Annals Phys. **148**, 95 (1983).

[56] K. Inoue, A. Kakuto, H. Komatsu, and S. Takeshita, Prog. Theor. Phys. **67**, 1889 (1982).

[57] The ATLAS collaboration, Report No. ATLAS-CONF-2015-067 (2015).

[58] The ATLAS collaboration, (2015), eprint: 1506.08616.

[59] The ATLAS collaboration, *Summary plots from the ATLAS Supersymmetry physics group*.

[60] S. Ferrara, L. Girardello, and F. Palumbo, Phys. Rev. **D20**, 403 (1979).

[61] J. Polonyi, (1977).

[62] H. P. Nilles, Phys. Lett. **B115**, 193 (1982).

[63] H. P. Nilles, Nucl. Phys. **B217**, 366 (1983).

[64] H. P. Nilles, M. Srednicki, and D. Wyler, Phys. Lett. **B120**, 346 (1983).

[65] H. P. Nilles, Phys. Rept. **110**, 1 (1984).

[66] J. R. Ellis, A. B. Lahanas, D. V. Nanopoulos, and K. Tamvakis, Phys. Lett. **B134**, 429 (1984).

[67] J. R. Ellis, C. Kounnas, and D. V. Nanopoulos, Nucl. Phys. **B241**, 406 (1984).

[68] J. R. Ellis, C. Kounnas, and D. V. Nanopoulos, Nucl. Phys. **B247**, 373 (1984).

[69] J. R. Ellis, C. Kounnas, and D. V. Nanopoulos, Phys. Lett. **B143**, 410 (1984).

[70] J. R. Ellis, K. Enqvist, G. Gelmini, C. Kounnas, A. Masiero, D. V. Nanopoulos, and A. Yu. Smirnov, Phys. Lett. **B147**, 27 (1984).

[71] G. Aad et al., JHEP **10**, 054 (2015), arXiv:1507.05525 [hep-ex].

[72] A. Brignole, L. E. Ibanez, and C. Munoz, Nucl. Phys. **B422**, [Erratum: Nucl. Phys.B436,747(1995)], 125 (1994), arXiv:hep-ph/9308271 [hep-ph].

[73] S. Ferrara, C. Kounnas, and F. Zwirner, Nucl. Phys. **B429**, [Erratum: Nucl. Phys.B433,255(1995)], 589 (1994), arXiv:hep-th/9405188 [hep-th].

[74] T. Kobayashi, D. Suematsu, K. Yamada, and Y. Yamagishi, Phys. Lett. **B348**, 402 (1995), arXiv:hep-ph/9408322 [hep-ph].

[75] A. Brignole, L. E. Ibanez, C. Munoz, and C. Scheich, Z. Phys. **C74**, 157 (1997), arXiv:hep-ph/9508258 [hep-ph].

[76] Z. Chacko, M. A. Luty, I. Maksymyk, and E. Ponton, JHEP **04**, 001 (2000), arXiv:hep-ph/9905390 [hep-ph].

[77] A. Pomarol and R. Rattazzi, JHEP **05**, 013 (1999), arXiv:hep-ph/9903448 [hep-ph].

[78] T. Gherghetta, G. F. Giudice, and J. D. Wells, Nucl. Phys. **B559**, 27 (1999), arXiv:hep-ph/9904378 [hep-ph].

[79] K. Choi, A. Falkowski, H. P. Nilles, M. Olechowski, and S. Pokorski, JHEP **11**, 076 (2004), arXiv:hep-th/0411066 [hep-th].

[80] K. Choi, A. Falkowski, H. P. Nilles, and M. Olechowski, Nucl. Phys. **B718**, 113 (2005), arXiv:hep-th/0503216 [hep-th].

[81] L. L. Everett, I.-W. Kim, P. Ouyang, and K. M. Zurek, JHEP **08**, 102 (2008), arXiv:0806.2330 [hep-ph].

[82] L. L. Everett, I.-W. Kim, P. Ouyang, and K. M. Zurek, Phys. Rev. Lett. **101**, 101803 (2008), arXiv:0804.0592 [hep-ph].

[83] M. Dine, W. Fischler, and M. Srednicki, Nucl. Phys. **B189**, 575 (1981).

[84] S. Dimopoulos and S. Raby, Nucl. Phys. **B192**, 353 (1981).

[85] M. Dine and W. Fischler, Phys. Lett. **B110**, 227 (1982).

[86] C. R. Nappi and B. A. Ovrut, Phys. Lett. **B113**, 175 (1982).

[87] L. Alvarez-Gaume, M. Claudson, and M. B. Wise, Nucl. Phys. **B207**, 96 (1982).

[88] S. Dimopoulos and S. Raby, Nucl. Phys. **B219**, 479 (1983).

[89] M. Dine and A. E. Nelson, Phys. Rev. **D48**, 1277 (1993), arXiv:hep-ph/9303230 [hep-ph].

[90] M. Dine, A. E. Nelson, and Y. Shirman, Phys. Rev. **D51**, 1362 (1995), arXiv:hep-ph/9408384 [hep-ph].

[91] M. Dine, A. E. Nelson, Y. Nir, and Y. Shirman, Phys. Rev. **D53**, 2658 (1996), arXiv:hep-ph/9507378 [hep-ph].

[92] G. F. Giudice and R. Rattazzi, Phys. Rept. **322**, 419 (1999), arXiv:hep-ph/9801271 [hep-ph].

[93] M. Dine, Y. Nir, and Y. Shirman, Phys. Rev. **D55**, 1501 (1997), arXiv:hep-ph/9607397 [hep-ph].

[94] S. P. Martin, Phys. Rev. **D55**, 3177 (1997), arXiv:hep-ph/9608224 [hep-ph].

[95] G. Giudice and R. Rattazzi, Nucl.Phys.B **511**, 25 (1998), eprint: hep-ph/9706540.

[96] N. Arkani-Hamed, G. F. Giudice, M. A. Luty, and R. Rattazzi, Phys. Rev. **D58**, 115005 (1998), arXiv:hep-ph/9803290 [hep-ph].

[97] P. Draper, P. Meade, M. Reece, and D. Shih, Phys. Rev. **D85**, 095007 (2012), arXiv:1112.3068 [hep-ph].

[98] M. A. Ajaib, I. Gogoladze, F. Nasir, and Q. Shafi, Phys. Lett. **B713**, 462 (2012), arXiv:1204.2856 [hep-ph].

[99] L. L. Everett, T. Garon, B. L. Kaufman, and B. D. Nelson, (2015), arXiv:1510.05692 [hep-ph].

[100] B. Altunkaynak, B. D. Nelson, L. L. Everett, Y. Rao, and I.-W. Kim, Eur. Phys. J. Plus **127**, 2 (2012), arXiv:1011.1439 [hep-ph].

[101] B. Altunkaynak, B. D. Nelson, L. L. Everett, I.-W. Kim, and Y. Rao, JHEP **05**, 054 (2010), arXiv:1001.5261 [hep-ph].

[102] H. Abe and J. Kawamura, JHEP **07**, 077 (2014), arXiv:1405.0779 [hep-ph].

[103] V. Barger, L. L. Everett, and T. S. Garon, (2015), arXiv:1512.05011 [hep-ph].

[104] Z. Chacko and E. Ponton, Phys. Rev. **D66**, 095004 (2002), arXiv:hep-ph/0112190 [hep-ph].

[105] J. L. Evans, M. Ibe, and T. T. Yanagida, Phys. Lett. **B705**, 342 (2011), arXiv:1107.3006 [hep-ph].

[106] Y. Shadmi and P. Z. Szabo, JHEP **06**, 124 (2012), arXiv:1103.0292 [hep-ph].

[107] M. J. Pérez, P. Ramond, and J. Zhang, Phys. Rev. **D87**, 035021 (2013), arXiv:1209.6071 [hep-ph].

[108] M. Abdullah, I. Galon, Y. Shadmi, and Y. Shirman, JHEP **06**, 057 (2013), arXiv:1209.4904 [hep-ph].

2.1 Introduction

With the resumption of data taking at the CERN Large Hadron Collider (LHC), time is running short for the theoretical community to examine the impact that searches for superpartners has had on well-motivated models of supersymmetry breaking. Of the models with some theoretical support, one of the most well studied is the so-called mirage model [1, 2]. In this scenario, the dynamical supersymmetry breaking triggered by strong coupling in a hidden sector is connected to the observable sector in a manner that is suppressed, thus allowing loop-induced Weyl anomaly contributions to soft supersymmetry breaking to be of comparable size to tree-level contributions. Surprisingly, this is a common outcome of many well-motivated string constructions [3–5]. The phenomenology of these models, in terms of LHC observables, has been recently described in [6] for heterotic models, and in [7] for type IIB orientifold models. In this section we generalize these results to the case of "deflected mirage mediation" [8, 9]. In this paradigm, a direct connection between a hidden sector, in which supersymmetry is broken, and the observable MSSM sector is contemplated, in which gauge-mediated contributions to soft supersymmetry breaking are of the same magnitude as those from gravity-induced terms. As such, deflected mirage mediation (DMM) is a natural generalization of the simple mirage models, and produces a theory space with the greatest possible richness for exploring current and future LHC supersymmetry searches. [1]

The $\sqrt{s} = 7$ TeV and $\sqrt{s} = 8$ TeV runs of the LHC resulted in the triumphant discovery of the Higgs boson. However, as the LHC paused to upgrade to higher energies and luminosities, the various searches for TeV-scale supersymmetry have thus far been fruitless. Previous research in the area of mirage models has suggested the following broad observations. Kähler-stabilized heterotic models involve very few free parameters, and thus robust predictions are possible. If the hidden sector

[1] This section was published previously in Ref. [10].

gaugino condensate involves E_6 or smaller-rank gauge groups, then the gluino is generally well below 3 TeV in mass. As such, much of the parameter space that remains after the $\sqrt{s} = 8$ TeV searches will be quickly probed in the first year or two after the LHC resumes operations [6]. In contrast, the type IIB orientifold models, of the type contemplated first by Kachru et al. (KKLT) [11] have a much more constrained parameter space. Achieving the observed CP-even Higgs mass of $m_h \simeq 125\,\text{GeV}$ tends to require far more massive gluinos and squarks. As such, much of the nominally allowed parameter space resides in areas in which no superpartners are accessible at the early runs at the LHC – and in many cases it is doubtful that superpartners would ever be accessible at the LHC [7].

Given the above statements, it is of interest to ask whether the inclusion of some amount of gauge mediation can affect these conclusions. Gross properties of the DMM model were studied in [12, 13], with LHC implications and dark matter detection studied in [14] and [15], respectively. All of these studies, however, were performed prior to the supersymmetry searches at the LHC at $\sqrt{s} = 8$ TeV and dark matter searches at the $\mathcal{O}(100\ \text{kg})$ target level. At that time, the primary conclusion was that the LSP is likely to be heavy [$\mathcal{O}(1\,\text{TeV})$] and that gluinos were likely to be much lighter than that predicted in the KKLT model without gauge mediation. It is of singular importance to revisit these early conclusions in light of the Higgs mass determination, and refine the predictions for the next run of the LHC, and larger dark matter detection experiments.

We begin our discussion in Section 2.2 with an overview of the theoretical structure that supports both mirage mediation and its deflected variant. We then exhibit the soft supersymmetry breaking terms, and identify the parameter space that defines the DMM model, in Section 2.3. This parameter space is quite a bit larger than that of the mirage/KKLT model, and we proceed to identify general features of this space, and correlations with physical observables, in Section 2.4. This will allow us to identify representative benchmark examples to study in greater detail in Section 2.5, where we focus on supersymmetry searches at the LHC. This is followed by a discussion of dark matter direct detection at current and future experiments in Section 2.6. We will find that the DMM paradigm spans cases

that resemble the so-called "simplified models", as well as compressed-spectrum models often motivated from appeals to "naturalness" [16]. We estimate the reach of the LHC at both $\sqrt{s} = 8$ TeV and 14 TeV and suggest cases in which the current search strategies can be approved to address the specific challenges of the DMM model framework.

2.2 Theoretical Framework

KKLT and Kähler Modulus Stabilization

In what follows we review Kähler modulus stabilization in minimal $N = 1$ supergravity, where we have in mind type IIB string theory compactified on a Calabi-Yau (CY) manifold in the presence of background fluxes. At the level of effective field theory, the precise origin of the various components of the effective Lagrangian is often irrelevant, so we will work in a simplified limit considered in [11], in which a single Kähler modulus T parameterizes the overall size of the compact space. It will be the non-vanishing vacuum expectation value $\left\langle F^T \right\rangle$ that will set the scale of soft supersymmetry breaking in the absence of gauge mediation.

The Kähler potential for the modulus T is taken to be $K(T, \overline{T}) = -3\ln(T + \overline{T})$. For gauge theories with group $\mathcal{G}_a$, living on $D7$ branes which wrap four-cycles in the CY manifold, the gauge coupling is determined by the Kähler modulus T via the (universal) gauge kinetic function $f_a = T$. Note that, with these assumptions,

$$< \text{Re } t > = 1/g^2_{\text{str}}, \tag{2.1}$$

where $t = T|_{\theta=0}$ is the lowest component of the superfield T, and g_{str} is the universal gauge coupling at the string scale.

In the effective supergravity theory just below the string compactification scale, the presence of the three-form fluxes is represented by a constant w_0 in the effective superpotential. It is presumed that these fluxes fix the value of the dilaton and the complex structure moduli, leaving only the Kähler moduli in the low-

energy four-dimensional effective theory [17]. Combined with the effect of gaugino condensation in the hidden sector the total effective superpotential is then

$$W_0 = w_0 + Ae^{-aT}\,, \tag{2.2}$$

where there is a single gaugino condensate, for simplicity, and the constant a is related to the beta-function coefficient of the hidden sector gauge group, with a normalization such that $a = 8\pi^2/N$ for the group $SU(N)$.

In $N = 1$ supergravity theories the scalar potential is determined by the auxiliary fields F^N, associated with the chiral supermultiplet Z^N, and the auxiliary field M of the supergravity multiplet. The equations of motion for these auxiliary fields are given by

$$F^M = -e^{K/2}K^{M\overline{N}}\left(\overline{W}_{\overline{N}} + K_{\overline{N}}\overline{W}\right), \quad \overline{M} = -3e^{K/2}\overline{W}, \tag{2.3}$$

with $W_{\overline{N}} = \partial W/\partial\overline{Z}^{\overline{N}}$, $K_{\overline{N}} = \partial K/\partial\overline{Z}^{\overline{N}}$ and $K^{M\overline{N}}$ being the inverse of the Kähler metric $K_{M\overline{N}} = \partial^2 K/\partial Z^M\partial\overline{Z}^{\overline{N}}$. Note that the gravitino mass is determined via the vacuum relation

$$\langle M\rangle = -3\left\langle e^{K/2}W\right\rangle = -3m_{3/2}\,. \tag{2.4}$$

Restoring the explicit Planck mass M_P, the scalar potential is then given by

$$V = K_{M\overline{N}}F^M\overline{F}^{\overline{N}} - 3m_{3/2}^2M_P^2\,, \tag{2.5}$$

where repeated indices are summed.

Minimizing the resulting scalar potential $V(t,\bar{t})$ generates a non-vanishing value for $\left\langle t+\bar{t}\right\rangle$ at which the auxiliary field F^T vanishes and the vacuum has an energy density given by $\langle V\rangle = -3m_{3/2}^2M_P^2$. The size of the VEV for $\mathrm{Re}\,t$, as well as the size of the gravitino mass $m_{3/2}$, are determined by the size of the constant term w_0 in (2.2), which must be tuned to a value $w_0 \sim \mathcal{O}(10^{-13})$ in Planck units to obtain an

acceptable phenomenology. In particular one has [1]

$$\begin{aligned} \langle a\ \mathrm{Re}\, t\rangle &\simeq \ln(A/w_0), \\ m_{3/2} &\simeq M_P \frac{w_0}{(2\,\langle\, \mathrm{Re}\, t\rangle)^{3/2}}\,. \end{aligned} \tag{2.6}$$

Combining these relations in (2.6) produces

$$\langle a\ \mathrm{Re}\, t\rangle \simeq \ln(M_P/m_{3/2})\,. \tag{2.7}$$

Much of the phenomenology that has come to be known as "mirage mediation" is dependent only on the emergence of the parameteric relation in (2.7), and not on the particulars of any constants that may appear in the nonperturbative stabilizing superpotential, such as the one in (2.2).

To discuss supersymmetry breaking, it is necessary to first address the vacuum energy problem, by adding some additional "uplift" sector which generates supersymmetry breaking in the observable sector while producing a Minkowski vacuum. Many such suggestions exist in the literature [18–22], and the precise choice will not affect our results provided that (a) the Kähler modulus dependence of the added terms in the Lagrangian is dictated solely by consistency of supergravity under Kähler $U(1)$ transformations, and (b) the vacuum expectation value $\langle\, \mathrm{Re}\, t\rangle$ is not perturbed greatly by the addition of the uplift sector [23]. If these conditions are satisfied, then the auxiliary field for the Kähler modulus no longer vanishes in the "lifted" vaccum, but instead satisfies the approximate solution

$$M_0 \equiv \left\langle \frac{F^T}{t+\bar{t}} \right\rangle \simeq \frac{2m_{3/2}}{a\left\langle t+\bar{t}\right\rangle}\,. \tag{2.8}$$

This quantity M_0 then serves as an order parameter of supersymmetry breaking in the observable sector.

The derivation of these soft supersymmetry terms is made considerably more transparent if one employs the chiral compensator technique for generating anomaly-mediated contributions to supersymmetry breaking. If C represents the conformal

compensator of the supergravity multiplet, and F^C is its corresponding auxiliary component, then $\left\langle F^C/C \right\rangle \simeq m_{3/2}$ and there is

$$\left\langle \frac{F^T}{t+\bar{t}} \right\rangle \simeq \left\langle \frac{1}{a\,\mathrm{Re\ t}} \frac{F^C}{C} \right\rangle . \tag{2.9}$$

When working out soft terms, it is convenient to write the above expression as an equality by introducing the parameter α_m [23] via

$$\alpha_m \equiv \frac{m_{3/2}}{M_0 \ln\left(M_P/m_{3/2}\right)} , \tag{2.10}$$

and thus

$$\left\langle \frac{F^C}{C} \right\rangle = \alpha_m \ln\left(\frac{M_P}{m_{3/2}}\right) \left\langle \frac{F^T}{T+\bar{T}} \right\rangle , \tag{2.11}$$

where we have used the vacuum condition in (2.7).

The Additional Singlets

In many string motivated models, additional pairs of fields Ψ, $\overline{\Psi}$ with SM gauge quantum number are not uncommon. Such vector-like pairs often have superpotential interactions with one or more SM singlets (here denoted by X) which can potentially serve as supersymmetric mass terms. Here the KKLT formalism is extended to include these fields acting as messengers, and shown that they couple to a moduli field that gets a vev at the right scale to produce potentially large gauge mediation-like deflection.

The superpotential is assumed to be of the form

$$W = W_0 + W_1(X) + \lambda X \Psi \overline{\Psi} + W_{\text{MSSM}}(\Phi), \tag{2.12}$$

in which W_0 is given by (2.2), $W_1(X)$ denotes the singlet self-interaction superpotential terms, and $W_{\text{MSSM}}(\Phi)$ is the standard MSSM superpotential, involving the observable sector fields Φ_i. The fields Ψ_i and $\overline{\Psi}_i$ are here after taken to be

one or more pairs of $SU(5)$ $\mathbf{5}$ and $\bar{\mathbf{5}}$ multiplets. Different forms of the singlet self-interaction $W_1(X)$ correspond to different ways of stabilizing the modulus X. The Kähler potential will be taken to be

$$K = -3\ln(T+\overline{T}) + Z_X(T,\overline{T})X\overline{X} + Z_i(T,\overline{T})\Phi_i\overline{\Phi}_i + \mathcal{O}\left((|\Phi|^4,|X|^4)\right), \tag{2.13}$$

in which Z_X and Z_i are the Kähler metrics of X and Φ^i, respectively. The Kähler metric for the messenger states Ψ_i and $\overline{\Psi}_i$ will not be relevant for our discussion, but can be taken to be of the same form as the observable sector states. The Kähler metrics $Z_X(T,\overline{T})$ and $Z_i(T,\overline{T})$ will be assumed to be of the standard form

$$Z_X = \frac{1}{(T+\overline{T})^{n_X}}, \quad Z_i = \frac{1}{(T+\overline{T})^{n_i}}, \tag{2.14}$$

in which n_X and n_i are the modular weights of X and Φ_i, respectively.

Successful gauge mediation will require the dynamical generation of a vev for both the lowest component $\langle X\rangle \neq 0$ and the highest component $\left\langle F^X\right\rangle \neq 0$ of the singlet chiral superfield. The simplest case is to have $W_1(X)=0$ and assume that the coupling between X and Ψ, $\overline{\Psi}$ generates $\langle X\rangle \neq 0$ at low energies, as in the electroweak sector of the Standard Model. In this case an F-term vev of approximately the right size is automatically generated [24]

$$F^X \simeq -e^{K_0/2}K^{X\bar{X}}D_{\bar{X}}W \simeq -e^{K_0/2}K^{X\bar{X}}K_{\bar{X}}W_0 \simeq -m_{3/2}X, \tag{2.15}$$

such that

$$\frac{F^X}{X} = -\frac{F^C}{C} \approx -m_{3/2}. \tag{2.16}$$

Alternatively, one can consider a very simple form for W_1 in Eq. (2.12), such as

$$W_1 = \lambda_n \frac{X^n}{\Lambda^{n-3}}, \tag{2.17}$$

in which Λ is some cutoff scale. In principle, the exponent n can have positive or negative values; a negative exponent would indicate that this term originates from

nonperturbative dynamics. In the case where $n > 3$ (stabilization by higher order terms), and the case where $n < 0$ (stabilziation by nonperturbative dynamics), the resulting non-vanishing F-term vev is of the form [9]

$$\frac{F^X}{X} = -\frac{2}{n-1}\frac{F^C}{C}\,. \tag{2.18}$$

Since the modulus and anomaly contributions are already comparable, this result indicates that all three contributions should be roughly equal for a very general class of superpotentials.[2]

2.3 Soft Supersymmetry Breaking

To derive the observable sector soft terms, it is convenient to use the spurion technique, in which the couplings of the effective supergravity Lagrangian are regarded as functions in superspace, with the θ-dependent parts of these couplings generated by the F-term vevs of the theory (for a review, see [26]). The MSSM soft supersymmetry breaking Lagrangian includes terms of the form

$$\mathcal{L}_{\text{soft}} = -m_i^2|\Phi^i|^2 - \left[\frac{1}{2}M_a\lambda^a\lambda^a + A_{ijk}y_{ijk}\Phi^i\Phi^j\Phi^k + \text{h.c.}\right], \tag{2.19}$$

in which m_i^2 are the soft scalar mass-squared parameters, M_a are the gaugino masses, and A_{ijk} are trilinear scalar interaction parameters. These terms are defined in the field basis in which the kinetic terms are canonically normalized. The expressions for the soft supersymmetry-breaking terms take the standard supergravity form

$$M_a = F^A\partial_A \log(\text{Re}\, f_a), \tag{2.20}$$

$$A_{ijk} = -F^A\partial_A \log\left(\frac{y^0_{ijk}}{Y_iY_jY_k}\right), \tag{2.21}$$

$$m_i^2 = -F^A\overline{F}^{\overline{B}}\partial_A\partial_{\overline{B}}\log Y_i\,, \tag{2.22}$$

[2]This result is the same as that obtained in the case of deflected anomaly mediation [25]. Further details of the calculation and the case of renormalizable $W_1(X)$ can be found in [9].

where f_a is the field-dependent, gauge kinetic function for the gauge group $\mathcal{G}_a$, y^0_{ijk} is the bare Yukawa coupling appearing in the superpotential, and the function Y_i is defined by

$$Y_i = \frac{1}{(T+\bar{T})^{n_i-1}} \,. \tag{2.23}$$

From here, one merely needs to specify the dependence of the relevant quantities on the fields X and T, as well as the spurious conformal compensator, C. The latter follows standard computations familiar from the study of anomaly mediation [25, 27–29]. For the gauge kinetic function we take

$$f_a(M_{\rm G}) = T^{\ell_a} \,, \tag{2.24}$$

where $M_{\rm G}$ is the boundary condition scale (taken as the energy scale at which $g_1^2(M_{\rm G}) = g_2^2(M_{\rm G})$), and $l_a = 0, 1$ depending on the type of D-branes from which the gauge groups originate. Since we wish to maintain gauge coupling unification at the GUT scale, we assume that $l_a = 1$ for each of the SM gauge group factors. For the unnormalized Yukawa couplings y^0_{ijk}, there is no C dependence due to the supersymmetric nonrenormalization theorem. Since y^0_{ijk} is also assumed to be independent of T and X, the expression for trilinear terms (2.21) can be reduced to

$$A_{ijk} = A_i + A_j + A_k \,, \tag{2.25}$$

in which

$$A_i = F^A \partial_A \log Y_i \,, \tag{2.26}$$

and Y_i is given by (2.23).

Let $M_{\rm mess}$ be the mass of the messenger fields, with $M_{\rm mess} \equiv \lambda \langle X \rangle$. Recalling that above the mass scale of the messengers the beta functions depend on not only the MSSM fields, but also on the messenger pairs, the soft terms at the GUT scale $M_{\rm G}$ and the messenger threshold effects at $M_{\rm mess}$ are as follows:

Gaugino Masses. The gaugino mass parameters are given by

$$M_a(\mu = M_{\rm G}) = \frac{F^T}{T+\overline{T}} + \frac{g_0^2}{16\pi^2} b'_a \frac{F^C}{C}, \tag{2.27}$$

$$M_a(\mu = M^-_{\rm mess}) = M_a(\mu = M^+_{\rm mess}) + \Delta M_a, \tag{2.28}$$

in which the threshold corrections are

$$\Delta M_a = -N \frac{g_a^2(M_{\rm mess})}{16\pi^2} \left(\frac{F^C}{C} + \frac{F^X}{X} \right). \tag{2.29}$$

Here g_0 is the unified gauge coupling at $M_{\rm G}$, $M^{\pm}_{\rm mess}$ represents an energy scale just above (just below) the messenger mass scale, and the beta functions b'_a are related to their MSSM counterparts by $b'_a = b_a + N$, with $(b_3, b_2, b_1) = (-3, 1, \frac{33}{5})$ (in our conventions, $b_a < 0$ for asymptotically free theories), and N the number of messenger fields Ψ_i, $\overline{\Psi}_i$, where $i = 1, \ldots, N$.

Trilinear terms. The trilinear terms are $A_{ijk} = A_i + A_j + A_k$, with

$$A_i(\mu = M_{\rm G}) \;\; = \;\; (1 - n_i) \frac{F^T}{T+\overline{T}} - \frac{\gamma_i}{16\pi^2} \frac{F^C}{C}, \tag{2.30}$$

where γ_i is the anomalous dimension of Φ_i.

Soft scalar masses. The scalar mass-squared parameters are given by

$$m_i^2(\mu = M_{\rm G}) = (1 - n_i) \left| \frac{F^T}{T+\overline{T}} \right|^2 - \frac{\theta'_i}{32\pi^2} \left(\frac{F^T}{T+\overline{T}} \frac{F^{\overline{C}}}{\overline{C}} + \text{h.c.} \right) - \frac{\dot{\gamma}'_i}{(16\pi^2)^2} \left| \frac{F^C}{C} \right|^2,$$

$$m_i^2(\mu = M^-_{\rm mess}) = m_i^2(\mu = M^+_{\rm mess}) + \Delta m_i^2, \tag{2.31}$$

where the threshold corrections are

$$\Delta m_i^2 = \sum_a 2c_a N \frac{g_a^4(M_{\rm mess})}{(16\pi^2)^2} \left(\left| \frac{F^X}{X} \right|^2 + \left| \frac{F^C}{C} \right|^2 + \frac{F^X}{X} \frac{F^{\overline{C}}}{\overline{C}} + \text{h.c.} \right). \tag{2.32}$$

In the above, c_a is the quadratic Casimir, and γ_i, $\dot{\gamma}_i$, θ_i (γ_i', $\dot{\gamma}_i'$, θ_i') are listed in Appendix A.

We now replace the F terms with the parameterization given in [8, 9], as follows:

$$\frac{F^C}{C} = \alpha_m \ln \frac{M_P}{m_{3/2}} \frac{F^T}{T+\overline{T}} = \alpha_m \ln \frac{M_P}{m_{3/2}} M_0, \tag{2.33}$$

$$\frac{F^X}{X} = \alpha_g \frac{F^C}{C} = \alpha_g \alpha_m \ln \frac{M_P}{m_{3/2}} M_0, \tag{2.34}$$

in which $M_0 \equiv F^T/(T+\overline{T})$ sets the overall scale of the soft terms. The dimensionless parameter α_m is the α parameter of mirage mediation: it denotes the relative importance of anomaly mediation with respect to gravity mediation. In the specific scenario considered by KKLT, $\alpha_m = 1$. The dimensionless parameter α_g denotes the relative importance of the gauge-mediated terms with respect to the anomaly-mediated terms. The values of α_g depend on the details of the stabilization of X, as described in Section 2.2.

With the parametrization given in Eqs. (2.33) and (2.34), the soft terms at $M_{\rm G}$ take the form

$$M_a(\mu = M_{\rm G}) = M_0 \left[1 + \frac{g_0^2}{16\pi^2} b_a' \alpha_m \ln \frac{M_P}{m_{3/2}} \right], \tag{2.35}$$

$$A_i(\mu = M_{\rm G}) = M_0 \left[(1-n_i) - \frac{\gamma_i}{16\pi^2} \alpha_m \ln \frac{M_P}{m_{3/2}} \right], \tag{2.36}$$

$$m_i^2(\mu = M_{\rm G}) = M_0^2 \left[(1-n_i) - \frac{\theta_i'}{16\pi^2} \alpha_m \ln \frac{M_P}{m_{3/2}} - \frac{\dot{\gamma}_i'}{(16\pi^2)^2} \left(\alpha_m \ln \frac{M_P}{m_{3/2}} \right)^2 \right], \tag{2.37}$$

where the anomalous dimensions are given in Appendix A, and the threshold

terms are given by

$$\Delta M_a(\mu = M_{\text{mess}}) = -M_0 N \frac{g_a^2(M_{\text{mess}})}{16\pi^2} \alpha_m \left(1 + \alpha_g\right) \ln \frac{M_P}{m_{3/2}}, \tag{2.38}$$

$$\Delta m_i^2(\mu = M_{\text{mess}}) = M_0^2 \sum_a 2 c_a N \frac{g_a^4(M_{\text{mess}})}{(16\pi^2)^2} \left[\alpha_m (1 + \alpha_g) \ln \frac{M_P}{m_{3/2}}\right]^2. \tag{2.39}$$

The parameters of the model are the mass scales M_0 and M_{mess}, as well as the dimensionless quantities α_m, α_g, the number of $SU(5)$ messenger pairs N, the modular weights n_i, $\tan\beta$, and sign μ (the model-dependent μ and B_μ parameters are replaced as usual by the Z boson mass, $\tan\beta$, and the sign of μ).

In the mirage mediation scenario, one of the most distinctive features of the soft terms is the unification of the gaugino masses at the mirage unification scale M_{mirage}:

$$M_{\text{mirage}} = M_{\text{G}} \left(\frac{m_{3/2}}{M_P}\right)^{\frac{\alpha_m}{2}}. \tag{2.40}$$

In deflected mirage mediation, one finds a similar mirage unification phenomenon for the gaugino masses. From the form of the soft terms of Eqs. (2.35) and (2.38), the new mirage unification scale for the gauginos (see also [8]) is

$$M_{\text{mirage}} = M_{\text{G}} \left(\frac{m_{3/2}}{M_P}\right)^{\frac{\alpha_m \rho}{2}}, \tag{2.41}$$

in which ρ is given by

$$\rho = \frac{1 + \frac{2Ng_0^2}{16\pi^2} \ln \frac{M_{\text{G}}}{M_{\text{mess}}}}{1 - \frac{\alpha_m \alpha_g N g_0^2}{16\pi^2} \ln \frac{M_P}{m_{3/2}}}. \tag{2.42}$$

The mirage unification scale of the gauginos is thus deflected from the mirage mediation result. The size of the deflection is dependent on α_g, N, and M_{mess}, which govern the size of the messenger thresholds.

For the A terms and the soft scalar mass-squares, the mirage unification behavior no longer happens in general in the presence of the messengers. The exception is when the messenger scale is below the scale of mirage unification which would

occur in the absence of the messenger thresholds, since the theory is then effectively the same as mirage mediation below M_{mess}. In Eqs. (2.41) and (2.42), the mirage mediation result of Eq. (2.40) is obtained only if $N = 0$. This demonstrates that the mirage mediation limit is not reached when gauge mediation is switched off ($\alpha_g \to 0$); it only occurs when the messengers are removed from the theory at all scales ($N = 0$). The reason is that the messengers affect the MSSM beta functions above the messenger scale, which in turn affects the boundary conditions for the anomaly-mediated terms.

2.4 Constraints on DMM Parameter Space

In deflected mirage mediation there are two distinct contributions to soft supersymmetry breaking, a KKLT-like contribution at the GUT or string scale, followed by a deflection at some messenger scale M_{mess}. For the first contribution, there are two independent mass scales, given by the (normalized) gravitino mass $m_{3/2}$ and the modulus contribution M_0. Alternatively, one can work with either of the mass scales and the derived parameter α_m. We use the latter, and will use M_0 as the independent mass scale. The value of $m_{3/2}$ is computed by fitting to the expression in (2.10), and the calculated value will then be input into the high scale soft term expressions in (2.35), (2.36) and (2.37).

In addition, one must specify the modular weights for the chiral supermultiplets that make up the MSSM field content. In this work we will allow only a limited amount of nonuniversality in assigning these weights. In particular, we will always assume that all matter multiplets arise from the same sector of the theory, so that they carry a universal modular weight n_M, while the two Higgs doublets may carry an independent modular weight which we will denote n_H. We let both take half-integer values between zero and one. Under these assumptions there are then nine possible combinations of modular weights to consider, which we can represent by the pair of weights (n_M, n_H). A theory defined solely by the choice of modular weights, $\tan\beta$, α_m, and M_0, represents a general mirage mediation model. Nevertheless, we will often refer to it (somewhat inappropriately) as a

"KKLT model," to distinguish it more clearly from a deflected mirage mediation model.

In DMM, there is an additional mass scale M_{mess}, where N SU(5) $\mathbf{5}\,\bar{\mathbf{5}}$ messengers integrate out with a strength given by a derived parameter α_g. The quantities α_g, N, and the KKLT parameters are input to the deflected contributions given by (2.38) and (2.39), which may be sizeable. Thus, the parameter space we will consider consists of a discrete choice of modular weights and three continuous parameters: M_0, α_m and $\tan\beta$. These quantities define a KKLT-like "base point". The deflection from this base point will be characterized by the three parameters α_g, M_{mess}, and N. These DMM parameters can be set by considering an explicit model, but here we choose to let them vary continuously.

To fully explore the entirety of this parameter space would require a scan over the five continuous parameters M_0, M_{mess}, α_m, α_g and $\tan\beta$ and the three discrete parameters n_M, n_H, and N. A comprehensive scan would quickly become unrealistically computationally expensive, as the parameter space is large. Because the DMM framework is an extension of the KKLT framework, we approach our scan in the same fashion. For each set of modular weights we will randomly select the three continuous parameters of the KKLT framework in the ranges $M_0 \in [1,5]$ TeV, $\tan\beta \in [5,50]$ and $\alpha_m \in [0,2]$. We then build a three-dimensional scan in the DMM parameter space around each base point, scanning $\alpha_g \in [-1,1]$ in steps of 0.05, $\log_{10}[M_{\text{mess}}/\text{GeV}] \in [5,14]$ in unit steps, and $N \in [1,5]$ in unit steps.

The range in α_g is chosen as in [14] to reflect a range of possible moduli stabilization mechanisms. The UV cutoff on the range in the messenger scale is chosen to avoid possible GUT threshold contributions, while the lower bound is meant to avoid large contributions to flavor-changing neutral current processes. The number of messengers N is chosen between 0 (where the model is identical to KKLT), and 5, which is the maximum number of messengers before couplings tend to run to nonperturbative values with an $\mathcal{O}(\text{TeV})$ messenger scale. We note that for the $N = 3$ case, the strong coupling does not run between the GUT and messenger scales at one loop order.

For each choice of KKLT input parameters $(n_M, n_H, M_0, \alpha_m, \tan\beta)$, the soft terms

are computed from (2.35), (2.36) and (2.37). The renormalization group (RG) equations are solved from the boundary condition scale to the electroweak scale using a version of the package SOFTSUSY 3.3.9 [30] that has been modified to account for the gauge mediation contributions [8, 9]. The modification introduces an intermediate messenger scale where the threshold corrections (2.38) and (2.39), determined by the DMM parameters $(N, \alpha_g, M_{\text{mess}})$, are added to the running masses. The software uses a modified set of renormalization group equations to include the effect of messengers above the scale determined by M_{mess}, at the two loop level.

At the electroweak scale, a combination of input parameters will be excluded from the data set if the soft supersymmetry breaking scalar mass-squared parameter is negative for one or more of the matter fields. At this stage, the radiatively corrected Higgs potential is minimized and physical masses are calculated. We again eliminate a combination of input parameters if no solution to the conditions for electroweak symmetry breaking can be found, or if the solution fails to converge adequately. Finally, we then ask that the lightest supersymmetric particle (LSP) for each model point be a neutralino, though stau, gluino and stop LSPs are all possible in various regions of parameter space. In total, 6.1 million points were generated from 2700 KKLT base points, evenly distributed across the nine modular weight combinations. After application of all phenomenological constraints, slightly less than 390,000 DMM points survive, originating from just over 2500 KKLT base points.

Having passed the minimal phenomenological requirements, the electroweak scale spectrum is then passed to MicrOMEGAS 2.2 [31] where the thermal relic abundance $\Omega_\chi h^2$ is computed for the stable neutralino. In addressing the issue of cold dark matter, we take a conservative approach and impose only an upper bound on the neutralino relic density. We use a cut on a 3σ upper bound on the calculation from MicrOMEGAS of $\Omega_\chi h^2 \leq 0.128$ taken from [32]. We further require the mass of the lightest chargino to exceed the LEP bound ($m_{\chi_1^\pm} \geq 103.5\,\text{GeV}$) and that the value of Br$(B_s \to \mu^+\mu^-)$ to be within 3σ of the LHCb and CMS measurements [33–35]. Finally, we take into account the recent measurements of the Higgs scalar mass [36–38] by requiring $123\,\text{GeV} \leq m_h \leq 127\,\text{GeV}$, which represents a rather generous

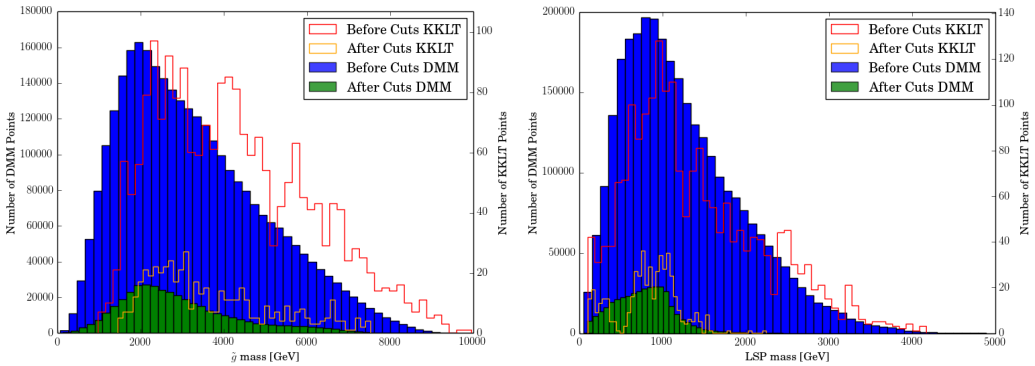

Figure 2.1: Distribution of gluino masses (left) and LSP masses (right), in units of GeV, for all modular weights in DMM and for the KKLT base points. The blue histogram represents all DMM points with an acceptable minimum and a neutralino LSP. Points in the green histogram also have an acceptable Higgs mass and neutralino relic density taken from the blue. The red and orange outlines represent the distributions for the KKLT base points where the red has an acceptable minimum and a neutralino LSP, and the orange has an acceptable Higgs mass and relic density, with the scale on the right side.

mass range for this parameter, given ongoing efforts to improve the reliability of Higgs mass calculations [39–41].

We display the results of our scan in two subsections. In the first subsection, we comment on some generic features of the DMM parameter space, using all of the data generated by our scan. In the following subsection, we focus on specific KKLT base points with reasonable low-energy phenomenology, and discuss modifications to the spectra arising from the introduction of gauge-charged messenger fields.

Generic Properties

In Fig. 2.1, we see the effect of our constraints on the parameter space. The left panel represents the distributions in the gluino mass, while the right panel gives the distributions in the LSP mass. In both panels, the blue histogram represents all points with an acceptable minimum and a neutralino LSP. Points in the green histogram also have an acceptable Higgs mass and neutralino relic density. The

red and orange outlines are the equivalent distributions for the KKLT base points. Although statistics are low for both KKLT distributions, we can see that the gluino masses of the base points are shifted to the right in relation to the solid DMM distributions. For the base points the minimum mass is roughly 1.5 TeV, with a peak roughly around 3 TeV, whereas for DMM, we have a peak closer to 2 TeV, with the possibility of very low-mass gluinos. Many, but not all, of these low mass points would have given a detectable signal at the past LHC run at $\sqrt{s} = 8$ TeV. The overall shift in these distributions means that more of the parameter space for DMM will be probed in the current LHC run, but there remains a long tail that extends beyond the expected reach of the LHC, even after 3000 fb^{-1} of data-taking. For the mass of the lightest neutralino, the distribution of KKLT base points and DMM points are not significantly different. When the current limits on the neutralino relic density and Higgs mass are taken into account, we expect that the entirety of the neutralino and gluino mass ranges should be accessible at a future 100 TeV collider [42, 43].

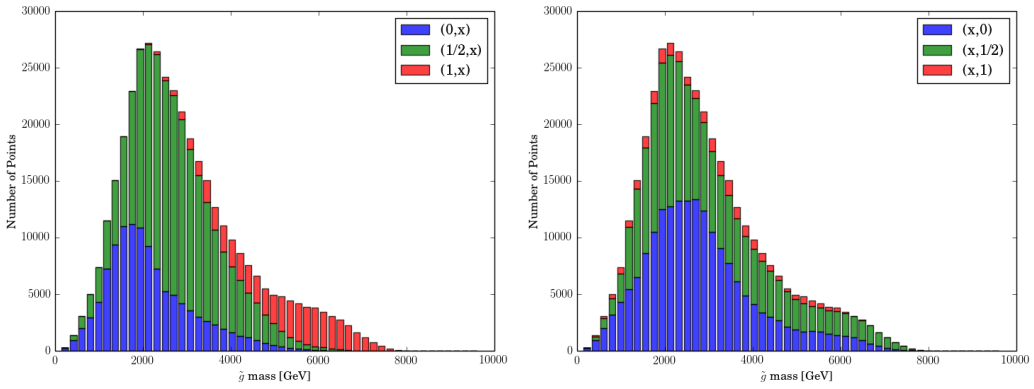

Figure 2.2: Distribution of gluino mass (in GeV), broken down by modular weight combinations. The left plot is broken down by n_M and the right is by n_H. All points have an acceptable electroweak (EW) vacuum, Higgs mass, and neutralino relic density.

Figure 2.2 breaks down the allowed region (green histogram) in the left panel of Fig. 2.1 by modular weight. In the left (right) panel, data is aggregated over various n_H (n_M) values, for particular n_M (n_H) values held constant. The typical value of the gluino mass correlates strongly with the matter modular weight, with

the distribution moving to larger values with increasing n_M. The origin of this behavior lies in the high scale boundary condition for the soft masses of the matter fields (2.37), which decreases with increasing n_M. The relatively large Higgs mass $m_h \simeq 125\,\text{GeV}$ requires a relatively heavy stop mass, and thus larger values of n_M require a larger value of M_0 to compensate. The effect is enhanced by the fact that larger modular weights n_M reduce the size of the trilinear A-terms (2.36), thereby reducing the left-right mixing in the stop sector. Conversely, as the values of n_H only affect the boundary conditions of the Higgs scalar masses, we do not expect the overall mass scale to be dependent on this parameter, and indeed the three distributions in the right panel of Figure 2.2 are qualitatively similar. A desire for a lighter, and hopefully LHC accessible, spectrum motivates model-building efforts in which MSSM fields are localized on stacks of $D7$-branes for which $n_i = 0$.

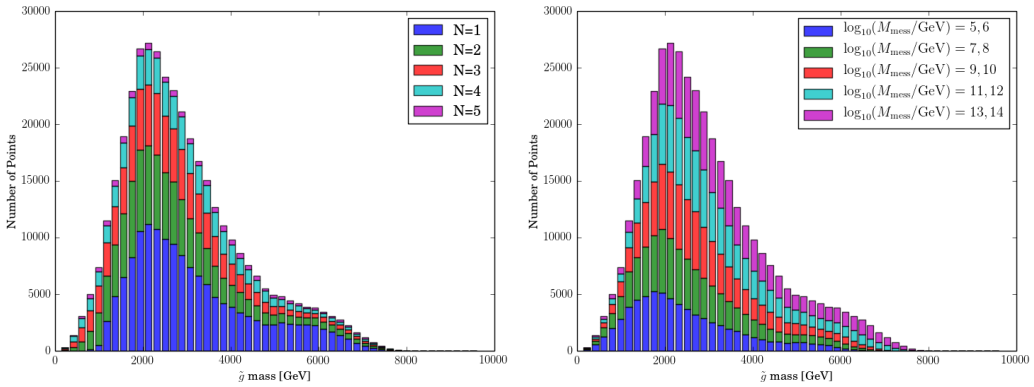

Figure 2.3: Distribution of gluino mass (in GeV), broken down by N (left) and $\log_{10}(M_{\text{mess}}/\text{GeV})$ (right). All points have an acceptable EW vacuum, Higgs mass, and neutralino relic density.

Figure 2.3 further studies the influence of the messenger sector on the predicted gluino mass. The left panel of Fig. 2.3 breaks down the distribution by number of messengers, while the right panel addresses the messenger scale. Points with lighter gluino masses tend to have two or more messengers and low messenger scales. For these points, the deflection contribution is comparable in size to the running mass itself, allowing for a cancellation to occur, while the small messenger scale prevents large corrections from RG effects. In contrast, for large gluino masses,

the messenger scale tends to be on the high end, with $\alpha_g \sim -1$, so that the gluino experiences the largest possible mass increase through RG evolution.

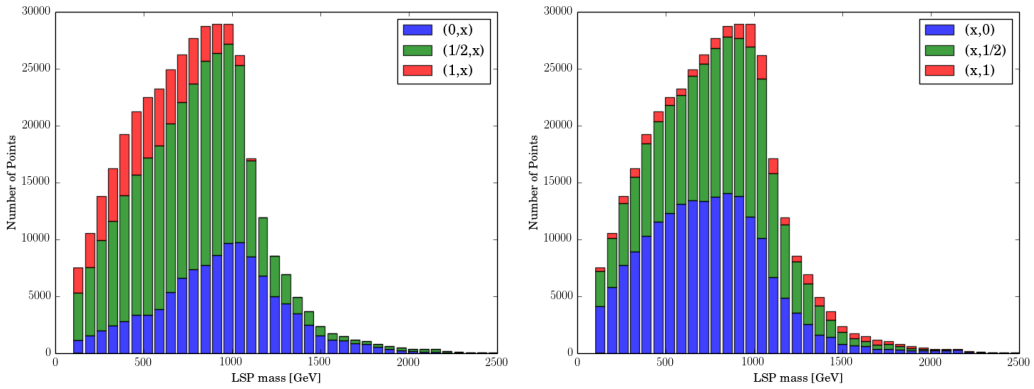

Figure 2.4: Distribution of the LSP mass (in GeV), broken down by modular weights. The left plot is broken down by n_M and the right is by n_H. All points have an acceptable EW vacuum, Higgs mass, and neutralino relic density.

In the right half of Fig. 2.1, we see that the majority of possible LSP masses are $\mathcal{O}(1\,\text{TeV})$ and likely accessible at the LHC. The sharp cutoff at 100 GeV is the result of the LEP limit on the chargino mass. The KKLT distributions for the LSP mass mirror those for DMM. Figure 2.4 breaks this plot down by modular weight combination, similar to Fig. 2.2. There is a weak dependence on n_H, with smaller n_H preferring smaller values of the LSP mass, but a strong dependence on n_M. Larger values of n_M push us towards smaller LSP masses, where the neutralino is almost exclusively Higgsino-like. For $n_M = 1$, the up-type Higgs soft mass is generally large at the GUT scale, and it must run to a negative value to achieve proper electroweak symmetry breaking; in this parameter range, $m_{H_u}^2$ achieves a small negative value, and the μ term needs to be small enough to satisfy the Z-mass constraint. For $n_M = 0$ or $\frac{1}{2}$ there are points where the LSP has a bino or winolike wave function. The winolike points tend to come from the negative gauge contribution (2.38) pushing the value of M_2 below zero, where $|M_2| < |M_1|,\ |\mu|$. We will come back to these winolike points in subsequent sections.

The distribution of relic density as a function of LSP mass, Fig. 2.5, shows

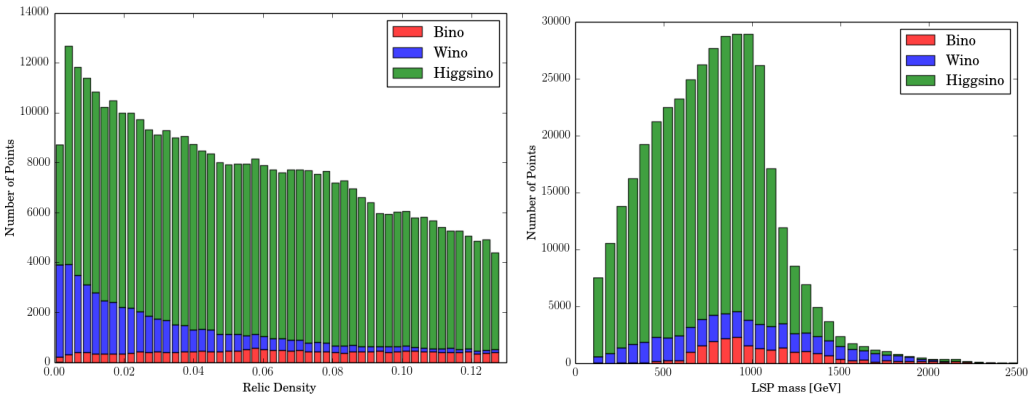

Figure 2.5: Distribution of the neutralino relic density $\Omega_\chi h^2$, left panel, and LSP mass (in GeV), right panel, aggregated for all modular weights. Both histograms are broken down by wave-function composition of the LSP. All points have an acceptable EW vacuum, Higgs mass, and neutralino relic density.

that winolike LSPs generally fail to saturate the Planck-preferred value of $\Omega_\chi h^2 \simeq 0.12$, with a proper relic density coming from Higgsino and binolike points. The distribution of LSP masses, in the right panel of Fig. 2.5, shows that the majority of possible LSPs are Higgsino-like with an average mass of approximately 800 GeV. Higgsino annihilation in the early universe becomes too inefficient to achieve $\Omega_\chi h^2 \lesssim 0.12$ when the mass exceeds about 1 TeV, as is clear from the sharp cutoff in the distribution. Meanwhile, most binolike points with an acceptable relic density arise from coannihilation, primarily with stops, but also occasionally with gluinos. Low mass winolike cases involve coannihilation with other low-mass gauginos [44, 45], while higher-mass winos involve standard thermal freeze-out. Compared to KKLT, there is a relative paucity, about 5% of the the sample, of binolike LSPs in Figure 2.5. As messengers are introduced, the values of the GUT-scale coupling and beta-function coefficients increase, leading to heavier Majorana masses at the GUT scale. At the messenger scale, the bino will experience the smallest deflection, so a point with a binolike LSP needs some sort of conspiracy in the RG-flow to get the bino lighter than the wino and Higgsino.

The winolike points, though relatively few in number, are worth exploring

further as such an outcome does not occur in the KKLT scenario [7]. Wino-like points tend to have large values for the parameter α_g, which controls the size of the correction in (2.38). When $\alpha_g \simeq 1$, the wino mass M_2 is pushed to values which are below that for M_1 and M_3. There is some correlation with the modular weights as well. These winolike points are common at small n_M, admitting the entire range in α_g, and vanish when $n_M = 1$, as the one-loop Higgs mass corrections are not large enough. These points tend to have larger values of n_H, though this is a weaker effect, likely the result of needing a lighter Higgs soft mass to get electroweak symmetry breaking to occur properly. There are points that yield an acceptable low-energy spectrum for the entire range in M_{mess}, and for $\alpha_m > 0.5$. This relative lack of points for small α_m is seen globally in the DMM parameter space, because small or vanishing α_m corresponds to the limit where the model looks like minimal supergravity with a single mass parameter.

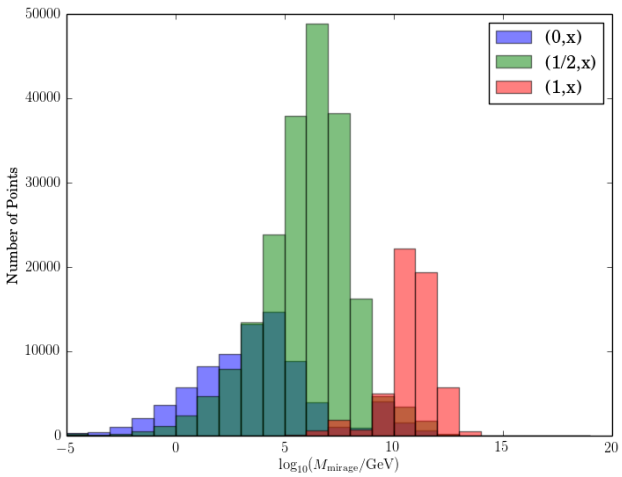

Figure 2.6: Distribution of the mirage scale, M_{mirage}, defined by equation (2.41). All points have an acceptable EW vacuum, Higgs mass, and neutralino relic density. The red distribution represents all cases with $n_M = 1$, the green those cases with $n_M = 1/2$, and the blue those cases with $n_M = 0$. Not shown is a long tail of cases with $n_M = 0, 1/2$, extending to very small mirage scales ($M_{\text{mirage}} \sim 10^{-30}$ GeV). Note that these histograms overlap, with the darker shaded green and red colors indicating the presence of cases with $n_M = 0$ and $n_M = 1/2$, respectively.

Finally, Fig. 2.6 gives the distribution in the mirage scale, M_{mirage}, from equation (2.41), broken down by the value of the matter field modular weight n_M. Though the mirage scale is not itself directly measurable, it can be inferred from a successful extraction of the gaugino mass hierarchy via measurements at the LHC [46], followed by RG evolution to discover the scale of unification [47, 48]. It is intriguing to note that such an exercise provides some information on the matter modulus weight; for instance, points with large mirage scales are more often points with $n_M = 1$. If instead one were to find that gaugino masses would unify at scales *below* a TeV, then the matter modular weight is more likely $n_M = 0$ or $n_M = 1/2$.

DMM Perturbations on KKLT Base Points

The previous subsection identified one particular qualitative difference between the pure mirage mediation/KKLT framework, and the allowed possibilities for deflected mirage mediation: the possibility of wino-like dark matter. In this section we will pursue other qualitative distinctions that arise from the addition of gauge-charged messenger fields. Previous work [7] performed an exhaustive search in the KKLT framework, from which we will make our departures from KKLT into DMM. This work scanned M_0, α_m, and $\tan\beta$ for each combination of modular weights (n_M, n_H). From these results, we can choose a small number of benchmarks of the most phenomenologically relevant points in this framework. The benchmark points chosen are listed in Table 2.1, and are representative of the most phenomenologically interesting points within the KKLT framework across a span of modular weight combinations. We can then use these particular combinations of M_0, α_m, $\tan\beta$, and the modular weights, then scan over α_g, M_{mess}, and N.

	KKLT Parameters					Key Masses [GeV]								
Point	n_M	n_H	M_0	α_M	$\tan\beta$	m_h	$m_{\tilde{\chi}_1^0}$	$m_{\tilde{\chi}_2^0}$	$m_{\tilde{\chi}_1^\pm}$	m_A	$m_{\tilde{\tau}_1}$	$m_{\tilde{g}}$	$m_{\tilde{t}_1}$	$\Omega_\chi h^2$
1	0	0	1900	1.05	9	125.1	1406	1715	1715	2966	1910	2873	1434	0.062
2	0	0	2900	1.80	9	123.8	1547	1553	1550	3224	2821	3084	1554	0.077
3	0	0.5	1950	1.65	27	125.2	1415	1429	1420	1647	1749	2264	1500	0.124
4	0	1	1350	0.63	29	123.5	837	1177	1177	1680	1217	2417	1685	0.114
5	0.5	0	2000	1.25	28	125.5	676	683	679	1825	1219	2727	1461	0.055
6	0.5	0.5	1800	0.70	9	123.3	1150	1554	1554	2327	1360	3055	1978	0.069
7	0.5	0.5	3200	1.45	7	123.9	974	978	976	2628	2286	3924	2478	0.106
8	0.5	1	4100	1.85	9	123.4	1090	1093	1092	855	2806	4072	2878	0.124
9	1	0	4000	0.65	6	124.1	667	669	668	4596	1181	6517	3683	0.048
10	1	0.5	3600	0.80	20	125.1	763	766	765	2987	891	5578	3473	0.063

Table 2.1: KKLT Benchmark Points. These cases with $N = 0$ will serve as reference points for our exploration of the much richer DMM parameter space.

	Ranges [GeV]													
	$m_{\tilde{\chi}_1^0}$		$m_{\tilde{\chi}_2^0} - m_{\tilde{\chi}_1^0}$		$m_{\tilde{\chi}_1^\pm} - m_{\tilde{\chi}_1^0}$		$m_{\tilde{g}}$		$m_{\tilde{\tau}_1}$		$m_{\tilde{t}_1}$		Ωh^2	
Point	Min	Max	Min	Max	Min	Max	Min	Max	Min	Max	Min	Max	Min	Max
1	234	1485	4.8	442	0.2	358	526	3162	1400	1910	514	1844	0.001	0.122
2	116	1638	4.6	1241	0.2	2.9	439	4094	1830	2824	982	4859	0.001	0.127
3	968	1422	7.9	33	3.3	5.9	1074	2672	1217	1753	989	1661	0.014	0.123
4	437	839	3.0	340	0.2	340	448	2421	1157	1217	1074	1687	0.006	0.128
5	64	1101	5.2	100	1.6	4.8	440	3398	879	1241	668	2387	0.001	0.127
6	654	1272	4.8	498	0.7	498	713	3560	1154	1385	1098	2334	0.019	0.128
7	74	1453	3.0	7.9	1.6	2.7	1228	4956	1640	2313	1366	3126	0.001	0.128
8	318	1111	2.5	1876	0.2	1.4	3767	5642	1779	2806	2700	7035	0.003	0.128
9	86	1083	2.7	6.3	1.4	2.7	3029	6843	898	1214	2537	3929	0.001	0.127
10	79	885	2.9	5.5	1.6	2.6	2169	5682	543	895	2707	3549	0.001	0.116

Table 2.2: Ranges for the superpartner masses in DMM for the KKLT Benchmark Points presented in Table 2.1. The minimum and maximum values give the observed range in each quantity over the three-dimensional scan in $(N, \alpha_g, M_{\text{mess}})$.

For a given KKLT point, deflection can lead to large changes in the spectrum. Table 2.1 gives the values for our benchmark KKLT points, and Table 2.2 shows the effect of scanning over the DMM extension of the parameter 3space for these points. That is, Table 2.2 gives the maximum and minimum value of each quantity, over the three-dimensional scan in $(N, \alpha_g, M_{\rm mess})$ described above. Consider, for example, point 1 in Table 2.1. The KKLT parameter set predicts a $1400\,$GeV LSP neutralino. However, the range of lightest neutralino masses for point 1 in Table 2.2 indicates that the deflection can reduce the neutralino mass down to $\sim 250\,$GeV, or (alternatively) push other superpartner masses to very low values. For all ten benchmarks the minimum LSP mass found is generally quite lower than that predicted by the KKLT base point.

The LSP for KKLT base point 1 is 99.8% binolike. The neutralino relic density is acceptable as the result of coannihilation between this binolike state and the nearly degenerate stop. From Table 2 we see that over the range of DMM variants of this point, there is a transition from binolike to winolike and Higgsino-like LSPs. This is evidenced by the minimum values obtained in the mass differences $m_{\tilde{\chi}_2^0} - m_{\tilde{\chi}_1^0}$ and $m_{\tilde{\chi}_1^\pm} - m_{\tilde{\chi}_1^0}$. As a consequence, coannihilation with light gauginos can produce a greatly reduced neutralino relic density. The LSP for KKLT base point 2 is 99.7% Higgsino-like, and again very close in mass to the lightest top squark. Much of the DMM parameter space based on this point also yields a Higgsino-like LSP, but the possibility of getting large $m_{\tilde{\chi}_2^0} - m_{\tilde{\chi}_1^0}$ for certain N and α_g combinations suggests that winolike LSPs are also possible. In such cases, the stop mass can be quite a bit larger than for the KKLT point. Similar behavior is seen with base point 5 in Tables 2.1 and 2.2.

We can visualize the content of these two tables by looking at Fig 2.7, which depicts the minimum and maximum values of Table 2.2 for point 1 (left panel), and point 2 (right panel), both involving the modular weight set $(n_M, n_H) = (0, 0)$. The heavy dot represents the KKLT base point from Table 2.1. The magnitude of the DMM corrections (2.38) and (2.39) increase as α_g moves from negative to positive values. In both cases we see the striking effects that the gauge messenger fields can have on the resulting low-energy spectrum. Notable is the great reduction in

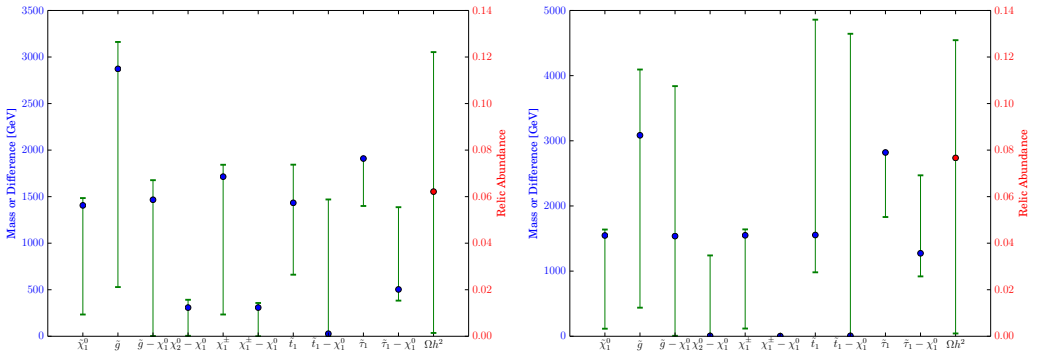

Figure 2.7: Low-energy mass ranges for point 1 (left) and point 2 (right) for the quantities in Table 2.2. The dots represent the values for the corresponding KKLT base point with zero messengers, from Table 2.1.

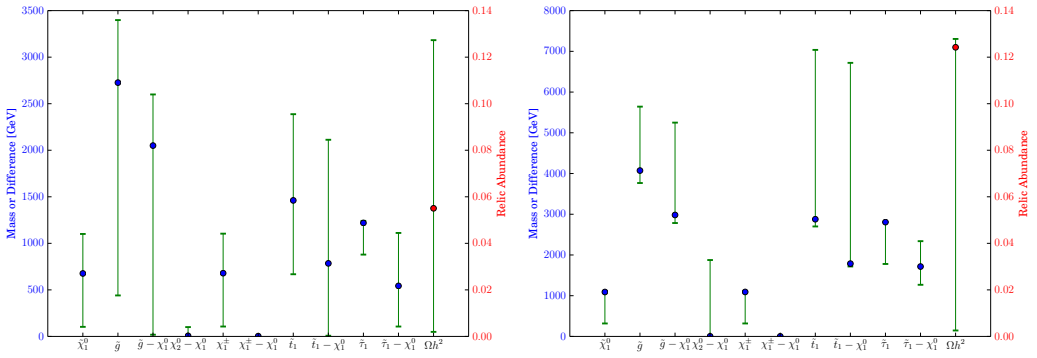

Figure 2.8: Low-energy mass ranges for point 5 (left) and point 8 (right) for the quantities in Table 2.2. The dots represent the values for the corresponding KKLT base point with zero messengers, from Table 2.1.

gluino mass that is possible, relative to the KKLT base point. This typically comes in conjunction with a great compression of the spectrum, with the mass difference $m_{\tilde{g}} - m_{\tilde{\chi}_1^0}$ often approaching zero in the extreme DMM limit.

As a general rule, the addition of deflected mirage mediation results in a more compressed superpartner spectrum, though there are variations depending on the KKLT base point. Figure 2.8 depicts the minimum and maximum values of Table 2.2 for point 5 (left panel), and point 8 (right panel). Consider first the DMM ensemble

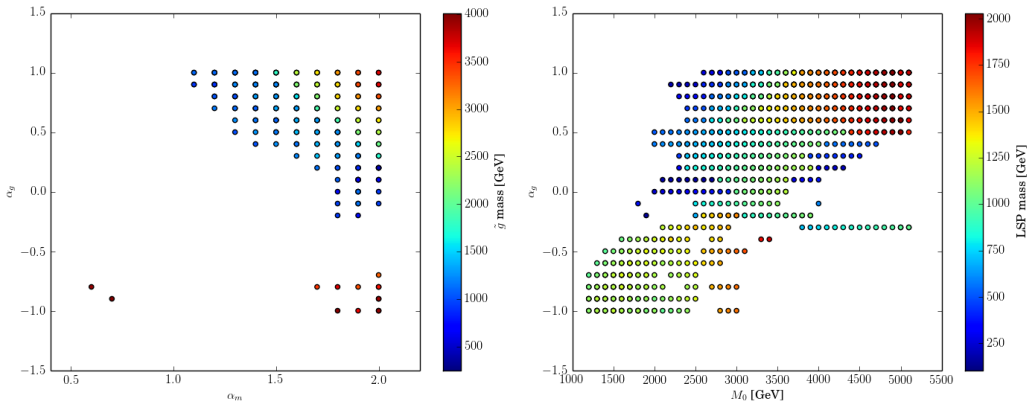

Figure 2.9: Allowed parameter space for DMM perturbations on point 2 of Table 2.1. In both cases we assume $(n_M, n_H) = (0, 0)$, $\tan\beta = 9$, and fix either $M_0 = 2900\,\text{GeV}$ (left panel) or $\alpha_m = 1.8$ (right panel), as is the case for the KKLT base point 2 in Table 2.1. The allowed region in the (α_m, α_g) plane (left) and (M_0, α_g) planes are displayed for $N = 3$.

based on point 5. Here we see a degenerate system of electroweak gauginos which is not significantly affected by the DMM deformation. For the base point in Table 2.1, the other superpartners (particularly those carrying color) are not close to the LSP in mass. The addition of gauge messengers, for positive α_g, has the potential to drive these masses down significantly, potentially yielding a rich diversity of particles at, or just around, the TeV scale. Similar behavior is seen with the DMM ensemble based on points 3, 4 and 7. Yet for base point 8, the KKLT point is already near the low end of the ranges for gluino and stop masses. The DMM addition can only increase these masses (and decrease the LSP mass), meaning that here the gauge messengers generally *reduce* the compression in the spectrum. Naturally, these effects have profound implications for superpartner searches at the LHC [49, 50], which will be our focus in Section 2.5.

Before proceeding to the LHC implications of deflected mirage mediation, it is instructive to consider how the inclusion of gauge messengers can affect the space of viable KKLT base points themselves. We focus here on the particular case of base point 2 from Table 2.1. Figure 2.9 shows the effect of adding $N = 3$

messenger multiplets, over all messenger mass scales, to this point. In the left panel, α_m is allowed to vary away from the original value of $\alpha_m = 1.8$, while keeping $M_0 = 2900\,\text{GeV}$ fixed. In the right panel, M_0 is allowed to vary while α_m is held fixed. Our KKLT base point is clearly part of the $\alpha_g = 0$ line in the left panel, but the inclusion of $\alpha_g \neq 0$ allows other α_m values, including the possibility of very light gluinos for $\alpha_g \to 1$ near the KKLT limit of $\alpha_m = 1$.

In the left panel of Figure 2.9 we see three distinct regions, two points where $\alpha_m \sim 0.5$ and $\alpha_g \sim -1$, an area with $\alpha_m \sim 1.8$ and $\alpha_g < -0.5$, and finally a large region with $\alpha_m > 1$ and $\alpha_g > -0.5$. The first region comes about due to points with a binolike LSP and an intermediate messenger scale $M_{\text{mess}} \sim 10^9\,\text{GeV}$, driving the gluino mass down and softening the running of the stop so that the Higgs mass for these points is boosted by a highly mixed, and light, stop. The other region, below $\alpha_g < -0.5$, are points with light Higgsino LSPs and mixed stops as well. The gap around $\alpha_g \simeq -0.5$ consists of points where the stop is either very light or the LSP. Here the anomaly mediated contributions are large, leading to a light stop mass in the UV, while the messenger-scale corrections are too small to drive the neutralino mass below that of the stop. The upper region consists of points with either a wino LSP or Higgsino LSP and heavy stops. As α_g decreases, α_m needs to increase to compensate to make the stop heavy and thereby obtain the correct Higgs mass.

In the right panel of Figure 2.9, we see that varying α_g allows for a large range of overall mass scales $1\ \text{TeV} \leq M_0 \leq 5\ \text{TeV}$. However, the resulting mass of the superpartners is not simply correlated with this quantity, once the phenomenological constraints are imposed on the parameter space. This is evidenced by the color in the right panel of Figure 2.9, which gives the LSP mass in GeV. Larger values of M_0 tend to require a smaller value of the messenger scale, and larger values of α_g, to get the correct Higgs mass. Thus, for a fixed value of α_g, the points in the figure at different M_0 values tend to have differing messenger mass scales. For positive α_g, the largest messenger scales are at the far right of the plot (large M_0). For negative α_g this relationship is inverted. Above $\alpha_g = 0.5$, the LSP is exclusively winolike, as the deflection is now large enough to push the wino mass to small values. This is significant, as winolike LSPs were not found in the pure KKLT scenario studied

in [6].

2.5 LHC Implications of Deflected Mirage Mediation

The discovery of the Higgs boson at the LHC in 2012 and ever-improving bounds on the dark matter relic density from the Planck experiment have placed considerable constraints on the form that any new model of physics might take. As the LHC begins running at 13 TeV, and later 14 TeV, these constraints are expected to further tighten. As we enter into this new era, we are particularly interested in how DMM will fare in the coming years. For pure mirage mediation, embedded in the KKLT framework for type IIB string theory, previous work [7] demonstrated that the heavy mass spectra left KKLT undiscoverable at $\sqrt{s} = 8$ TeV, with rather dim discovery prospects at $\sqrt{s} = 14$ TeV. Further, direct detection of dark matter was left nearly impossible. However, with DMM we have seen that the addition of a small, fixed number of vector-like messengers can affect the running of these masses at some scale between the electroweak and the Planck. As was shown in the previous section, this ultimately results in lighter superpartners which could be within the reach of the LHC for detection in the near future. In the following section we will determine those portions of the parameter space which have been ruled out by direct searches at $\sqrt{s} = 8$ TeV, and evaluate the extent to which DMM modifications can enhance accessibility at $\sqrt{s} = 14$ TeV.

Benchmark Points

The DMM framework leaves us with a large number of possible input parameters consistent with the constraints we have placed. While we are interested in the detection prospects of the entirety of the remaining parameter space, we can gain a sense of the reach that an experiment would have by considering the extrema of the parameter space, and using these benchmarks to evaluate whether or not a given subsection of the parameter space would be accessible for a given experiment. In [7] it was found that for the KKLT framework, roughly a dozen benchmark points

could be chosen to give a sense of the discoverability of the parameter space at large. Here too we will consider a small number of benchmark points that are representative of the DMM framework.

We will consider each of the benchmark points discussed in Table 2.1, around which we performed a scan in the DMM parameter space. For each grid of DMM points, we consider the following: the point with the lightest LSP, the point with the lightest gluino, and the point with the lightest stop $\tilde{t}_1$. We further isolate only the points where $N = 3$, and again choose the same trio of points. We do not impose a lower bound on the gluino mass in this exercise, and will often find cases with gluino masses below the often-quoted bound of about 1200 GeV. In fact, as we shall see below, many of these cases would indeed have been discovered at the previous LHC run, while still others would have escaped detection due to compression between the gluino mass and that of the LSP.

The points that we have chosen to present in detail represent a subset of the entirety of the DMM parameter space, and are collected in Table 2.3. We choose this set to gain a fuller understanding of the amount of DMM parameter space that the LHC can probe, while exhibiting a large range in the input parameters, LSP type, mass spectra, and mass scales we consider. For example, point 1.1 in Table 2.3 represents a case described in the previous section, near the lower range of the vertical bars in the left panel of Fig. 2.7. The KKLT base point (1.0) has a primarily binolike LSP, while the DMM perturbation produces a primarily winolike LSP, with a significantly smaller mass. All superpartner masses are reduced by the gauge mediation in this case, with a highly compressed spectrum emerging.

Quantity	Point 1		Point 2					Point 3			Point 5		Point 6			Point 7	
	1.0	1.1	2.0	2.1	2.2	2.3	2.4	3.0	3.1	3.2	5.0	5.1	6.0	6.1	6.2	7.0	7.1
(n_M, n_H)	$(0,0)$				$(0,0)$				$(0,0.5)$		$(0.5,0)$			$(0.5,0.5)$		$(0.5,0.5)$	
M_0	1900				2900				1950		2000			1800		3200	
α_m	1.05				1.80				1.65		1.25			0.7		1.45	
$\tan\beta$	9				9				27		28			9		7	
α_g	0	0.55	0	0.35	0.10	0.2	0.1	0	0.15	-0.90	0	0.2	0	0.3	0.1	0	-0.35
$M_{\rm mess}$	–	10^5	–	10^{14}	10^5	10^6	10^{12}	–	10^{14}	10^6	–	10^9	–	10^5	10^5	–	10^5
N	0	2	0	3	3	3	4	0	5	3	0	3	0	3	3	0	3
$m_{\tilde{g}}$	2873	1002	3084	1448	1061	1010	1065	2264	1074	1901	2727	1013	3055	713	902	3924	1228
$m_{\tilde{t}_1}$	1434	1265	1554	1061	2582	2536	1008	1500	1062	1109	1461	668	1978	1227	1171	2478	1630
$m_{\tilde{\chi}_1^0}$	1406	986	1547	836	147	942	727	1415	1042	1101	676	661	1150	654	696	974	1067
B%	99.8%	0.4%	0.1%	0.1%	0.0%	0.1%	0.1%	0.9%	0.5%	0.3%	0.1%	0.4%	99.6%	5.6%	98.7%	0.0%	0.1%
H%	0.2%	0.4%	99.7%	99.5%	99.7%	97.6%	99.7%	97.3%	96.5%	98.8%	99.6%	98.2%	0.38%	72.6%	0.3%	99.9%	99.3%
Ωh^2	0.062	0.028	0.077	0.070	0.003	0.091	0.057	0.124	0.044	0.041	0.055	0.018	0.069	0.019	0.113	0.106	0.107

Table 2.3: Benchmarks for LHC study of DMM parameter space. A subset of the KKLT base points in Table 2.1 is here reproduced, together with one or more perturbations that involve gauge-charged messengers. The collection represents a variety of input parameters, LSP type, thermal relic densities, and mass scales. These example parameter points will be the focus of our detailed study of LHC phenomenology to follow.

The four perturbations on KKLT base point 2.0 all involve a relatively small and positive α_g, and at least three messenger fields, thus reducing the masses of the gauginos (the LSP mass and gluino mass are given explicitly in Table 2.3). Yet the effect on the stop mass depends crucially on the messenger mass scale, M_{mess}. Larger messenger scales means fewer decades in energy for the messenger-corrected renormalization group equations to operate, and consequently lighter stops. This is the complement to the discussion in the previous section regarding the right panel of Fig. 2.9. As we will see in the following section, the discovery prospects for points 2.1 - 2.4 are quite different, despite the roughly similar key masses.

The two perturbations on KKLT base point 3.0 show two very different types of compressed spectra that can emerge at opposite ends of the α_g parameter space. Cases with large numbers of messengers, positive α_g, and high messenger scale tend to exhibit the largest amount of compression, while negative α_g has less impact on the gluino mass, while still compressing the stop and LSP masses. The stop mass $m_{\tilde{t}_1}$ and LSP mass $m_{\tilde{\chi}_1^0}$ are roughly similar for points 3.1 and 3.2, yet we will see that the former point will be discovered within the first 40 fb^{-1} at $\sqrt{s} = 14$ TeV, while the latter will require as much as 240 fb^{-1} for discovery.

We round out our benchmarks with a perturbation each on KKLT base points 5.0 and 7.0, and two for base point 6.0. This latter case is particularly interesting, in that the KKLT base point is in the region identified in [7] as giving purely binolike LSP neutralinos. Indeed, case 6.2 is such a point, with roughly the correct thermal relic density. But the pertrubation in 6.1, with only slightly larger α_g, and identical M_{mess} and N, gives a mixed wave-function LSP and much lighter gluino. As we will discuss in the next section, both points 6.1 and 6.2 would have escaped detection at the previous LHC run, but both are prime candidates for discovery in the first 5 fb^{-1} in the upcoming run.

Relevant LHC Searches

In addressing, more specifically, the issue of detection at the LHC, we hope to identify some commonalities among these points, and the larger set of 60 bench-

marks from which they are chosen, that will guide our search strategies. In order to simulate the LHC signature for each of these benchmark points, we take the electroweak-scale SLHA file generated by SoftSUSY (as discussed previously), then generate the full decay table with SUSY-HIT [51]. For several of the benchmark points, the mass spectrum features a neutralino LSP with a stop NLSP only slightly heavier. For these points, the decay $\tilde{t}_1 \to t\tilde{\chi}_1^0$ is highly suppressed, as is the decay $\tilde{t}_1 \to bW\tilde{\chi}_1^0$, which are the dominant decay channels when $\Delta m(\tilde{t}_1, \tilde{\chi}_1^0) > m_t$ and $\Delta m(\tilde{t}_1, \tilde{\chi}_1^0) > m_W + m_b$, respectively. With such a small mass gap, the only decay processes allowed are $\tilde{t}_1 \to c\tilde{\chi}_1^0$ and $\tilde{t}_1 \to bf\bar{f}\tilde{\chi}_1^0$. These processes require additional calculations separate from the main SUSY-HIT routines [52]. Once these decay tables are generated, we use MadGraph5_aMC@NLO 2.2.2 [53] to simulate production of all pp $\to \tilde{X}\tilde{X}$ processes, where $\tilde{X}$ represents any supersymmetric particle. We then use MadEvent to generate 10,000 events for each parameter point, followed by PYTHIA 6.4 to perform the showering and hadronization. Detector simulation is performed in Delphes-3.1.2 using the default ATLAS detector card [54]. In total, we generated events for 60 parameter points, including those of Table 2.3.

When considering the LHC implications of DMM, we consider the results published by the ATLAS and CMS collaborations. Both have conducted many searches for possible SUSY signatures in the $\sqrt{s} = 8$ TeV data they have collected. To date, however, no signal above background expectations has been found by either of the two collaborations. For the sake of simplicity, we will consider only the ATLAS search results; the searches conducted by ATLAS tend to utilize geometric cuts in their signal region definitions, which are better suited to simple computer simulation. To date, ATLAS has published 32 searches using the full $\sqrt{s} = 8$ TeV data set, as well as a number of summary documents. By considering the properties of the 60 DMM points generated, we can focus on a small number of these searches to target the event topologies most likely to be produced.

For example, of the 60 benchmark points for which we performed simulations at $\sqrt{s} = 8$ TeV, we find that lepton production is generally rare for the DMM points, though it can be substantial for the associated KKLT base points. Before considering lepton p_T and angular distribution, we find that across the benchmarks, events

with leptons generally make up less than 10% of the total number of events; events with two leptons or more are even rarer, typically making up no more than 5% of the total number of events. Conversely, 51 of the 60 benchmark points have zero reconstructed leptons for at least 80% of the events. At $\sqrt{s} = 14$ TeV, this property persists. Only in two cases do signatures with leptons become the predominant topology, and in only two others does it surpass 33% of the total event count. At $\sqrt{s} = 14$ TeV, these points have a total SUSY production cross section of $\mathcal{O}(10^{-4})$ fb and $\mathcal{O}(10^{-2})$ fb, respectively. These cross sections are sufficiently low that, despite their high lepton production rates, they will not result in a significant number of leptons produced at the LHC during the 14 TeV run. With this in mind, we can safely consider only searches that contain a lepton veto.

Jet multiplicities tend to be relatively low for these 60 benchmarks, with two-thirds of the cases studied having a peak jet multiplicity of $N_{\text{jet}} \leq 5$. A small subset of the remainder have a broad distribution of jet multiplicities, peaking at $N_{\text{jet}} = 7 - 8$, with long tails that extend to very large multiplicities. But the vast majority of our cases will be visible first in the low jet-multiplicity channels. As most of the cases that are accessible at the 8 TeV run involve light stops, it is not surprising that a large fraction of the events we simulated have one or more b-tagged jets. Across the 60 cases studied, just under 40% of events contain at least one b-tagged jet, with several of the benchmarks exhibiting twice that fraction of events with b-tagged jets.

We summarize the gross LHC phenomenology of some of our benchmark points in Table 2.4, which includes all ten KKLT base points from Table 2.1, as well as the perturbations listed in Table 2.3. Displayed are the overall SUSY production cross sections at both $\sqrt{s} = 8$ TeV and $\sqrt{s} = 14$ TeV, the percentage of events containing at least one high-p_T lepton, the peak in the jet multiplicity distribution, and the percentage of events containing at least one b-tagged jet. Given the broad features of the benchmarks, we have chosen to pursue the general-purpose ATLAS SUSY searches which involve low jet and lepton multiplicity. More specifically, we will consider the general (low-multiplicity) jets plus missing transverse energy ($\not{E}_T$) search [55], the so-called "monojet" signatures of the stop search [56] for small

Benchmark	$\sigma_{8\text{TeV}}$ (fb)	$\sigma_{14\text{TeV}}$ (fb)	% Lepton	Peak N_{jets}	% B-Jets
1.0	5.1×10^{-3}	0.67	3.6%	3	27.8%
1.1	10.1	2.6×10^{2}	0%	3	4.6%
2.0	1.8×10^{-3}	0.31	0%	2	23.0%
2.1	0.3	22.9	21.1%	8	85.3%
2.2	6.0	1.7×10^{2}	21.9%	8	87.5%
2.3	9.9	2.4×10^{2}	0.3%	4	5.1%
2.4	5.6	1.8×10^{2}	10.5%	6	53.6%
3.0	1.3×10^{-2}	3.9	18.6%	6	54.5%
3.1	7.7	2.8×10^{2}	0.4%	4	6.2%
3.2	0.7	35.8	6.7%	4	31.7%
4.0	3.8×10^{-3}	2.1	14.9%	5	43.1%
5.0	6.7×10^{-3}	1.8	27.0%	5	42.5%
5.1	20.0	4.6×10^{2}	0%	6	57.7%
6.0	1.2×10^{-4}	0.32	12.8%	4	32.1%
6.1	2.0×10^{2}	2.6×10^{3}	0%	4	19.1%
6.2	26.9	5.9×10^{2}	4.1%	5	36.3%
7.0	7.7×10^{-7}	3.1×10^{-2}	41.3%	4	30.6%
7.1	1.4	86.1	0.1%	4	7.9%
8.0	3.5×10^{-6}	7.8×10^{-2}	0.1%	3	9.7%
9.0	7.5×10^{-15}	4.9×10^{-6}	26.6%	4	58.0%
10.0	2.4×10^{-12}	1.9×10^{-4}	76.7%	4	17.2%

Table 2.4: This table contains the SUSY production cross sections at $\sqrt{s} = 8$ TeV and $\sqrt{s} = 14$ TeV, as well as the percentage of events containing at least one high-p_T lepton, the peak in the jet-multiplicity distribution, and the percentage of events containing at least one b-tagged jet. Note that this is simply the number of jets whose $p_T > 20$ GeV, and does not include other quality requirements placed on jets. Note that the highest lepton multiplicities occur for the KKLT base points, whose cross-sections are well below the femptobarn scale.

$\Delta m(\tilde{t}_1, \tilde{\chi}_1^0)$, and the dedicated stop searches of [57] and [58], which require b-tagged jets, for large $\Delta m(\tilde{t}_1, \tilde{\chi}_1^0)$. Though we expect leptonic signatures to be sub-dominant, we nevertheless also simulate the signatures of the one-lepton search of [57], which requires at least three b-tagged jets in the final state, as well as the single hard lepton plus multijets searches of [58].

Each of the search strategies utilized by ATLAS divides the search into two parts: object reconstruction and event selection. The object reconstruction sets requirements for each object in an event, typically the jets, leptons, photons, and missing energy. For the ATLAS searches conducted at 8 TeV, jets are reconstructed

using the anti-k_T algorithm with a radius parameter of 0.4. Jets are required to be isolated from leptons by calculating $\Delta R \equiv \sqrt{\Delta\eta^2 + \Delta\phi^2}$, and demanding $\Delta R > 0.2$. If $\Delta R < 0.2$ between any jet candidate and any electron, the jet is discarded. For any surviving jet candidates, if $\Delta R < 0.4$ between a jet candidate and any leptons, the lepton is discarded. For remaining jet and lepton candidates, further requirements are placed on $|\eta|$ and p_T that vary from one search to another. Further isolation requirements are placed on each of the jet and lepton candidates. Finally, the missing transverse energy, $\not{E}_T$, is calculated to be the negative of the vector sum of the p_T of all reconstructed objects with $|\eta| < 4.9$, not belonging to other reconstructed objects.

Low multiplicity jets plus missing transverse energy

Requirement	Signal Region												
	2jl	**2jm**	**2jt**	**3j**	**4jl-**	**4jl**	**4jm**	**4jt**	**5j**	**6jl**	**6jm**	**6jt**	**6jt+**
$\not{E}_T/\sqrt{H_T}$ [GeV$^{1/2}$]	8	15		–	10		–						
$\not{E}_T/m_{\text{eff}}(N)$	–			0.3	–		0.4	0.25	0.2			0.25	0.15
m_{eff}(incl.) [TeV]	0.8	1.2	1.6	2.2	0.7	1.0	1.3	2.2	1.2	0.9	1.2	1.5	1.7
Observed Events	12315	715	33	7	2169	608	24	0	121	121	39	5	6
S_{95}^{obs}	1200	90	38	8.2	270	91	10	3.1	35	39	25	6.6	7.9

Table 2.5: Signal region definitions, observed number of events, and S_{95}^{obs} for the low-multiplicity jets plus $\not{E}_T$ search of [55]. The numbers in the first three rows represent the minimum value for the kinematic quantity in the first column. Further description of the signal characteristics is given in the text. All data corresponds to 20.3 fb^{-1} of integrated luminosity.

The ATLAS low-multiplicity jets plus missing transverse energy search contains a number of signal regions, each requiring between two and six jets. This is typical in events with production of $\tilde{q}\tilde{q}$, $\tilde{q}\tilde{g}$ and $\tilde{g}\tilde{g}$, where the decay $\tilde{g} \to q\bar{q}\tilde{\chi}_1^0$ produces two jets, and the decay $\tilde{q} \to q\tilde{\chi}_1^0$ produces a single jet. It thus represents a very general search that fits the gross phenomenology of a wide range of SUSY models.

The most recent iteration of this search was published in May of 2014 [55], and extends the reach of possible SUSY production beyond previous searches. This search defines 15 signal regions, 13 of which were studied in this work and are

defined in Table 2.5.[3] For each signal region, $\not{E}_T > 150$ GeV is required, as is at least one jet with $p_T > 130$ GeV. A lepton veto is placed on all events containing a single electron or muon with $p_T > 10$ GeV. Between two and six jets are required for these signal regions, with each additional jet requiring $p_T > 60$ GeV. The first three jets are required to be separated from the reconstructed $\not{E}_T$ direction with a minimum $\Delta\phi(\text{Jet}, \not{E}_T) > 0.4$, while any additional jets must be separated by $\Delta\phi(\text{Jet}, \not{E}_T) > 0.2$. Signal regions are then defined using the ratio $\not{E}_T/\sqrt{H_T}$, $\not{E}_T/m_{\text{eff}}(N)$, and $\not{E}_T/m_{\text{eff}}(\text{incl.})$ where H_T is the sum of the p_T of all jets with $p_T > 40$ GeV, $m_{\text{eff}}(N)$ the scalar sum of $\not{E}_T$ and the N hardest jets, and $m_{\text{eff}}(\text{incl.})$ is the scalar sum of $\not{E}_T$ and all jets with $p_T > 40$ GeV. The signal regions are named by the number of jets, and a criterion "loose", "medium", or "tight", depending on the values of each of these discriminants.

Monojet signatures for light stops

Requirement	Signal Region		
	M1	M2	M3
$p_T(\text{Jet}, 1)$ [GeV]	280	340	450
$\not{E}_T$ [GeV]	220	340	450
Observed Events	33054	8606	1776
S_{95}^{obs}	1951	575	195

Table 2.6: Signal region definitions, observed number of events, and S_{95}^{obs} for the the three monojet-like searches of [56]. The numbers in the first three rows represent the minimum value for the kinematic quantity in the first column. Further description of the signal characteristics is given in the text. All data corresponds to 20.3 fb^{-1} of integrated luminosity.

For some SUSY spectra, particularly those with small mass gaps between $SU(3)$-charged superpartners and the LSP, production in association with a single hard jet

[3] Two of the signal regions involved attempting to identify hadronically-decaying W-bosons via a particular jet-pairing algorithm, and will not be included in our study.

is of particular interest. The most recent relevant search for such "monojet" topologies was published by ATLAS in July of 2014 [56] with an integrated luminosity of 20.3 fb^{-1}. This search was designed to target direct stop production via the two-body decay $\tilde{t} \to c\tilde{\chi}_1^0$, as well as the 4-body decay $\tilde{t} \to bf\bar{f}\tilde{\chi}_1^0$ for compressed spectra.[4] This is of particular interest for points which feature a heavy LSP, a stop NSLP, and the remaining superpartners sufficiently heavy as to be effectively integrated out. Each event is required to have a reconstructed primary vertex with at least five associated tracks. Further, each event is required to have $\not{E}_T > 150$ GeV, and at least one jet with $p_T > 150$ GeV and $|\eta| < 2.8$. To eliminate multiple jets, a maximum of two additional jets are permitted with $p_T > 30$ GeV; events with additional hard jets are rejected. Each of these jets must have a minimum $\Delta\Phi(\text{Jet}, \not{E}_T) > 0.4$. Events with reconstructed electrons or muons are also rejected. Three signal regions are then defined by additional requirements on the p_T of the hardest jet and the $\not{E}_T$. Signal M1 is defined to have $p_T(\text{Jet}, 1) > 280$ GeV and $\not{E}_T > 220$ GeV, M2 is defined to have $p_T(\text{Jet}, 1) > 340$ GeV and $\not{E}_T > 340$ GeV, and M3 is defined to have $p_T(\text{Jet}, 1) > 450$ GeV and $\not{E}_T > 450$ GeV. The number of observed events for each signal region is listed in Table 2.6.

B-tagged jets and missing transverse energy with a lepton veto

In this category we will discuss two separate ATLAS publications, each representing a stop search via b-tagged jets. The first analysis focuses on stop production where the stop decays via $\tilde{t}_1 \to t\tilde{\chi}_1^0$ or $\tilde{t}_1 \to b\tilde{\chi}_1^\pm \to bW^{(*)}\tilde{\chi}_1^0$, where the W is assumed to decay hadronically [59]. In either case, the result will be an LSP, a b-tagged jet and 2 non-b-tagged jets per $\tilde{t}$ produced. For all signal regions, a minimum of $\not{E}_T > 150$ GeV is required, a minimum of six jets, two of which must be b-tagged, and no reconstructed leptons (electrons or muons). The two highest p_T jets must have an energy of at least 80 GeV, with remaining jets satisfying $p_T > 35$ GeV, and the three highest p_T jets must be separated from the missing energy by at least $\Delta\phi > \pi/5$. A further requirement is placed on the b-tagged jet closest in angle to

[4] Additionally, there are two signal regions that require charm-tagged jets; we will not be considering these, as Delphes does not incorporate charm-tagging.

Requirement	Signal Region						
	SRA1	SRA2	SRA3	SRA4	SRC1	SRC2	SRC3
m^0_{bjj} [GeV]	< 225		$[50, 250]$		–	–	–
m^1_{bjj} [GeV]	< 225		$[50, 400]$		–	–	–
min$[m_T(Jet_i, \not{E}_T)]$ [GeV]	–		> 50		–	–	–
$m_T^{b,\text{min}}$ [GeV]	> 175				> 185	> 200	
$m_T^{b,\text{ max}}$ [GeV]	–				> 205	> 290	> 325
$\not{E}_T$ [GeV]	> 150	> 250	> 300	> 350	> 160		> 210
Observed Events	11	4	5	4	59	30	15
S_{95}^{obs}	6.6	5.7	6.7	6.5	15.7	12.4	8.0

Table 2.7: Signal region definitions, observed number of events, and S_{95}^{obs} for the two classes of b-tagged jets plus $\not{E}_T$ searches of [59]. The numbers in the first six rows represent the minimum, maximum, or allowed range of values for the kinematic quantity in the first column. Further description of the signal characteristics is given in the text. All data corresponds to 20.1 fb^{-1} of integrated luminosity.

the missing energy. The transverse mass, defined as

$$m_T^{b,\text{ min}} = \sqrt{2p_T^b \not{E}_T \left[1 - \cos\Delta\phi(p_T^b, \not{E}_T)\right]} \tag{2.43}$$

must have a minimum of $m_T^{b,\text{min}} > 175$ GeV.

The search is then divided into three subsections. We will consider only the first (SRA) and third (SRC). For the first (SRA), the two jets with the highest b-tag weight are selected, then of the remaining jets, the two closest in the $\eta - \phi$ plane are combined to form a W candidate, which is then combined with the first b-tagged jet to form a top candidate with mass m^0_{bjj}. A second W candidate is formed by repeating the procedure with the remaining jets. Lastly, the value min$[m_T(\text{Jet}_i, \not{E}_T)]$ is calculated as the minimum m_T of each of the signal jets and the missing energy. With all of these quantities, the signal regions are defined as in the first four columns of Table 2.7.

The second subsection that we consider (SRC) focuses on the specific case when one of the stops decays via $\tilde{t}_1 \rightarrow b\tilde{\chi}_1^{\pm}$; $\tilde{\chi}_1^{\pm} \rightarrow W^{(*)}\tilde{\chi}_1^0$. Only five jets are now required, and a minimum of $\Delta\phi > 0.2\pi$ between the two hardest b-tagged jets is required. The m_T is further constrained: for SRC1, $m_T^{b,\text{min}} > 185$ GeV while for

SRC2 and SRC3, $m_T^{b,\text{min}} > 200$ GeV. A further quantity, $m_T^{b,\text{max}}$, is computed similarly to $m_T^{b,min}$ in (2.43), but now with the b-tagged jet being that with the largest $\Delta\phi$ from $\not{E}_T$. For SRC1, $m_T^{b,\text{max}} > 205$ GeV, for SRC2, $m_T^{b,\text{max}} > 290$ GeV, and for SRC3, $m_T^{b,\text{max}} > 325$ GeV. These values are collected in the final three columns of Table 2.7.

Requirement	Signal Region					
	SR-4jA	SR-4jB	SR-4jC	SR-7jA	SR-7jB	SR-7jC
$\Delta\phi_{\text{min}}^{4j}$	0.5					
$\not{E}_T/m_{\text{eff}}^{4j}$	0.2					
m_{eff}^{4j} [GeV]	1300	1100	1000	–	–	–
$\not{E}_T/\sqrt{H_T^{4j}}$ [GeV$^{1/2}$]	–	–	16	–	–	–
m_{eff}^{incl} [GeV]	–	–	–	1000	1000	1500
$\not{E}_T$ [GeV]	250	350	400	200	350	250
Observed Events	2	3	1	21	3	1
S_{95}^{obs}	5.2	6.5	3.9	13.9	6.1	4.2

Table 2.8: Signal region definitions, observed number of events, and S_{95}^{obs} for the two classes of b-tagged jets plus $\not{E}_T$ searches of [57]. The numbers in the first six rows represent the minimum value for the kinematic quantity in the first column. Further description of the signal characteristics is given in the text. All data corresponds to 20.1 fb^{-1} of integrated luminosity.

The second analysis we include is a more general search that targets third generation squark production and/or gluino production. Like the previous analysis, it relies heavily on the presence of b-tagged jets and requires large $\not{E}_T$. For this study we will focus on the channels which impose a veto on electrons with $p_T > 20$ GeV and muons with $p_T > 10$ GeV. Events are separated into two categories. The first category (4jA,B,C) requires at least four jets, all four of which having a minimum jet $p_T > 50$ GeV. The second category (7jA,B,C) requires at least seven jets, all seven of which having a minimum jet $p_T > 30$ GeV. All channels require the leading jet to satisfy $p_T(Jet, 1) \geq 90$ GeV, and require the presence of at least three b-tagged jets, all with $p_T > 30$ GeV.

Additional global cuts for all signal regions are given in terms of H_T^{4j}, defined as the scalar sum of the p_T of the four hardest jets in the event, m_{eff}^{4j}, defined as the scalar sum of $\not{E}_T$ and the p_T of the four hardest jets in the event, $\Delta\phi_{\text{min}}^{4j}$, defined as the minimum azimuthal separation between any of the four leading jets and the

direction of the missing transverse energy, and $m_{\text{eff}}^{\text{incl}}$ defined as the scalar sum of $\not{E}_T$ and the sum of the p_T of all jets in the event with $p_T > 30$ GeV. These cuts are given in Table 2.8, along with the observed number of events, and S_{95}^{obs} for the six signal regions.

Results and Case Studies

We begin this section by considering the reach of the already completed searches at $\sqrt{s} = 8$ TeV, described in the previous subsection, on the parameter space of the DMM framework. We then investigate a number of case studies motivated by the points in Table 2.3, which are representative of the LHC phenomenology of the model space as a whole.

As stated previously, none of the parameter combinations in Tables 2.3 and 2.4 would have given a significant excess over background at the previous LHC run. This is despite some relatively large cross-sections at $\sqrt{s} = 8$ TeV (see Table 2.4). In general, we can determine the likelihood that a given parameter point would have produced a detectable signal above background by comparing the simulated number of signal events at $\sqrt{s} = 8$ TeV versus the reported S_{95}^{obs} value, which gives the 95% confidence-level upper bound on the number of signal events compatible with the ATLAS observations. Thus, for example, our simulation of point 6.1 (the benchmark point with the largest production cross-section) suggests an overall production of 4060 events in all channels after 20.3 fb^{-1} of data-taking, but the compression between the gluino mass and LSP mass translates into only 282 events in the 2jl channel, 34 events in the 2jt channel, and 39 events in the 4jl channel, all of which are below the reported S_{95}^{obs} values of 1200, 38 and 91 events, respectively (see Table 2.5). We estimate the greatest excess would have been in the 2jt channel, but the signal significance would be only 0.7σ in this channel.

We find that while none of the KKLT base points would have been discovered thus far, a fair fraction of the DMM parameter space involving stop or gluinos with masses at or below 1 TeV would now be ruled out. In general, we find the best channels at $\sqrt{s} = 8$ TeV are in the low-multiplicity jets plus $\not{E}_T$ search, with

a reach of $m_{\tilde{g}} \lesssim 600$ GeV for small mass gaps between the gluino and the LSP $\Delta m(\tilde{g}, \tilde{\chi}_1^0) \lesssim 50$ GeV, and $m_{\tilde{g}} \lesssim 900$ GeV for mass gaps of greater than 50-100 GeV. We find the reach in the lightest stop mass to be about 100 GeV less for the two different mass gaps between the stop and the LSP. However, DMM corrections tend to move the masses of $SU(3)$-charged objects in a correlated way, tending to compress both the gluino and the stop toward the lightest neutralino mass. In extreme cases, a nearly degenerate trio of masses $(m_{\tilde{\chi}_1^0},\, m_{\tilde{t}_1},\, m_{\tilde{g}})$ would have escaped detection, even at a mass scale of 500-600 GeV. Such outcomes are rare in the DMM landscape, but not impossible (see point 3.1 of Table 2.3, to be discussed in more detail below). In terms of theoretical parameters, the modular weight combinations most likely to produce spectra detectable at $\sqrt{s} = 8$ TeV are the $(n_M, n_H) = (0,\, 0)$, $(0,\, 0.5)$ and $(0.5,\, 0)$ cases, with low messenger scale and $\alpha_g > 0$.

To discuss detection in the near future, we will use the signal definitions at $\sqrt{s} = 8$ TeV described above as a first approximation to what will be done at 14 TeV. Signal significance is estimated by calculating the background counts using the pre-generated Snowmass 2013 published backgrounds at $\sqrt{s} = 14$ TeV [60], which were generated in a manner identical to that in which our signal files were produced. In general, we find that the loosest possible cuts tends to preferentially populate the signal relative to background, as most of the parameter space within reach at the LHC will feature a compressed spectrum allowing less phase space for hard jets and leptons. We thus do not attempt to optimize beyond the $\sqrt{s} = 8$TeV criteria by tightening the requirements on various distributions, though we will consider a modified monojet, or "lopsided jet", signature in what follows.

A summary of the results of our simulations at $\sqrt{s} = 14$ TeV is given in Table 2.9 for the DMM perturbations shown in Table 2.3. We show results for the quantity L_{min}, defined as the minimum amount of integrated luminosity needed to achieve a 5σ ($S/\sqrt{B} = 5$) signal significance in that particular channel. The most effective discovery channels are uniformly found to be from the low-multiplicity jets plus $\not{E}_T$ search. The first two columns give the best signal region from Table 2.5 with the corresponding L_{min} value. The next two columns give the corresponding L_{min} from the best signal region of the monojet search in Table 2.6, as well as a monojet-

			Monojet L_{min}		B-tagged jet L_{min}		
Benchmark	Over-all L_{min}	Best Chan-nel	2jl (opt)	mono-jet M2	B-tag SRA2	B-tag 4jB	B-tag 7jC
1.1	80	**2jt**	159	303	–	–	–
2.1	94	**6jt+**	–	–	–	249	133
2.2	1.9	**6jt+**	64	–	123	4	2
2.3	141	**2jl**	185	2909	–	–	–
2.4	22	**5j**	46	–	216	97	100
3.1	22	**2jm**	29	96	–	–	–
3.2	240	**2jt**	574	–	–	–	–
5.1	2.9	**5j**	11	2466	55	5	7
6.1	1.7	**3j**	2.3	32	90	–	929
6.2	4.6	**4jl**	12	–	69	70	53
7.1	65	**4jl**	168	–	–	–	–

Table 2.9: Minimum integrated luminosity L_{min} (in fb^{-1}) to achieve a 5σ signal significance in a given channel, at $\sqrt{s} = 14$ TeV. In all cases, the strongest signal will be in the low-multiplicity jets plus $\not{E}_T$ search. The overall L_{min} therefore reflects the strongest of the 13 channels in Table 2.5, given in the third column. The value of L_{min} to achieve the same signal significance in certain sub-dominant channels is also given, for reference. Columns 4 and 5 represent monojet-like channels, while the final three columns represent various signatures that involve b-tagged jets. Signal region descriptions are given in the text. Note that none of the KKLT base points (X.0) will yield a 5σ excess after 3000 fb^{-1} of integrated luminosity.

oriented perturbation on the 2jl channel introduced in [61] and to be discussed below. Finally, the last three columns indicate the L_{min} value for the best signal regions involving multiple b-tagged jets. If a 5σ excess is not expected within 3000 fb^{-1} the entry is left empty. Note that none of the KKLT base points (X.0) will yield a 5σ excess after 3000 fb^{-1} of integrated luminosity. We will now discuss the details behind many of the numbers in Table 2.9 via a sequence of case studies.

Case Study 1: Signatures involving b-tagged jets; Points 2.2, 6.1 and 6.2

Let us begin our study of comparative LHC signatures of DMM parameter points by considering the case of point 2.2 versus 6.1. These two points share common gauge mediation parameters: $N = 3$, $\Lambda_{\text{mess}} = 10^5$ GeV and α_g positive, but relatively small. Point 2.2 has a relatively large large mirage parameter, $\alpha_m = 1.8$, while that

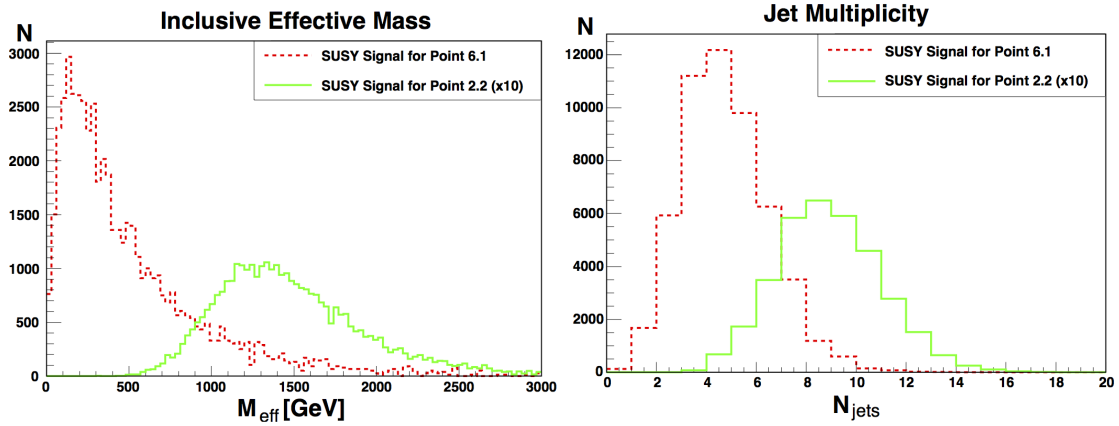

Figure 2.10: Effective mass and total jet multiplicity for points 2.2 and 6.1. Left panel gives the effective mass distribution m_{eff} for points 2.2 and 6.1, while the right panel gives the total jet multiplicity N_{jets} for the same two points. Both plots are normalized to 20 fb^{-1} at $\sqrt{s} = 14$ TeV, but with the distributions for point 2.2 multiplied by a factor of ten to allow for greater readability.

of point 6.1 has $\alpha_m = 0.7$. Both involve universal scalar masses (to leading order) at the unification scale, with modular weights (n_m, n_H) equal to $(0, 0)$ and $(1/2, 1/2)$, respectively.

Point 2.2, with vanishing modular weights, produces a heavier stop mass than that of point 6.1 as indicated in Table 2.3: $m_{\tilde{t}_1} = 2582$ GeV versus 1227 GeV. More relevant to LHC phenomenology is the differences in the gaugino sector. Point 2.2 has a gluino mass of $m_{\tilde{g}} = 1061$ GeV and LSP mass of $m_{\tilde{\chi}_1^0} = 147$ GeV, while point 6.1 has a gluino mass of 713 GeV and LSP mass of 654 GeV. As a consequence, at $\sqrt{s} = 14$ TeV, the cross-section for overall superpartner production for point 6.1 is 2.6 pb, versus 169 fb for point 2.2. The difference is entirely accounted for by the gluino mass, as gluino pair production represents over 94% of the total production cross-section in both cases. Despite the huge disparity in total production cross-sections, the two points have nearly identical values of the overall L_{min} value needed for discovery (just under 2 fb^{-1}).

It is not difficult to understand why this is. Despite the light gluino, point 6.1 has a mass difference between the gluino and the LSP of roughly 60 GeV, while point 2.2

has a spectrum not dramatically different from the so-called "simplified" models that are often used as benchmarks in the interpretation of LHC search results. Indeed, in the left panel of Fig. 2.10 we see the effective mass distribution at $\sqrt{s} = 14$ TeV. Despite the much larger signal size for point 6.1 (note that distributions for point 2.2 are multiplied by a factor of ten for readability), the small mass gap between the gluino and the LSP translates into an effective mass distribution heavily weighted towards those bins below the cut value of 700-800 GeV which defines the 2jl and 4jl signal regions. Table 2.9 indicates that within the first 2 fb^{-1} at $\sqrt{s} = 14$ TeV both models would be "discovered" at the LHC, in the six-jet channel for point 2.2, and in the three-jet channel for point 6.1. The large mass gap between the gluino and LSP in the case of point 2.2 allows more phase space to generate jets with $p_T > 40$ GeV, as indicated by the jet multiplicity distributions shown in the right panel of Figure 2.10.

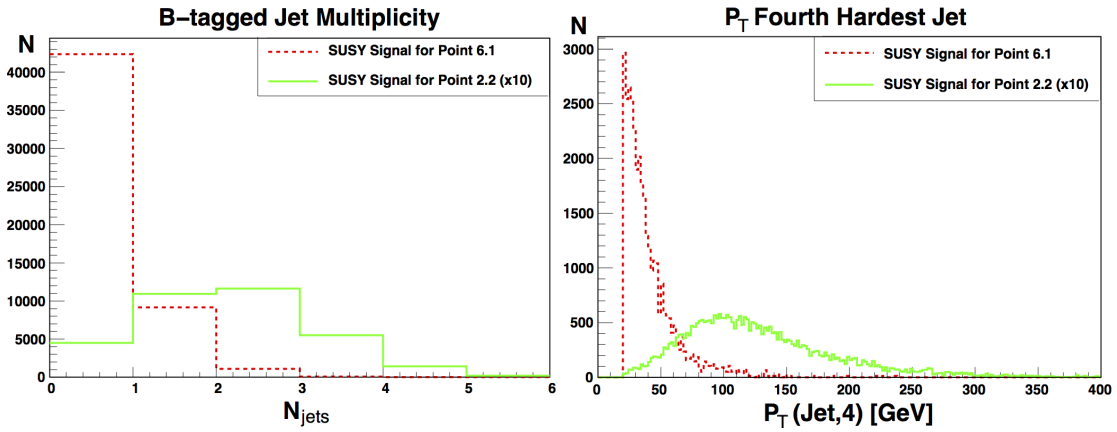

Figure 2.11: Multiplicity of b-tagged jets and fourth jet p_T for points 2.2 and 6.1. Left panel gives the number of events with one or more b-tagged jets. The right panel gives the $p_T(\text{Jet}, 4)$ of the fourth hardest jet in the event, a key discriminant in the b-tagged searches described in Table 2.8. Both distributions are generated prior to the imposition of any other signal region cuts, and are normalized to 20 fb^{-1} of data. The signal distribution for point 2.2 is multiplied by a factor of ten to allow for greater readability.

It is instructive to consider sub-dominant channels, as these signals will pro-

vide corroboration of new physics and a powerful descriminant between potential models of this new physics. In the case of points 2.2 and 6.1 all of the signal regions in the general class of jets plus missing transverse energy will show signals in the first 30-40 fb^{-1}. Thus we consider those signal regions that are defined as having one or more b-tagged jets. Here we find the corroborating signals will arise nearly immediately for point 2.2, while requiring approximately 100 fb^{-1} for point 6.1, despite the much larger overall production cross-section. The precise values of L_{min} for the particular signatures SRA2 of Table 2.7, and 4jB and 7jC of Table 2.8, are given in the last three columns of Table 2.9.

As mentioned previously, both points are dominated by gluino pair production. For point 2.2, the gluino decays to $\tilde{\chi}^0_{1,2} t\bar{t}$ 40% of the time, and $\tilde{\chi}^{\pm}_1 bt$ 54% of the time, thus assuring at least four genuine b-jets in the vast majority of signal events, with up to four leptons possible from the $W^{\pm}$ bosons produced in the top decays. The high probability of b-tagged jets and leptons in the final state is reflected in Table 2.4. The smaller mass gap in the case of point 6.1 eliminates the possibility of top pairs from the gluino decay, all but eliminating the prospect of high-p_T leptons in the final state.[5] Furthermore, the gluino decays into $\tilde{\chi}^0_{1,2} b\bar{b}$ only 14% of the time, decaying to lighter flavors for the vast majority of events. Thus we expect, on average, fewer b-tagged jets per event for point 6.1, which is only partially mitigated by the much higher cross-section for this point relative to point 2.2. This is displayed in the left panel of Figure 2.11, where the multiplicity of b-tagged jets is given for both points. Of the b-jet searches in Table 2.7, the signal region SRA2 tends to be the most promising of the cases that require only two b-tagged jets. Here we find comparable values of $L_{\text{min}} \simeq \mathcal{O}(100\ \text{fb}^{-1})$ in this channel, despite the great disparity in production cross-sections.

This outcome is somewhat disappointing, given that point 6.1 still produces ample events with at least one b-tagged jet. The signatures of Table 2.7 have the advantage of only requiring two b jets, but they simultaneously require a minimum of six jets overall, a property satisfied by less than a quarter of the event sample

[5] Thus we expect no signal in the most promising single-lepton channel for point 6.1, even after 3000 fb^{-1} of integrated luminosity.

for point 6.1. Given the low overall jet multiplicity, we might have hoped that the four-jet channels of Table 2.7 would be particularly effective, but note that the signal region definition calls for $p_T(\text{Jet}, 4) \geq 50\,\text{GeV}$, while the small mass difference $\Delta m(\tilde{g}, \tilde{\chi}_1^0)$ implies that such sub-leading jets will generally have very low p_T, often only slightly above the threshold p_T to be classified as a jet in the initial event reconstruction (see the right panel of Figure 2.11). Furthermore, only a negligible fraction of the events for point 6.1 have three b-tagged jets – a fraction roughly consistent with the mis-tagging rate for assigning a b tag to a light quark jet in Delphes. By contrast, point 2.2, with its substantial mass differences between the gluino and the light electroweak gauginos, seems ideally suited to these general-purpose b-jet searches, and should produce signals in the 4j and 7j channels of Table 2.8 roughly simultaneous with the initial discovery in the 6jt+ channel.

Let us now extend this discussion to include point 6.2 from Table 2.3. Point 6.2 shares all KKLT base point parameters with point 6.1, and differs in the gauge mediation sector only in the value of α_g, which is slightly smaller. The spectrum of point 6.2 therefore is, not surprisingly, rather similar to that of point 6.1, though the gaugino sector is slightly different. Note that the LSP of point 6.2 is almost entirely binolike, with a thermal relic density consistent with WMAP/Planck, while that of point 6.1 is a mixed state that is mostly Higgsino-like with a relic density that is smaller by an order of magnitude. The gluino mass for point 6.2 is $m_{\tilde{g}} = 902\,\text{GeV}$, and the cross-section for superpartner production is therefore intermediate between points 2.5 and 6.1 (though now gluino pair production constitutes only 84% of the total production cross-section, with associated production of a gluino with a light-flavor squark representing 15% of the total). Gluinos decay via various three-body decays involving top and bottom quarks, suggesting relatively high jet multiplicity with many b-tagged jets in the final state.

We might, therefore, expect that this point would have an L_{min} in the low-multiplicity jets plus $\not{E}_T$ channel that is similar to the other two points. And indeed, Table 2.9 shows that the best discovery channel is 4jl for this point, with $L_{\text{min}} = 4.6\,\text{fb}^{-1}$. It is noteworthy that this point has the lowest L_{min} of the trio in the sub-dominant b-jet channel SRA2 and the monojet channel M2. The branching

fractions of the gluino and lightest stop are nearly identical for points 6.1 and 6.2, but the increased signal in the three b-jet channels of Table 2.9 is entirely due to the large mass gaps between the gluino and the light electroweak gauginos. We note that all b-jet channels studied are equally effective in this case.

Case Study 2: "Optimized" monojet signatures; Points 3.1, 3.2 and 5.1

Of the previous trio of points, we might note a curious fact about the data presented in Table 2.9: point 6.1 is the only one of the three that yields a 5σ excess in the most advantageous "monojet" channel, signal region M2 from Table 2.6. In fact, it yields a signal in this channel well before the corroborating b-jet channels studied in the previous subsection. This is particularly odd, in that gluino pair production dominates the signal, with gluinos decaying universally via three-body decays involving two quarks and an electroweak gaugino. In short, there is no reason to anticipate this particular model would be a natural candidate for a monojet signal at all. Clearly, then, these signatures are not adequately addressing the topologies they were designed to attack (at least within our model framework). This begs an obvious question – just how "monojetlike" are the events captured by the so-called monojet signature M2? As it happens, this signal region is not really a monojet search at all, but rather a skewed two- and three-jet search in which stringent demands are placed on the leading jet; see the conditions outlined in Table 2.6. Thus, point 6.1 produces a signal in this channel primarily because it produces no leptons, has a long tail in the p_T distribution of the hardest jet, and (crucially) has a jet multiplicity skewed towards small numbers of jets. In other words, the monojet channel here simply captures the same sorts of events that appear in the two and three-jet channels of Table 2.5.

To get a clearer picture of this phenomenon, let us now consider points 3.1, 3.2 and 5.1 from Table 2.3. Point 3.1 is the most compressed model in Table 2.3. The heaviest squarks in this case have masses of roughly 1760 GeV, while the gluino and lightest stop are nearly degenerate with the LSP at just above 1 TeV. Thus, the entire spectrum is compressed and all cascade decays will involve soft outgoing

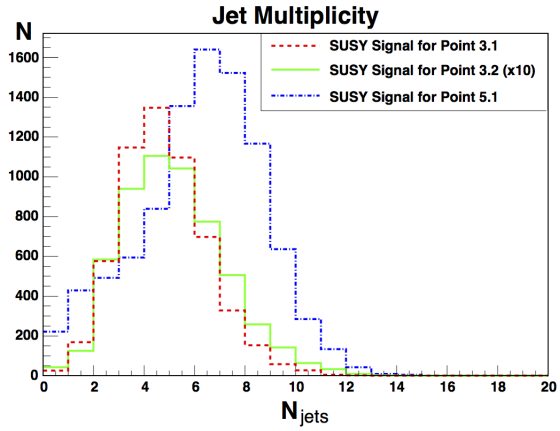

Figure 2.12: Total jet multiplicity for points 3.1, 3.2 and 5.1. Distributions give the total number of reconstructed jets, prior to any event selection cuts, normalized to 20 fb^{-1} of data. Red (dotted) distribution is for point 3.1, green (solid) distribution is for point 3.2, and blue (dot-dashed) distribution is for point 5.1. The signal distribution for point 3.2 is multiplied by a factor of ten to allow for greater readability.

particles. We might therefore expect this point to be one for which the monojetlike search strategies would be most effective.

Production is roughly evenly split between gluino pair production and (light-flavored) squark production in association with a gluino. These light-flavored squarks decay back to a light quark and a gluino 95-99% of the time, while the gluino decays 100% of the time to a gluon and a LSP. So we can expect a small number of very soft jets, with the potential that one jet will have larger p_T from the decay of a light squark (or from initial state radiation). Indeed, the peak in the jet-multiplicity distribution for point 3.1 is at four jets (see Figure 2.12), with less than 1% of all events containing a high-p_T, isolated lepton. But the best discovery channel for this point is the two-jet channel with relatively mild kinematic requirements (2jm), with an associated L_{min} of 22 fb^{-1}. In contrast, the best monojet-based search is M2, with a comparatively large $L_{\text{min}} = 96\,\text{fb}^{-1}$. The failure of the monojet signal to be competitive is mostly due to the veto placed on events with a fourth jet satisfying $p_T(\text{Jet}, 4) > 30\,\text{GeV}$, which effectively vetoes *all* events with $N_{\text{jets}} > 3$. This is a

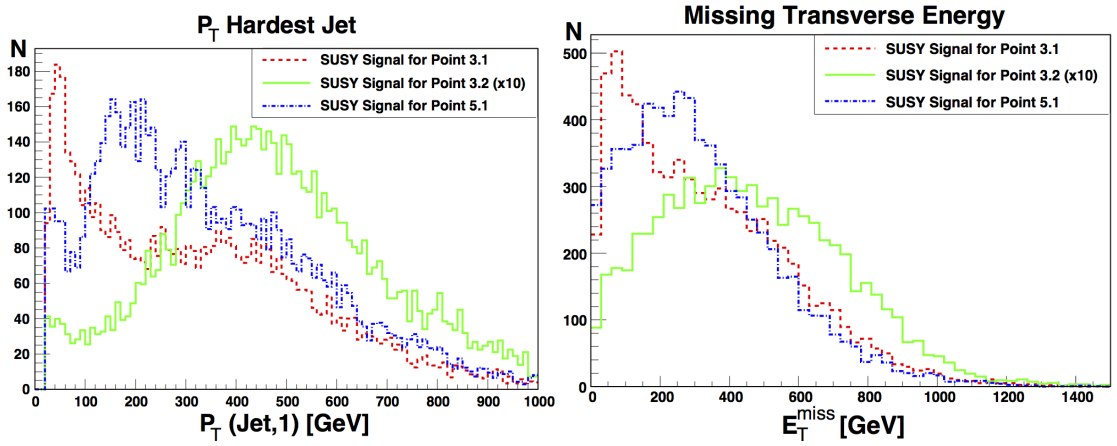

Figure 2.13: Transverse momentum of leading jet (left) and missing transverse energy (right) for points 3.1, 3.2 and 5.1. Distributions are constructed prior to any event selection cuts and normalized to 20 fb^{-1} of data. Red (dotted) distributions are for point 3.1, green (solid) distributions are for point 3.2, and blue (dot-dashed) distributions are for point 5.1. The signal distributions for point 3.2 are multiplied by a factor of ten to allow for greater readability.

sizeable fraction of the total event sample, as Figure 2.12 indicates.

It would seem, therefore, that there is potential for improvement in the choice of cuts for monojetlike signatures, just as there were for b-jet searches in the previous case study. Here we consider an "optimized" two-jet signature, originally introduced in the recent work by the authors [61] in the context of searching for light stops in minimal supergravity models. This signature is a simple modification of the 2jl signature of Table 2.5, in which the separation cuts between the direction of the $\not\!\!E_T$ and that of the two hardest jets are significantly increased from $\Delta\phi(\text{Jet}, \not\!\!E_T) > 0.4$ to $\Delta\phi(\text{Jet1}, \not\!\!E_T) > \pi/2$ and $\Delta\phi(\text{Jet2}, \not\!\!E_T) > 1$ for the hardest and second-hardest jet, respectively. This preferentially selects signal events with a highly lopsided nature, more in keeping with the notion of soft cascade decay products recoiling against a single hard jet from initial state radiation. For point 3.1 we find that this optimized 2jl signature far outperforms the traditional monojet signature M2, becoming comparable in effectiveness to the discovery channel itself.

A comparison of the distribution for $p_T(\text{Jet}, 1)$ with that of the $\not{E}_T$ for this point (Figure 2.13) shows that a large portion of events will indeed be characterized by $p_T(\text{Jet}, 1) \simeq \not{E}_T$, but that these events are in the lowest p_T bins, often below the cutoff of 340 GeV imposed on both quantities by signature M2.

These sorts of gains in L_{min} depend on the details of the SUSY model, so generalizations are difficult to state unequivocally. For example, consider point 3.2, which might appear to be an ideal candidate for the optimized, or 'lopsided', two jet signature. The work in [61] was motivated by the decay $\tilde{t}_1 \to \tilde{\chi}_1^0 c$, and in the case of point 3.2 we have only an 8 GeV mass difference between the lightest stop and the LSP. Here the gluino mass is heavier ($m_{\tilde{g}} = 1901\,\text{GeV}$) and thus gluino pair production accounts for a minuscule fraction of the total signal, which is instead composed primarily of light-flavored squark pairs (51%) and (light-flavored) squark production in association with a gluino (32%). Stop pairs account for only 9% of the total SUSY production cross-section. Thus, the 2jl-optimized search is, in fact, optimal for only a small sub-component of the total production cross-section. The L_{min} value of 574 fb^{-1} for 2jl(opt) is actually slightly worse than the original 2jl signature, for which $L_{\text{min}} = 500\,\text{fb}^{-1}$. Again, this is because 91% of the events for point 3.2 are *not* monojetlike in nature at all. This is despite the fact that a large proportion of these events have $p_T(\text{Jet}, 1) \simeq \not{E}_T$, as can be seen from the distributions in Figure 2.13. We note that these tend to be the events in the lowest p_T bins, where the cuts of 340 GeV on both quantities from signature M2 would eliminate most of the monojetlike subcomponent of the signal.

The improvement from "standard" monojet to "optimal" monojet is most dramatic for point 5.1, where the L_{min} for the monojet signal reduces by two orders of magnitude, making this channel extremely competitive with the five-jet "discovery" channel. Again, the $N_{\text{jet}} \leq 3$ requirement effectively eliminates the "standard" monojet signal, even though a high proportion of these events really do have a lopsided kinematic profile. Conversely, the requirements on inclusive effective mass and $\not{E}_T$ listed in Table 2.5 are relatively easy to satisfy (see the distributions in Figure 2.13). The greatest impact is on the more restrictive separation requirements, $\Delta\phi(\text{Jet1}, \not{E}_T) > \pi/2$ and $\Delta\phi(\text{Jet2}, \not{E}_T) > 1$, which greatly enhance

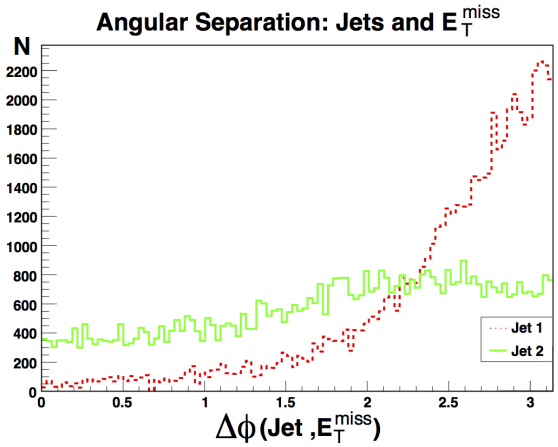

Figure 2.14: Separation in azimuthal angle between leading jets and $\not{E}_T$ for point 5.1. The separation $\Delta\Phi$ between the hardest jet (red, dotted), and second-hardest jet (green, solid), in all events is shown. Both distributions are generated prior to the imposition of any other signal region cuts, and are normalized to 20 fb^{-1} of data.

signal-to-background. We plot these quantities for point 5.1 in Figure 2.14, where the concentration of events near $\Delta\phi(\text{Jet1}, \not{E}_T) \to \pi$ is apparent.

Table 2.9 summarizes the effectiveness of the traditional monojet channel M2 as well as the lopsided two-jet channel we call 2jl(opt). The lopsided two-jet channel is always superior in these cases, mostly due to the relaxation of the strict $N_{\text{jet}} \leq 3$ requirement, and (to a lesser extent) the replacement of specific requirements on $p_T(\text{Jet}, 1)$ with a strict requirement on $\Delta\phi(\text{Jet1}, \not{E}_T)$ and $\Delta\phi(\text{Jet2}, \not{E}_T)$. In cases where the spectrum is indeed highly compressed, where the hardest jet arises from a prompt decay of a squark on one side of the event, or from ISR, the 2jl(opt) signature outperforms other two-jet signatures from Table 2.5. When the model in question is not particularly monojetlike in the first case, this signature is slightly less effective than those in Table 2.5.

Case Study 3: Stop-gluino orderings; 2.1 vs. 7.1

Our final case study is a comparison of points 2.1 and 7.1, in which we will study the impact of the gluino-stop mass hierarchy on detection prospects at the upcoming

run of the LHC. Both points involve a certain degree of universality among the scalar masses, with point 2.1 having modular weights $(n_M, n_H) = (0, 0)$ and $M_0 = 3200$ GeV, while point 7.1 has modular weights $(n_M, n_H) = (1/2, 1/2)$ and $M_0 = 2900$ GeV. The values of α_m are 1.45 and 1.85, respectively. In pure mirage mediation, these values would imply a smaller mass gap between the gluino and neutralino LSP for point 7.1, but the introduction of gauge messengers inverts this. Both points involve three generations of messenger fields, with equal and opposite values of α_g ($\alpha_g = 0.35$ for point 2.1, and $\alpha_g = -0.35$ for point 7.1). Consequently, point 2.1 features the mass hierarchy $m_{\tilde{t}_1} < m_{\tilde{g}}$, with $\Delta m(\tilde{t}_1, m_{\tilde{\chi}_1^0}) = 225$ GeV, while point 7.1 exhibits $m_{\tilde{g}} < m_{\tilde{t}_1}$ with mass separation $\Delta m(\tilde{g}, m_{\tilde{\chi}_1^0}) = 161$ GeV.

Despite the different mass orderings of the lightest SU(3)-charged states, the overall mass scales between the two points are roughly the same. This allows us to address questions like the ultimate 'reach' of the LHC at $\sqrt{s} = 14$ TeV for this class of models. The overall production cross-section for supersymmetry is correlated to the gluino mass, and thus we find $\sigma^{2.1}_{\text{SUSY}} = 22.9$ fb while $\sigma^{7.1}_{\text{SUSY}} = 86.1$ fb, despite the heavier LSP and stop. For both points, approximately 55% of the total cross-section for superpartners is gluino pair production. For point 7.1 an additional 40% of the total production cross-section involves associated production of a gluino with a light-flavored squark, while the light stop of point 2.1 reduces gluino/light squark production to 26% of total events, with 17% associated with stop pair production.

For point 2.1, with the more massive gluino, there is a universal decay $\tilde{g} \to \tilde{t}_1 t$, with the subsequent decay of the stop to $\tilde{\chi}_1^\pm b$ 62% of the time, and $\tilde{\chi}_{1,2}^0 t$ for the remainder. As the three states $\tilde{\chi}_1^\pm$ and $\tilde{\chi}_{1,2}^0$ are highly degenerate, all three effectively represent missing transverse energy. For these gluino pair-production events, we therefore expect four *bona fide* b-jets and as many as four leptons in the final state from leptonic decays of W-bosons. Alternatively, we can expect up to four b-tagged jets and up to eight additional jets. If, instead, we consider associated production of a gluino and a light squark, the fact that the light-flavored squarks decay universally into a corresponding light quark and a gluino means the above analysis applies in this production channel as well, with perhaps one additional high-p_T jet in the final state. Indeed, Table 2.4 confirms this reasoning, with the percentage of events

with at least one lepton for point 2.1 being 21.1%, the percentage with at least one b-tagged jet being 85.3%, and the peak in the jet multiplicity distribution being $N_{\text{jet}} = 8$. It is therefore not surprising that the most effective discovery channel for this point is the six-jet (6jt+) channel, with an eventual confirmation in the single-lepton channel occuring much later in the lifetime of the LHC. Specifically, we find that the first leptonic signal will arise in the six-jets plus muon channel of [58] after 1100 fb^{-1} of integrated luminosity.

Point 2.1 would appear to be a prime candidate for searches involving b-tagged jets. Given the high overall jet multiplicity for this point, it is not surprising that the strongest signal (or lowest L_{min}) occurs for the seven-jet channels of Table 2.8, as demonstrated in Table 2.9. What is, perhaps, surprising is that there is no signal expected, even after 3000 fb^{-1}, for signature SRA2 involving at least six jets, two of which carry b-tags. Here is a case of signatures that are very effectively tailored to certain exclusive event categories – that is to say, signatures that do their respective jobs very well. The b-jet based signatures of Table 2.8 are based on gluino pair production, which is the dominant component of the production cross-section for point 2.1. The SRA signatures of Table 2.7 target stop pair production, followed by the decay $\tilde{t}_1 \to t\tilde{\chi}_1^0$. Stop pair production is only 17% of the total, and the lightest stop decays to $t\tilde{\chi}_1^0$ only 38% of the time, decaying to $b\tilde{\chi}_1^\pm$ the remaining 62% of the time. Thus signature SRA2 captures only about 2.5% of the total events. We note that the SRC channels on Table 2.7, which are designed to target the $b\tilde{\chi}_1^\pm$ decays of the stop, do give a signal significance roughly twice that for the SRA channels, with SRC3 providing a five sigma excess in $L_{\text{min}} = 1650\,\text{fb}^{-1}$ of integrated luminosity.

The situation for point 7.1 is nearly identical with regard to light squark decays, only now gluinos decay overwhelmingly into a gluon and one of the two lightest neutralinos, which are highly degenerate in mass. As $\tilde{g}\tilde{g}$ and $\tilde{g}\tilde{q}$ processes represent 94% of the total SUSY production cross-section, we now expect zero leptons or b-tagged jets in the events, and at most three high p_T jets, with others arising from soft decay products of $\tilde{\chi}_2^0$ and/or initial and final state radiation. This is borne out by Table 2.4 where we find zero events with a high-p_T, isolated lepton and very few with a b-tagged jet (consistent with the mis-tagging rate built into the Delphes

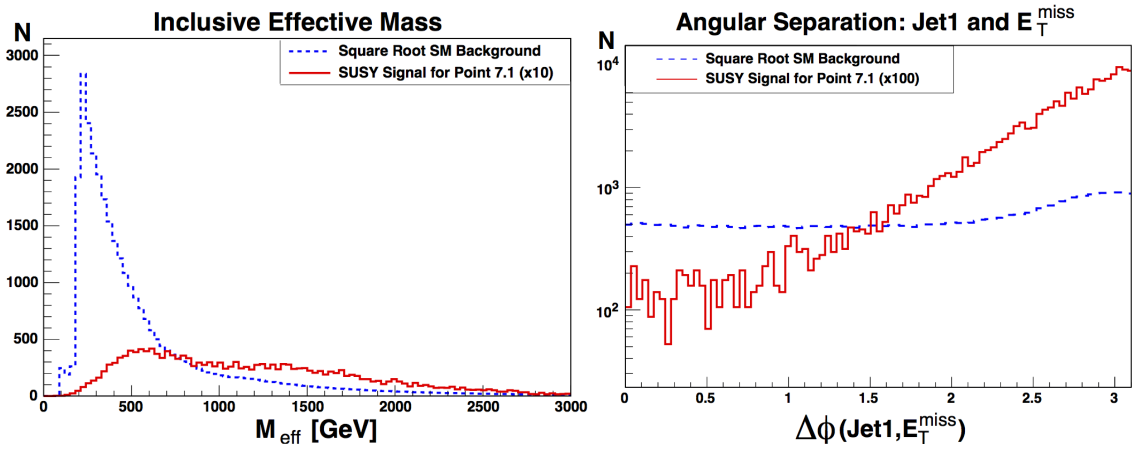

Figure 2.15: Inclusive effective mass (left) and $\Delta\phi(\text{Jet1}, \not{E}_T)$ distribution (right) for point 7.1 versus combined Standard Model background. Distributions are for the signal (red, solid) prior to any event selection cuts, while the background distributions (blue, dashed) have a pre-cut of $\not{E}_T > 150$ GeV applied. Background distributions represents the square root of the total counts in each bin, with the total data set normalized to 20 fb^{-1}. The signal has been augmented by a factor of 10 for the left panel, and a factor of 100 for the right panel, to allow for an easier comparison of the relative shapes of the distributions.

detector simulator). We find that the strongest signal for this point is in the four-jet (4jl) channel, with an L_{min} of 65 fb^{-1}, though the dijet channel (2jt) is competitive with an L_{min} of 88 fb^{-1}. In this case, the generic two-jet search performs much better than our monojet-motivated "unbalanced" two-jet signature (2jl-opt), which requires almost twice as much integrated luminosity to reach a five-sigma excess. While these two signatures are very similar, the relative efficacy can be understood in terms of competing cuts on m_{eff} versus the jet separation variable $\Delta\phi(\text{Jet1}, \not{E}_T)$, and their comparative effects on the signal versus the background sample. To improve signal-to-background, the 2jt signal makes a cut on the inclusive effective mass of $m_{\text{eff}} > 1600\,\text{GeV}$, versus 800 GeV for the "unbalanced" two-jet signature (2jl-opt). Alternatively, the latter makes a cut on $\Delta\phi(\text{Jet1}, \not{E}_T) > \pi/2$, versus 0.4 for the signatures in Table 2.6. These two quantities are plotted in the left and right panels, respectively, of Figure 2.15. The signal distribution (red, solid line) is

shown prior to any event selection cuts, while the background distribution (blue, dashed line) has a pre-cut of $\not{E}_T > 150$ GeV applied. Background distributions represent the square root of the total counts in each bin, with the total data set normalized to 20 fb^{-1}. The signal has been augmented by a factor of 10 for the left panel, and a factor of 100 for the right panel, to allow for an easier comparison of the relative shapes of the distributions. Clearly, both the m_{eff} cut and the $\Delta\phi$ cut prefer the signal distribution, but the stringent effective mass cut does so much more powerfully than the angular separation cut – at least when considered in isolation. Thus, when the superpartner spectrum provides enough phase space to use large m_{eff} and or $\not{E}_T$ cuts to reduce the background, the classic multijet channels will be preferred. The angular separation cut can be a useful tool for those cases in which aggregate quantities such as m_{eff} are low, as in cases with a compressed superpartner spectrum.

Many pairs such as points 2.1 and 7.1 were generated in the course of our analysis, in which the relative masses of the gluino and light squarks are inverted, but with the overall superpartner scale roughly the same. The aggregation of such pairs allows us to make a very crude estimate of the reach (in the sense of a five sigma excess of signal over background in at least one search channel) in terms of the gluino mass and general squark mass for a broad array of DMM parameter sets. For the case $m_{\tilde{g}} > m_{\tilde{t}_1}$ we estimate a reach to be approximately $m_{\tilde{g}} \lesssim 1800\,\text{GeV}$ in 100 fb^{-1} of data, while for the case $m_{\tilde{t}_1} > m_{\tilde{g}}$ we estimate the reach to be $m_{\tilde{t}_1} \lesssim 1270\,\text{GeV}$ in 100 fb^{-1} of data.

2.6 Dark Matter Detection in Deflected Mirage Mediation

Even with the discovery of the Higgs, and increasingly stringent measurements of the dark matter relic density, model points with binolike, winolike and/or Higgsino-like LSPs remain from every combination of modular weights. One may now ask if any of these points, not yet excluded by searches for superpartners at the LHC,

could be detected in the near future in dark matter direct detection experiments. We focus on direct detection here, as indirect detection signals (gamma rays, positrons, anti-protons, neutrino fluxes, etc.) tend to be well below estimated astrophysical backgrounds once the signal is scaled by the predicted thermal relic density. That is, winolike and Higgsino-like LSPs in the DMM scenario tend to have thermal relic densities below that preferred by measurements of the CMB. Once any nonthermal mechanism for populating these LSPs is posited, the constraints from indirect detection become highly constraining [62–65].

To date, discovery prospects for neutralino dark matter ($100\,\text{GeV} \leq m_\chi \leq 1000\,\text{GeV}$) have been dominated by the liquid xenon direct detection experiments: the Xenon100 Dark Matter Project in Gran Sasso, Italy [66], and the South Dakota-based LUX experiment [67]. The former released data in 2012 for 224.6 live days of exposure on a 34 kg target [68]. In 2013, the LUX experiment released a preliminary result from 85.3 live days of exposure on a 118 kg target [69]. In the near future, LUX will release data from approximately 300 days of exposure, while the extension of Xenon100 to the one ton level, Xenon1T, will follow soon thereafter [70]. We can therefore discuss the discovery prospects for dark matter in two stages. First we determine what, if any, parameter space is already in conflict with existing results from Xenon100 and LUX. We then project what part of the parameter space might yield a signal in future results from LUX, Xenon1T, or LZ, the next generation of the LUX experiment [71].[6] In what follows we will consider a subset of 258,225 DMM points, all of which satisfy $m_{\tilde{g}} \geq 1$ TeV, which can reasonably be expected to have passed the LHC supersymmetry searches at $\sqrt{s} = 8$ TeV.

Binolike LSPs

A nearly binolike LSP can be found for nearly all modular weight combinations. For the purposes of discussing dark matter phenomenology, it is convenient to

[6] We focus exclusively on those experiments which are sensitive to the spin-independent part of the scattering cross-section, as our investigations indicate that experiments sensitive to spin-dependent cross-sections, such as the PICO-2L experiment [72], and its future upgrades, are always less sensitive to any given parameter point than the large-scale spin-independent measurements.

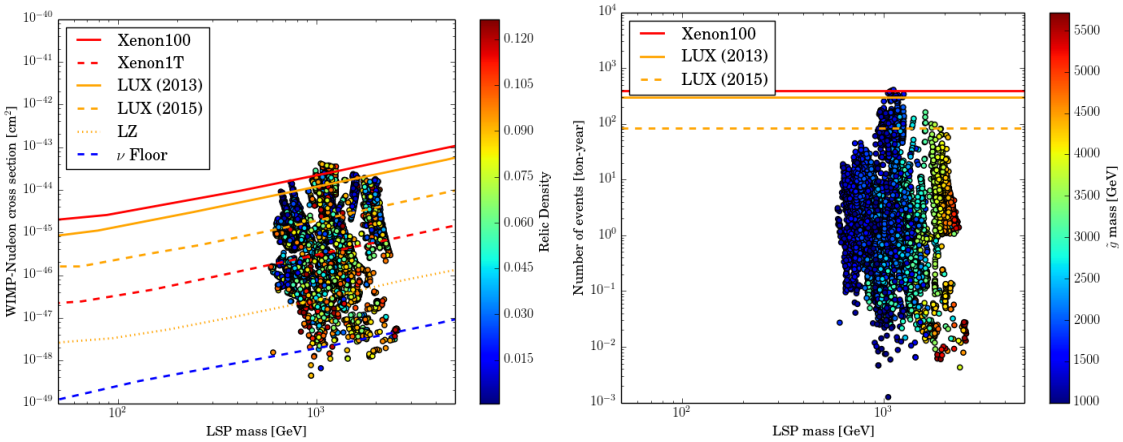

Figure 2.16: The left plot shows the distribution in neutralino-nucleon scattering cross sections versus neutralino mass for the binolike segment of the DMM parameter space. The lines represents the current and future limits set by the recent results from Xenon100 and LUX, and future limits from LUX, Xenon1T, and LZ under the assumption that the relic density is saturated. The predicted thermal relic density is indicated by the color code. The right plot gives the rate of nuclear recoils, rescaled by the relic density, and integrated over the recoil energy range of 5-25 keV, after one ton-year of exposure. Current limits from Xenon100 and current/future limits from LUX are represented as straight lines where 10 events would be observed. The color in the right figure indicates the gluino mass in GeV. Both plots aggregate all the cases with a binolike LSP for all modular weight combinations.

aggregate these modular weight combinations and consider the bulk properties of all binolike neutralino cases as one phenomenologically similar region. For this combined region, the LSP is heavy, ranging from 590 to 2570 GeV. The left plot in Figure 2.16 shows the familiar neutralino-nucleon cross section versus LSP mass for all of the targeted scan regions with binolike LSPs. The lines represent the results from various dark matter direct detection experiments under the assumption that the relic density constraints are saturated. The color scheme in the left panel gives the predicted thermal relic density for each point. Clearly, many of these points would need to rely on some non-thermal production mechanism for this figure to be valid.

More realistic, perhaps, is the right panel in Figure 2.16, which gives the number of expected events for an exposure of 300 days for 1000 kg of liquid Xenon (*i.e.* one ton-year), within the recoil energy range of 5-25 keV. In this case, we have renormalized the count rate to the expectation for the predicted relic density. That is, we have scaled the prediction by the ratio $(\Omega h^2)_{\rm pred}/0.12$. In this panel, current limits from Xenon100 and current/future limits from LUX are represented as straight lines where ten events would be observed.

The 2013 LUX data for LSPs in the appropriate mass range, corresponding to a fiducial volume of 118 kg and an exposure of 85 days [69] has already begun to cut into the binolike parameter space, but only marginally so. While there are a handful of points with very large cross sections, the bulk of the binolike parameter space in the DMM scenario is currently outside the reach of these experiments. The 2015 run of LUX, Xenon1T and LZ expect to improve the limiting cross section on (WIMP)-nucleon scattering by orders of magnitude. For many of these points, more than $\mathcal{O}(1)$ events per ton-year are expected, which could lead to significant signals in future direct detection experiments. Note that upcoming LUX data should begin to eliminate models with characteristic gluino masses up to $\mathcal{O}(3\,\text{TeV})$ (see color key in right panel of Fig. 2.16).

However, for binolike LSPs in the DMM paradigm, that improvement is likely to leave a significant portion of the parameter space unexplored, including many of the points with a Planck-preferred relic density of $\Omega_\chi h^2 \simeq 0.12$. This data set also includes points below the cross section for coherent neutrino scattering [73], the blue line on Fig. 2.16. For all of the points below the neutrino floor, the LSP is nearly degenerate with either the stop or the gluino giving us significant coannihilation effect in the early Universe. Many of these points should still be accessible at the LHC or a future 100 TeV collider.

Winolike and Higgsino-like LSPs

In contrast to pure mirage mediation, as in KKLT, a winolike LSP can be found for many modular weight combinations in DMM. As was done in the previous

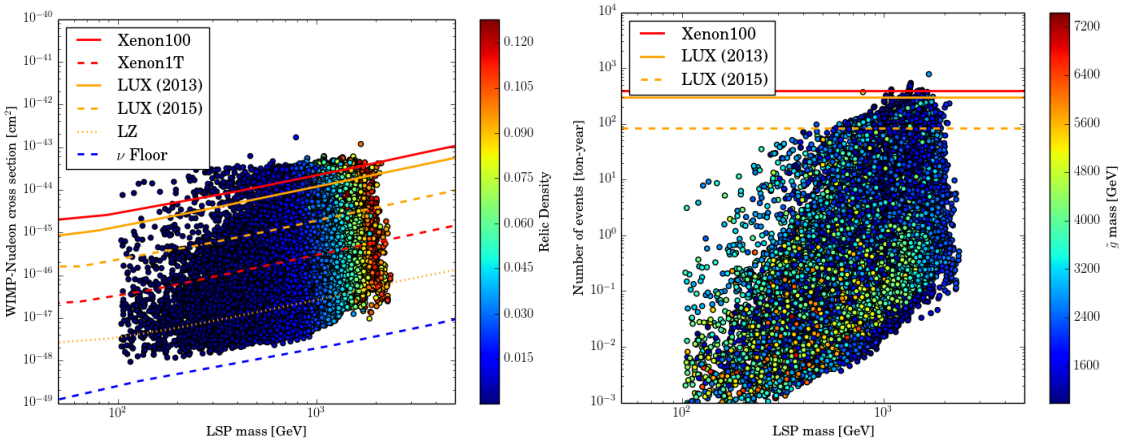

Figure 2.17: The left plot shows the distribution in neutralino-nucleon scattering cross-sections versus neutralino mass for the winolike segment of the DMM parameter space. The lines represents the current and future limits set by the recent results from Xenon100 and LUX, and future limits from LUX, Xenon1T, and LZ under the assumption that the relic density is saturated. The predicted thermal relic density is indicated by the color code. The right plot gives the rate of nuclear recoils, rescaled by the relic density, and integrated over the recoil energy range of 5-25 keV, after one ton-year of exposure. The color in the right figure indicates the gluino mass in GeV. Both plots aggregate all the cases with a winolike LSP for all modular weight combinations.

subsection, we combine our analysis for all modular weights. The left plot in Fig. 2.17 shows the neutralino-nucleon cross section versus LSP mass for all of the targeted scan regions with winolike LSPs, analogously to Figure 2.16. The lines again represent the results from various dark matter direct detection experiments under the assumption that the relic density constraints are saturated. The right panel gives the number of expected events for an exposure of 300 days for 1000 kg of liquid Xenon (*i.e.* one ton-year), within the recoil energy range of 5-25 keV, scaled by the ratio $(\Omega h^2)_{\text{pred}}/0.12$. The winolike region extends from roughly the LEP chargino limit of 103.5 GeV, to 2.5 TeV, spanning much of the region from 10^{-44} to 10^{-48} cm^2. Note that the predicted thermal relic density is a strong function of the LSP mass, saturating the Planck limit at approximately 2 TeV.

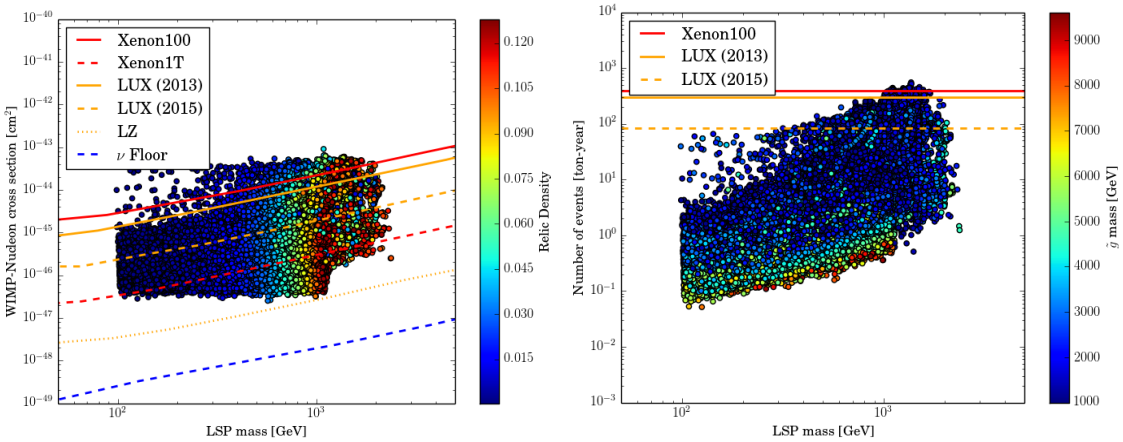

Figure 2.18: The left plot shows the distribution in neutralino-nucleon scattering cross-sections versus neutralino mass for the Higgsino-like segment of the DMM parameter space. The lines represents the current and future limits set by the recent results from Xenon100 and LUX, and future limits from LUX, Xenon1T, and LZ under the assumption that the relic density is saturated. The predicted thermal relic density is indicated by the color code. The right plot gives the rate of nuclear recoils, rescaled by the relic density, and integrated over the recoil energy range of 5-25 keV, after one ton-year of exposure. The color in the right figure indicates the gluino mass in GeV. Both plots aggregate all the cases with a Higgsino-like LSP for all modular weight combinations.

In the alternative case for which the neutralino is almost purely Higgsino-like, we again aggregate all eight combinations of modular weights that admit a Higgsino-like LSP into a single region. For this combination, the LSP can be as heavy as 2.4 TeV, which is slightly lighter than the maximum value in the bino- or winolike case. However, LSPs as light as 100 GeV are also present. The neutralino-nucleon scattering cross section is similarly spread over a wide range of values. The entirety of the parameter space has a cross section of between 10^{-46} and 10^{-43} cm^2.

As with the previous two figures, the left plot in Figure 2.18 shows the neutralino-nucleon cross section versus LSP mass for all of the targeted scan regions with Higgsino-like LSPs, analogously to Fig. 2.16. The lines again represent the results from various dark matter direct detection experiments under the assumption that

the relic density constraints are saturated. The right panel gives the number of expected events for an exposure of 300 days for 1000 kg of liquid Xenon (*i.e.* one ton-year), within the recoil energy range of 5-25 keV, scaled by the ratio $(\Omega h^2)_{\rm pred}/0.12$.

While more of the winolike and Higgsino-like parameter space is being constrained by current experiments than in the binolike case, the bulk of the viable points lie outside the reach of Xenon100 and LUX, (see the right panels of Figs. 2.17 and 2.18). The anticipated release of new LUX data will begin to probe models with relatively light gluinos in the Higgsino-like LSP regime, thus largely overlapping with anticipated early LHC results. In the more limited wino-like regime, however, some model points within reach of LUX correspond to gluino masses of 3 - 4 TeV, likely outside of the LHC reach even after 3000 fb^{-1}. LUX claims a future background expectation of approximately 1 event per ton-year at these recoil energies [67]. It is therefore plausible to expect an even larger fraction of spectra with a Higgsino-like LSP may be within reach in the near future. Note that all of the DMM parameter space with a winolike or Higgsino-like LSP should give signals well-above the background signal from coherent neutrino scattering. In fact, it is conceivable that the entire parameter space with Higgsino-like LSPs in the DMM model will be definitely probed by the LZ experiment in future years.

2.7 Conclusions

If there is any single paradigm for supersymmetry breaking that could claim to be considered a consensus within the string phenomenology community, as of this writing, it would undoubtedly be the mirage mediation scenario popularized in the period following the celebrated paper detailing moduli-stabilization in certain type IIB flux compactifications by Kachru et al. (KKLT) in 2003 [11]. The pattern of soft terms, which was soon referred to as mixed modulus-anomaly mediation [23], or more simply "mirage mediation" [74], is not unique to type IIB constructions. In fact, the so-called mirage pattern of gaugino masses were first identified in heterotic string constructions that achieved acceptable moduli phenomenology using the technique of Kähler stabilization [29, 75–77]. In the years following the KKLT

publication, ever more manifestations of the mirage pattern of guagino masses were motivated, culminating in the original papers describing deflected mirage mediation [8, 9].

Given the ubiquity of the mirage mediation paradigm, and its general acceptance as a realistic outcome of moduli stabilization and supersymmetry breaking in a variety of string theoretic contexts, it is absolutely natural to begin an in-depth study of the implications of LHC data on string-motivated models on this subset of theories. The first two papers on this series were conducted in the heterotic [6] and original type IIB contexts [7], so a natural completion to this study is the present work.

Deflected mirage mediation models offer the broadest possible paradigm for investigating supersymmetry breaking of any ultraviolet-complete theory, in that they allow for similar-sized contributions form gravity mediation, anomaly mediation and gauge mediation. The present work expands upon earlier treatments of the parameter space of DMM models [13–15] by updating the constraints implied by collider-based superpartner searches, dark matter search constraints and, critically, the measurement of the Higgs boson mass. The latter has profound implications for all supersymmetric theories, and this is particularly acute for the models of the KKLT/fluxed type IIB paradigm.

In the previous work [7], which studied the simplest mirage mediation models motivated by flux compactifications of Type IIB string theory, it was found that the relatively large CP-even Higgs mass of $m_h \simeq 125\,\text{GeV}$ puts very strong constraints on the allowed parameter space. Some combinations of modular weights for the matter and Higgs sectors are very hard to reconcile with all current experimental constraints, while other can persist only for very special ranges of parameters like α_m, M_0 and $\tan\beta$. Overall, points in the parameter space that would give a sufficient Higgs boson mass would tend to imply superpartners that are so massive as to avoid detection at the LHC, even after 3000 fb^{-1} of integrated luminosity. This is also in evidence in the current work, in the form of the KKLT "base points" of Table 2.1, none of which are estimated to generate a discovery at the LHC.

Yet the inclusion of a sector which mediates supersymmetry breaking via gauge

interactions radically alters this prediction, allowing for much lower superpartner masses – particularly for the gluinos and quarks – while still satisfying the requirement that $m_h \simeq 125\,\text{GeV}$. In fact, it is possible to achieve gluino and squark masses so low that a discovery would have been made in the previous LHC runs at $\sqrt{s} = 8\,\text{TeV}$. Roughly speaking, we find a reach of $m_{\tilde{g}} \lesssim 600\,\text{GeV}$ for $\Delta m(\tilde{g}, \tilde{\chi}_1^0) \lesssim 50\,\text{GeV}$, and $m_{\tilde{g}} \lesssim 900\,\text{GeV}$ for more sizable mass gaps. Moreover, DMM corrections tend to alter the masses of $SU(3)$-charged objects in a correlated way, tending to compress both the gluino and the stop toward the lightest neutralino mass. The modular weight combinations most likely to produce spectra detectable at $\sqrt{s} = 8\,\text{GeV}$ are the $(n_M, n_H) = (0,\, 0)$, $(0,\, 0.5)$ and $(0.5,\, 0)$ cases, with low messenger scale and $\alpha_g > 0$ – precisely the most interesting cases from the point of view of string model building. This gives hope that the next round of LHC data taking will probe deeply into this rich parameter space.

At the end of 2015, ATLAS release a handful of studies searching for supersymmetry in 3.2 fb^{-1} at center-of-mass energies of $\sqrt{s} = 13\,\text{TeV}$ [78–84]. Of these searches, the cases with low-multiplicity jets plus missing transverse energy, both with a lepton veto [78] and with a single lepton [81], are the most sensitive to low-mass points such as those presented in Table 2.9. Based on the reported limits translated into the $m_{\tilde{g}} - m_{\tilde{\chi}_1^0}$ plane, we estimate that point 2.2 from Table 2.9 would have been discovered in both of these channels. Other potential early discovery cases, such as points 5.1, 6.1, and 6.2, would lie within the one-sigma band about the reported observed limit. As our simulations suppose a center-of-mass energy at 14 TeV, a direct comparison with the reported observations is not possible.

We have estimated the reach of the LHC at $\sqrt{s} = 14$ TeV center-of-mass energies within the DMM parameter space by sampling parameter combinations that give the lowest possible values of key superpartner masses. For the case $m_{\tilde{g}} > m_{\tilde{t}_1}$ we estimate a reach to be approximately $m_{\tilde{g}} \lesssim 1800$ GeV in 100 fb^{-1} of data, while for the case $m_{\tilde{t}_1} > m_{\tilde{g}}$ we estimate the reach to be $m_{\tilde{t}_1} \lesssim 1270$ GeV in 100 fb^{-1} of data. Much of the $\alpha_g > 0$ parameter space will be probed, including those regions around the theoretically motivated area of $\alpha_m \simeq 1$. The most likely discovery channel will be in the low-multiplicity jets plus missing transverse energy channel, with lepton

vetoes, but corroborating signals should be expected in various channels utilizing b-tagged jets, or those channels which emphasize a lopsided two or three-jet event, which will resemble the classic "monojet" signature. In fact, the presence of these corroborating signals will be precisely the indication that a compressed spectrum is present.

The search strategies we employ were defined for applicability at $\sqrt{s} = 8$ TeV. Surely, the kinematic cuts can be adjusted to more fully optimize the signal to background. Some suggestions were identified in the course of discussing the strengths and weakness of various b-jet-based signatures, and various monojetlike signatures, through various case studies involving the DMM points of Table 2.3. One can undoubtedly do even better, and we encourage our experimental and theoretical colleagues to consider such top-down motivated models for honing signal definitions in the forthcoming LHC run. There has been much interest of late in two opposite extremes: the study of so-called simplified models, which posit a very simple superpartner spectrum with large mass gaps generating energetic decay products, and compressed-spectrum models which are motivated from the bottom-up in terms of some abstract sense of "naturalness". The former are popular with the experimental community, while the latter seem to be enjoying popularity with model-builders. The DMM paradigm allows a unified, ultraviolet-complete and string-motivated framework that spans both extremes. We therefore hope that studies such as this one will serve as motivation to continue to refine search strategies to maximize the impact of the coming LHC data.

References

[1] K. Choi, A. Falkowski, H. P. Nilles, M. Olechowski, and S. Pokorski, JHEP **11**, 076 (2004), arXiv:hep-th/0411066 [hep-th].

[2] K. Choi, A. Falkowski, H. P. Nilles, and M. Olechowski, Nucl. Phys. **B718**, 113 (2005), arXiv:hep-th/0503216 [hep-th].

[3] K. Choi and H. P. Nilles, JHEP **04**, 006 (2007), arXiv:hep-ph/0702146 [HEP-PH].

[4] M. K. Gaillard and B. D. Nelson, Int. J. Mod. Phys. **A22**, 1451 (2007), arXiv:hep-th/0703227 [HEP-TH].

[5] P. Nath et al., Nucl. Phys. Proc. Suppl. **200-202**, 185 (2010), arXiv:1001.2693 [hep-ph].

[6] B. L. Kaufman, B. D. Nelson, and M. K. Gaillard, Phys. Rev. **D88**, 025003 (2013), arXiv:1303.6575 [hep-ph].

[7] B. Kaufman and B. D. Nelson, Phys. Rev. **D89**, 085029 (2014), arXiv:1312.6621 [hep-ph].

[8] L. L. Everett, I.-W. Kim, P. Ouyang, and K. M. Zurek, Phys. Rev. Lett. **101**, 101803 (2008), arXiv:0804.0592 [hep-ph].

[9] L. L. Everett, I.-W. Kim, P. Ouyang, and K. M. Zurek, JHEP **08**, 102 (2008), arXiv:0806.2330 [hep-ph].

[10] L. L. Everett, T. Garon, B. L. Kaufman, and B. D. Nelson, (2015), arXiv:1510.05692 [hep-ph].

[11] S. Kachru, R. Kallosh, A. D. Linde, and S. P. Trivedi, Phys. Rev. **D68**, 046005 (2003), arXiv:hep-th/0301240 [hep-th].

[12] K. Choi, K. S. Jeong, S. Nakamura, K.-I. Okumura, and M. Yamaguchi, JHEP **04**, 107 (2009), arXiv:0901.0052 [hep-ph].

[13] B. Altunkaynak, B. D. Nelson, L. L. Everett, Y. Rao, and I.-W. Kim, Eur. Phys. J. Plus **127**, 2 (2012), arXiv:1011.1439 [hep-ph].

[14] B. Altunkaynak, B. D. Nelson, L. L. Everett, I.-W. Kim, and Y. Rao, JHEP **05**, 054 (2010), arXiv:1001.5261 [hep-ph].

[15] M. Holmes and B. D. Nelson, JCAP **0907**, 019 (2009), arXiv:0905.0674 [hep-ph].

[16] H. Abe and J. Kawamura, JHEP **07**, 077 (2014), arXiv:1405.0779 [hep-ph].

[17] S. B. Giddings, S. Kachru, and J. Polchinski, Phys. Rev. **D66**, 106006 (2002), arXiv:hep-th/0105097 [hep-th].

[18] A. Achucarro, B. de Carlos, J. A. Casas, and L. Doplicher, JHEP **06**, 014 (2006), arXiv:hep-th/0601190 [hep-th].

[19] K. Choi and K. S. Jeong, JHEP **08**, 007 (2006), arXiv:hep-th/0605108 [hep-th].

[20] E. Dudas and Y. Mambrini, JHEP **10**, 044 (2006), arXiv:hep-th/0607077 [hep-th].

[21] E. Dudas, C. Papineau, and S. Pokorski, JHEP **02**, 028 (2007), arXiv:hep-th/0610297 [hep-th].

[22] H. Abe, T. Higaki, T. Kobayashi, and Y. Omura, Phys. Rev. **D75**, 025019 (2007), arXiv:hep-th/0611024 [hep-th].

[23] K. Choi, K. S. Jeong, and K.-i. Okumura, JHEP **09**, 039 (2005), arXiv:hep-ph/0504037 [hep-ph].

[24] G. L. Kane, J. D. Lykken, S. Mrenna, B. D. Nelson, L.-T. Wang, and T. T. Wang, Phys. Rev. **D67**, 045008 (2003), arXiv:hep-ph/0209061 [hep-ph].

[25] A. Pomarol and R. Rattazzi, JHEP **05**, 013 (1999), arXiv:hep-ph/9903448 [hep-ph].

[26] G. F. Giudice and R. Rattazzi, Phys. Rept. **322**, 419 (1999), arXiv:hep-ph/9801271 [hep-ph].

[27] G. F. Giudice, M. A. Luty, H. Murayama, and R. Rattazzi, JHEP **12**, 027 (1998), arXiv:hep-ph/9810442 [hep-ph].

[28] L. Randall and R. Sundrum, Nucl. Phys. **B557**, 79 (1999), arXiv:hep-th/9810155 [hep-th].

[29] M. K. Gaillard and B. D. Nelson, Nucl. Phys. **B588**, 197 (2000), arXiv:hep-th/0004170 [hep-th].

[30] B. C. Allanach, Comput. Phys. Commun. **143**, 305 (2002), arXiv:hep-ph/0104145 [hep-ph].

[31] G. Belanger, F. Boudjema, A. Pukhov, and A. Semenov, Comput. Phys. Commun. **149**, 103 (2002), arXiv:hep-ph/0112278 [hep-ph].

[32] P. A. R. Ade et al., Astron. Astrophys. **571**, A16 (2014), arXiv:1303.5076 [astro-ph.CO].

[33] R Aaij et al., Phys. Rev. Lett. **110**, 021801 (2013), arXiv:1211.2674 [hep-ex].

[34] R. Aaij et al., Phys. Rev. Lett. **111**, 101805 (2013), arXiv:1307.5024 [hep-ex].

[35] S. Chatrchyan et al., Phys. Rev. Lett. **111**, 101804 (2013), arXiv:1307.5025 [hep-ex].

[36] The ATLAS collaboration, Report No. ATLAS-CONF-2013-014 (2013).

[37] S. Chatrchyan et al., JHEP **06**, 081 (2013), arXiv:1303.4571 [hep-ex].

[38] G. Aad et al., Phys. Rev. Lett. **114**, 191803 (2015), arXiv:1503.07589 [hep-ex].

[39] O. Buchmueller et al., Eur. Phys. J. **C74**, 2809 (2014), arXiv:1312.5233 [hep-ph].

[40] T. Hahn, S. Heinemeyer, W. Hollik, H. Rzehak, and G. Weiglein, in International Workshop on Future Linear Colliders (LCWS13) Tokyo, Japan, November 11-15, 2013 (2014), arXiv:1404.0186 [hep-ph].

[41] S. Borowka, T. Hahn, S. Heinemeyer, G. Heinrich, and W. Hollik, Eur. Phys. J. **C75**, 424 (2015), arXiv:1505.03133 [hep-ph].

[42] T. Cohen, T. Golling, M. Hance, A. Henrichs, K. Howe, J. Loyal, S. Padhi, and J. G. Wacker, JHEP **04**, 117 (2014), arXiv:1311.6480 [hep-ph].

[43] S. Jung and J. D. Wells, Phys. Rev. **D89**, 075004 (2014), arXiv:1312.1802 [hep-ph].

[44] A. Birkedal-Hansen and B. D. Nelson, Phys. Rev. **D64**, 015008 (2001), arXiv:hep-ph/0102075 [hep-ph].

[45] A. Birkedal-Hansen and B. D. Nelson, Phys. Rev. **D67**, 095006 (2003), arXiv:hep-ph/0211071 [hep-ph].

[46] B. Altunkaynak, P. Grajek, M. Holmes, G. Kane, and B. D. Nelson, JHEP **04**, 114 (2009), arXiv:0901.1145 [hep-ph].

[47] H. Baer, E.-K. Park, X. Tata, and T. T. Wang, Phys. Lett. **B641**, 447 (2006), arXiv:hep-ph/0607085 [hep-ph].

[48] K. Huitu, P. N. Pandita, and P. Tiitola, Phys. Rev. **D92**, 075037 (2015), arXiv:1505.03455 [hep-ph].

[49] S. Krippendorf, H. P. Nilles, M. Ratz, and M. W. Winkler, Phys. Rev. **D88**, 035022 (2013), arXiv:1306.0574 [hep-ph].

[50] A. Anandakrishnan, B. C. Bryant, and S. Raby, Phys. Rev. **D90**, 015030 (2014), arXiv:1404.5628 [hep-ph].

[51] A. Djouadi, M. M. Muhlleitner, and M. Spira, Acta Phys. Polon. **B38**, 635 (2007), arXiv:hep-ph/0609292 [hep-ph].

[52] R. Gröber, M. M. Mühlleitner, E. Popenda, and A. Wlotzka, Eur. Phys. J. **C75**, 420 (2015), arXiv:1408.4662 [hep-ph].

[53] J. Alwall, R. Frederix, S. Frixione, V. Hirschi, F. Maltoni, O. Mattelaer, H. S. Shao, T. Stelzer, P. Torrielli, and M. Zaro, JHEP **07**, 079 (2014), arXiv:1405.0301 [hep-ph].

[54] J. de Favereau, C. Delaere, P. Demin, A. Giammanco, V. Lemaître, A. Mertens, and M. Selvaggi, JHEP **02**, 057 (2014), arXiv:1307.6346 [hep-ex].

[55] G. Aad et al., JHEP **09**, 176 (2014), arXiv:1405.7875 [hep-ex].

[56] G. Aad et al., Phys. Rev. **D90**, 052008 (2014), arXiv:1407.0608 [hep-ex].

[57] G. Aad et al., JHEP **10**, 24 (2014), arXiv:1407.0600 [hep-ex].

[58] G. Aad et al., JHEP **04**, 116 (2015), arXiv:1501.03555 [hep-ex].

[59] G. Aad et al., JHEP **09**, 015 (2014), arXiv:1406.1122 [hep-ex].

[60] A. Avetisyan et al., in Community Summer Study 2013: Snowmass on the Mississippi (CSS2013) Minneapolis, MN, USA, July 29-August 6, 2013 (2013), arXiv:1308.1636 [hep-ex].

[61] B. Kaufman, P. Nath, B. D. Nelson, and A. B. Spisak, Phys. Rev. **D92**, 095021 (2015), arXiv:1509.02530 [hep-ph].

[62] J. Fan and M. Reece, JHEP **10**, 124 (2013), arXiv:1307.4400 [hep-ph].

[63] T. Cohen, M. Lisanti, A. Pierce, and T. R. Slatyer, JCAP **1310**, 061 (2013), arXiv:1307.4082.

[64] N. Blinov, J. Kozaczuk, A. Menon, and D. E. Morrissey, Phys. Rev. **D91**, 035026 (2015), arXiv:1409.1222 [hep-ph].

[65] G. L. Kane, P. Kumar, B. D. Nelson, and B. Zheng, (2015), arXiv:1502.05406 [hep-ph].

[66] E. Aprile et al., Astropart. Phys. **35**, 573 (2012), arXiv:1107.2155 [astro-ph.IM].

[67] D. S. Akerib et al., Nucl. Instrum. Meth. **A704**, 111 (2013), arXiv:1211.3788 [physics.ins-det].

[68] E. Aprile et al., Phys. Rev. Lett. **109**, 181301 (2012), arXiv:1207.5988 [astro-ph.CO].

[69] D. S. Akerib et al., Phys. Rev. Lett. **112**, 091303 (2014), arXiv:1310.8214 [astro-ph.CO].

[70] E. Aprile, Springer Proc. Phys. **148**, 93 (2013), arXiv:1206.6288 [astro-ph.IM].

[71] D. C. Malling et al., (2011), arXiv:1110.0103 [astro-ph.IM].

[72] C. Amole et al., Phys. Rev. Lett. **114**, 231302 (2015), arXiv:1503.00008 [astro-ph.CO].

[73] P. Cushman et al., in Community Summer Study 2013: Snowmass on the Mississippi (CSS2013) Minneapolis, MN, USA, July 29-August 6, 2013 (2013), arXiv:1310.8327 [hep-ex].

[74] O. Loaiza-Brito, J. Martin, H. P. Nilles, and M. Ratz, AIP Conf. Proc. **805**, [,198(2005)], 198 (2006), arXiv:hep-th/0509158 [hep-th].

[75] P. Binetruy, M. K. Gaillard, and B. D. Nelson, Nucl. Phys. **B604**, 32 (2001), arXiv:hep-ph/0011081 [hep-ph].

[76] B. D. Nelson, in 1st String Phenomenology 2002 (StringPheno 2002) Oxford, England, July 6-11, 2002 (2002), arXiv:hep-ph/0211087 [hep-ph].

[77] B. D. Nelson, in Search for SUSY and unification. Proceedings, International Conference, 20 years of SUGRA, SUGRA20, Boston, USA, March 17-21, 2003 (2003), pp. 231–253, arXiv:hep-ph/0307255 [hep-ph].

[78] The ATLAS collaboration, Report No. ATLAS-CONF-2015-062 (2015).

[79] The ATLAS collaboration, Report No. ATLAS-CONF-2015-066 (2015).

[80] The ATLAS collaboration, Report No. ATLAS-CONF-2015-067 (2015).

[81] The ATLAS collaboration, Report No. ATLAS-CONF-2015-076 (2015).

[82] The ATLAS collaboration, Report No. ATLAS-CONF-2015-077 (2015).

[83] The ATLAS collaboration, Report No. ATLAS-CONF-2015-078 (2015).

[84] The ATLAS collaboration, Report No. ATLAS-CONF-2015-082 (2015).

3 ELECTROWEAK NATURALNESS AND DEFLECTED MIRAGE MEDIATION

3.1 Introduction

Theories with TeV-scale supersymmetry, such as the minimal supersymmetric standard model (MSSM) and its extensions, have long been considered to be leading candidates for new physics that can elucidate the origin of electroweak symmetry breaking and address the gauge hierarchy problem associated with the Standard Model Higgs boson. With the null result to date of searches for superpartners, and with the very recent turn-on of the Large Hadron Collider (LHC) which will probe TeV-scale energies at an unprecedented level, the issue of theoretical “naturalness" is a key question for this class of theories. [1]

Of course, the question of how “fine-tuned" a specific model is depends on the criteria used to gauge it. One general method, which has become a standard approach, is to evaluate the sensitivity to observables such as the Z boson mass m_Z to changes in the input parameters at a high scale, for example by the Barbieri-Giudice fine-tuning measure [2–4],

$$\Delta_{\rm BG} = \max_i \left| \frac{\partial \ln m_Z^2}{\partial \ln a_i} \right|, \tag{3.1}$$

in which the a_i represent the parameters at the theory. This measure quantifies the extent to which electroweak to TeVscale observables are sensitive to variations in the high scale parameters and as such is a gauge of the naturalness of the theory.

However, it has recently been emphasized (see, e.g., [5]) that to address the specific question associated with naturalness in light of the nonobservation of supersymmetry at the LHC, which is how the observed value of m_Z emerges when the superpartners must generically have masses that far exceed this value, fine-tuning measures other than $\Delta_{\rm BG}$ may yield valuable information. One specific

[1] This section was published previously in Ref. [1].

fine-tuning measure of this type is known as the electroweak fine-tuning measure Δ_{EW}, [5–17], which assesses the extent to which cancellations occur in the prediction of the Z boson mass as a function of the model parameters. In practical terms, fine-tuning by this measure is a reflection of the degree to which the model parameters that enter in the expression for m_Z are of order m_Z themselves at the electroweak scale (low fine-tuning) or are much larger (high fine-tuning). It has been emphasized previously that the naturalness measure Δ^{-1} can serve as a Bayesian prior and as a likelihood estimate [18, 19].

More precisely, in the MSSM, the Z boson mass is given at one loop by the following well-known relation:

$$\frac{m_Z^2}{2} = \frac{m_{H_d}^2 + \Sigma_d^d - \left(m_{H_u}^2 + \Sigma_u^u\right)\tan^2\beta}{\tan^2\beta - 1} - \mu^2, \tag{3.2}$$

in which the $\Sigma_{u,d}^{u,d}$ are the one-loop corrections for down-type and up-type quarks, respectively (explicit expressions can be found in Ref. [7]). The expression for Δ_{EW} then takes the form

$$\Delta_{\text{EW}} = \text{max}_i|C_i|/(m_Z^2/2), \tag{3.3}$$

in which the C_i are the terms in Eq (3.2), for example $-m_{H_u}^2\tan^2\beta/(\tan^2\beta - 1)$. As each of the C_i are defined at the electroweak scale, each is determined purely by the supersymmetric spectrum, independent of the high-scale dynamics and renormalization group running effects that yield that spectrum. For this reason, this fine-tuning assessment is often referred to as a determination of the degree of "electroweak naturalness" of a given model.

In studies of electroweak naturalness for various models of the MSSM soft terms, it has been noted that several general conditions at the electroweak scale result in low values of Δ_{EW} and hence a small degree of fine-tuning. These conditions include (i) $|\mu| \sim 100$ GeV, which results in light Higgsino-like neutralinos; (ii) $m_{H_u}^2(m_Z) \sim -m_Z^2/2$,as easily seen from Eq. (3.2); and (iii) large A_t, which is needed to raise the Higgs mass without requiring heavy stops. These conditions are not

easily met within certain classes of models but can be achieved in others. In the 19-parameter phenomenological MSSM (pMSSM) [20], it is to be expected that there are regions of parameter space that meet these criteria and hence yield low values for $\Delta_{\rm EW}$, which was shown explicitly in a recent study [16]. Similarly, this can also be achieved in the 19-parameter supergravity mode (SUGRA19) [9].

However, in models with fewer free parameters, clearly these conditions are more difficult to achieve. For example, minimal gauge mediation has difficulty because the A-terms are generated at two loops, and $m_{H_u}^2$ tends to run large and negative. Models of mirage mediation (the mixed moduli-anomaly mediation scenario [21–24] based on the Kachru-Kallosh-Linde-Trivedi (KKLT) construction [25]), also have difficulties, tending to have either large values of μ, for similar reasons as minimal gauge mediation, or small values of μ and fail constraints on B meson decays [14] (see Refs. [26–28] for studies of the phenomenology of mirage mediation). However, the variation on minimal supergravity known as NUHM2 [29], a nonuniversal Higgs model that has six free parameters, can satisfy all of these criteria, yielding results for $\Delta_{\rm EW}$ as low as $\sim 5-10$ [8, 14, 16]. The low fine-tuning allowed in this scenario is quite striking given that the NUHM2 is only a six-parameter model. As such, it has been dubbed “radiative natural supersymmetry" (RNS), wherein the MSSM and electroweak symmetry breaking arise naturally as the low energy limit of an underlying supersymmetric grand unified theory, and its phenomenological implications at the LHC and for dark matter physics have been thoroughly explored [5, 7, 10–13, 15, 17].

The purpose of this section is to explore the question of electroweak naturalness within a class of supersymmetric models known as deflected mirage mediation (DMM) models. This framework is a natural extension of mirage mediation to include additional contributions from gauge mediation [30, 31]. In deflected mirage mediation, the gauge-mediated contributions to the soft supersymmetry breaking parameters can be comparable to the gravity-mediated and anomaly-mediated contributions at the GUT scale, which in turn produces distinct phenomenology and a rich theory space for exploring current and future LHC supersymmetry searches, including examples of both simplified and compressed supersymmetric

spectra [32–34]. It is worth noting that the question of fine-tuning using high-scale fine-tuning measures such as $\Delta_{\rm BG}$ within the DMM framework has been explored [33], particularly in light of the Higgs mass measurement at the LHC [35–37], though there is no prior fine-tuning study of DMM using the electroweak naturalness criterion.

As will be discussed in more detail shortly, the deflected mirage mediation framework, in its most general form, has a rich parameter space that can include regions that are outside the realm of the pMSSM (e.g., that predicts nonuniversal scalar masses for the first and second generations). However, for phenomenological reasons, it is useful to consider only the subspace of DMM theory space that falls within the pMSSM guidelines. Hence, we consider this restricted DMM parameter region within this section. This will allow for a straightforward comparison with the pMSSM. We will demonstrate that within DMM models of this type, there are regions of parameter space with $\Delta_{\rm EW}$ as low as ~ 3.7; *i.e.*, it is roughly equivalent to the best-case scenarios in SUGRA19 and slightly better than the best-case scenarios in the NUHM2/RNS scenario. (Here, we note that direct comparisons with the pMSSM scan done in Ref. [15] are difficult as they likely have not sampled enough of the space to capture the low fine-tuned regions that SUGRA19, NUMH2, and DMM explore, which are all embeddable at low energy in the pMSSM.)

This section of the thesis is organized as follows. In the next section, we quickly review the soft terms in DMM and discuss the parameter space for the subspace of DMM models of interest. In Sec. III, we investigate the question of electroweak naturalness for this class of models, and show that there is a region of parameter space with extremely low values of the fine-tuning measure $\Delta_{\rm EW}$. We then summarize and conclude in Sec. IV.

3.2 Overview of Deflected Mirage Mediation Models

Deflected mirage mediation models are characterized by three classes of contributions to the soft supersymmetry breaking parameters. As is the case in mirage models, there is a KKLT-like contribution to the soft masses that consists of tree-level

supergravity contributions associated with a modulus field, as well as comparable anomaly mediation terms at a high scale, which is taken for simplicity to be the GUT scale $M_{\rm G}$. Deflected mirage mediation scenarios also include gauge-mediated contributions, which take the form of a deflection of the soft terms at some messenger scale $M_{\rm mess}$. The messenger fields associated with the gauge mediation terms are typically taken to be N vectorlike pairs of fundamental representations of $SU(5)$. In these scenarios, the MSSM matter and Higgs fields are also each characterized by a modular weight label n_i that appears in the respective Kähler potential terms for each of these fields. (To be more rigorous, the Kähler potential for the MSSM matter fields is taken to be diagonal in family space. For the matter and Higgs fields, it generically takes the form $K \sim \sum_i \widetilde{K_i}\overline{\Phi}_i\Phi_i$, with $\widetilde{K_i} = (T+\overline{T})^{-n_i}$.

More explicitly, the high-scale soft terms at M_G take the form

$$M_a(\mu = M_{\rm G}) = M_0 \left[1 + \frac{g_0^2}{16\pi^2} b'_a \alpha_m \ln\frac{M_P}{m_{3/2}}\right], \tag{3.4}$$

$$A_i(\mu = M_{\rm G}) = M_0 \left[(1-n_i) - \frac{\gamma_i}{16\pi^2}\alpha_m \ln\frac{M_P}{m_{3/2}}\right], \tag{3.5}$$

$$m_i^2(\mu = M_{\rm G}) = M_0^2 \left[(1-n_i) - \frac{\theta'_i}{16\pi^2}\alpha_m \ln\frac{M_P}{m_{3/2}} - \frac{\dot{\gamma}'_i}{(16\pi^2)^2}\left(\alpha_m \ln\frac{M_P}{m_{3/2}}\right)^2\right], \tag{3.6}$$

in which $m_{3/2}$ is the gravitino mass ($m_{3/2}$ generically exceeds M_0 by about a loop factor in magnitude, and thus is typically of order $10 - 100$ TeV). Note that the physical trilinear terms are $A_{ijk}y_{ijk}$, in which $A_{ijk} = A_i + A_j + A_k$.

In the above expressions, $b'_a = b_a + N$, in which b_a are the one-loop beta functions for the gauge couplings [$b_{1,2,3} = (33/5, 1, -3)$ in the MSSM]. The anomalous dimensions $\gamma'_i = \gamma_i$ are given by $\gamma_i = 2\sum_a g_a^2 c_a(\Phi_i) - (1/2)\sum_{lm}|y_{ilm}|^2$, in which the y_{ijk} are the normalized MSSM Yukawa couplings and the c_a are the quadratic Casimirs. The $\dot{\gamma}_i$'s are given by $\dot{\gamma}_i = 2\sum_a g_a^4 b_a c_a(\Phi_i) - \sum_{lm}|y_{ilm}|^2 b_{yilm}$, in which b_{yilm} is the beta function of the Yukawa coupling y_{ilm}. The quantities $\theta'_i = \theta_i$ are given by $\theta_i = 4\sum_a g_a^2 c_a(Q_i) - \sum_{ijk}|y_{ijk}|^2(3 - n_i - n_j - n_k)$. (see Appendix A for explicit expressions)

The threshold contributions due to gauge mediation at $M_{\rm mess}$ take the form

$$\Delta M_a(\mu = M_{\rm mess}) = -M_0 N \frac{g_a^2(M_{\rm mess})}{16\pi^2} \alpha_m \left(1 + \alpha_g\right) \ln \frac{M_P}{m_{3/2}}, \tag{3.7}$$

$$\Delta m_i^2(\mu = M_{\rm mess}) = M_0^2 \sum_a 2 c_a N \frac{g_a^4(M_{\rm mess})}{(16\pi^2)^2} \left[\alpha_m (1 + \alpha_g) \ln \frac{M_P}{m_{3/2}}\right]^2 . \tag{3.8}$$

Note that the trilinear terms do not receive threshold contributions at one-loop order, and hence these contributions are negligible.

From Eqs. (3.4) to (3.8), we see that the model parameters for a general DMM scenario thus include (i) an overall mass scale M_0 associated with the tree-level supergravity mediation; (ii) a dimensionless parameter α_m, which denotes the relative importance of anomaly mediation with respect to the tree-level gravity mediation (the KKLT scenario predicts $\alpha_m = 1$); (iii) the number of messenger pairs N; (iv) the messenger scale $M_{\rm mess}$; (v) the dimensionless parameter α_g, which denotes the relative importance of gauge mediation with respect to anomaly mediation; (vi) the modular weights n_i; (vii) the ratio of electroweak Higgs vacuum expectation values; and (viii) the sign of μ. Here, the standard procedure has been followed in which the model-dependent Higgs parameters μ and $b = B\mu$ are replaced by $\tan\beta$, m_Z, and the sign of μ.

In a general DMM model of this type, the soft scalar mass-squared parameters have generation-dependent labels given by the possibility of family-dependent n_i values, as well as the presence of Yukawa couplings in the θ_i' and $\dot{\gamma}_i'$ quantities. While the contributions to the anomalous dimensions, etc. are typically negligible for all practical purposes for the first and second generations due to the hierarchical Standard Model fermion masses, a general assignment of the modular weights n_i can yield a sizable nonuniversal contribution. For simplicity as well as phenomenological reasons, we thus will always restrict ourselves to a subspace of DMM parameter space in which the matter fields all carry a universal modular weight n_M. In addition, we will assume that the two electroweak Higgs fields also carry an independent modular weight n_H, which introduces an amount of no-universality.

The DMM scenarios studied here thus have nine independent parameters (two masses, six dimensionless parameters, and one sign): the mass scales M_0 and M_{mess}, the dimensionless quantities α_m and α_g, the number of $SU(5)$ messenger pairs N, the modular weights n_M and n_H, $\tan\beta$, and sign μ. We note that with this assumption regarding the modular weights these scenarios represent a subset of the full 19-parameter pMSSM.

3.3 Electroweak Naturalness in DMM Models

In our analysis of electroweak naturalness in this class of DMM models, we use a subset of the data set as studied in Chapter 2 (Ref. [34]). This data set was determined as follows: for a randomly chosen mirage mediation point in the region $M_0 \in [1, 5]$ TeV, $\tan\beta \in [5, 50]$, and $\alpha_m \in [0, 2]$, we build a three-dimensional scan in the DMM parameter, scanning $\alpha_g \in [-1, 1]$ in steps of 0.05, $\log_{10}[M_{\text{mess}}/\text{GeV}] \in [5, 14]$ in unit steps, and $N \in [1, 5]$ in unit steps. The modular weights n_M and n_H for the matter and Higgs fields, respectively, are allowed to vary independently between 0 and 1 in half-integer steps. The renormalization group (RG) equations were solved using a version of the package SOFTSUSY 3.3.9 [38] that has been modified to account for the gauge mediation contributions [30, 31, 34].

The phenomenological constraints applied to these model points are as follows. At the electroweak scale, points with negative mass squares or that do not result in electroweak symmetry breaking or that do not have a neutralino LSP are excluded. The surviving points are then cut according to an upper bound on the relic density, $\Omega_\chi h^2 \leq 0.128$, taken from Ref. [39], as calculated by MicrOMEGAs 2.2 [40], and a (conservative) Higgs mass bound $123\,\text{GeV} \leq m_h \leq 127\,\text{GeV}$ [35–37]. Finally, we apply constraints from $B_s \to \mu^+\mu^-$ and $b \to s\gamma$, with the values of $\text{Br}(B_s \to \mu^+\mu^-)$ taken within $(1.5 - 4.3) \times 10^{-11}$ [41–43] and a value of $\text{Br}(b \to s\gamma)$ within $(3.03 - 4.08) \times 10^{-4}$ [44]. These cuts follow the ranges used in the previous work on Δ_{EW} [14, 16] to facilitate comparisons with these studies. In total, we use a 2 million point subset and after application of all phenomenological constraints, leading to slightly more than 200,000 viable DMM model points.

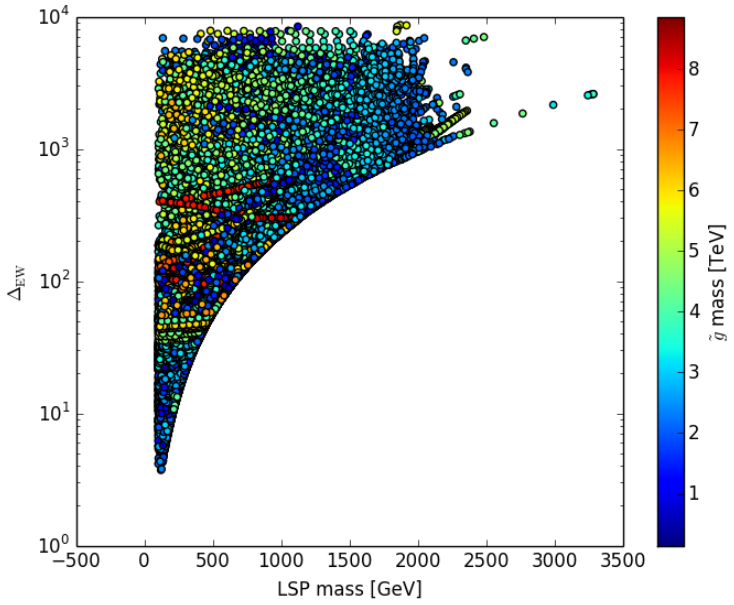

Figure 3.1: $\Delta_{\rm EW}$ as a function of the LSP mass for the full data set without a cut on the gluino mass, and shaded by the gluino mass in TeV.

We now turn to the determination of $\Delta_{\rm EW}$ for these model points. Figure 3.1 shows the results for $\Delta_{\rm EW}$ from the entire scan described previously and used in Ref. [34]. The results of the figure do not change if we require $m_{\tilde{g}} > 1.3$ TeV, consistent with current generic bounds from the LHC [45], because the cut on Br$(b \to s\gamma)$ removes some of the low mass gluinos. We use this bound on the gluino henceforth.

In Fig. 3.1 and the left panel of Fig. 3.2, we see that there is a large region that is less than 1% fine-tuned. The minimum fine-tuning is of order 27%, $\Delta_{\rm EW} \approx 3.7$. These are smaller than the minimum values for the NUHM2 model of $\Delta_{\rm EW} \approx 7$ [8, 16] or ≈ 10 [14], slightly larger than the values found in SUGRA19 [9]. Furthermore, we see that if we want less than 1% EWFT, then gluino masses less than about 8 TeV are allowed in DMM.

The right panel of Fig. 3.2, shows the relic density as a function of the LSP mass. The points with the smallest fine-tuning typically have $O(150$ GeV$)$ LSPs and do not fulfill the relic density constraint, and another nonthermal species such as an

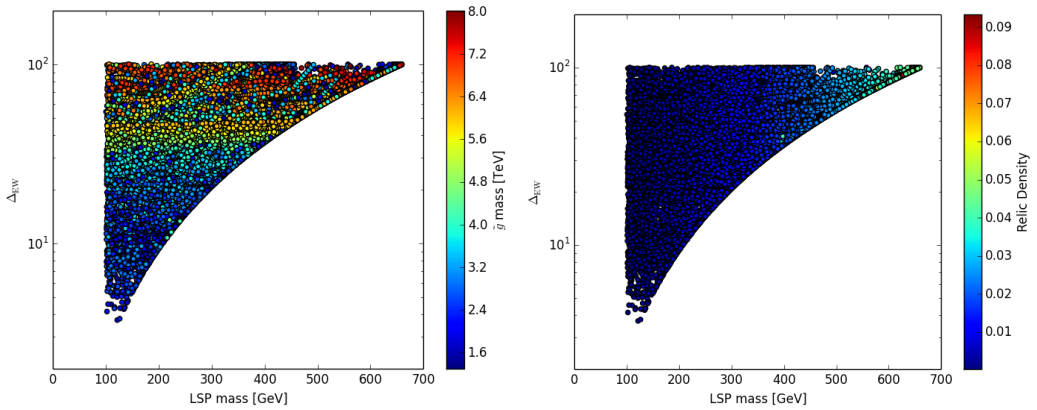

Figure 3.2: A plot of $\Delta_{\rm EW}$ as a function of the LSP mass for points with $\Delta_{\rm EW} < 100$, (left) shaded by the gluino mass in TeV, and (right) shaded by the relic density.

axion is needed [17]. This does not need to be the case if there are coannihilations between a heavier Higgsino-like LSP and the right-handed sleptons. An example of this sort of spectra is shown in the right panel of Fig. 3.3, in which less than 0.5% fine-tuning can be achieved in a corner of parameter space with large M_0 and α_m, and both modular weights equal to 1. Removing the upper bound on the amount of fine-tuning admits spectra where the proper relic density can be achieved through coannihilation with a stop or gluino as well. Over much of the Higgsino-like parameter space, the difference between $\tilde{\chi}_2^0 - \tilde{\chi}_1^0$ is typically < 10 GeV and often less than < 5 GeV, leading to very soft and likely hard to detect signals at LHC13 [10].

The region with $\Delta_{\rm EW}$ less than ~ 100 is made up of points with mass spectra similar to the two example spectra shown in Fig. 3.3. These two points share a light, highly mixed stop and very light pure Higgsino LSP, but they also share a near degeneracy among the next heaviest particles after the Higgsino-like neutralinos and charginos. In the left panel, we have a near degenerate gluino and stop, and in the right a near degenerate stau, smuon, and selectron. As mentioned earlier, coannihillation with the stau allows the spectrum to generate a value of the dark matter relic density near the measured value from the Planck experiment [39]. The

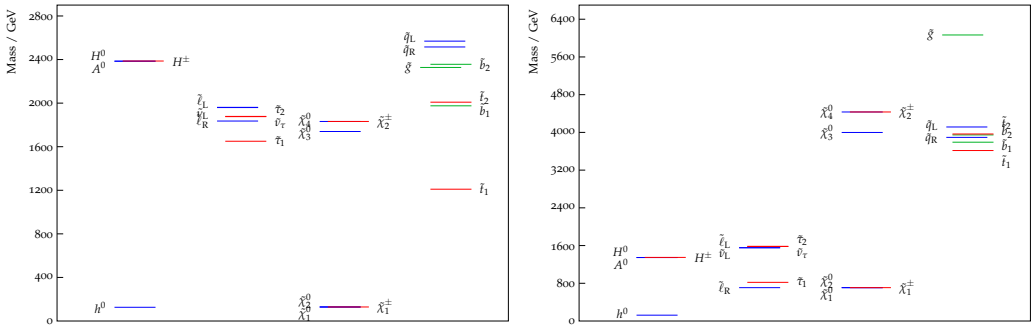

Figure 3.3: Examples of the Higgs and superpartner spectra for two representative points with small(ish) values of Δ_{EW}. The left panel is a point with $\Delta_{\text{EW}} < 4$ and a low value of the relic density ($\Omega_\chi h^2 = 2.4 \times 10^{-3}$), for which $M_0 = 2600$ GeV, $\alpha_m = 1.21$, $\tan\beta = 22$, $(n_M, n_H) = (0.5, 0)$, $\alpha_g = 0.1$, $M_{\text{Mess}} = 10^9$ GeV, and $N = 2$. The right panel is a point with $\Delta_{\text{EW}} < 120$ and a large value of the relic density ($\Omega_\chi h^2 = 0.113$), for which $M_0 = 4800$ GeV, $\alpha_m = 1.36$, $\tan\beta = 38$, $(n_M, n_H) = (1, 1)$, $\alpha_g = -0.4$, $M_{\text{Mess}} = 10^{14}$ GeV, and $N = 1$.

left-hand spectra in Fig. 3.3 are similar to the spectra found in points with low fine-tuning in the NUHM2 model. In this model, and similarly in the SUGRA19 model, the least tuned points tend to have a ~ 1 TeV, highly mixed stop and a plethora of particles above ~ 1.5 TeV, including a ~ 2 TeV gluino. Unlike NUMH2, DMM does not have universal gaugino masses and so M_1 and M_2 can and tend to be much larger.

If we further use a tighter bound of 3.3% fine-tuning, we can compare the bounds in the NUHM2 model from Ref. [16]. In most respects, the two models agree. In DMM, the gluino mass is capped at about 5 TeV, larger than the upper bound in Ref. [16]. Similarly, the bounds on M_1 and M_2 of 900 and 1700 GeV, respectively, from Ref. [16] are instead 4.35 and 4.15 TeV in DMM. Nonuniversal gaugino masses, like those in DMM Eq (3.4), relax the limits in mSUGRA-like models. Other bounds, like those on the lightest stop, are similar to NUHM2 and below the upper bounds from the pMSSM or SUGRA19 from Refs. [9, 16]. The results indicate that as we increase the number of degrees of freedom the bounds on particle masses, other than the lightest stop, and parameters, other than μ and $m_{H_u}^2$, weaken but are still

within the range of future colliders and Higgs factorylike experiments [46].

Wino- and binolike LSPs are typically more fine-tuned than Higgsino-like points. The minimum point with a winolike LSP has $\Delta_{\rm EW} \approx 60$ and the minimum binolike point in the sample has $\Delta_{\rm EW} \approx 176$. These are both more fine-tuned than the values explored in the natural supersymmetry phenomenological study in the NUHM2 model of Ref. [15] because they allow for other hierarchies in the soft terms other than the $M_1 > M_2 > M_3$ in DMM at the GUT scale. The messenger-scale contribution E. (3.8) preserves the same hierarchy in gaugino masses, although the hierarchy in terms of the absolute value of the gaugino masses may change. This allows for winolike LSPs while there were none in mirage mediation. For winolike points, the deflection must be large, $N \geq 3$ and $\alpha_g \sim 1$, and at a low scale. The deflection to the Higgs masses for these points are large, positive, and leads to large values of $m_{H_u}^2$ at $M_{\rm SUSY}$, requiring a larger value of μ or the corrections to compensate, either solution leads to larger fine-tuning. If we were to allow a lower messenger scale or larger α_g, we would likely admit wino-like DMM points with smaller fine-tuning. Running may also modify this hierarchy, opening up the possibility of regions with binolike LSPs. Light, pure-bino dark matter tends to be overproduced, setting a lower bound on M_1 and μ, leading to increased fine-tuning in the binolike sample.

An investigation of the Higgs mass as a function of the stop mass and the stop mixing parameter X_t, as shown in Fig 3.4, demonstrates that points with low fine-tuning are typically those that are near maximally mixed $|X_t/\tilde{t}_1| \sim 2.5$ and have TeV-scale stops [47, 48]. In the left panel, we see that in the $X_t/m_{\tilde{t}_1}$ versus $\Delta_{\rm EW}$ plane. a lighter Higgs will typically allow points with lower fine-tuning. The notch in the lower left corner of both distributions corresponds to a region that is excluded by the constraint on Br$(b \to s\gamma)$.

In Fig. 3.5, we see that there are two distinctive regimes for the μ parameter. In one regime, $m_{H_u}^2$ is negative at $M_{\rm SUSY}$, and in the other, $m_{H_u}^2$ is positive and runs to negative values below $M_{\rm SUSY}$. For Higgsino-like points, the latter set forms a tight band, while the former has a spread. For the same value of μ, points where $m_{H_u}^2$ is already negative are less fine-tuned than points where it is positive, but the

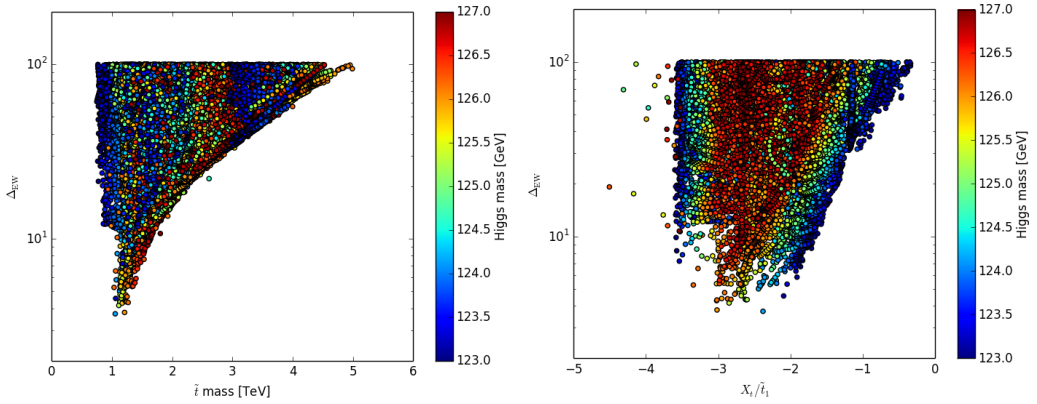

Figure 3.4: A plot of $\Delta_{\rm EW}$ as a function of the stop mass (left) and $\Delta_{\rm EW}$ vs. X_t divided by the stop mass (right), with $\Delta_{\rm EW} < 100$ and a 1.3 TeV cut on the gluino mass. The notches in the lower left corners correspond to regions that are excluded by Br$(b \to s\gamma)$ and Br$(B_s \to \mu^+\mu^-)$.

positive points reach lower overall values of μ and of $\Delta_{\rm EW}$. The gap between the two branches comes from the dearth of points where $m^2_{H_u} \sim 0$ at values of $\mu \gtrsim 1$ TeV, above which electroweak symmetry breaking is difficult to achieve. For bino-like points, all have negative $m^2_{H_u}$, with lower fine-tuning occuring for points with larger values of the up-type Higgs mass. Wino-like points arise from all values of $m^2_{H_u}$, with positive values typically having a smaller μ parameter and lower fine-tuning.

If we break the sample down by modular weights as shown in Fig. 3.6, we see that the majority of points with extremely low fine-tuning have $n_H = 0$. $n_H = 0$ implies that the tree-level supergravity contribution to the Higgs soft mass-squared parameters is maximized [see Eq. (3.6)], leading to small masses at the GUT scale, since the anomaly contribution has the opposite sign. In mirage mediation models, $m^2_{H_u}$ will typically run to large and negative, leading to large values of $\Delta_{\rm EW}$. In DMM, the addition of the messenger fields deflects the soft masses upward, leading typically to shallower values at $M_{\rm SUSY}$ compared to mirage mediation. This is the radiatively natural scenario explored in Ref. [7, 10–13, 15, 17]. Since the corrections can be large, there are regions in DMM, where for $\Delta_{\rm EW} \gtrsim 7$, $n_H = 1/2$ can lead to low fine-tuning as well.

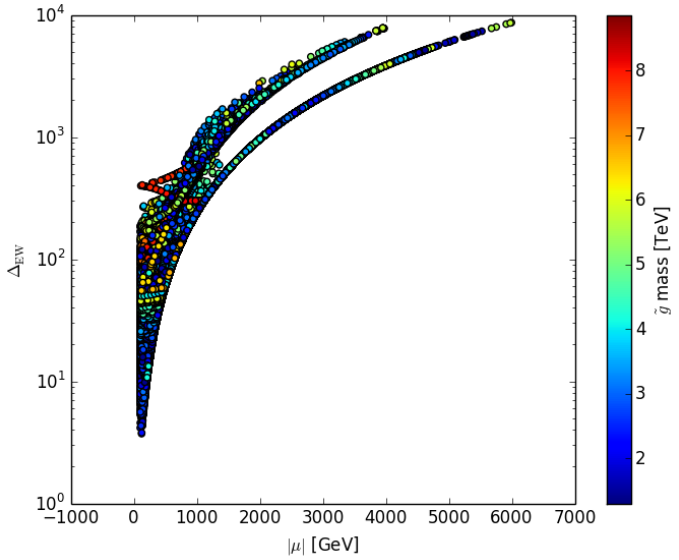

Figure 3.5: A plot of Δ_{EW} vs. the μ parameter, colored by the gluino mass. The two tails correspond to points in which $m_{H_u}^2$ is positive (top) and negative (bottom) at M_{SUSY}.

Our results show that in DMM all values of n_M studied can result in low electroweak fine-tuning, as opposed to the case of mirage models, which single out $n_M = 1$ [14]. That being said, the best results in DMM tend to occur for $n_M = 1$ or $1/2$. These DMM points tend to have soft mass-squared parameters that are negative at the GUT scale but are positive at M_{SUSY} through RG evolution and the positive messenger-scale deflection due to the gauge mediation terms. The addition of messengers in DMM leads to larger values for the gauge couplings at the GUT scale, causing the anomaly mediation contribution to become increasingly large and negative, and so it may require a nonzero tree-level gravity contribution, $n_M \neq 1$, to moderate the soft mass-squared parameters to get light, $\mathcal{O}(1\,\text{TeV})$ stops. In mirage models, the GUT-scale value of the couplings is smaller, leading to a small positive anomaly mediation contribution at the GUT scale, which then runs to give us light stops. If $n_M \neq 1$ in these models, the addition of moduli would lead to a heavy stop and the model would be fine-tuned.

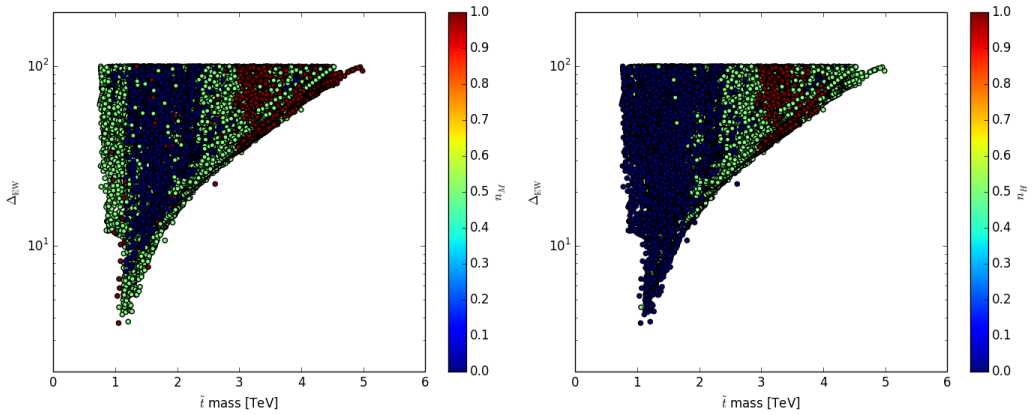

Figure 3.6: $\Delta_{\rm EW}$ vs the stop mass, with the values of the matter modular weight n_M indicated on the left and of the Higgs modular weight n_H on the right, for points with $\Delta_{\rm EW} < 100$.

Breaking the results down by other parameters reveals a few other trends in the fine-tuning results. DMM points with low fine-tuning tend to have one or two messengers which integrate out at a possibly high scale with potentially any value of α_g. Large values of N also tend to deflect $m^2_{H_u}$ too much to run to a shallow minimum over much of the parameter space, giving large fine-tuning. Furthermore, M_0 must be greater than roughly 1.5 TeV, to get mixed stops to bolster the Higgs mass, which leads to gluino masses between 2 and 4 TeV that are accessible at the LHC.

3.4 Conclusions

In this section, we have shown that that deflected mirage mediation, a nine-parameter scenario in which gravity, anomaly, and gauge mediation all can contribute comparably to the soft supersymmetry breaking parameters of the MSSM, admits spectra with low electroweak fine-tuning. A comparison of the electroweak fine-tuning ranges in DMM with many standard models for the soft terms of the MSSM is shown in Fig. 3.7. Here, we note that an upper bound was not determined in Ref.

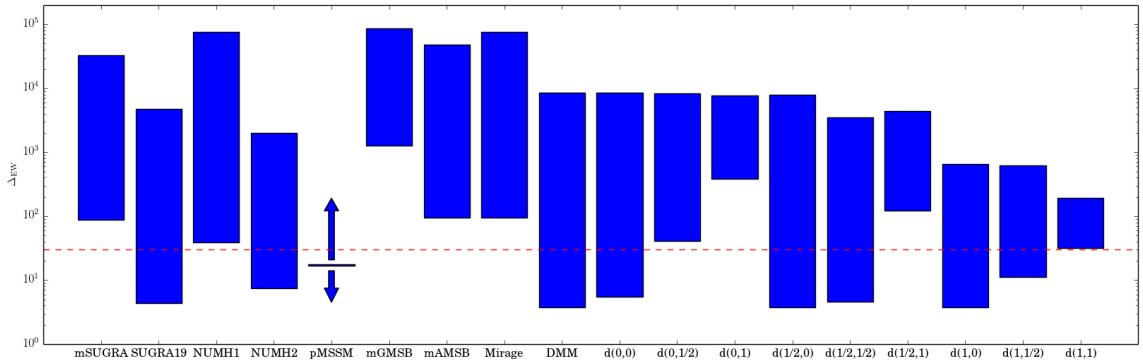

Figure 3.7: A comparison of our results with the fine-tuning ranges found in many SUSY models as taken from Ref. [9, 14, 16]. The line for the pMSSM denotes the lower bound determined in Ref. [16]; the arrows denote that the fine-tuning ranges may go below as well as above this line if a more comprehensive scan is performed. The DMM points are further broken down by the modular weights n_M and n_H for the matter and Higgs fields; these points are denoted by $d(n_M, n_H)$. The dashed line represents $\Delta_{\text{EW}} < 30$, which is considered not fine-tuned.

[16] for the pMSSM. Hence, here we quote the lowest Δ_{EW} presented (the line) and use the arrows to denote that the range of fine-tuning likely goes far up and down, past models that can be embedded in the pMSSM like mGMSB, and at least as low as models like DMM. Given the large parameter space of the pMSSM, we suspect that a more thorough scan of this scenario would lead to points that are at least as, or less, fine-tuned than DMM or SUGRA19.

The results show that DMM does better in general than these standard scenarios, and is comparable to high-scale models with many more parameters such as SUGRA19. We saw that in DMM models with low numbers of messengers can lead to values with low fine-tuning. The other parameters that enter into the deflection, α_g and M_{mess}, do not have any preferred values. For the parameters that enter into the GUT-scale masses, we notice $\alpha_m > 1$, with some points near $\alpha_m = 2$, $M_0 > 1500$ GeV, and with any value of $\tan\beta$. Similarly $n_H = 1$, almost exclusively leads to high fine-tuning, but other combinations of modular weights lead to acceptable values of Δ_{EW}. Hence, we see that in DMM models the combination of gravity

mediation, anomaly mediation, and gauge mediation opens up new avenues with lower fine-tuning and should motivate us to look at models beyond the minimal set, where correlations between parameters can lead to unexpected results.

References

[1] V. Barger, L. L. Everett, and T. S. Garon, (2015), arXiv:1512.05011 [hep-ph].

[2] J. R. Ellis, K. Enqvist, D. V. Nanopoulos, and F. Zwirner, Mod. Phys. Lett. **A1**, 57 (1986).

[3] R. Barbieri and G. F. Giudice, Nucl. Phys. **B306**, 63 (1988).

[4] G. W. Anderson and D. J. Castano, Phys. Lett. **B347**, 300 (1995), arXiv:hep-ph/9409419 [hep-ph].

[5] H. Baer, V. Barger, P. Huang, and X. Tata, JHEP **05**, 109 (2012), arXiv:1203.5539 [hep-ph].

[6] H. Baer, V. Barger, P. Huang, D. Mickelson, A. Mustafayev, and X. Tata, Phys. Rev. **D87**, 035017 (2013), arXiv:1210.3019 [hep-ph].

[7] H. Baer, V. Barger, P. Huang, D. Mickelson, A. Mustafayev, and X. Tata, Phys. Rev. **D87**, 115028 (2013), arXiv:1212.2655 [hep-ph].

[8] H. Baer, V. Barger, and D. Mickelson, Phys. Rev. **D88**, 095013 (2013), arXiv:1309.2984 [hep-ph].

[9] H. Baer, V. Barger, and M. Padeffke-Kirkland, Phys. Rev. **D88**, 055026 (2013), arXiv:1304.6732 [hep-ph].

[10] H. Baer, V. Barger, P. Huang, D. Mickelson, A. Mustafayev, W. Sreethawong, and X. Tata, JHEP **12**, [Erratum: JHEP06,053(2015)], 013 (2013), arXiv:1310.4858 [hep-ph].

[11] H. Baer, V. Barger, and D. Mickelson, Phys. Lett. **B726**, 330 (2013), arXiv:1303.3816 [hep-ph].

[12] H. Baer, V. Barger, P. Huang, D. Mickelson, A. Mustafayev, W. Sreethawong, and X. Tata, Phys. Rev. Lett. **110**, 151801 (2013), arXiv:1302.5816 [hep-ph].

[13] K. J. Bae, H. Baer, N. Nagata, and H. Serce, Phys. Rev. **D92**, 035006 (2015), arXiv:1505.03541 [hep-ph].

[14] H. Baer, V. Barger, D. Mickelson, and M. Padeffke-Kirkland, Phys. Rev. **D89**, 115019 (2014), arXiv:1404.2277 [hep-ph].

[15] H. Baer, V. Barger, P. Huang, D. Mickelson, M. Padeffke-Kirkland, and X. Tata, Phys. Rev. **D91**, 075005 (2015), arXiv:1501.06357 [hep-ph].

[16] H. Baer, V. Barger, and M. Savoy, (2015), arXiv:1509.02929 [hep-ph].

[17] K. J. Bae, H. Baer, V. Barger, M. R. Savoy, and H. Serce, Symmetry **7**, 788 (2015), arXiv:1503.04137 [hep-ph].

[18] L. Giusti, A. Romanino, and A. Strumia, Nucl. Phys. **B550**, 3 (1999), arXiv:hep-ph/9811386 [hep-ph].

[19] B. C. Allanach, Phys. Lett. **B635**, 123 (2006), arXiv:hep-ph/0601089 [hep-ph].

[20] C. F. Berger, J. S. Gainer, J. L. Hewett, and T. G. Rizzo, JHEP **02**, 023 (2009), arXiv:0812.0980 [hep-ph].

[21] K. Choi, A. Falkowski, H. P. Nilles, and M. Olechowski, Nucl. Phys. **B718**, 113 (2005), arXiv:hep-th/0503216 [hep-th].

[22] K. Choi, K. S. Jeong, and K.-i. Okumura, JHEP **09**, 039 (2005), arXiv:hep-ph/0504037 [hep-ph].

[23] M. Endo, M. Yamaguchi, and K. Yoshioka, Phys. Rev. **D72**, 015004 (2005), arXiv:hep-ph/0504036 [hep-ph].

[24] A. Falkowski, O. Lebedev, and Y. Mambrini, JHEP **11**, 034 (2005), arXiv:hep-ph/0507110 [hep-ph].

[25] S. Kachru, R. Kallosh, A. D. Linde, and S. P. Trivedi, Phys. Rev. **D68**, 046005 (2003), arXiv:hep-th/0301240 [hep-th].

[26] H. Baer, E.-K. Park, X. Tata, and T. T. Wang, Phys. Lett. **B641**, 447 (2006), arXiv:hep-ph/0607085 [hep-ph].

[27] H. Baer, E.-K. Park, X. Tata, and T. T. Wang, JHEP **06**, 033 (2007), arXiv:hep-ph/0703024 [hep-ph].

[28] B. Kaufman and B. D. Nelson, Phys. Rev. **D89**, 085029 (2014), arXiv:1312.6621 [hep-ph].

[29] D. Matalliotakis and H. P. Nilles, Nucl. Phys. **B435**, 115 (1995), arXiv:hep-ph/9407251 [hep-ph].

[30] L. L. Everett, I.-W. Kim, P. Ouyang, and K. M. Zurek, Phys. Rev. Lett. **101**, 101803 (2008), arXiv:0804.0592 [hep-ph].

[31] L. L. Everett, I.-W. Kim, P. Ouyang, and K. M. Zurek, JHEP **08**, 102 (2008), arXiv:0806.2330 [hep-ph].

[32] B. Altunkaynak, B. D. Nelson, L. L. Everett, Y. Rao, and I.-W. Kim, Eur. Phys. J. Plus **127**, 2 (2012), arXiv:1011.1439 [hep-ph].

[33] H. Abe and J. Kawamura, JHEP **07**, 077 (2014), arXiv:1405.0779 [hep-ph].

[34] L. L. Everett, T. Garon, B. L. Kaufman, and B. D. Nelson, (2015), arXiv:1510.05692 [hep-ph].

[35] The ATLAS collaboration, Report No. ATLAS-CONF-2013-014 (2013).

[36] S. Chatrchyan et al., JHEP **06**, 081 (2013), arXiv:1303.4571 [hep-ex].

[37] G. Aad et al., Phys. Rev. Lett. **114**, 191803 (2015), arXiv:1503.07589 [hep-ex].

[38] B. C. Allanach, Comput. Phys. Commun. **143**, 305 (2002), arXiv:hep-ph/0104145 [hep-ph].

[39] P. A. R. Ade et al., Astron. Astrophys. **571**, A16 (2014), arXiv:1303.5076 [astro-ph.CO].

[40] G. Belanger, F. Boudjema, A. Pukhov, and A. Semenov, Comput. Phys. Commun. **149**, 103 (2002), arXiv:hep-ph/0112278 [hep-ph].

[41] R Aaij et al., Phys. Rev. Lett. **110**, 021801 (2013), arXiv:1211.2674 [hep-ex].

[42] R. Aaij et al., Phys. Rev. Lett. **111**, 101805 (2013), arXiv:1307.5024 [hep-ex].

[43] S. Chatrchyan et al., Phys. Rev. Lett. **111**, 101804 (2013), arXiv:1307.5025 [hep-ex].

[44] D. Asner et al., (2010), arXiv:1010.1589 [hep-ex].

[45] G. Aad et al., JHEP **10**, 134 (2015), arXiv:1508.06608 [hep-ex].

[46] T. Cohen, T. Golling, M. Hance, A. Henrichs, K. Howe, J. Loyal, S. Padhi, and J. G. Wacker, JHEP **04**, 117 (2014), arXiv:1311.6480 [hep-ph].

[47] H. Baer, V. Barger, and A. Mustafayev, Phys. Rev. **D85**, 075010 (2012), arXiv:1112.3017 [hep-ph].

[48] F. Brummer, S. Kraml, and S. Kulkarni, JHEP **08**, 089 (2012), arXiv:1204.5977 [hep-ph].

4 NON-ABELIAN DISCRETE SYMMETRIES IN MODELS OF FLAVORED GAUGE MEDIATION

4.1 Introduction

It is now well understood that minimal gauge mediation [1] is particularly constrained by the LHC Higgs measurements [2–4]. These models predict family-universal scalar masses and vanishing soft triscalar mass parameters (A terms) at the messenger scale, requiring a significant amount of renormalization group (RG) evolution to generate the needed structure. Even with this structure, it is generally the case that the Higgs mass bound requires a very heavy superpartner spectrum that is largely inaccessible at the LHC. Therefore, it is desirable to go beyond minimal gauge mediation and consider models in which the messengers have nontrivial Yukawa couplings to the SM sector, as first discussed in [1, 5, 6] and more recently considered in light of the Higgs data in [7–18]. The soft terms in these models now include two-loop contributions to the scalar masses and one-loop contributions to the A terms that depend on the messenger Yukawa couplings (and depending on the model, there can also be one-loop contributions to the scalar masses). Hence, while the flavor-blind structure of minimal gauge mediation is sacrificed in these scenarios, what is gained is a much greater ease in accommodating the Higgs mass constraints, and thus in constructing viable models of the MSSM parameter space.

An issue then is to handle the flavor violation that results from the new contributions to the soft supersymmetry breaking parameters. In many (though not all) cases considered in the literature, the models are constructed such that new contributions are consistent with minimal flavor violation (MFV), and thus are safe from large flavor-violating effects beyond the SM. Furthermore, in cases in which there is not precise alignment of this type, viable models can also be constructed in which the messenger Yukawas can share the same parametric suppression as the SM Yukawas. In such models, which are known as “flavored gauge mediation" (FGM) [7], this feature of the messenger Yukawas can also result in acceptably small

flavor violation [7, 12, 16, 17].

These models use one or more $U(1)$ symmetries to control the couplings between their messenger and matter fields. The choice of $U(1)$ charges is model dependent, allowing a hierarchy of couplings through a Froggatt-Nielsen mechanism [19], and explicitly forbidding couplings between the hidden sector and Higgs fields.

One novel model-building direction, as proposed by Perez, Ramond, and Zhang [13] (hereafter referred to as "PRZ"), is to consider scenarios in which the $SU(2)$ doublet messenger fields and the electroweak Higgs doublets $H_{u,d}$ transform as a multiplet under a non-Abelian family symmetry $\mathcal{G}_F$. In these scenarios, the fields that break the family symmetry may also break supersymmetry, resulting in soft supersymmetry breaking terms with a nontrivial flavor dependence that originates both from the details of the family symmetry breaking and the mixing of the Higgs and messenger fields. PRZ constructed a toy two-generation model in which the SM fermions and the Higgs-messenger multiplets are doublets under an $\mathcal{S}_3$ family symmetry which not only generates a hierarchy in the SM Yukawas, it also predicts an inverted hierarchy for the messenger Yukawas [13]. PRZ's work is striking in that it dispels the standard folklore that the unification of family symmetry breaking and supersymmetry breaking inevitably leads to excessive flavor violation. As noted in [13], PRZ's approach also suggests new flavor model-building directions in which the Higgs fields transform nontrivially under the family symmetry group, replacing the ad hoc charges of a $U(1)$ model with the constraints imposed by a non-abelian discrete symmetry.

Here we extend the PRZ framework and look at models with three generations. We will see that in this context, the Higgs mass and a viable particle spectrum can be accommodated within models with three pairs of Higgs doublets, two of which become the heavy messengers of gauge mediation. Along the way we will look at the μ/B_μ problem and the constraints it leads to on the messenger-Higgs structure, discuss different Yukawa couplings and the problems of the top quark coupling, and note how this structure affects the resulting phenomenology.

The models we construct here will not be complete, in that they are not fully realizable models of the fermion masses and mixings as well as the soft breaking

terms. Instead, they will be toy models, which represent the first steps in building three family models of this type. We will not attempt to build a GUT embedding, to explain doublet-triplet splitting, or accurately model the triplet messengers, which we will later put in by hand. More precisely, we will also not attempt to model the entirety of the flavor structure of the Standard Model, preferring to focus on the phenomenology of the soft supersymmetry breaking terms in such scenarios with a non-abelian family symmetry that connects the Higgs and the messenger fields.

The structure of this section of the thesis is as follows. In the succeeding section, we will review the framework prosed by PRZ and discuss the μ/B_μ problem in this context. We will then examine the Higgs sector in models with $\mathcal{S}_3$. We will then discuss two model building directions motivated by the interplay of the Higgs-messenger group and the Yukawa couplings: (i) the Higgs-messengers are coupled at the non-renormalizable level to the matter sector; (ii) the Higgs-messengers are directly coupled to the matter sector so the top Yukawa comes from a renormalizable operator. In each case we will discuss how it fits into the FGM framework and phenomenology.

4.2 Theoretical Framework

General Considerations.

Here we introduce the general properties of these models. Let $\mathcal{G}_F$ be a finite non-abelian family symmetry group, under which the MSSM quarks and leptons are charged. Under $\mathcal{G}_F$, the MSSM electroweak Higgs superfields $H_{u,d}$ and a pair(s) of $SU(2)_W$ doublet messenger superfields $M_{u,di}$ are part of non-Abelian multiplets $\mathcal{H}_{u,d}$ of $\mathcal{G}_F$, as follows:

$$\mathcal{H}_u = \begin{pmatrix} \mathcal{H}_{u1} \\ \mathcal{H}_{u2} \\ \vdots \end{pmatrix} = \mathcal{R}_u \begin{pmatrix} H_u \\ M_{u1} \\ \vdots \end{pmatrix}, \qquad \mathcal{H}_d = \begin{pmatrix} \mathcal{H}_{d1} \\ \mathcal{H}_{d2} \\ \vdots \end{pmatrix} = \mathcal{R}_d \begin{pmatrix} H_d \\ M_{d1} \\ \vdots \end{pmatrix}, \tag{4.1}$$

in which $\mathcal{R}_{u/d}$ are rotation matrices that are obtained upon diagonalizing the Higgs/doublet messenger sector of the theory.

In addition to the MSSM and messenger superfields, the field content may include a number of flavon supermultiplets. The flavon fields are SM singlets charged under $\mathcal{G}_F$, and two different types may be needed. First, there may be a set of fields that we will collectively call $\{\phi\}$ which are charged under $\mathcal{G}_F$, which develop scalar component vacuum expectation values (vevs) and are used to generate fermion masses and mixings above the SUSY breaking scale. In addition, we include a set of flavons $\{\Delta\}$ that will obtain supersymmetry-breaking F-component vevs, as well as scalar vevs, through some hidden sector dynamics that will remain unspecified.

Let us schematically introduce the superpotential,

$$W_Y = y_u(Q\overline{u}\mathcal{H}_u) + y_d(Q\overline{d}\mathcal{H}_d) + y_e(L\overline{e}\mathcal{H}_d), \tag{4.2}$$

where y_u, y_d, and y_e are arbitrary order one factors and the parentheses denote contractions of the flavor symmetry. Once SUSY is broken and any flavons get vevs, we can diagonalize the Higgs sector and rotate into mass eigenstates for our matter or Higgs fields. Thus, the effective Yukawa couplings of the MSSM fields to the MSSM Higgs fields $H_{u,d}$ and to the heavy messenger doublets $M_{u,di}$, take the form

$$\begin{aligned} W_Y = {} & Y_u Q\overline{u}H_u + Y_d Q\overline{d}H_d + Y_e L\overline{e}H_d \\ & + Y'_{iu} Q\overline{u}M_{iu} + Y'_{di} Q\overline{d}M_{di} + Y'_{ei} L_m\overline{e}M_{di}. \end{aligned} \tag{4.3}$$

The MSSM Yukawa couplings can be diagonalized by rotations of the quark and lepton superfields and the new superpotential is

$$\begin{aligned} W_Y = {} & Y_u^D Q_m\overline{u}_m H_u + Y_d^D Q_m\overline{d}_m H_d + Y_e^D L_m\overline{e}_m H_d \\ & + Y'_{iu} Q_m\overline{u}_m M_{iu} + Y'_{di} Q_m\overline{d}_m M_{di} + Y'_{ei} L_m\overline{e}_m M_{di}, \end{aligned} \tag{4.4}$$

where the subscript m denotes mass eigenstates for our matter fields, and the superscript D denotes that the couplings are diagonal. The messenger Yukawa

couplings are not necessarily diagonal in the same basis as the MSSM Yukawas and may generate nonzero off-diagonal entries in the scalar mass squares and A terms from the messenger-matter mixing corrections. The non-abelian nature of G_F relates the matter and messenger Yukawa couplings and forces these couplings to be modeled simultaneously.

A minimal Higgs-messenger sector and the μ/B_μ problem.

To proceed, it is necessary to specify the details of the Higgs-messenger sector. The structure of this sector will determine the form of the rotation matrices $\mathcal{R}_{u,d}$ that enter into Eqs. (4.1) and (4.4), as well determine the Higgs masses. Here we will first do this by introducing a minimal Higgs-messenger sector, following the general example of PRZ, and then point out that a μ/B_μ problem arises, which will require an extension of this minimal sector. More precisely, this minimal sector consists of a field Δ that is a doublet with respect to $\mathcal{G}_F$; this field will break supersymmetry as well as $\mathcal{G}_F$. The Higgs-messenger interactions in the superpotential then take the form

$$W_H = m\mathcal{H}_u\mathcal{H}_d + \lambda(\Delta\mathcal{H}_u\mathcal{H}_d), \tag{4.5}$$

in which λ is a dimensionless coupling, m is a supersymmetric mass parameter (*i.e.*, a μ term), and the parentheses will denote $\mathcal{G}_F$ contractions. In this argument we will assume that $\mathcal{G}_F = \mathcal{S}_3$, in line with what is used in PRZ. $\mathcal{S}_3$ is the symmetric group of 6 elements with two one-dimensional representations and one doublet representation (more details, including the Clebsch-Gordon coefficients for the tensor products of group representations, are given in Appendix B).

Through some hidden sector dynamics Δ acquires a vacuum expectation value for its scalar and F-components, which is parametrized as follows:

$$\langle\lambda\Delta\rangle = v\begin{pmatrix}\sin\phi\\ \cos\phi\end{pmatrix} + \theta^2 F\begin{pmatrix}\sin\xi\\ \cos\xi\end{pmatrix}. \tag{4.6}$$

Here ϕ and ξ characterize the vacuum directions of the scalar and F components, respectively, and in which it is assumed that $F \ll v^2$. After symmetry breaking, the effective superpotential takes the following form:

$$W_H = \mathcal{H}_u^T \begin{pmatrix} v\sin\phi & m \\ m & v\cos\phi \end{pmatrix} \mathcal{H}_d + \theta^2 \mathcal{H}_u^T \begin{pmatrix} F\sin\xi & 0 \\ 0 & F\cos\xi \end{pmatrix} \mathcal{H}_d \tag{4.7}$$

$$\equiv \mathcal{H}_u^T \mathbb{M} \mathcal{H}_d + \theta^2 \mathcal{H}_u^T \mathbb{F} \mathcal{H}_d \tag{4.8}$$

where $\mathcal{H}_{u/d}$ have been taken to be doublets of $\mathcal{S}_3$. As discussed in PRZ, when $[\mathbb{M}, \mathbb{F}] \neq 0$, the resulting fermion soft mass-squared terms have contributions at one-loop due to the Yukawa interactions between the Higgs and matter fields, while when $[\mathbb{M}, \mathbb{F}] = 0$, these one-loop terms are suppressed $\mathcal{O}\left(\frac{F^4}{M^6}\right)$ and the leading contributions are at two-loop order (see also [1, 5] for discussions of the cancellation of the one-loop contributions in this case), which is phenomenologically preferable. Thus, we will focus on the case of the vanishing commutator, which from Eq. (4.8) yields the condition

$$[\mathbb{M}, \mathbb{F}] = \begin{pmatrix} 0 & mF(\cos\xi - \sin\xi) \\ -mF(\cos\xi - \sin\xi) & 0 \end{pmatrix} = 0. \tag{4.9}$$

Thus there are three solutions; (i) $m = 0$, (ii) $F = 0$, and (iii) $\xi = \pi/4$ with $m \neq 0$ and $F \neq 0$. In the first case, there are no off-diagonal entries and so no mixing between the Higgs-messenger states, and so we ignore this case. In the second, supersymmetry is not broken, and we ignore this case as well. Finally, when $\xi = \pi/4$ with $m \neq 0$ and $F \neq 0$, $\mathbb{F}$ must be proportional to the identity to satisfy Eq. (4.9). $\mathbb{M}$ is not constrained by this requirement.

Proceeding with an analysis of the Higgs sector for Eq. (4.8) with $\xi = \pi/4$, we see immediately that this scenario suffers from a severe μ/B_μ problem. More precisely, $\mathbb{F}$ is proportional to the identity, and the symmetric structure of $\mathbb{M}$ results in $\mathcal{R}_u = \mathcal{R}_d$ for $\mathcal{H}_{u,d}$ as given in Eq. (4.1). The diagonalization of the Higgs sector into the electroweak Higgs fields and the messenger fields thus clearly results in

equivalent $b = \mu B_\mu \sim O(F)$ terms for each set of fields. Recalling that $F \gg m_{\text{soft}} \sim (1/(16\pi^2))F/v$, it is clear that since μ can be much smaller than $\sqrt{F}$ (for example, in PRZ there is an effective seesaw structure for the μ term [13]), generally we have $B_\mu \gg \mu$ and $B_\mu \gg m_{\text{soft}}$.

The μ/B_μ problem of this framework is not surprising given the well-known fact that gauge-mediated models generically suffer from a μ/B_μ problem (see e.g. [1] for an overview). However, we wish to point out that the problem is particularly acute for scenarios of this type in which the Higgs and doublet messenger fields are related by nontrivial family symmetry transformations. To see this more clearly, recall that it has long been realized that a direct superpotential coupling of the supersymmetry breaking field to the electroweak Higgs doublets $H_{u,d}$ is particularly dangerous. Following the usual notation that the supersymmetry-breaking field is denoted by X (here X collectively denotes the components of Δ), the superpotential coupling

$$W_{\text{H}} = \lambda X H_u H_d, \tag{4.10}$$

generates a tree-level value for both μ and $B\mu$:

$$\mu = \lambda\langle X\rangle, \qquad b = B\mu = \lambda\langle F_X\rangle, \tag{4.11}$$

and hence

$$B = \langle F_X\rangle/\langle X\rangle \sim 16\pi^2 m_{\text{soft}}, \tag{4.12}$$

and so it is desirable in general to eliminate the coupling of Eq. (4.10). In this scenario, however, $H_{u,d}$ are embedded together with the doublet messengers $M_{u,di}$. Hence the need to have a superpotential coupling between X and $\mathcal{H}_{u,d}$ to generate the soft supersymmetry breaking terms means that the superpotential coupling of X to the Higgs fields as in Eq. (4.10) is automatically also present, resulting in a severe μ/B_μ problem.

Methods to alleviate this problem are not obvious. Most approaches to resolving

the μ/B_μ problem of gauge mediation without fine-tuning begin by forbidding the coupling of Eq. (4.10) and generating μ and B_μ from alternative operators (see e.g. [20]); however, this is precisely what we cannot do because couplings of the form Eq. (4.10) are unavoidable. Even with fine-tuning, we recall from Eq. (4.9) that merely setting the F term component of Δ that couples to the eventual electroweak Higgs doublets to zero is not possible in this minimal Higgs sector, as doing so would then result in $[\mathbb{M}, \mathbb{F}] \neq 0$, and thus unwanted one-loop contributions to the soft scalar mass-squared parameters would be reintroduced.

Therefore, to construct a working (toy) model, we need to enlarge the minimal Higgs-messenger sector to include additional fields and to avoid $B_\mu = \mathcal{O}\left(\frac{F}{M}\right)$. Options include:

- Add additional singlets that do not develop F terms and attempt to address the μ/B_μ problem via a next-to-minimal supersymmetric standard model (NMSSM)-like approach in which at least one singlet field is tied with electroweak symmetry breaking (See Ref. [1, 21]).

- Another is to simply introduce another supersymmetry breaking flavon field Δ' such that the large B_μ term of the Higgs fields can be fine-tuned to acceptable values. We would need another field Δ' (like Δ) to couple to $\mathcal{H}_{u,d}$ in the superpotential and obtain both scalar and F-component vevs, and we will also assume that Δ and Δ' have different $\mathcal{G}_F$ quantum numbers. $\mathbb{F}$ can then have enough degrees of freedom such that a hierarchy of eigenvalues can be engineered while still maintaining $[\mathbb{M}, \mathbb{F}] = 0$.

- One final way is to enlarge the Higgs sector while keeping a single SUSY breaking flavon. In this solution, the additional degrees of freedom gained through using more Higgs fields opens up a direction where the mass and F term matrices can simultaneously have one small eigenvalue through tuning the direction of $\langle \lambda \Delta \rangle$.

We explore the this final option in the next section, because it shares the the most similarities with the setup explored in PRZ, and leave the other options for

future work.

4.3 An Extended Higgs and SUSY breaking sector

In PRZ, they introduced $\mathcal{S}_3$ doublets of up and down type Higgs and a SUSY breaking $\mathcal{S}_3$ doublet Δ. We extend our Higgs sector by adding an up- and down-type Higgs doublet, which are $\mathcal{S}_3$ singlets. The superpotential couplings are

$$W_H \supset \lambda(\Delta\mathcal{H}_{u\mathbf{2}}\mathcal{H}_{d\mathbf{2}}) + \lambda'(\Delta\mathcal{H}_{u\mathbf{1}}\mathcal{H}_{d\mathbf{2}}) + \lambda''(\Delta\mathcal{H}_{u\mathbf{2}}\mathcal{H}_{d\mathbf{1}}), \tag{4.13}$$

$$\supset m\mathcal{H}_u^T\mathbb{M}\mathcal{H}_d + \theta^2 F\mathcal{H}_u^T\mathbb{F}\mathcal{H}_d, \tag{4.14}$$

where $\mathcal{H}_u^T = (\mathcal{H}_{u\mathbf{2}1}, \mathcal{H}_{u\mathbf{2}2}, \mathcal{H}_{u\mathbf{1}})$ with a similar embedding for $\mathcal{H}_d$, the bold subscript denotes the S_3 representation of a field, and

$$\mathbb{M} = \begin{pmatrix} \sin\phi & 0 & \epsilon'\cos\phi \\ 0 & \cos\phi & \epsilon'\sin\phi \\ \epsilon''\cos\phi & \epsilon''\sin\phi & 0 \end{pmatrix}, \quad \mathbb{F} = \begin{pmatrix} \sin\xi & 0 & \epsilon'\cos\xi \\ 0 & \cos\xi & \epsilon'\sin\xi \\ \epsilon''\cos\xi & \epsilon''\sin\xi & 0 \end{pmatrix}, \tag{4.15}$$

in which $\epsilon' = \lambda'/\lambda$ and $\epsilon'' = \lambda''/\lambda$. Without bare mass terms, the commutation condition $[\mathbb{M}, \mathbb{F}] = 0$ only has solutions when $\epsilon' = \epsilon'' = 0$ or $\phi = \xi$. In the latter, the singlets are uncoupled and do not mix with the $\mathcal{S}_3$ doublets; and in the former, our two matrices are identical and the eigenvalues will be proportional. The ratio of the smallest eigenvalues B_μ will be then proportional the F/m, exactly the μ/B_μ problem.

One way to modify this relationship is to introduce bare mass terms for the messenger-Higgs multiplets and induce some amount of misalignment between our two matrices. If we introduce bare terms $\kappa m(\mathcal{H}_{u2}\mathcal{H}_{d2}) + \kappa' m(\mathcal{H}_{u1}\mathcal{H}_{d1})$, filling in the zeros in Eq. (4.14), the commutation condition is satisfied only when either:

1. $\epsilon' = \epsilon'' = \kappa = 0$,

2. $\kappa = \kappa'$, $\epsilon' = \epsilon'' = 1$, and $\phi = \xi + \arcsin\left(\kappa(\cos\xi - \sin\xi)\right)$,

3. $\kappa = \kappa'$, $\epsilon' = 1/\epsilon''$, and $\phi = \xi + \arcsin(\kappa(\cos\xi - \sin\xi))$.

In the first case, our Higgs eigenstates are uncoupled and there is no mixing. The second is a special case of the third where the mass and F term matrices are symmetric. We choose here to focus on the cases where $\mathbb{M}$ and $\mathbb{F}$ are symmetric. In the case of interest, when $\kappa = \kappa'$, $\epsilon' = \epsilon'' = 1$, and $\phi = \xi + \arcsin(\kappa(\cos\xi - \sin\xi))$, the mass matrices are

$$W_H \supset m\mathcal{H}_u^T \begin{pmatrix} \sin\phi & \kappa & \cos\phi \\ \kappa & \cos\phi & \sin\phi \\ \cos\phi & \sin\phi & \kappa \end{pmatrix} \mathcal{H}_d + \theta^2 F \mathcal{H}_u^T \begin{pmatrix} \sin\xi & 0 & \cos\xi \\ 0 & \cos\xi & \sin\xi \\ \cos\xi & \sin\xi & 0 \end{pmatrix} \mathcal{H}_d, \quad (4.16)$$

with eigenvalues, which are masses and F terms, given by

$$\begin{aligned} \frac{m_1}{m} &= \kappa + \cos\phi + \sin\phi, & \frac{f_1}{F} &= \cos\xi + \sin\xi, \\ m_{2/3} &= \pm\sqrt{1 + \kappa^2 - \kappa\sin\phi - \cos\phi(\kappa + \sin\phi)}, & \frac{f_{2/3}}{F} &= \pm\sqrt{1 - \cos\xi\sin\xi}. \end{aligned} \quad (4.17)$$

We have two parameters κ and ξ which determine our system, giving us the residual freedom to tune the model. If $\xi \sim -\frac{\pi}{4} + \eta$, where η is small, the eigenvalues become

$$\begin{aligned} \frac{m_1}{m} &= 3\kappa + \eta\sqrt{2 - 4\kappa^2}, & \frac{f_1}{F} &= \eta\sqrt{2}, \\ \frac{m_{2/3}}{m} &= \pm\left(\sqrt{\frac{3}{2} - 3\kappa^2} - \sqrt{3}\kappa\eta\right), & \frac{f_{2/3}}{F} &= \pm\sqrt{\frac{3}{2}}. \end{aligned} \quad (4.18)$$

and $\mathcal{R}_{u/d}$ are

$$\mathcal{R}_{u/d} = \begin{pmatrix} \frac{1}{\sqrt{3}} & \frac{1}{6}\left(3 - \sqrt{3}\right) & \frac{1}{6}\left(-\sqrt{3} - 3\right) \\ \frac{1}{\sqrt{3}} & \frac{1}{6}\left(-\sqrt{3} - 3\right) & \frac{1}{6}\left(3 - \sqrt{3}\right) \\ \frac{1}{\sqrt{3}} & \frac{1}{\sqrt{3}} & \frac{1}{\sqrt{3}} \end{pmatrix} + \mathcal{O}(\eta), \quad (4.19)$$

and $|\kappa| < \frac{1}{\sqrt{2}}$ so that the masses are real. By placing Δ in a doublet and working in the $-\frac{\pi}{4}$ direction, the mass matrix preserves a residual Z_2 symmetry which forces

two degenerate eigenvalues.

This structure has also realized a way to accommodate the μ/B_μ problem. We see that

$$\mu \sim (3\kappa + \eta\sqrt{2-4\kappa^2})m, \qquad B_\mu \sim \frac{\sqrt{2}\eta}{3\kappa + \eta\sqrt{2-4\kappa^2}}\frac{F}{m}. \tag{4.20}$$

There are two limits of interest. If κ is $\mathcal{O}(0.5)$, we would have $B \sim \eta\frac{F}{m}$, however the μ term is $\mathcal{O}(m)$ and too large. If $\kappa \sim 0$, μ is $\mathcal{O}(\kappa m)$ and $B_\mu \propto \frac{\eta}{\kappa}\frac{F}{m}$. This latter case allows μ and B_μ to be separately fine-tuned. Although, this is not a solution to a μ problem since μ must be tuned to be much less than m, it is still progress compared to minimal gauge mediation or models with an operator like Eq. (4.10).

We could also reassign one or more of our singlets to the $\mathbf{1}'$ representation. If we reassign both singlets, it is equivalent to introducing a sign in Eq. (4.14). Reassigning a single singlet will not lead to a symmetric mass matrix. We may also promote the bare mass term to a flavon in a larger representation. This will perturb the eigenvalues and eigenvectors, but the messenger-Higgs spectrum will fundamentally look like the previous case.

4.4 A Nonrenormalizable Model

In most flavor models with a family symmetry, the Higgs is inert with respect to the family symmetry. However, in the models we are looking at, the Higgs must have flavor structure, necessarily complicating the model. One may be motivated to get around charging the Higgs under the same horizontal symmetry as matter by breaking $\mathcal{G}_F$ into something like $\mathcal{G}_F = \mathcal{G}_f \otimes \mathcal{G}_h$, in which $\mathcal{G}_f$ is a “traditional" family symmetry group and $\mathcal{G}_h$ is the (non-Abelian) Higgs-messenger group. By “traditional," what we mean is that the MSSM quarks and leptons are charged under $\mathcal{G}_f$, while the Higgs fields and the messengers are inert. The messenger-Higgs group $\mathcal{G}_h$, is another non-abelian group that governs the Higgs and messenger fields. This framework closely parallels the approach of PRZ [13], with the main difference that PRZ takes $\mathcal{S}_3$ to be the full family symmetry group while we would take it to be the

Higgs-messenger group. As a result, one of the primary differences between these approaches is the nature of the superpotential Yukawa couplings of the MSSM matter fields. While such couplings are renormalizable operators at leading order in PRZ's approach, in the most minimal version of this scenario they must originate from higher-dimensional operators, for example:

$$W \supset \frac{1}{\Lambda} Q_m^T Y_u \bar{u}_m (\phi \mathcal{H}_u) + \frac{1}{\Lambda} Q_m^T Y_d \bar{d}_m (\phi \mathcal{H}_d) + \frac{1}{\Lambda} L_m^T Y_e \bar{e}_m (\phi \mathcal{H}_d), \tag{4.21}$$

where the matter fields are in mass eigenstates, $Y_{u/d/e}$ are diagonal matrices of Yukawa couplings, the parentheses denote contractions under $\mathcal{G}_h$, ϕ is at least one flavon charged $\mathcal{G}_h$ and under possibly charged under $\mathcal{G}_f$, Λ is a (presumably high) scale, and we have suppressed other indices for notational simplicity.

One model-building issue that immediately arises is that, as seen in Eq. (4.21), all quark and charged lepton masses result from nonrenormalizable operators. Obtaining a sufficiently large top quark mass thus would require field variations $\langle \phi \rangle \sim \Lambda$, which signify that a tower of higher-dimensional operators can result in competitive contributions. [1] Since v_ϕ / Λ must be of order one, higher dimension operators like $Q^T Y_u \bar{u} (\phi^2 \mathcal{H}_u)/\Lambda^2$ will be similar in size to the leading term unless they are sufficiently suppressed.

One way to generate this suppression is to introduce a global U(1) or Z_n. As an example, let the charges for a field f under a new $U(1)$ be q_f. Wanting the Higgs sector of Eq (4.14) and the Yukawa couplings of Eq. (4.21), the charges have to satisfy

$$\begin{aligned} q_\phi + q_{\mathcal{H}_u} &= 1, \\ q_\phi + q_{\mathcal{H}_d} &= 1, \\ q_\Delta + q_{\mathcal{H}_u} + q_{\mathcal{H}_d} &= 0, \end{aligned} \tag{4.22}$$

where we have chosen to define our symmetry such that terms like $Q\bar{u}$ have net

[1] This problem is avoided altogether if there is an additional up-type Higgs field that is a singlet under $\mathcal{G}_f$ and that only couples to the top sector at the renormalizable level. Of course, in practice an additional Higgs pair would then need to be introduced to avoid anomalies. These new Higgs fields will mix with the Higgs-messenger fields of Eq. (4.1), and depending on the details of the Higgs potential, can in principle result in another pair of light Higgs in the effective TeV-scale theory.

charge -1. For example, if $q_{\mathcal{H}_u} = q_{\mathcal{H}_d} = n$, $q_\phi = 1 - n$ and $q_\Delta = -2n$, there will still be operators like $\frac{Y_u}{\Lambda^4} Q\bar{u}(\phi\mathcal{H}_u)(\Delta\mathcal{H}_u\mathcal{H}_d)$, which filters SUSY breaking effects into our matter fields. This operator must be verboten or Λ must be large.

We could also use R-symmetry. Since each of the terms in the superpotential would need to have R-charge 2, terms like $\frac{1}{\Lambda^4} Q\bar{u}(\phi\mathcal{H}_u)(\Delta\mathcal{H}_u\mathcal{H}_d)$ would not be allowed. Depending on the choice of charge and field content other higher order operators may be forbidden as well. In this process we have seen that dangerous operators will often arise when trying to work at the nonrenormalizable level. Assuming these operators are suppressed, we now move to analyzing the phenomenology of these models.

An example

For the nonrenormalizable Yukawa couplings of Eq. (4.21), let $\langle\phi\rangle = v_\phi \hat{e}$, where $\hat{e}$ is a normalized vector in the $\vec{\phi}$ vacuum direction. The Higgs fields can be expanded in terms of this direction

$$W \supset \frac{v_\phi}{\Lambda} Q_m^T Y_u \bar{u}_m \sum_i \hat{e}_i \mathcal{H}_{ui} + \frac{v_\phi}{\Lambda} Q_m^T Y_d \bar{d}_m \sum_i \hat{e}_i \mathcal{H}_{di} + \frac{v_\phi}{\Lambda} L_m^T Y_e \bar{e}_m \sum_i \hat{e}_i \mathcal{H}_{di}, \tag{4.23}$$

and rotated into mass eigenstates

$$W \supset \frac{v_\phi}{\Lambda} Q_m^T Y_u \bar{u}_m \left(\sum_i \hat{e}_i \mathcal{R}_{ui1} H_u + \sum_{ij} \hat{e}_i \mathcal{R}_{uij} M_{uj} \right) + \text{Down Quarks and Leptons.} \tag{4.24}$$

The sums are equivalent up to a multiplicative factor, so if we define $Y_u' = \frac{v_\phi}{\Lambda} Y_u \sum_i \hat{e}_i \mathcal{R}_{ui1}$,

$$W \supset Q_m^T Y_u' \bar{u}_m \left(H_u + \sum_j \lambda_{uj} M_{uj} \right) + \text{Down Quarks and Leptons}, \tag{4.25}$$

where the $\lambda_{uj} = \frac{\sum_i \hat{e}_i \mathcal{R}_{uij}}{\sum_i \hat{e}_i \mathcal{R}_{ui1}} = \mathcal{O}(1)$. If we use a Higgs sector like Eq. (4.14), and if the mass matrix is symmetric, then these order one numbers will be the same for each family. The structure of the Higgs messenger-sector did not influence the couplings because the vacuum direction of ϕ is not modeled and so we can only schematically parameterize the couplings.

This setup is very similar to that explored in Refs. [7–9, 11, 12, 14, 15]. In these references, they introduce a single third generation messenger coupling which can generate large A terms for the third generation and a sizable mass splitting for the left- and right-handed scalars though the two loop messenger-matter mixing corrections, leading to a large one loop contribution to the Higgs mass. Their goal was to generate light stops through the interplay of the guage-Yukawa terms in the messenger corrections. For a single messenger Higgs, the corrections look schematically like

$$\delta\tilde{m}^2 \propto ay^4 - bg^2y^2 \tag{4.26}$$

where a and b are coefficients. If the gauge contribution were larger, the correction would be negative, splitting the third generation from the first two generations.

If we work with the symmetric Higgs sector as given in Eq. (4.16), we can accommodate different values for μ and B_μ. In this setup, there are two heavy messenger doublets and so there will be additional messenger-matter mixing corrections from the couplings of the two messenger Higgs states. These corrections are shown in general in Appendix C. These corrections are positive, lessening the splitting for the third generation. If we assume only third family Yukawa couplings, the corrections

are

$$
\begin{aligned}
\delta\tilde{m}_Q^2 &= \frac{1}{2}\left(\delta\tilde{m}_{\bar{u}}^2 + \delta\tilde{m}_{\bar{d}}^2\right), \\
\delta\tilde{m}_{\bar{u}}^2 &= \frac{\Lambda^2 y_t^2\sigma^2}{128\pi^4}\left(y_b^2\sigma^2 + 6y_t^2(1+\sigma^2) - \frac{13}{15}g_1^2 - 3g_2^2 - \frac{16}{3}g_3^2\right), \\
\delta\tilde{m}_{\bar{d}}^2 &= \frac{\Lambda^2 y_b^2\sigma^2}{128\pi^4}\left(y_t^2\sigma^2 + 6y_b^2(1+\sigma^2) + y_\tau(2+\sigma^2) - \frac{7}{15}g_1^2 - 3g_2^2 - \frac{16}{3}g_3^2\right), \\
\delta\tilde{m}_L^2 &= \frac{1}{2}\delta\tilde{m}_{\bar{e}}^2, \\
\delta\tilde{m}_{\bar{e}}^2 &= \frac{\Lambda^2 y_b^2\sigma^2}{128\pi^4}\left(3y_t^2\sigma^2 + 3y_b^2(2+\sigma^2) + \frac{2}{5}y_\tau(1+2\sigma^2) - \frac{9}{5}g_1^2 - 3g_2^2\right), \\
\delta m_{H_u}^2 &= -3\frac{\Lambda^2}{128\pi^4}y_t^2(3y_t^2 + y_b^2)\sigma^2, \\
\delta m_{H_d}^2 &= -3\frac{\Lambda^2}{128\pi^4}(y_t^2y_b^2 + 3y_b^4 + y_\tau^4)\sigma^2, \\
A_t &= -\frac{\Lambda}{16\pi^2}y_t(y_b^2 + 3y_t^2)\sigma^2, \\
A_b &= -\frac{\Lambda}{16\pi^2}y_b(3y_b^2 + y_t^2)\sigma^2, \\
A_\tau &= -\frac{\Lambda}{16\pi^2}3y_\tau^3\sigma^2,
\end{aligned}
\tag{4.27}
$$

where $\sigma^2 = \lambda_1^2 + \lambda_2^2$. We see that the corrections all scale with σ and for most values of σ these will be negative, leading to a slightly lighter third generation.

We also need to introduce two pairs of $SU(3)$ triplets with mass M_3 and with F term vev F_3 to the theory to preserve anomaly cancellation, gauge coupling, unification, and generate a nonzero gluino mass.

We now analyze the low energy mass spectrum of this model, using SoftSUSY 3.6.2 [22]. We set the mass of the heavy Higgs eigenstate m_2 equal to the triplet mass M_3 and also $f_2 = F_3$ to simplify calculations. Figure 4.1 shows an example spectra for this sort of model with two messenger Higgs equally coupled to matter fields with $m_2 = M_3 = 10^{12}$ GeV, $\Lambda = \frac{F}{M} = 6 \times 10^5$ GeV, and $\tan\beta = 10$, sign(μ)=1 and $\sigma^2 = \frac{1}{2}$. The lightest stop eigenstate is typically lighter than the other colored particles because the A terms are large and the third generation starts split from

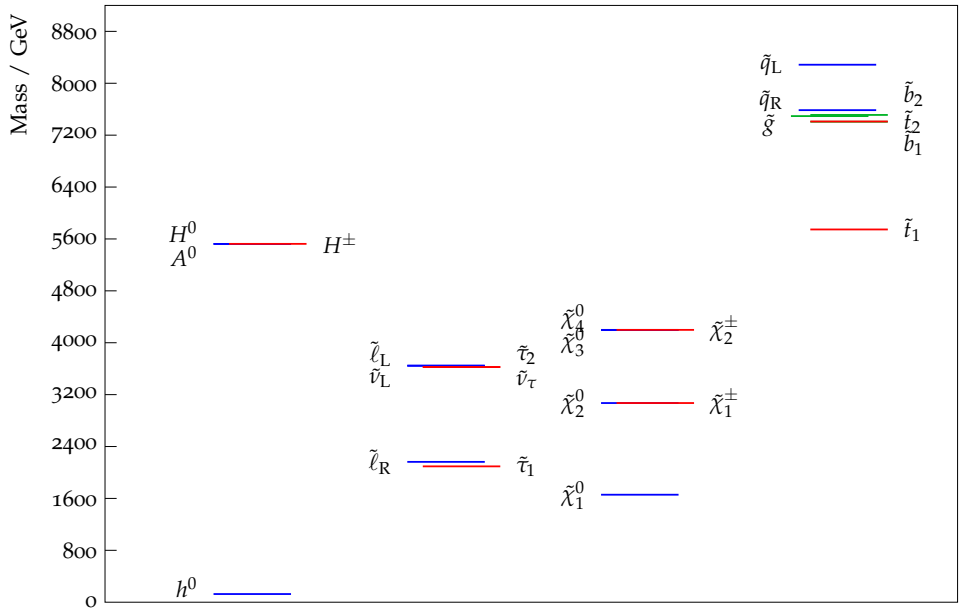

Figure 4.1: A plot of the spectrum for a third family model with $M_2 = M_3 = 10^{12}$ GeV, $\Lambda = 6 \times 10^5$ GeV, and $\tan\beta = 10$, sign(μ)=1 and $\sigma^2 = \frac{1}{2}$.

the first two generations. However, the stops are still heavy and the Higgs mass bolstered by the loop correction and not from mixing, preventing an overall lighter spectrum. Throughout much of the parameter space only the binolike $\tilde{\chi}_1^0$ and right-handed sleptons are likely LHC accessible.

Figures 4.2 and 4.3 shows the effect of increasing and decreasing the various input parameters from the point shown in Fig. 4.1. Increasing (decreasing) Λ moves the entire spectrum up (down). Changing the mass scale M, has a small effect, but leads to lighter and more-mixed stops because μ needs to be larger, to get the Z mass, and A_t is driven more negative lowering the mass of the Higgs. At fixed σ^2 the spectrum gets lighter with increasing M, however at fixed M the σ^2 dependance is complex. For small σ^2 the messenger-matter mixing corrections are small decreasing in size until about $\sigma^2 = 1/2$ and then increasing, until they change sign in the upper left hand corner of Fig. 4.3. When the corrections are largest and there is time to run, the upper left corner, the stops tend to be lighter and mixed.

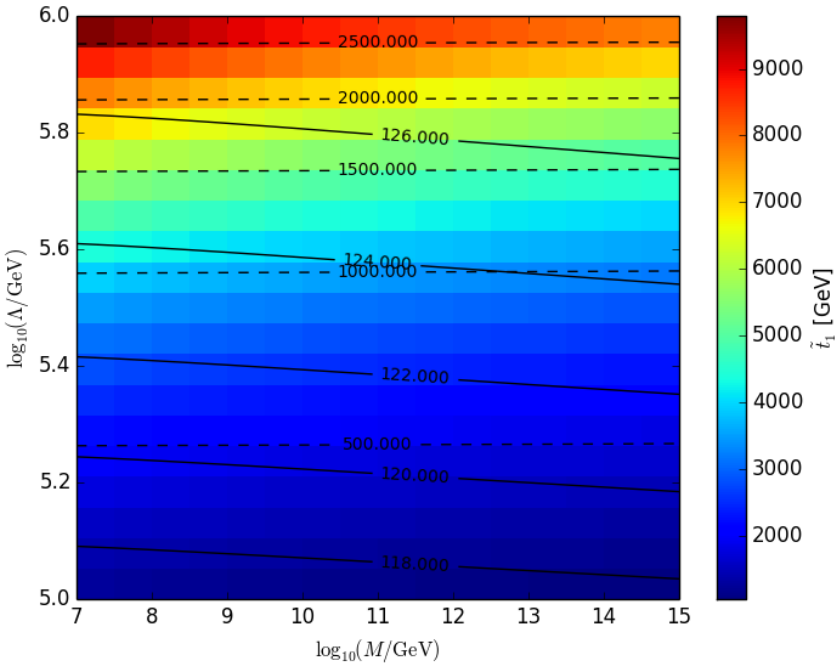

Figure 4.2: A plot of the Higgs, solid contours, and NLSP mass, dashed contours, on top of a distribution of the stop mass as a function of $\log_{10}(\Lambda/\mathrm{GeV})$ and $\log_{10}(M/\mathrm{GeV})$ with $\sigma^2 = \frac{1}{2}$ and $\tan\beta = 10$.

4.5 A Renormalizable Model

Preliminaries

Another way around the problem of the large field range in the nonrenormalizable model is to introduce a renormalizable top quark Yukawa coupling. In this case, the Higgs-messenger multiplets directly talk to matter fields, leveraging the strength of the non-abelian discrete symmetry. Table 4.1 shows the superfield content in a model with $\mathcal{S}_3$. Additional symmetries may need to be introduced to prevent additional messenger-matter couplings like QQT which could lead to FCNCs. The

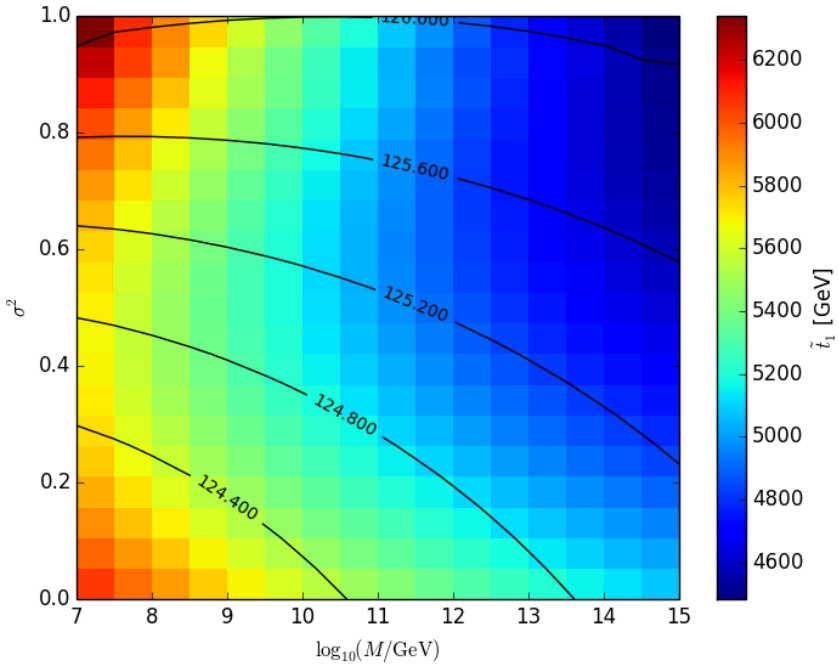

Figure 4.3: A plot of the Higgs, solid contours on top of a distribution of the stop mass as a function of $\log_{10}(M/\mathrm{GeV})$ and σ^2 with $\Lambda = 5 \times 10^5$ GeV and $\tan\beta = 10$.

Higgs sector is given by Eq. (4.16), with eigenvalues

$$\begin{aligned} \frac{m_1}{m} &= 3\kappa + \sqrt{2}\eta, \qquad \frac{f_1}{F} = \eta\sqrt{2}, \\ \frac{m_{2/3}}{m} &= \pm\sqrt{\frac{3}{2}}, \qquad \frac{f_{2/3}}{F} = \pm\sqrt{\frac{3}{2}}, \end{aligned} \tag{4.28}$$

where $\kappa, \eta \ll 1$. The rotation from mass to flavor is

$$\mathcal{R}_{u,d} = \begin{pmatrix} \frac{1}{\sqrt{3}} & \frac{1}{12}\left(\sqrt{3}\eta + \eta - 2\sqrt{3} + 6\right) & \frac{1}{12}\left(\left(\sqrt{3}-1\right)\eta - 2\sqrt{3} - 6\right) \\ \frac{1}{\sqrt{3}} & \frac{1}{12}\left(-\sqrt{3}\eta + \eta - 2\sqrt{3} - 6\right) & \frac{1}{12}\left(-2\sqrt{3} - \left(\sqrt{3}+1\right)\eta + 6\right) \\ \frac{1}{\sqrt{3}} & \frac{1}{\sqrt{3}} - \frac{\eta}{6} & \frac{\eta}{6} + \frac{1}{\sqrt{3}} \end{pmatrix}, \tag{4.29}$$

where H_u is the MSSM-like eigenstates and the M_{ui} are the messengers.

	$\mathcal{H}_{u\mathbf{2}}$	$\mathcal{H}_{u\mathbf{1}}$	$\mathcal{H}_{d\mathbf{2}}$	$\mathcal{H}_{d\mathbf{1}}$	$Q_{\mathbf{2}}$	$Q_{\mathbf{1}}$	$\bar{u}_{\mathbf{2}}$	$\bar{u}_{\mathbf{1}}$	$\bar{d}_{\mathbf{2}}$	$\bar{d}_{\mathbf{1}}$	Δ
$\mathcal{S}_3$	$\mathbf{2}$	$\mathbf{1}$	$\mathbf{2}$	$\mathbf{1}$	$\mathbf{2}$	$\mathbf{1}$	$\mathbf{2}$	$\mathbf{1}$	$\mathbf{2}$	$\mathbf{1}$	$\mathbf{2}$

Table 4.1: Charges for an $\mathcal{S}_3$ model where the Higgs-messenger fields and quarks are broken into doublets and singlets of $\mathcal{S}_3$.

We again introduce two pairs of $SU(3)$ triplets with mass M_3 and with F term vev F_3 to the theory to preserve anomaly cancellation, gauge coupling, unification, and generate a nonzero gluino mass.

If matter fields are charged under $\mathcal{G}_F$ then there will be renormalizable couplings with the messenger-Higgs multiplets. One choice of field content is shown in Table 4.1. The up quark Yukawa couplings are generically

$$\begin{aligned} W_Y &= y_u\Big[(Q_{\mathbf{2}}\bar{u}_{\mathbf{2}}\mathcal{H}_{u\mathbf{2}}) + \beta_1(Q_{\mathbf{2}}\bar{u}_{\mathbf{1}}\mathcal{H}_{u\mathbf{2}}) + \beta_2(Q_{\mathbf{2}}\bar{u}_{\mathbf{2}}\mathcal{H}_{u\mathbf{1}}) \\ &\quad + \beta_3(Q_{\mathbf{1}}\bar{u}_{\mathbf{2}}\mathcal{H}_{u\mathbf{2}}) + \beta_4(Q_{\mathbf{1}}\bar{u}_{\mathbf{1}}\mathcal{H}_{u\mathbf{1}})\Big], \qquad (4.30) \\ &= y_u Q^T \begin{pmatrix} \mathcal{H}_{u\mathbf{2}1} & \beta_1\mathcal{H}_{u\mathbf{1}} & \beta_2\mathcal{H}_{u\mathbf{2}2} \\ \beta_1\mathcal{H}_{u\mathbf{1}} & \mathcal{H}_{u\mathbf{2}2} & \beta_2\mathcal{H}_{u\mathbf{2}1} \\ \beta_3\mathcal{H}_{u\mathbf{2}2} & \beta_3\mathcal{H}_{u\mathbf{2}1} & \beta_4\mathcal{H}_{u\mathbf{1}} \end{pmatrix} \bar{u}, \qquad (4.31) \end{aligned}$$

where $Q = (Q_{\mathbf{2}}, Q_{\mathbf{1}})^T$, with $\bar{u}$ similarly embedded, and the β_i are coefficients. Different UV completions may set some or all of the coefficients in front of the operators equal and we look at these cases in the following sections. We can modify the texture of the Yukawa couplings by change the representations of our fields, but this is equivalent to introducing signs in our coefficients.

The down quarks and charged leptons may have similar operators, which can be suppressed by a Frogatt-Nielsen mechanism. We also note however that we must forbid physics that would generate the Weinberg operator $LHLH$ until after the messengers integrate out, or there would be one loop contributions to neutrino masses.

Equal Couplings

One simple possibility is that all the coefficients in Eq. (4.31) are equal. In this case we have

$$W_Y = y_u Q^T \begin{pmatrix} \mathcal{H}_{u\mathbf{2}1} & \mathcal{H}_{u\mathbf{1}} & \mathcal{H}_{u\mathbf{2}2} \\ \mathcal{H}_{u\mathbf{1}} & \mathcal{H}_{u\mathbf{2}2} & \mathcal{H}_{u\mathbf{2}1} \\ \mathcal{H}_{u\mathbf{2}2} & \mathcal{H}_{u\mathbf{2}1} & \mathcal{H}_{u\mathbf{1}} \end{pmatrix} \bar{u}, \tag{4.32}$$

and we can now rotate to Higgs mass eigenstates using Eq. (4.29)

$$\begin{aligned} W_Y = & \frac{y_u}{\sqrt{3}} Q^T \begin{pmatrix} 1 & 1 & 1 \\ 1 & 1 & 1 \\ 1 & 1 & 1 \end{pmatrix} \bar{u} H_u \\ & + y_u Q^T \begin{pmatrix} \frac{1}{\sqrt{3}} & \frac{1}{6}\left(-\sqrt{3}-3\right) & \frac{1}{12}\left(6-2\sqrt{3}\right) \\ \frac{1}{6}\left(-\sqrt{3}-3\right) & \frac{1}{12}\left(6-2\sqrt{3}\right) & \frac{1}{\sqrt{3}} \\ \frac{1}{12}\left(6-2\sqrt{3}\right) & \frac{1}{\sqrt{3}} & \frac{1}{6}\left(-\sqrt{3}-3\right) \end{pmatrix} \bar{u} M_{u1} \\ & + y_u Q^T \begin{pmatrix} \frac{1}{\sqrt{3}} & \frac{1}{6}\left(3-\sqrt{3}\right) & \frac{1}{6}\left(-\sqrt{3}-3\right) \\ \frac{1}{6}\left(3-\sqrt{3}\right) & \frac{1}{6}\left(-\sqrt{3}-3\right) & \frac{1}{\sqrt{3}} \\ \frac{1}{6}\left(-\sqrt{3}-3\right) & \frac{1}{\sqrt{3}} & \frac{1}{6}\left(3-\sqrt{3}\right) \end{pmatrix} \bar{u} M_{u2}, \end{aligned} \tag{4.33}$$

where η, the ratio of b to F, has been set to zero as its effect will be small. The MSSM-like Higgs Yukawa couplings are diagonalized by the matrix

$$U = \begin{pmatrix} -\frac{1}{\sqrt{6}} & -\frac{1}{\sqrt{2}} & \frac{1}{\sqrt{3}} \\ \sqrt{\frac{2}{3}} & 0 & \frac{1}{\sqrt{3}} \\ -\frac{1}{\sqrt{6}} & \frac{1}{\sqrt{2}} & \frac{1}{\sqrt{3}} \end{pmatrix}. \tag{4.34}$$

This looks the familiar tribimaximal mixing matrix, up to permutations of rows and columns, because the mass matrix preserves a Klein symmetry generated by the S

and U generators of $\mathcal{S}_4$ (see Appendix B for details of $\mathcal{S}_4$). These new couplings are

$$\begin{aligned}
&= y_u Q_m^T \begin{pmatrix} 0 & 0 & 0 \\ 0 & 0 & 0 \\ 0 & 0 & \sqrt{3} \end{pmatrix} \bar{u}_m H_u + \frac{y_u}{4} Q_m^T \begin{pmatrix} \left(\sqrt{3}-3\right) & \left(\sqrt{3}+3\right) & 0 \\ \left(\sqrt{3}+3\right) & \left(3-\sqrt{3}\right) & 0 \\ 0 & 0 & 0 \end{pmatrix} \bar{u}_m M_{u1} \\
&+ \frac{y_u}{4} Q_m^T \begin{pmatrix} \left(\sqrt{3}+3\right) & \left(3-\sqrt{3}\right) & 0 \\ \left(3-\sqrt{3}\right) & \left(-\sqrt{3}-3\right) & 0 \\ 0 & 0 & 0 \end{pmatrix} \bar{u}_m M_{u2}.
\end{aligned} \tag{4.35}$$

We notice that this structure generates one non-zero Yukawa coupling, for the top quark, and messenger Yukawa couplings only for the first two generations. This effective seesaw structure is the result of the flavor symmetry.

The top does not couple to the messengers and so there will not be corrections to the stop masses from messenger-matter mixing. We can calculate the corrections to the soft masses as a function of the Yukawa couplings following [12]. There will be additional corrections because we have two heavy messenger Higgs doublets, these are discussed in Appendix C. The contributions here are all diagonal and at this order and there are no dangerous FCNCs. Let $y_t = \sqrt{3} y_u$ with similar definitions for y_τ and y_b, and the corrections are

$$\begin{aligned}
\delta m_Q^2 &= \frac{1}{2}\left(\delta m_{\bar{u}}^2 + \delta m_{\bar{d}}^2\right), \\
\delta m_{\bar{u}}^2 &= \frac{\Lambda^2}{128\pi^4}\frac{y_t^2}{15}\left(90 y_t^2 + 15 y_b^2 - 13 g_1^2 - 45 g_2^2 - 80 g_3^2\right) \text{Diag}\left[1,1,0\right], \\
\delta m_{\bar{d}}^2 &= \frac{\Lambda^2}{128\pi^4}\frac{y_b^2}{15}\left(90 y_b^2 + 15 y_t^2 + 15 y_\tau^2 - 7 g_1^2 - 45 g_2^2 - 80 g_3^2\right) \text{Diag}\left[1,1,0\right], \\
\delta m_L^2 &= \frac{1}{2}\delta m_{\bar{e}}^2, \\
\delta m_{\bar{e}}^2 &= \frac{\Lambda^2}{128\pi^4}\frac{y_\tau^2}{5}\left(20 y_\tau^2 + 15 y_b^2 - 15 g_2^2 - 9 g_1^2\right) \text{Diag}\left[1,1,0\right], \\
\delta m_{H_u}^2 &= \delta m_{H_u}^2 = A_u = A_d = A_e = 0.
\end{aligned} \tag{4.36}$$

We see that the corrections influence only the first two generations. They are also very likely to be negative for the squarks, pushing the first and second generation

below the third.

This $\mathcal{S}_3$ model is governed by a handful of free parameters: the mass of the two heavy doublets and triplets m_2 and m_3, the ratio of $\Lambda = F/M$ for the doublets and triplets, the small parameters η and κ which gives values to μ and b are replaced as usual by $\tan\beta$, sign(μ), and the Z boson mass. Finally we have the third generation Yukawa couplings. In total we have seven parameters. However, the Yukawa couplings are set at the UV boundary condition by SoftSUSY leaving us a three parameter model with one sign.

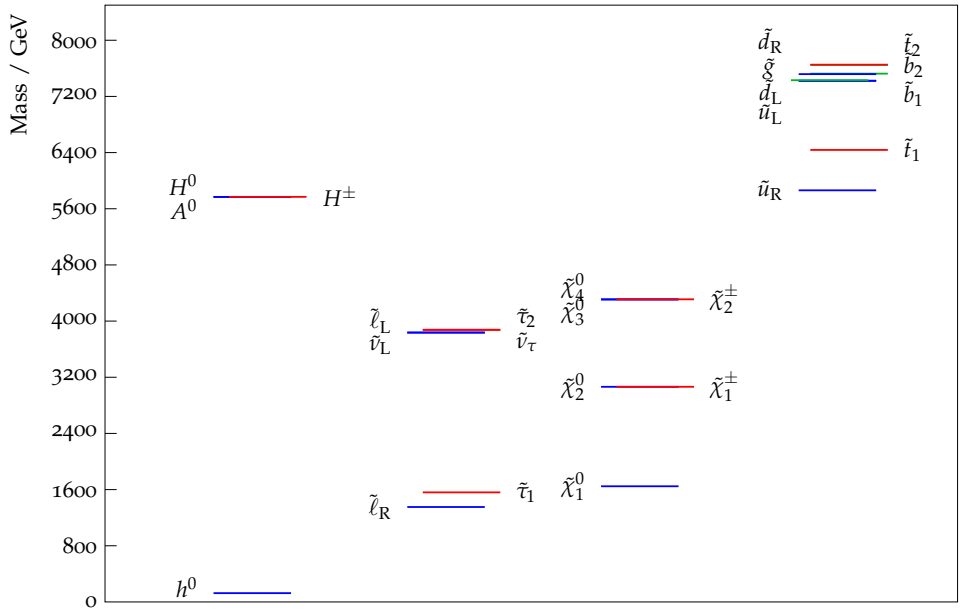

Figure 4.4: A plot of the spectrum for the $\mathcal{S}_3$ model with $M_2 = M_3 = 10^{12}$ GeV, $\Lambda = 6 \times 10^5$, and $\tan\beta = 10$, with sign(μ)=1.

Figure 4.4 is a plot of the spectrum for the $\mathcal{S}_3$ model with $M_2 = M_3 = 10^{12}$ GeV, $\Lambda = 6 \times 10^5$, and $\tan\beta = 10$, and sign(μ)=1. The SM Higgs mass in this model is bolstered by heavy stops, because the A terms are zero. The seesaw structure in the Yukawa couplings is the result of the non-abelian discrete symmetry and prevents generating large messenger and MSSM Yukawas simultaneously, as evidenced by the A terms, proportional to $Y_u Y_u'$, vanishing. The lightest $SU(3)$ charged particle

		Changing M		Changing Λ	
M [GeV]	10^{12}	10^9	10^{15}	10^{12}	
Λ [GeV]	6×10^5	6×10^5		4×10^5	8×10^5
$\tan\beta$	10	10		10	
h [GeV]	125.2	124.8	125.6	123.6	126.3
A^0 [TeV]	5.77	5.17	6.20	3.98	7.52
$\tilde{g}$ [TeV]	7.43	7.45	7.41	5.12	9.68
$\tilde{\chi}_1^0$ [TeV]	1.65	1.65	1.65	1.09	2.20
$\tilde{\chi}_2^0$ [TeV]	3.06	3.08	3.05	2.05	4.07
$\tilde{\chi}_3^0$ [TeV]	4.31	3.85	4.51	3.02	5.54
$\tilde{t}_1$ [TeV]	6.44	6.86	6.14	4.40	8.42
$\tilde{t}_2$ [TeV]	7.62	7.86	7.54	5.24	10.02
$\tilde{u}_R$ [TeV]	5.86	5.62	6.11	4.07	7.59
$\tilde{u}_L$ [TeV]	7.42	7.35	7.54	5.10	9.69
$\tilde{b}_1$ [TeV]	7.52	7.73	7.39	5.17	9.82
$\tilde{b}_2$ [TeV]	7.65	7.86	7.54	5.23	10.02
$\tilde{d}_R$ [TeV]	7.52	7.70	7.40	5.17	9.82
$\tilde{d}_L$ [TeV]	7.42	7.35	7.54	5.10	9.69
$\tilde{\tau}_1$ [TeV]	1.56	1.2	2.24	1.03	2.09
$\tilde{\tau}_2$ [TeV]	3.88	3.49	4.31	2.61	5.13
$\tilde{e}_R$ [TeV]	1.35	0.86	2.13	0.89	1.82
$\tilde{e}_L$ [TeV]	3.84	3.44	4.28	2.59	5.07

Table 4.2: The effect of changing our input parameters in the renormalizable model from the example point with $M_2 = M_3 = 10^{12}$ GeV, $\Lambda = 6 \times 10^5$, and $\tan\beta = 10$, with sign(μ)=1 and shown in Fig. 4.4.

are the right-handed squarks because the corrections deflect the soft mass squares down.

Table 4.2 and Fig. 4.5 show the effect of varying our input parameters. Changing M leaves the colored particles untouched, but moves the leptons up or down. Changing F moves the entire spectrum up or down. In either case, we see that the NLSP will likely be a long lived right-handed slepton. The corrections from messenger matter mixing pushes the smuon and selecton below the stau and because the spectra are split, there are large corrections from the running at large M from the STr(m^2) term in the β function, as illustrated in Fig. 4.5. These models can

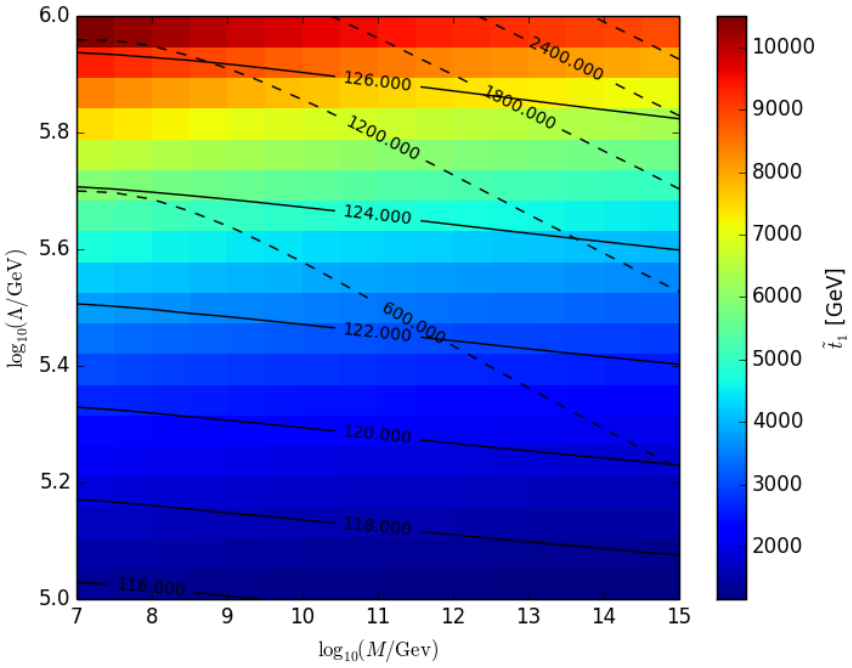

Figure 4.5: A plot of the Higgs, solid contours, and NLSP slectron mass, dashed contours, on top of a distribution of the stop mass as a function of $\log_{10}(\Lambda/\mathrm{GeV})$ and $\log_{10}(M/\mathrm{GeV})$.

be constrained by searches for charged tracks at LHC13 [23]. The lightest neutralino is always binolike and generally near the sleptons.

One interesting aspect of Figs. 4.1 and 4.4 is the mass of colored particles at about 7 TeV. The messenger matter mixing corrections will split the first and second from the third generation in the UV and this difference is somewhat ameliorated as we run towards an IR fixed point. In Ref. [13], they called this IR fixed point "focusing," and found it at low scales because they used a larger messenger scale top coupling than is used here.

Having shown that a model based on $\mathcal{S}_3$ with a renormalizable top can produce realistic spectra, we can notice some deficiencies. The stop is almost always heavy, because the A terms are zero at the high energy boundary condition. We would

also like to generate two different Yukawa couplings for the first two generations and generate $\mathcal{O}(\lambda_C)$ perturbations to the CKM. We can do the former and the latter by loosing the requirement that the couplings in Eq. (4.31) are all identical. A small symmetric perturbation will lead to nonzero Yukawas and a perturbation that is not symmetric will lead to nontrivial rotations. We explore the former and latter in the next subsection.

Perturbations

Nonzero light Yukawa couplings

In the previous section, Eq. (4.31) was assumed to have uniform couplings. In this section we look at the effect of adding a symmetric perturbation. Let $\beta_2 = \beta_3 = 1$, $\beta_1 = \beta_4 = 1 + \sqrt{3}\gamma$ in Eq. (4.31), where γ is a small parameter and the factor of $\sqrt{3}$ and sign are chosen for convenience. The Yukawa couplings are

$$W_Y = y_u Q^T \begin{pmatrix} \mathcal{H}_{u\mathbf{2}1} & (1+\sqrt{3}\gamma)\mathcal{H}_{u\mathbf{1}} & \mathcal{H}_{u\mathbf{2}2} \\ (1+\sqrt{3}\gamma)\mathcal{H}_{u\mathbf{1}} & \mathcal{H}_{u\mathbf{2}2} & \mathcal{H}_{u\mathbf{2}1} \\ \mathcal{H}_{u\mathbf{2}2} & \mathcal{H}_{u\mathbf{2}1} & (1+\sqrt{3}\gamma)\mathcal{H}_{u\mathbf{1}} \end{pmatrix} \bar{u}. \tag{4.37}$$

Running through the same procedure as in the previous section leads to Yukawa couplings for the mass eigenstates of

$$\begin{aligned} W_Y = y_u Q^T \begin{pmatrix} \gamma & 0 & 0 \\ 0 & \gamma & 0 \\ 0 & 0 & \sqrt{3}+\gamma \end{pmatrix} \bar{u} H_u + y_u Q^T \begin{pmatrix} \frac{\sqrt{3}}{2}+\gamma & -\frac{\sqrt{3}}{2} & 0 \\ \frac{\sqrt{3}}{2} & \frac{\sqrt{3}}{2}+\gamma & 0 \\ 0 & 0 & \gamma \end{pmatrix} \bar{u} M_{u1} \\ + y_u Q^T \begin{pmatrix} \frac{\sqrt{3}}{2}+\gamma & \frac{\sqrt{3}}{2} & 0 \\ -\frac{\sqrt{3}}{2} & \frac{\sqrt{3}}{2}+\gamma & 0 \\ 0 & 0 & \gamma \end{pmatrix} \bar{u} M_{u2}. \end{aligned} \tag{4.38}$$

The rotation to mass eigenstates is

$$U = \begin{pmatrix} 0 & \sqrt{\frac{2}{3}} & \frac{1}{\sqrt{3}} \\ -\frac{1}{\sqrt{2}} & -\frac{1}{\sqrt{6}} & \frac{1}{\sqrt{3}} \\ \frac{1}{\sqrt{2}} & -\frac{1}{\sqrt{6}} & \frac{1}{\sqrt{3}} \end{pmatrix}. \tag{4.39}$$

The messenger couplings are linear combinations of those we saw in the previous section, and so the bulk of the corrections to the soft masses will be the same. However, there will now be $\mathcal{O}(\gamma)$ A terms for the first two generations and $\mathcal{O}(\gamma^2)$ corrections to the third generation soft masses, third generation A terms, and Higgs mass squares.

Left handed rotations

Small perturbations away from Eq. (4.32) can also generate nontrivial left- and right-handed rotations. If we let $\beta_3 = \beta_4 = (1 + \sqrt{3}\gamma)$ in Eq. (4.31), with γ small, the Yukawa couplings to the up quarks are

$$W_Y = y_u Q^T \begin{pmatrix} \mathcal{H}_{u\mathbf{2}1} & \mathcal{H}_{u\mathbf{1}} & \mathcal{H}_{u\mathbf{2}2} \\ \mathcal{H}_{u\mathbf{1}} & \mathcal{H}_{u\mathbf{2}2} & \mathcal{H}_{u\mathbf{2}1} \\ (1+\sqrt{3}\gamma)\mathcal{H}_{u\mathbf{2}2} & (1+\sqrt{3}\gamma)\mathcal{H}_{u\mathbf{2}1} & (1+\sqrt{3}\gamma)\mathcal{H}_{u\mathbf{1}} \end{pmatrix} \bar{u}, \tag{4.40}$$

and we can now rotate to Higgs and matter fields to mass eigenstates using Eq. (4.29) and we have

$$
\begin{aligned}
&= \frac{y_u}{\sqrt{3}} Q_m^T \begin{pmatrix} 0 & 0 & 0 \\ 0 & 0 & 0 \\ 0 & 0 & \sqrt{3}+\gamma \end{pmatrix} \bar{u}_m H_u \\
&+ y_u Q_m^T \begin{pmatrix} \frac{1}{4}\left(-\sqrt{3}-3\right)+\frac{1}{8}\gamma\left(5-3\sqrt{3}\right) & \frac{1}{4}\left(\sqrt{3}-3\right)+\frac{1}{8}\gamma\left(-3\sqrt{3}-5\right) & 0 \\ \frac{1}{4}\left(\sqrt{3}-3\right)-\frac{3}{8}\left(\sqrt{3}-1\right)\gamma & \frac{3}{8}\gamma\left(\sqrt{3}+1\right)+\frac{1}{4}\left(\sqrt{3}+3\right) & 0 \\ \sqrt{2-\sqrt{3}\gamma} & \sqrt{\sqrt{3}+2\gamma} & 0 \end{pmatrix} \bar{u}_m M_{u1} \\
&+ y_u Q_m^T \begin{pmatrix} \frac{1}{4}\left(3-\sqrt{3}\right)+\frac{1}{8}\gamma\left(3\sqrt{3}+5\right) & \frac{1}{4}\left(-\sqrt{3}-3\right)+\frac{1}{8}\gamma\left(5-3\sqrt{3}\right) & 0 \\ \frac{1}{4}\left(-\sqrt{3}-3\right)-\frac{3}{8}\left(\sqrt{3}+1\right)\gamma & \frac{1}{4}\left(\sqrt{3}-3\right)-\frac{3}{8}\left(\sqrt{3}-1\right)\gamma & 0 \\ -\sqrt{\sqrt{3}+2\gamma} & \sqrt{2-\sqrt{3}\gamma} & 0 \end{pmatrix} \bar{u}_m M_{u2},
\end{aligned}
\tag{4.41}
$$

where the left-handed rotations are

$$
U = \begin{pmatrix} \frac{5\gamma}{6\sqrt{2}} - \frac{1}{\sqrt{6}} & -\frac{1}{2}\gamma\sqrt{\frac{3}{2}} - \frac{1}{\sqrt{2}} & \frac{1}{\sqrt{3}} - \frac{\gamma}{3} \\ \frac{\gamma}{3\sqrt{2}} + \sqrt{\frac{2}{3}} & 0 & \frac{1}{\sqrt{3}} - \frac{\gamma}{3} \\ -\frac{\gamma}{6\sqrt{2}} - \frac{1}{\sqrt{6}} & \frac{1}{\sqrt{2}} - \frac{1}{2}\sqrt{\frac{3}{2}}\gamma & \frac{2\gamma}{3} + \frac{1}{\sqrt{3}} \end{pmatrix} + \mathcal{O}(\gamma^2). \tag{4.42}
$$

The right-handed rotations are still the tribimaximal mixing matrix, because $\mathbb{Y}_u^\dagger \mathbb{Y}_u$ inherits the Klein symmetry seen in Eq. (4.32), whereas $\mathbb{Y}_u \mathbb{Y}_u^\dagger$ does not.

Calculating the corrections generates $\mathcal{O}(\gamma)$ off-diagonal entries in the left-handed sfermion mass matrices and no corrections to the off-diagonal entries for the right-handed sfermions. This lack of correction to the right-handed soft masses is inherited from the enhanced symmetry of $\mathbb{Y}_u^\dagger \mathbb{Y}_u$

$$
\mathbb{Y}_u^\dagger \mathbb{Y}_u \propto \begin{pmatrix} 1 & 1 & 1 \\ 1 & 1 & 1 \\ 1 & 1 & 1 \end{pmatrix} \tag{4.43}
$$

compared to $\mathbb{Y}_u \mathbb{Y}_u^\dagger$. A terms are generated for the (13) and (23) entries and are suppressed by a factor of γ.

A case of mixed perturbations

We can combine the previous two types of perturbations. If we let $\beta_2 = \beta_3 = \beta_4 = (1+\sqrt{3}\gamma)$ in Eq. (4.31), with γ small, the Yukawa couplings to the up quarks are

$$W_Y = y_u Q^T \begin{pmatrix} \mathcal{H}_{u\mathbf{2}1} & (1+\sqrt{3}\gamma)\mathcal{H}_{u\mathbf{1}} & \mathcal{H}_{u\mathbf{2}2} \\ (1+\sqrt{3}\gamma)\mathcal{H}_{u\mathbf{1}} & \mathcal{H}_{u\mathbf{2}2} & \mathcal{H}_{u\mathbf{2}1} \\ (1+\sqrt{3}\gamma)\mathcal{H}_{u\mathbf{2}2} & (1+\sqrt{3}\gamma)\mathcal{H}_{u\mathbf{2}1} & (1+\sqrt{3}\gamma)\mathcal{H}_{u\mathbf{1}} \end{pmatrix} \bar{u}. \tag{4.44}$$

These Yukawa couplings follow a similar path as the previous two examples. In terms of the mass eigenstates, the couplings are

$$\begin{aligned} W_Y = {} & y_u Q_m^T \begin{pmatrix} \frac{\gamma}{3} & 0 & 0 \\ 0 & \gamma & 0 \\ 0 & 0 & \frac{5\gamma}{3}+\sqrt{3} \end{pmatrix} \bar{u}_m H_u \\ & + y_u Q_m^T \begin{pmatrix} \frac{1}{6}\left(8\gamma+3\sqrt{3}\right) & \gamma+\frac{\sqrt{3}}{2} & -\frac{\gamma}{\sqrt{2}} \\ -\frac{\sqrt{3}}{2} & \gamma+\frac{\sqrt{3}}{2} & \frac{\gamma}{3\sqrt{2}} \\ \frac{\gamma}{\sqrt{2}} & \frac{5\gamma}{3\sqrt{2}} & \frac{2\gamma}{3} \end{pmatrix} \bar{u}_m M_{u1} \\ & + y_u Q_m^T \begin{pmatrix} \gamma+\frac{\sqrt{3}}{2} & -\gamma-\frac{\sqrt{3}}{2} & -\frac{\gamma}{3\sqrt{2}} \\ \frac{\sqrt{3}}{2} & \frac{\sqrt{3}}{2} & -\frac{\gamma}{3\sqrt{2}} \\ \frac{5\gamma}{3\sqrt{2}} & -\frac{5\gamma}{3\sqrt{2}} & 0 \end{pmatrix} \bar{u}_m M_{u2}, \end{aligned} \tag{4.45}$$

with the left-handed rotations

$$U = \begin{pmatrix} -\frac{1}{9}2\gamma\sqrt{2}-\frac{1}{\sqrt{6}} & \frac{1}{\sqrt{2}} & \frac{1}{\sqrt{3}}-\frac{2\gamma}{9} \\ -\frac{1}{9}2\gamma\sqrt{2}-\frac{1}{\sqrt{6}} & -\frac{1}{\sqrt{2}} & \frac{1}{\sqrt{3}}-\frac{2\gamma}{9} \\ \sqrt{\frac{2}{3}}-\frac{2\sqrt{2}\gamma}{9} & 0 & \frac{4\gamma}{9}+\frac{1}{\sqrt{3}} \end{pmatrix} + \mathcal{O}(\gamma^2). \tag{4.46}$$

The off-diagonal corrections to the soft masses will be $\mathcal{O}(\gamma)$ and corrections to the third generation will be $\mathcal{O}(\gamma^2)$.

Discussion

We have seen that the structure of Eq. (4.32) can be perturbed by introducing symmetric perturbations Eq. (4.38), asymmetric perturbations Eq. (4.42), and both Eq. (4.45). In all these cases bounds on flavor observables might be troubling. Here, we run these models using the flavored routines in SoftSUSY [22] for different values of γ, with the same perturbation for every family. We look at two values of γ, $\gamma = 0.1$ and $\gamma = 0.25$, which are chosen to show the effect of a small perturbation and one that is slightly larger $\mathcal{O}(\sin\theta_c)$, where θ_c is the Cabibbo angle.

Table 4.3 shows the effects of these perturbations. In all these cases, the mass of the uncolored particles is roughly unchanged. For a perturbation like Eq. (4.38), which induces Yukawa couplings for the first two generations, increasing the size of the perturbation shifts the entire spectrum up. There is some splitting between the lightest two up-type eigenstates this is typically on the order of 100 GeV. If we have nontrivial left-handed rotations, this splitting becomes negligible, and the spectrum looks otherwise unperturbed. Finally, if we mix the two sorts of perturbations, the splitting between the lightest two states is smaller for $\gamma = 0.1$ and larger for $\gamma = 0.25$ than for the case with just a symmetric perturbation, but otherwise similar. In these cases, we see that perturbing the Yukawa structure, does not fundamentally affect the sparticle spectrum.

One potential problem is the presence of dangerous flavor changing neutral currents. One way to quantify this assertion is to work in terms of the mass insertion approximation [24–27]. In this approximation, we define

$$(\delta^q_{ij})_{MM} \propto \frac{\Delta\tilde{m}^2_{ji}}{\tilde{m}^2_q}, \tag{4.47}$$

where $\Delta\tilde{m}^2_{ji} = \tilde{m}^2_{q_j} - \tilde{m}^2_{q_i}$, $\tilde{m}^2_q$ is the averaged squark mass squared, M labels the chirality, and the constants of proportionality are combinations of mixing angles and phases of the super-CKM matrix and most $\mathcal{O}(1)$ numbers. The constraints on these insertions are tightest between the first two generations of squarks $|(\delta^d_{12})_{MM}| < 0.07\frac{\tilde{m}_q}{1\,\text{TeV}}$ and $|(\delta^u_{12})_{MM}| < 0.1\frac{\tilde{m}_q}{1\,\text{TeV}}$ [17, 28, 29]. In these models, the mass differences

between the up squarks is at most 10% and since the squarks in these models are typically ~ 5 TeV, the bounds loosen because they scale with squark mass. In general, FCNCs are not problematic for the small perturbations we are working with.

		Nonzero y_c		Nontrivial CKM		Mixed	
M [GeV]	10^{12}	10^{12}		10^{12}		10^{12}	
Λ [GeV]	6×10^5	6×10^6		6×10^6		6×10^6	
$\tan\beta$	10	10		10		10	
γ		0.1	0.25	0.1	0.25	0.1	0.25
h [GeV]	125.2	125.7	125.5	125.7	126.6	126.0	126.6
A^0 [TeV]	5.78	5.80	5.92	5.78	5.78	5.79	5.80
$\tilde{g}$ [TeV]	7.43	7.43	7.45	7.43	7.43	7.43	7.43
$\tilde{\chi}_1^0$ [TeV]	1.65	1.65	1.65	1.65	1.65	1.65	1.65
$\tilde{\chi}_2^0$ [TeV]	3.06	3.06	3.07	3.06	3.06	3.06	3.06
$\tilde{\chi}_3^0$ [TeV]	4.31	4.36	4.54	4.32	4.33	4.33	4.36
$\tilde{u}_1$ [TeV]	5.86	5.85	6.16	5.87	5.86	5.84	5.83
$\tilde{u}_2$ [TeV]	5.86	5.95	6.27	5.87	5.86	5.89	5.95
$\tilde{u}_3$ [TeV]	6.43	6.43	6.48	6.43	6.43	6.43	6.45
$\tilde{d}_1$ [TeV]	7.41	7.41	7.52	7.37	7.37	7.38	7.28
$\tilde{d}_2$ [TeV]	7.42	7.46	7.52	7.46	7.47	7.46	7.52
$\tilde{d}_3$ [TeV]	7.52	7.51	7.53	7.52	7.52	7.52	7.53
$\tilde{e}_1$ [TeV]	1.48	1.48	1.62	1.48	1.48	1.48	1.49
$\tilde{e}_2$ [TeV]	1.48	1.49	1.65	1.48	1.48	1.48	1.50
$\tilde{e}_3$ [TeV]	1.56	1.58	1.73	1.56	1.56	1.56	1.57

Table 4.3: The effect of perturbing the structure of Eq. (4.35) by introducing symmetric, asymmetric, or both sorts of perturbations. The first column is the point with $M_2 = M_3 = 10^{12}$ GeV, $\Lambda = 6 \times 10^5$, and $\tan\beta = 10$, with sign(μ)=1 and shown in Fig. 4.4, there is a slight $< 5\%$ difference in the values of this column compared to Fg. 4.2 because we are using different SoftSUSY routines, which incorporate flavor.

We can of course mix and match different perturbations in the up, down, and charged lepton sectors. In any combination, the structure of the off-diagonal entries will be the same as the most perturbed sector, so if the down quarks are like Eq. (4.44) and the up quark couplings are like Eq. (4.32), the up quarks will inherit the same

structure of off-diagonal entries as the down quark sector. These off-diagonal entries as we have seen will be small and will not lead to excessive flavor violation.

However, the Yukawa structures we examined here do not lead to sufficiently hierarchical structures in the CKM. All the off-diagonal entries will be at the same order in the small parameters and so we cannot generate $\mathcal{O}(\lambda)$ entries without generating other large elements. For example, if both the up and down quarks only have the left-handed perturbations Eq. (4.42), the CKM is proportional to

$$U_{\text{CKM}} \propto \begin{pmatrix} 1 & \gamma_u - \gamma_d & \gamma_u - \gamma_d \\ \gamma_u - \gamma_d & 1 & \gamma_u - \gamma_d \\ \gamma_u - \gamma_d & \gamma_u - \gamma_d & 1 \end{pmatrix}, \tag{4.48}$$

where γ_u and γ_d are the small parameters in the up and down sector, respectively. Mixing perturbations, like using Eq. (4.46) in the up quarks and Eq. (4.42) in the down quarks, results in large off-diagonal entries,

$$U_{\text{CKM}} \propto \begin{pmatrix} -\frac{\sqrt{3}}{2}\gamma_d & -\frac{4\gamma_u+3\gamma_d}{6\sqrt{3}} & 1 \\ 1 & -\frac{4\gamma_u+3\gamma_d}{6\sqrt{3}} & \frac{\sqrt{3}}{2}\gamma_d \\ \frac{1}{18}\left(3\sqrt{3}\gamma_d + 4\gamma_u\sqrt{3}\right) & 1 & \frac{1}{18}\left(3\sqrt{3}\gamma_d + 4\gamma_u\sqrt{3}\right) \end{pmatrix}, \tag{4.49}$$

and so is verboten.

4.6 Conclusions

We have seen that a horizontal symmetry coupling the SU(2) messengers of gauge mediation to the Higgs doublets of the MSSM, can lead to toy models that can yield acceptable Higgs masses and phenomenology. Within $\mathcal{S}_3$ with three pairs of Higgs doublets, two become the heavy messengers and the remaining pair become the MSSM-like Higgs doublets. The MSSM-like and matter Yukawa couplings are nontrivially related, allowing one to model both sets of couplings simultaneously. These couplings generate additional messenger-matter mixing contributions and so there will be nontrivial correlation in the masses. μ and B_μ may also be separately

tuned to small values.

We also saw that viable models can be constructed when the messenger-Higgs multiplet is coupled at nonrenormalizable or renormalizable levels. In the nonrenormalizable case, the model is quite a bit like FGM; however, additional messengers push us towards a heavier spectrum. In the renormalizable case, we saw different spectra with long-lived sleptons and relatively light right-handed up-type squarks. These renormalizable models can be perturbed to generate nontrivial mixing without FCNC constraints, but with some difficulty getting CKM-like structure signifying in general the difficulty of needing to fully address the SM fermion mass puzzle in this approach.

There are a number of open questions and ways forward within this framework. Within a complete flavor model for the quarks, we could look at how promoting the Higgs fields to a messenger-Higgs group will affect the spectrum. This will result in off-diagonal entries with nontrivial CP phases in the sparticle mass squares and A terms. We could also develop a renormalizable flavor model with Cabibbo sized entries in the CKM matrix and first and second generation Yukawa couplings. Finally we may also be motivated to look at larger groups like $\mathcal{S}_4$ or $\Delta(96)$, or non-minimal matter content like in the 4HDM. Any of these directions will utilize the rich structure of non-abelian discrete symmetry to connect the messengers and Higgs fields, and thus yield concrete predictions of messenger-MSSM Yukawa couplings that must be put up against experimental limits.

References

[1] G. F. Giudice and R. Rattazzi, Phys. Rept. **322**, 419 (1999), arXiv:hep-ph/9801271 [hep-ph].

[2] P. Draper, P. Meade, M. Reece, and D. Shih, Phys. Rev. **D85**, 095007 (2012), arXiv:1112.3068 [hep-ph].

[3] A. Arbey, M. Battaglia, A. Djouadi, F. Mahmoudi, and J. Quevillon, Phys. Lett. **B708**, 162 (2012), arXiv:1112.3028 [hep-ph].

[4] M. A. Ajaib, I. Gogoladze, F. Nasir, and Q. Shafi, Phys. Lett. **B713**, 462 (2012), arXiv:1204.2856 [hep-ph].

[5] M. Dine, Y. Nir, and Y. Shirman, Phys. Rev. **D55**, 1501 (1997), arXiv:hep-ph/9607397 [hep-ph].

[6] Z. Chacko and E. Ponton, Phys. Rev. **D66**, 095004 (2002), arXiv:hep-ph/0112190 [hep-ph].

[7] Y. Shadmi and P. Z. Szabo, JHEP **06**, 124 (2012), arXiv:1103.0292 [hep-ph].

[8] J. L. Evans, M. Ibe, and T. T. Yanagida, Phys. Lett. **B705**, 342 (2011), arXiv:1107.3006 [hep-ph].

[9] Z. Kang, T. Li, T. Liu, C. Tong, and J. M. Yang, Phys. Rev. **D86**, 095020 (2012), arXiv:1203.2336 [hep-ph].

[10] N. Craig, S. Knapen, D. Shih, and Y. Zhao, JHEP **03**, 154 (2013), arXiv:1206.4086 [hep-ph].

[11] A. Albaid and K. S. Babu, Phys. Rev. **D88**, 055007 (2013), arXiv:1207.1014 [hep-ph].

[12] M. Abdullah, I. Galon, Y. Shadmi, and Y. Shirman, JHEP **06**, 057 (2013), arXiv:1209.4904 [hep-ph].

[13] M. J. Pérez, P. Ramond, and J. Zhang, Phys. Rev. **D87**, 035021 (2013), arXiv:1209.6071 [hep-ph].

[14] P. Byakti and T. S. Ray, JHEP **05**, 055 (2013), arXiv:1301.7605 [hep-ph].

[15] J. A. Evans and D. Shih, JHEP **08**, 093 (2013), arXiv:1303.0228 [hep-ph].

[16] L. Calibbi, P. Paradisi, and R. Ziegler, JHEP **06**, 052 (2013), arXiv:1304.1453 [hep-ph].

[17] I. Galon, G. Perez, and Y. Shadmi, JHEP **09**, 117 (2013), arXiv:1306.6631 [hep-ph].

[18] W. Fischler and W. Tangarife, JHEP **05**, 151 (2014), arXiv:1310.6369 [hep-ph].

[19] C. D. Froggatt and H. B. Nielsen, Nucl. Phys. **B147**, 277 (1979).

[20] G. R. Dvali, G. F. Giudice, and A. Pomarol, Nucl. Phys. **B478**, 31 (1996), arXiv:hep-ph/9603238 [hep-ph].

[21] K. Agashe and M. Graesser, Nucl. Phys. **B507**, 3 (1997), arXiv:hep-ph/9704206 [hep-ph].

[22] B. C. Allanach, Comput. Phys. Commun. **143**, 305 (2002), arXiv:hep-ph/0104145 [hep-ph].

[23] J. L. Feng, S. Iwamoto, Y. Shadmi, and S. Tarem, JHEP **12**, 166 (2015), arXiv:1505.02996 [hep-ph].

[24] F. Gabbiani and A. Masiero, Nucl. Phys. **B322**, 235 (1989).

[25] J. S. Hagelin, S. Kelley, and T. Tanaka, Nucl. Phys. **B415**, 293 (1994).

[26] F. Gabbiani, E. Gabrielli, A. Masiero, and L. Silvestrini, Nucl. Phys. **B477**, 321 (1996), arXiv:hep-ph/9604387 [hep-ph].

[27] G. Raz, Phys. Rev. **D66**, 037701 (2002), arXiv:hep-ph/0205310 [hep-ph].

[28] G. Isidori, Y. Nir, and G. Perez, Ann. Rev. Nucl. Part. Sci. **60**, 355 (2010), arXiv:1002.0900 [hep-ph].

[29] N. Ierushalmi, S. Iwamoto, G. Lee, V. Nepomnyashy, and Y. Shadmi, (2016), arXiv:1603.02637 [hep-ph].

5 CONCLUSION

We have explored the phenomenology of two non-minimal models of supersymmetry breaking. We have seen that for DMM, the large parameter space opens up previously forbidden avenues with low fine-tuning and new collider phenomenology, and that it can serve as a UV-completion for simplified or compressed spectra. We have also developed tools for looking at models flavored gauge mediation with a non-abelian discrete symmetry. We have seen that these models force us to model the messenger and MSSM Yukawa couplings simultaneously. These models point the way towards new flavor models incorporating both supersymmetry and flavor symmetry breaking, with predictive and nontrivial correlations within the supersymmetric spectrum.

A ANOMALOUS DIMENSIONS

At one loop, the anomalous dimensions are given by

$$\gamma_i = 2\sum_a g_a^2 c_a(\Phi_i) - \frac{1}{2}\sum_{lm} |y_{ilm}|^2, \tag{A.1}$$

in which c_a is the quadratic Casimir, and y_{ilm} are the normalized Yukawa couplings. Here we will consider only the Yukawa couplings of the third generation y_t, y_b, and y_τ. For the MSSM fields Q, U^c, D^c, L, E^c, H_u and H_d, the anomalous dimensions are

$$\begin{aligned}
\gamma_{Q,i} &= \frac{8}{3}g_3^2 + \frac{3}{2}g_2^2 + \frac{1}{30}g_1^2 - (y_t^2 + y_b^2)\delta_{i3}, \\
\gamma_{U,i} &= \frac{8}{3}g_3^2 + \frac{8}{15}g_1^2 - 2y_t^2\delta_{i3}, \\
\gamma_{D,i} &= \frac{8}{3}g_3^2 + \frac{2}{15}g_1^2 - 2y_b^2\delta_{i3}, \\
\gamma_{L,i} &= \frac{3}{2}g_2^2 + \frac{3}{10}g_1^2 - y_\tau^2\delta_{i3}, \\
\gamma_{E,i} &= \frac{6}{5}g_1^2 - 2y_\tau^2\delta_{i3}, \\
\gamma_{H_u} &= \frac{3}{2}g_2^2 + \frac{3}{10}g_1^2 - 3y_t^2, \\
\gamma_{H_d} &= \frac{3}{2}g_2^2 + \frac{3}{10}g_1^2 - 3y_b^2 - y_\tau^2,
\end{aligned} \tag{A.2}$$

respectively. Above M_{mess}, the beta function of the gauge couplings changes because of the messenger fields. However, γ_i does not change according to Eq. (A.1), and hence $\gamma_i' = \gamma_i$. The $\dot{\gamma}_i$'s are given by the expression

$$\dot{\gamma}_i = 2\sum_a g_a^4 b_a c_a(\Phi_i) - \sum_{lm} |y_{ilm}|^2 b_{y_{ilm}}, \tag{A.3}$$

in which $b_{y_{ilm}}$ is the beta function for the Yukawa coupling y_{ilm}. The $\dot{\gamma}_i$'s are given by

$$\begin{aligned}
\dot{\gamma}_{Q,i} &= \frac{8}{3}b_3 g_3^4 + \frac{3}{2}b_2 g_2^4 + \frac{1}{30}b_1 g_1^4 - (y_t^2 b_t + y_b^2 b_b)\delta_{i3}, \\
\dot{\gamma}_{U,i} &= \frac{8}{3}b_3 g_3^4 + \frac{8}{15}b_1 g_1^4 - 2y_t^2 b_t \delta_{i3}, \\
\dot{\gamma}_{D,i} &= \frac{8}{3}b_3 g_3^4 + \frac{2}{15}b_1 g_1^4 - 2y_b^2 b_b \delta_{i3}, \\
\dot{\gamma}_{L,i} &= \frac{3}{2}b_2 g_2^4 + \frac{3}{10}b_1 g_1^4 - y_\tau^2 b_\tau \delta_{i3}, \\
\dot{\gamma}_{E,i} &= \frac{6}{5}b_1 g_1^4 - 2y_\tau^2 b_\tau \delta_{i3}, \\
\dot{\gamma}_{H_u} &= \frac{3}{2}b_2 g_2^4 + \frac{3}{10}b_1 g_1^4 - 3y_t^2 b_t, \\
\dot{\gamma}_{H_d} &= \frac{3}{2}b_2 g_2^4 + \frac{3}{10}b_1 g_1^4 - 3y_b^2 b_b - y_\tau^2 b_\tau,
\end{aligned} \tag{A.4}$$

where $b_t = 6y_t^2 + y_b^2 - \frac{16}{3}g_3^2 - 3g_2^2 - \frac{13}{15}g_1^2$, $b_b = y_t^2 + 6y_b^2 + y_\tau^2 - \frac{16}{3}g_3^2 - 3g_2^2 - \frac{7}{15}g_1^2$, and $b_\tau = 3y_b^2 + 4y_\tau^2 - 3g_2^2 - \frac{9}{5}g_1^2$. $\dot{\gamma}_i'$ is obtained by replacing b_a with $b_a' = b_a + N$ in Eq. (A.4).

Finally, θ_i, which appears in the mixed modulus-anomaly term in the soft scalar mass-squared parameters, is given by

$$\theta_i = 4\sum_a g_a^2 c_a(Q_i) - \sum_{i,j,k} |y_{ijk}|^2 (3 - n_i - n_j - n_k). \tag{A.5}$$

For the MSSM fields, they take the form

$$\theta_{Q,i} = \frac{16}{3}g_3^2 + 3g_2^2 + \frac{1}{15}g_1^2 - 2(y_t^2(3 - n_{H_u} - n_Q - n_U) + y_b^2(3 - n_{H_d} - n_Q - n_D))\delta_{i3},$$
$$\theta_{U,i} = \frac{16}{3}g_3^2 + \frac{16}{15}g_1^2 - 4y_t^2(3 - n_{H_u} - n_Q - n_U)\delta_{i3},$$
$$\theta_{D,i} = \frac{16}{3}g_3^2 + \frac{4}{15}g_1^2 - 4y_b^2(3 - n_{H_d} - n_Q - n_D)\delta_{i3},$$
$$\theta_{L,i} = 3g_2^2 + \frac{3}{5}g_1^2 - 2y_\tau^2(3 - n_{H_d} - n_L - n_E)\delta_{i3},$$
$$\theta_{E,i} = \frac{12}{5}g_1^2 - 4y_\tau^2(3 - n_{H_d} - n_L - n_E)\delta_{i3},$$
$$\theta_{H_u} = 3g_2^2 + \frac{3}{5}g_1^2 - 6y_t^2(3 - n_{H_u} - n_Q - n_U),$$
$$\theta_{H_d} = 3g_2^2 + \frac{3}{5}g_1^2 - 6y_b^2(3 - n_{H_d} - n_Q - n_D) - 2y_\tau^2(3 - n_{H_d} - n_L - n_E).$$

(A.6)

As in the case of γ_i, θ_i' is the same as θ_i.

$\mathcal{S}_3$ is the permutation group with three objects, and the smallest non-abelian group, with presentation

$$\langle S, T | S^2 = T^3 = 1, (ST)^3 = 1 \rangle. \tag{B.1}$$

It has two singlets $\mathbf{1}$ and $\mathbf{1}'$ and a doublet $\mathbf{2}$. The irreducible representations are

$$\begin{aligned} &\mathbf{1} : S = 1, T = 1, \\ &\mathbf{1}' : S = -1, T = 1, \\ &\mathbf{2} : S = \begin{pmatrix} 0 & 1 \\ 1 & 0 \end{pmatrix}, T = \begin{pmatrix} \omega & 0 \\ 0 & \omega^2 \end{pmatrix} \end{aligned} \tag{B.2}$$

where $\omega = e^{\frac{2\pi i}{3}}$. The Kronecker products are

$$\begin{aligned} &\mathbf{1} \otimes \mathbf{1}' = \mathbf{1}', \\ &\mathbf{1}' \otimes \mathbf{2} = \mathbf{2}, \\ &\mathbf{2} \otimes \mathbf{2} = \mathbf{1} \oplus \mathbf{1}' \oplus \mathbf{2}. \end{aligned} \tag{B.3}$$

and Clebsch-Gordan coefficients are

$$\begin{aligned} x_{\mathbf{1}} \otimes \begin{pmatrix} \alpha_1 \\ \alpha_2 \end{pmatrix} &= \begin{pmatrix} x_{\mathbf{1}} \alpha_1 \\ x_{\mathbf{1}} \alpha_2 \end{pmatrix}, \\ x_{\mathbf{1}'} \otimes \begin{pmatrix} \alpha_1 \\ \alpha_2 \end{pmatrix} &= \begin{pmatrix} -x_{\mathbf{1}'} \alpha_1 \\ x_{\mathbf{1}'} \alpha_2 \end{pmatrix}, \\ \begin{pmatrix} \alpha_1 \\ \alpha_2 \end{pmatrix} \otimes \begin{pmatrix} \beta_1 \\ \beta_2 \end{pmatrix} &= (\alpha_1 \beta_2 + \alpha_2 \beta_1)_{\mathbf{1}} \oplus (\alpha_1 \beta_2 - \alpha_2 \beta_1)_{\mathbf{1}'} \oplus \begin{pmatrix} \alpha_2 \beta_2 \\ \alpha_1 \beta_1 \end{pmatrix}. \end{aligned} \tag{B.4}$$

$\mathcal{S}_4$ is the permutation group of four objects, with presentation

$$\langle S,T,U|S^2=T^3=U^2=(ST)^3=(SU)^2=(SU)^2=(STU)^4=1\rangle \tag{B.5}$$

It has two singlets $\mathbf{1}$ and $\mathbf{1}'$, a doublet $\mathbf{2}$, and two triplets $\mathbf{3}$ and $\mathbf{3}'$. The irreducible representations are

$$\begin{aligned}
&\mathbf{1},\mathbf{1}': S=1, T=1, U=\pm 1,\\
&\mathbf{2}: S=\begin{pmatrix}1&0\\0&1\end{pmatrix}, T=\begin{pmatrix}\omega&0\\0&\omega^2\end{pmatrix}, U=\begin{pmatrix}0&1\\1&0\end{pmatrix},\\
&\mathbf{3},\mathbf{3}': S=\frac{1}{3}\begin{pmatrix}-1&2&2\\2&-1&2\\2&2&-1\end{pmatrix}, T=\begin{pmatrix}1&0&0\\0&\omega^2&0\\0&0&\omega\end{pmatrix}, U=\mp\begin{pmatrix}1&0&0\\0&0&1\\0&1&0\end{pmatrix}.
\end{aligned} \tag{B.6}$$

The Kronecker products are

$$\begin{aligned}
\mathbf{1}\otimes\mathbf{1}'&=\mathbf{1}',\\
\mathbf{1}'\otimes\mathbf{2}&=\mathbf{2},\\
\mathbf{1}\otimes\mathbf{3}'&=\mathbf{3}'\\
\mathbf{1}'\otimes\mathbf{3}&=\mathbf{3}'\\
\mathbf{1}'\otimes\mathbf{3}'&=\mathbf{3}\\
\mathbf{2}\otimes\mathbf{2}&=\mathbf{1}\oplus\mathbf{1}'\oplus\mathbf{2}\\
\mathbf{2}\otimes\mathbf{3}&=\mathbf{3}\oplus\mathbf{3}'\\
\mathbf{2}\otimes\mathbf{3}'&=\mathbf{3}\oplus\mathbf{3}'\\
\mathbf{3}\otimes\mathbf{3}&=\mathbf{1}\oplus\mathbf{2}\oplus\mathbf{3}\oplus\mathbf{3}'\\
\mathbf{3}\otimes\mathbf{3}'&=\mathbf{1}'\oplus\mathbf{2}\oplus\mathbf{3}\oplus\mathbf{3}'\\
\mathbf{3}'\otimes\mathbf{3}'&=\mathbf{1}\oplus\mathbf{2}\oplus\mathbf{3}\oplus\mathbf{3}'.
\end{aligned} \tag{B.7}$$

The Clebsch-Gordan coefficients are

$$
\begin{aligned}
x_{\mathbf{1}} \otimes \begin{pmatrix}\alpha_1\\ \alpha_2\end{pmatrix} &= \begin{pmatrix}x_{\mathbf{1}}\alpha_1\\ x_{\mathbf{1}}\alpha_2\end{pmatrix},\\
x_{\mathbf{1'}} \otimes \begin{pmatrix}\alpha_1\\ \alpha_2\end{pmatrix} &= \begin{pmatrix}x_{\mathbf{1'}}\alpha_1\\ -x_{\mathbf{1'}}\alpha_2\end{pmatrix},\\
x_{\mathbf{1}} \otimes \begin{pmatrix}\alpha_1\\ \alpha_2\\ \alpha_3\end{pmatrix}_{\mathbf{3}} &= \begin{pmatrix}x_{\mathbf{1}}\alpha_1\\ x_{\mathbf{1}}\alpha_2\\ x_{\mathbf{1}}\alpha_3\end{pmatrix}_{\mathbf{3}},\\
x_{\mathbf{1}} \otimes \begin{pmatrix}\alpha_1\\ \alpha_2\\ \alpha_3\end{pmatrix}_{\mathbf{3'}} &= \begin{pmatrix}x_{\mathbf{1}}\alpha_1\\ x_{\mathbf{1}}\alpha_2\\ x_{\mathbf{1}}\alpha_3\end{pmatrix}_{\mathbf{3'}},\\
x_{\mathbf{1'}} \otimes \begin{pmatrix}\alpha_1\\ \alpha_2\\ \alpha_3\end{pmatrix}_{\mathbf{3}} &= \begin{pmatrix}x_{\mathbf{1'}}\alpha_1\\ x_{\mathbf{1'}}\alpha_2\\ x_{\mathbf{1'}}\alpha_3\end{pmatrix}_{\mathbf{3'}},\\
x_{\mathbf{1'}} \otimes \begin{pmatrix}\alpha_1\\ \alpha_2\\ \alpha_3\end{pmatrix}_{\mathbf{3'}} &= \begin{pmatrix}x_{\mathbf{1'}}\alpha_1\\ x_{\mathbf{1'}}\alpha_2\\ x_{\mathbf{1'}}\alpha_3\end{pmatrix}_{\mathbf{3}},\\
\begin{pmatrix}\alpha_1\\ \alpha_2\end{pmatrix} \otimes \begin{pmatrix}\beta_1\\ \beta_2\end{pmatrix} &= (a\beta_2 + b\beta_1)_{\mathbf{1}} \oplus (\alpha_1\beta_2 - \alpha_2\beta_1)_{\mathbf{1'}} \oplus \begin{pmatrix}\alpha_2\beta_2\\ \alpha_1\beta_1\end{pmatrix},\\
\begin{pmatrix}\alpha_1\\ \alpha_2\end{pmatrix} \otimes \begin{pmatrix}\beta_1\\ \beta_2\\ \beta_3\end{pmatrix}_{\mathbf{3}} &= \begin{pmatrix}\alpha_1\beta_2 + \alpha_2\beta_3\\ \alpha_1\beta_3 + \alpha_2\beta_1\\ \alpha_1\beta_1 + \alpha_2\beta_2\end{pmatrix}_{\mathbf{3}} \oplus \begin{pmatrix}\alpha_1\beta_2 - \alpha_2\beta_3\\ \alpha_1\beta_3 - \alpha_2\beta_1\\ \alpha_1\beta_1 - \alpha_2\beta_2\end{pmatrix}_{\mathbf{3'}},\\
\begin{pmatrix}\alpha_1\\ \alpha_2\end{pmatrix} \otimes \begin{pmatrix}\beta_1\\ \beta_2\\ \beta_3\end{pmatrix}_{\mathbf{3'}} &= \begin{pmatrix}\alpha_1\beta_2 - \alpha_2\beta_3\\ \alpha_1\beta_3 - \alpha_2\beta_1\\ \alpha_1\beta_1 - \alpha_2\beta_2\end{pmatrix}_{\mathbf{3}} \oplus \begin{pmatrix}\alpha_1\beta_2 + \alpha_2\beta_3\\ \alpha_1\beta_3 + \alpha_2\beta_1\\ \alpha_1\beta_1 + \alpha_2\beta_2\end{pmatrix}_{\mathbf{3}},\\
\begin{pmatrix}\alpha_1\\ \alpha_2\\ \alpha_3\end{pmatrix}_{\mathbf{3}} \otimes \begin{pmatrix}\beta_1\\ \beta_2\\ \beta_3\end{pmatrix}_{\mathbf{3}} &= (\alpha_1\beta_1 + \alpha_2\beta_3 + \alpha_3\beta_2)_{\mathbf{1}} \oplus \begin{pmatrix}\alpha_2\beta_2 + \alpha_1\beta_3 + \alpha_3\beta_1\\ \alpha_3\beta_3 + \alpha_1\beta_2 + \alpha_2\beta_1\end{pmatrix}\\
&\quad \oplus \begin{pmatrix}\alpha_2\beta_3 - \alpha_3\beta_2\\ \alpha_1\beta_2 - \alpha_2\beta_1\\ \alpha_3\beta_1 - \alpha_1\beta_3\end{pmatrix}_{\mathbf{3}} \oplus \begin{pmatrix}2\alpha_1\beta_1 - \alpha_2\beta_3 - \alpha_3\beta_2\\ 2\alpha_3\beta_3 - \alpha_2\beta_1 - \alpha_1\beta_2\\ 2\alpha_2\beta_2 - \alpha_1\beta_3 - \alpha_3\beta_1\end{pmatrix}_{\mathbf{3'}},\\
\begin{pmatrix}\alpha_1\\ \alpha_2\\ \alpha_3\end{pmatrix}_{\mathbf{3}} \otimes \begin{pmatrix}\beta_1\\ \beta_2\\ \beta_3\end{pmatrix}_{\mathbf{3'}} &= (\alpha_1\beta_1 + \alpha_2\beta_3 + \alpha_3\beta_2)_{\mathbf{1'}} \oplus \begin{pmatrix}\alpha_2\beta_2 + \alpha_1\beta_3 + \alpha_3\beta_1\\ -(\alpha_3\beta_3 + \alpha_1\beta_2 + \alpha_2\beta_1)\end{pmatrix}\\
&\quad \oplus \begin{pmatrix}2\alpha_1\beta_1 - \alpha_2\beta_3 - \alpha_3\beta_2\\ 2\alpha_3\beta_3 - \alpha_2\beta_1 - \alpha_1\beta_2\\ 2\alpha_2\beta_2 - \alpha_1\beta_3 - \alpha_3\beta_1\end{pmatrix}_{\mathbf{3}} \oplus \begin{pmatrix}\alpha_2\beta_3 - \alpha_3\beta_2\\ \alpha_1\beta_2 - \alpha_2\beta_1\\ \alpha_3\beta_1 - \alpha_1\beta_3\end{pmatrix}_{\mathbf{3'}}.
\end{aligned}
\tag{B.8}
$$

C CORRECTIONS TO THE SOFT TERMS FROM MESSENGERS-MATTER COUPLINGS

Reported here are the multiple messenger Higgs corrections, when the messenger Higgs have Yukawa couplings to matter fields, following Evans and Shih [1]. In the limit where there are only one messenger pairs, each messenger will have a suppressed one loop contribution as well as the two loop contributions from messenger-matter mixing as reported in Ref. [2]. We reproduce those corrections here

$$\begin{aligned}\delta_{1\,\text{Higgs}} m_Q^2 = \Bigg[& \left(3\text{Tr}\left(Y_u'^\dagger Y_u'\right) - \frac{16}{3}g_3^2 - 3g_2^2 - \frac{13}{15}g_1^2\right) Y_u' Y_u'^\dagger + 3Y_u' Y_u'^\dagger Y_u' Y_u'^\dagger \\ & + \left(\text{Tr}\left(3Y_d'^\dagger Y_d' + Y_\tau'^\dagger Y_\tau'\right) - \frac{16}{3}g_3^2 - 3g_2^2 - \frac{7}{15}g_1^2\right) Y_d' Y_d'^\dagger + 3Y_d' Y_d'^\dagger Y_d' Y_d'^\dagger \\ & + Y_u' Y_u'^\dagger Y_d' Y_d'^\dagger + Y_d' Y_d'^\dagger Y_u' Y_u'^\dagger + 2Y_u' Y_u^\dagger Y_u Y_u'^\dagger + 2Y_d' Y_d^\dagger Y_d Y_u'^\dagger \\ & - 2Y_u Y_u'^\dagger Y_u' Y_u^\dagger + 3Y_u' Y_u^\dagger \text{Tr}\left(Y_u^\dagger Y_u'\right) + 3Y_u Y_u'^\dagger \text{Tr}\left(Y_u'^\dagger Y_u\right) \\ & - 2Y_d Y_d'^\dagger Y_d' Y_d^\dagger + Y_d' Y_d^\dagger \text{Tr}\left(3Y_d^\dagger Y_d' + Y_\tau^\dagger Y_\tau'\right) + Y_d Y_d'^\dagger \text{Tr}\left(3Y_d'^\dagger Y_d + Y_\tau'^\dagger Y_\tau\right) \Bigg] \frac{\Lambda^2}{256\pi^4},\end{aligned} \tag{C.1}$$

$$\begin{aligned}\delta_{1\,\text{Higgs}} \tilde{m}_{\bar{u}}^2 = \Bigg[& 2\left(3\text{Tr}\left(Y_u'^\dagger Y_u'\right) - \frac{16}{3}g_3^2 - 3g_2^2 - \frac{13}{15}g_1^2\right) Y_u'^\dagger Y_u' + 6Y_u'^\dagger Y_u' Y_u'^\dagger Y_u' \\ & + 2Y_u'^\dagger Y_u Y_u^\dagger Y_u' + 2Y_u'^\dagger Y_d Y_d^\dagger Y_u' + 2Y_u'^\dagger Y_d' Y_d'^\dagger Y_u' - 2Y_u^\dagger Y_u' Y_u'^\dagger Y_u \\ & - 2Y_u^\dagger Y_d' Y_d'^\dagger Y_u + 6Y_u'^\dagger Y_u \text{Tr}\left(Y_u^\dagger Y_u'\right) + 6Y_u^\dagger Y_u' \text{Tr}\left(Y_u'^\dagger Y_u\right) \Bigg] \frac{\Lambda^2}{256\pi^4},\end{aligned} \tag{C.2}$$

$$\begin{aligned}\delta_{1\,\text{Higgs}} \tilde{m}_{\bar{d}}^2 = \Bigg[& 2\left(\text{Tr}\left(3Y_d'^\dagger Y_d' + Y_\tau'^\dagger Y_\tau'\right) - \frac{16}{3}g_3^2 - 3g_2^2 - \frac{7}{15}g_1^2\right) Y_d'^\dagger Y_d' + 6Y_d'^\dagger Y_d' Y_d'^\dagger Y_d' \\ & + 2Y_d'^\dagger Y_d Y_d^\dagger Y_d' + 2Y_d'^\dagger Y_u Y_u^\dagger Y_d' + 2Y_d'^\dagger Y_u' Y_u'^\dagger Y_d' - 2Y_d^\dagger Y_d' Y_d'^\dagger Y_d - 2Y_d^\dagger Y_u' Y_u'^\dagger Y_d \\ & + 2Y_d'^\dagger Y_d \text{Tr}\left(3Y_d^\dagger Y_d' + Y_\tau^\dagger Y_\tau'\right) + 2Y_d^\dagger Y_d' \text{Tr}\left(3Y_d'^\dagger Y_d + Y_\tau'^\dagger Y_\tau\right) \Bigg] \frac{\Lambda^2}{256\pi^4},\end{aligned} \tag{C.3}$$

$$\begin{aligned}\delta_{1\,\text{Higgs}} \tilde{m}_L^2 = \Bigg[& \left(\text{Tr}\left(3Y_d'^\dagger Y_d' + Y_\tau'^\dagger Y_\tau'\right) - 3g_2^2 - \frac{9}{5}g_1^2\right) Y_\tau' Y_\tau'^\dagger \\ & + 3Y_\tau' Y_\tau'^\dagger Y_\tau' Y_\tau'^\dagger + 2Y_\tau' Y_\tau^\dagger Y_\tau Y_\tau'^\dagger - 2Y_\tau Y_\tau'^\dagger Y_\tau' Y_\tau^\dagger \\ & + Y_\tau' Y_\tau^\dagger \text{Tr}\left(3Y_d^\dagger Y_d' + Y_\tau^\dagger Y_\tau'\right) + Y_\tau Y_\tau'^\dagger \text{Tr}\left(3Y_d'^\dagger Y_d + Y_\tau'^\dagger Y_\tau\right) \Bigg] \frac{\Lambda^2}{256\pi^4},\end{aligned} \tag{C.4}$$

$$\begin{aligned}\delta_{1\,\text{Higgs}}\tilde{m}_{\bar{e}}^2 = \Bigg[&2\left(\text{Tr}\left(3Y_d'^{\dagger}Y_d' + Y_\tau'^{\dagger}Y_\tau'\right) - 3g_2^2 - \frac{9}{5}g_1^2\right)Y_\tau'^{\dagger}Y_\tau'Y_\tau' \\ &+ 6Y_\tau'^{\dagger}Y_\tau'Y_\tau'^{\dagger} + 2Y_\tau'^{\dagger}Y_\tau Y_\tau^{\dagger}Y_\tau' - 2Y_\tau^{\dagger}Y_\tau'Y_\tau'^{\dagger}Y_\tau \\ &+ 2Y_\tau'^{\dagger}Y_\tau\text{Tr}\left(3Y_d^{\dagger}Y_d' + Y_\tau^{\dagger}Y_\tau'\right) + 2Y_\tau^{\dagger}Y_\tau'\text{Tr}\left(3Y_d'^{\dagger}Y_d + Y_\tau'^{\dagger}Y_\tau\right)\Bigg]\frac{\Lambda^2}{256\pi^4},\end{aligned} \tag{C.5}$$

$$\delta_{1\,\text{Higgs}}\tilde{m}_{H_u}^2 = \left[-3\text{Tr}\left(Y_u^{\dagger}Y_u'Y_u'^{\dagger}Y_u + Y_u^{\dagger}Y_d'Y_d'^{\dagger}Y_u + 2Y_u^{\dagger}Y_uY_u'^{\dagger}Y_u'\right)\right]\frac{\Lambda^2}{256\pi^4}, \tag{C.6}$$

$$\begin{aligned}\delta_{1\,\text{Higgs}}\tilde{m}_{H_d}^2 = \Bigg[&-3\text{Tr}\left(Y_d^{\dagger}Y_u'Y_u'^{\dagger}Y_d + Y_d^{\dagger}Y_d'Y_d'^{\dagger}Y_d + 2Y_d^{\dagger}Y_dY_d'^{\dagger}Y_d'\right) \\ &-3\text{Tr}\left(Y_\tau^{\dagger}Y_\tau'Y_\tau'^{\dagger}Y_\tau + 2Y_\tau^{\dagger}Y_\tau Y_\tau'^{\dagger}Y_\tau'\right)\Bigg]\frac{\Lambda^2}{256\pi^4},\end{aligned} \tag{C.7}$$

and the A terms are

$$\begin{aligned}A_u^* &= -\frac{\Lambda}{16\pi^2}\left(\left(Y_u'Y_u'^{\dagger} + Y_d'Y_d'^{\dagger}\right)Y_u + 2Y_uY_u'^{\dagger}Y_u'\right), \\ A_d^* &= -\frac{\Lambda}{16\pi^2}\left(\left(Y_u'Y_u'^{\dagger} + Y_d'Y_d'^{\dagger}\right)Y_d + 2Y_dY_d'^{\dagger}Y_d'\right), \\ A_\tau^* &= -\frac{\Lambda}{16\pi^2}\left(Y_\tau'Y_\tau'^{\dagger}Y_\tau + 2Y_\tau Y_\tau'^{\dagger}Y_\tau'\right).\end{aligned} \tag{C.8}$$

When there are more messenger-Higgs pairs there are corrections from couplings between the pairs of messengers. One term like this generated per pair of Higgs fields, for example in a three Higgs model there will be corrections from 1 coupling to 2 and 3 and from 2 coupling to 3. These corrections are

$$\begin{aligned}\delta_{2\,\text{Higgs}}m_Q^2 = \Bigg[&3Y_{u1}'Y_{u2}'^{\dagger}\text{Tr}\left(Y_{u2}'^{\dagger}Y_{u1}'\right) + 3Y_{u2}'Y_{u1}'^{\dagger}\text{Tr}\left(Y_{u1}'^{\dagger}Y_{u2}'\right) + 2\left(Y_{u1}'Y_{u1}'^{\dagger}Y_{u2}'Y_{u2}'^{\dagger} + Y_{u2}'Y_{u2}'^{\dagger}Y_{u1}'Y_{u1}'^{\dagger}\right) \\ &\left(Y_{u1}'Y_{u2}'^{\dagger}Y_{u2}'Y_{u1}'^{\dagger} + Y_{u2}'Y_{u1}'^{\dagger}Y_{u1}'Y_{u2}'^{\dagger}\right) + \left(Y_{u1}'Y_{d2}'^{\dagger}Y_{d2}'Y_{u1}'^{\dagger} + Y_{u2}'Y_{d1}'^{\dagger}Y_{d1}'Y_{u2}'^{\dagger}\right) \\ &+ Y_{d1}'Y_{d2}'^{\dagger}\text{Tr}\left(3Y_{d2}'^{\dagger}Y_{d1}' + Y_{e2}'^{\dagger}Y_{e1}'\right) + Y_{d2}'Y_{d1}'^{\dagger}\text{Tr}\left(3Y_{d1}'^{\dagger}Y_{d2}' + Y_{e1}'^{\dagger}Y_{e2}'\right) \\ &+ 2\left(Y_{d1}'Y_{d1}'^{\dagger}Y_{d2}'Y_{d2}'^{\dagger} + Y_{d2}'Y_{d2}'^{\dagger}Y_{d1}'Y_{d1}'^{\dagger}\right) + \left(Y_{d1}'Y_{d2}'^{\dagger}Y_{d2}'Y_{d1}'^{\dagger} + Y_{d2}'Y_{d1}'^{\dagger}Y_{d1}'Y_{d2}'^{\dagger}\right) \\ &+ \left(Y_{d1}'Y_{u2}'^{\dagger}Y_{u2}'Y_{d1}'^{\dagger} + Y_{d2}'Y_{u1}'^{\dagger}Y_{u1}'Y_{d2}'^{\dagger}\right)\Bigg]\frac{\Lambda^2}{256\pi^4},\end{aligned} \tag{C.9}$$

$$\delta_{2\,\text{Higgs}} m_{\bar{u}}^2 = \Big[6 Y'^{\dagger}_{u1} Y'_{u2} \text{Tr}\left(Y'_{u2} Y'^{\dagger}_{u1}\right) + 6 Y'^{\dagger}_{u2} Y'_{u1} \text{Tr}\left(Y'_{u1} Y'^{\dagger}_{u2}\right) + 4\left(Y'^{\dagger}_{u1} Y'_{u1} Y'^{\dagger}_{u2} Y'_{u2} + Y'^{\dagger}_{u2} Y'_{u2} Y'^{\dagger}_{u1} Y'_{u1}\right) \\ 2\left(Y'^{\dagger}_{u1} Y'_{u2} Y'^{\dagger}_{u2} Y'_{u1} + Y'^{\dagger}_{u2} Y'_{u1} Y'^{\dagger}_{u1} Y'_{u2}\right) + 2\left(Y'^{\dagger}_{u1} Y'_{d2} Y'^{\dagger}_{d2} Y'_{u1} + Y'^{\dagger}_{u2} Y'_{d1} Y'^{\dagger}_{d1} Y'_{u2}\right) \Big] \frac{\Lambda^2}{256\pi^4}, \tag{C.10}$$

$$\delta_{2\,\text{Higgs}} m_{\bar{d}}^2 = \Big[2 Y'^{\dagger}_{d1} Y'_{d2} \text{Tr}\left(3 Y'_{d2} Y'^{\dagger}_{d1} + Y'_{e2} Y'^{\dagger}_{e1}\right) + 2 Y'^{\dagger}_{d2} Y'_{d1} \text{Tr}\left(3 Y'_{d1} Y'^{\dagger}_{d2} + Y'_{e1} Y'^{\dagger}_{e2}\right) \\ + 4\left(Y'^{\dagger}_{d1} Y'_{d1} Y'^{\dagger}_{d2} Y'_{d2} + Y'^{\dagger}_{d2} Y'_{d2} Y'^{\dagger}_{d1} Y'_{d1}\right) + 2\left(Y'^{\dagger}_{d1} Y'_{d2} Y'^{\dagger}_{d2} Y'_{d1} + Y'^{\dagger}_{d2} Y'_{d1} Y'^{\dagger}_{d1} Y'_{d2}\right) \\ + 2\left(Y'^{\dagger}_{d1} Y'_{u2} Y'^{\dagger}_{u2} Y'_{d1} + Y'^{\dagger}_{d2} Y'_{u1} Y'^{\dagger}_{u1} Y'_{d2}\right) \Big] \frac{\Lambda^2}{256\pi^4}, \tag{C.11}$$

$$\delta_{2\,\text{Higgs}} m_{L}^2 = \Big[Y'_{e1} Y'^{\dagger}_{e2} \text{Tr}\left(3 Y'^{\dagger}_{d2} Y'_{d1} + Y'^{\dagger}_{e2} Y'_{e1}\right) + Y'_{e2} Y'^{\dagger}_{e1} \text{Tr}\left(3 Y'^{\dagger}_{d1} Y'_{d2} + Y'^{\dagger}_{e1} Y'_{e2}\right) \\ + 2\left(Y'_{e1} Y'^{\dagger}_{e1} Y'_{e2} Y'^{\dagger}_{e2} + Y'_{e2} Y'^{\dagger}_{e2} Y'_{e1} Y'^{\dagger}_{e1}\right) + \left(Y'_{e1} Y'^{\dagger}_{e2} Y'_{e2} Y'^{\dagger}_{e1} + Y'_{e2} Y'^{\dagger}_{e1} Y'_{e1} Y'^{\dagger}_{e2}\right) \Big] \frac{\Lambda^2}{256\pi^4}, \tag{C.12}$$

$$\delta_{2\,\text{Higgs}} m_{\bar{e}}^2 = \Big[2 Y'^{\dagger}_{e1} Y'_{e2} \text{Tr}\left(3 Y'_{d2} Y'^{\dagger}_{d1} + Y'_{e2} Y'^{\dagger}_{e1}\right) + 2 Y'^{\dagger}_{e2} Y'_{e1} \text{Tr}\left(3 Y'_{d1} Y'^{\dagger}_{d2} + Y'_{e1} Y'^{\dagger}_{e2}\right) \\ + 4\left(Y'^{\dagger}_{e1} Y'_{e1} Y'^{\dagger}_{e2} Y'_{e2} + Y'^{\dagger}_{e2} Y'_{e2} Y'^{\dagger}_{e1} Y'_{e1}\right) + 2\left(Y'^{\dagger}_{e1} Y'_{e2} Y'^{\dagger}_{e2} Y'_{e1} + Y'^{\dagger}_{e2} Y'_{e1} Y'^{\dagger}_{e1} Y'_{e2}\right) \Big] \frac{\Lambda^2}{256\pi^4}. \tag{C.13}$$

The MSSM-like Higgs will not get a correction from having multiple messengers outside of copies of the single messenger result. The A terms are also unmodified.

The corrections, in the third family limit with real Yukawa couplings, are

$$\begin{aligned}
\delta_{2\,\text{Higgs}} m_Q^2 &= \frac{\Lambda^2}{128\pi^4}(6 y_t'^2 y_t''^2 + 6 y_b'^2 y_b''^2 + y_b'' y_b' y_e' y_e'' + y_b'^2 y_t''^2 + y_t'^2 y_b''^2), \\
\delta_{2\,\text{Higgs}} m_{\bar{u}}^2 &= \frac{\Lambda^2}{128\pi^4}(12 y_t'^2 y_t''^2 + y_b'^2 y_t''^2 + y_t'^2 y_b''^2), \\
\delta_{2\,\text{Higgs}} m_{\bar{d}}^2 &= \frac{\Lambda^2}{128\pi^4}(12 y_b'^2 y_b''^2 + 2 y_b'' y_b' y_e' y_e'' + y_b'^2 y_t''^2 + y_t'^2 y_b''^2), \\
\delta_{2\,\text{Higgs}} m_L^2 &= \frac{\Lambda^2}{128\pi^4}(4 y_\tau'^2 y_\tau''^2 + 3 y_\tau'' y_\tau' y_b'' y_b'), \\
\delta_{2\,\text{Higgs}} m_{\bar{e}}^2 &= \frac{\Lambda^2}{64\pi^4}(4 y_\tau'^2 y_\tau''^2 + 3 y_\tau'' y_\tau' y_b'' y_b').
\end{aligned} \tag{C.14}$$

Let us check if these results are consistent. If we work with a simplified superpotential with only leptons and messengers, where our messenger Yukawas are

degenerate and diagonal, the superpotential is

$$W = Y_e L\bar{e}H_d + Y_e' L\bar{e}M_{d1} + Y_e' L\bar{e}M_{d2} + (M + \theta^2 F)M_{ui}M_{di}, \tag{C.15}$$

We introduce two new linear combinations of messengers

$$\Phi_{u/d} = \frac{1}{\sqrt{2}}\left(M_{u/d1} + M_{u/d2}\right), \qquad \Theta_{u/d} = \frac{1}{\sqrt{2}}\left(-M_{u/d1} + M_{u/d2}\right), \tag{C.16}$$

and so the superpotential becomes

$$W = Y_e L\bar{e}H_d + \sqrt{2}Y_e' L\bar{e}\Phi_d + (M + \theta^2 F)\left(\Phi_u\Phi_d + \Theta_u\Theta_d\right). \tag{C.17}$$

The rotation has decoupled the Θ fields, leaving us with messenger-matter mixing through Φ, and so the single messenger case with an additional factor of $\sqrt{2}$. We can look at the structure of the single messenger corrections $\delta m_{\tilde{L}}^2$ for instance, and notice that the terms that are quadratic our messenger Yukawas will not contribute to the correction from two sets of messengers, but terms quartic in messenger couplings will. These quartic terms are

$$\begin{aligned}
\delta m_{\tilde{L}}^2(\sqrt{2}Y') &\supset \frac{\Lambda^2}{256\pi^4}\left[3(\sqrt{2}Y_e')^4 + \mathrm{Tr}\left(3(\sqrt{2}Y_d')^2 + (\sqrt{2}Y_e')^2\right)(\sqrt{2}Y_e')^2\right], \\
&\to \frac{\Lambda^2}{256\pi^4}\left[6Y_e'^4 + 2\mathrm{Tr}\left(3Y_d'^2 + Y_e'^2\right)Y_e'^2\right] + \\
&\quad \frac{\Lambda^2}{256\pi^4}\left[6Y_e'^4 + 2\mathrm{Tr}\left(3Y_d'^2 + Y_e'^2\right)Y_e'^2\right].
\end{aligned} \tag{C.18}$$

The second term agrees with (C.12) taken in the same limit.

References

[1] J. A. Evans and D. Shih, JHEP **08**, 093 (2013), arXiv:1303.0228 [hep-ph].

[2] M. Abdullah, I. Galon, Y. Shadmi, and Y. Shirman, JHEP **06**, 057 (2013), arXiv:1209.4904 [hep-ph].